

# **Light-Matter Interaction and Quantum Chaos in Semiconductor Nanostructures and Optical Microcavities**

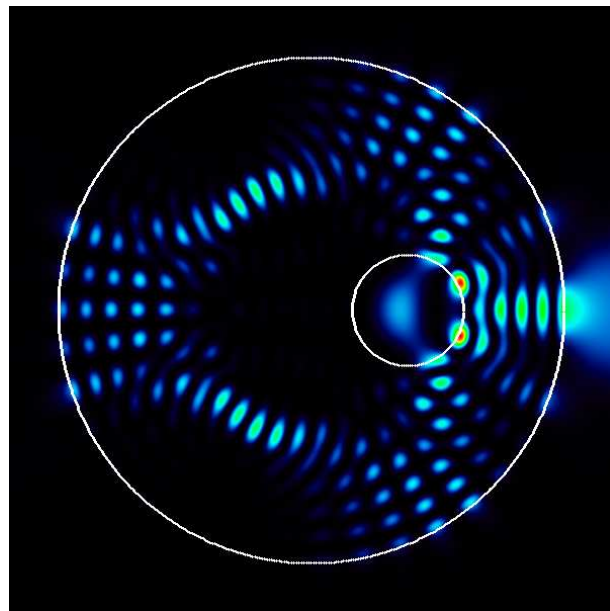
Habilitationsschrift

von

**Dr. Jan Wiersig**

dem Fachbereich Physik  
der Universität Bremen  
vorgelegt im

Juli 2007





# Contents

<b>1</b>	<b>Introduction</b>	<b>3</b>
<b>2</b>	<b>Optical properties of microcavities</b>	<b>9</b>
2.1	Mode equations . . . . .	15
2.2	Boundary element method . . . . .	18
2.3	Unidirectional light emission from high- $Q$ modes . . . . .	29
2.4	Microcrystals . . . . .	38
2.5	Formation of long-lived, scarlike modes . . . . .	54
2.6	Unidirectional light emission and unstable manifolds . . . . .	61
2.7	Micropillar cavities . . . . .	66
<b>3</b>	<b>Light-matter interaction in semiconductor nanostructures</b>	<b>73</b>
3.1	Theoretical framework . . . . .	74
3.2	Luminescence from semiconductor quantum dots . . . . .	80
3.3	Time-resolved photoluminescence in microcavities . . . . .	93
3.4	Quantum dot-based microcavity lasers . . . . .	99
<b>4</b>	<b>Nonlinear dynamics and quantum chaos in nanostructures</b>	<b>123</b>
4.1	Two-dimensional electron gas . . . . .	126
4.2	Coupled nanomechanical shuttles . . . . .	133
4.3	Multi-walled carbon nanotubes . . . . .	141
<b>5</b>	<b>Conclusions and future directions</b>	<b>147</b>
<b>Bibliography</b>		<b>151</b>
<b>Appendix</b>		<b>179</b>

*Contents*

---

# 1 Introduction

The fabrication and analysis of semiconductor nanostructures is one of the most rapidly developing areas of condensed-matter physics [1]. Such structures allow the confinement of charge carriers in one, two or three directions on nanometer scales. The corresponding low-dimensional structures are called quantum wells, quantum wires and quantum dots.

Most of the interesting physical effects in nanostructures are related to the modification of the density of states (DOS) of carriers that arises from the quantization of the energy due to the confinement. In a bulk semiconductor the free single-particle DOS has a square root dependence on the energy above the band gap edge. In two dimensions the DOS reduces to a step-like function. An example of quantum wells (QWs) is depicted in Fig. 1.1(a). A single QW consists of a thin sheet of a semiconductor material with a lower band gap sandwiched between layers of a semiconductor material with a wider band gap. The carriers are trapped in the low-band gap material. In a one-dimensional system, the DOS is strongly peaked. Figure 1.1(b) shows as an example a carbon nanotube, a one-atom thick sheet of graphite seamlessly rolled up to a cylinder with a diameter of the order of a nanometer [2]. For zero-dimensional systems, the free single-particle DOS is discrete as in the case of an atom. Semiconductor quantum dots (QDs) are therefore often referred to as “artificial atoms”; see Fig. 1.1(c). In QDs, carriers are fully confined by the wider band gap of the surrounding material. These systems attract considerable attention due to their potential for fundamental studies as well as device applications, such as cavity-quantum electrodynamics [3–5], quantum information and computation [6, 7], lasers [8] and non-classical light sources [9–11].

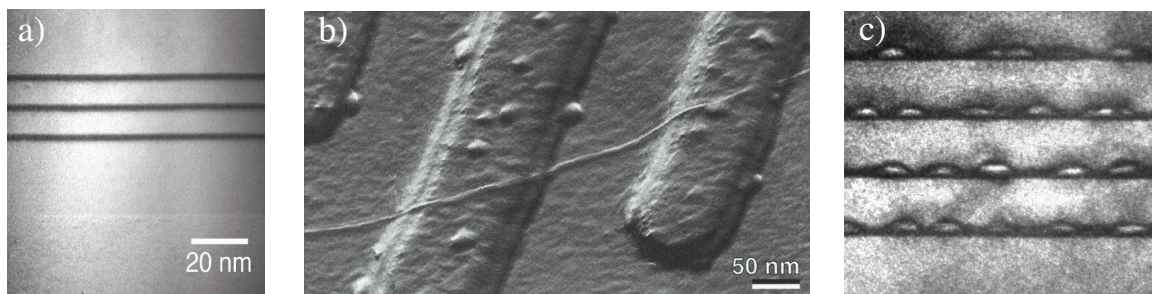


**Figure 1.1:** Nanostructures of two, one and zero dimension: (a) three  $\text{Cd}_{0.4}\text{Zn}_{0.6}\text{Se}$  quantum wells embedded in  $\text{ZnSe}$  [12], (b) individual carbon nanotube connected to two electrodes [13], and (c)  $\text{InGaAs}$  quantum dots embedded in  $\text{GaAs}$  [14].

Dielectric microstructures are the photonic analogs of semiconductor nanostructures. Decreasing the dimensionality of the structure modifies the *optical* DOS in a similar way as the carrier DOS changes when going from bulk to quantum well, quantum wire and

quantum dot. The photonic equivalents are planar cavities, waveguides and microcavities. Figure 1.2 shows some examples of optical microstructures.

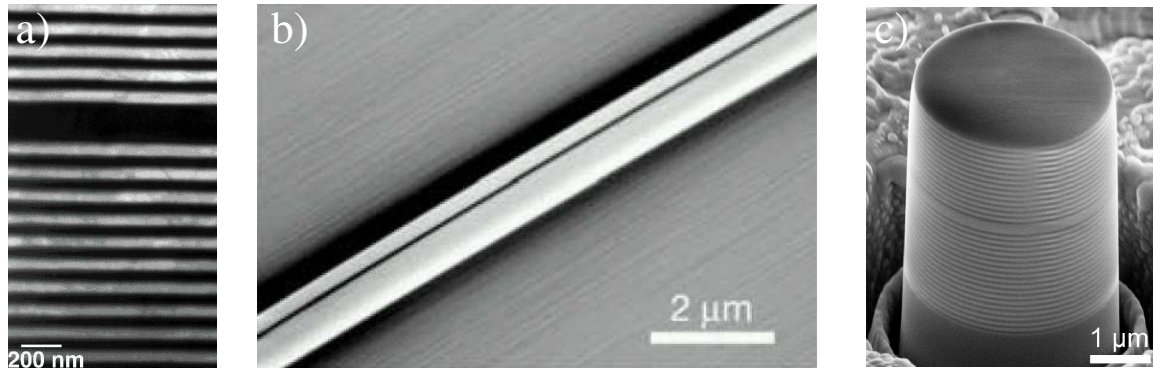


**Figure 1.2:** Optical microstructures of two, one and zero dimension: (a) vertical-cavity surface-emitting laser (VCSEL) [15], (b) silica waveguide [16], and (c) VCSEL-micropillar cavity [17,18].

Optical microcavities, such as the micropillar in Fig. 1.2(c), confine photons in all three directions of space. This is important for a wide range of applications and research areas [19]. There are two basic mechanisms for light confinement in microcavities. The first mechanism is total internal reflection at the sidewalls of the cavity. Microcavities based on total internal reflection are for instance microdisks [20–22], microspheres [23], and microtori [24]. The second mechanism is distributed Bragg reflection at a periodic dielectric structure which lead to the formation of a photonic band gap. This effect is exploited in photonic crystal defect cavities [25] and vertical-cavity surface-emitting laser- (VCSEL-) micropillars [26, 27]. For principle reasons, the light confinement in microcavities is not perfect. Even if we ignore absorptive losses in the material, there is always light continuously lost to the outside. This leakage of light is often desired to a certain degree, for example for light emission from a microlaser. Thus, optical microcavities are inherently open systems, and consequently, the corresponding electromagnetic eigenmodes are quasi-bound states. Each such mode is characterized by its resonance frequency  $\omega$  and lifetime  $\tau$ , which are typically summarized in the quality factor  $Q = \omega/\Delta\omega$ , where  $\Delta\omega = 1/\tau$  is the mode linewidth. While the  $Q$ -factor characterizes the temporal light confinement, the spatial confinement is quantified by the effective mode volume  $V$ , defined as the spatial integral over the electric-field intensity normalized to unity at the field maximum.

Optical microcavities permit to tailor the emission characteristics of a light source. For example, the isotropic emission of a light source can be made directional by coupling it to a suitable cavity mode. Moreover, quantum aspects of light-matter interaction, such as the rate of spontaneous emission, can be controlled by modifying the optical DOS, as proposed by E. M. Purcell [28]. The strength of this Purcell effect is in the ideal case proportional to  $Q/V$ . In order to observe a strong enhancement of spontaneous emission, the microcavities should have both a high  $Q$ -factor and a small effective mode volume  $V$ . The Purcell effect has been demonstrated for molecules [29], atoms [30], and electrons [31]. In the case of solid-state nanostructures, the Purcell effect was first observed for QWs [32,33] and later for QDs [34–36]. The control of spontaneous emission

---

is essential for novel light sources, like single-photon sources [37] and lasers with ultralow threshold-current densities [38, 39].

Semiconductor lasers based on microcavity resonators have properties superior to those of conventional semiconductor lasers. For instance, the microscale size of the cavities ensures that the resonance frequencies are well separated allowing for genuine single-mode laser operation. Moreover, together with the Purcell effect a large spontaneous emission factor  $\beta$  can be obtained. In laser physics, the  $\beta$ -factor is defined as the ratio of the spontaneous emission rate into the laser mode divided by the total spontaneous emission rate. In conventional lasers, the  $\beta$ -factor is very small, say  $\beta \approx 10^{-5}$ , because the laser cavity supports many modes [40]. Since the spontaneous emission into nonlasing modes is a loss channel, a low  $\beta$ -factor results in a large threshold current needed to achieve lasing. High- $\beta$  laser have therefore ultra-low thresholds. In the limit  $\beta \rightarrow 1$ , i.e., all spontaneous emission goes into the lasing mode, the threshold even vanishes, and one speaks about the “thresholdless laser” [41–44]. There is, however, still a transition from spontaneous to mainly stimulated emission. In order to investigate this transition, one can measure the photon statistics of the emitted light [44] in a Hanbury-Brown and Twiss measurement setup [45].

Concerning the gain medium, QDs are particularly promising for laser applications because they in principle offer several advantages compared to bulk material or QWs [1, 8]: enhanced spectral purity, a small linewidth enhancement factor, high temperature stability, and ultralow threshold-current densities, to name only a few. For semiconductor lasers based on planar cavities and bulk material or QWs as active medium a microscopic theory including many-body effects already exists [46–49]. Some important aspects for these semiconductor lasers are carrier heating [50], transient instabilities and relaxation oscillations [51], and the laser linewidth [22]. It is of great importance to have such a microscopic theory also for QDs-based microcavity lasers.

A very different class of nanostructures are nanoelectromechanical systems (NEMS). These are nanosized systems where mechanical degrees of freedom are strongly coupled to electronic degrees of freedom [52, 53]. NEMS are potentially useful in a wide variety of technological applications, including ultrafast sensors, actuators, and signal processing components. Due to the nonlinear coupled degrees of freedom NEMS can exhibit complex dynamics. Nonlinear dynamics in NEMS and other nanostructures forms an interesting research topic on its own. Under certain conditions, nonlinear dynamical systems show a phenomenon known as chaos. The most important characteristic of chaotic systems is the sensitivity to initial conditions as it was discovered at the beginning of the twentieth century by H. Poincaré and others [54]. Important model systems to study chaos are planar billiards, see, e.g., Refs. [55–57]. In a billiard a point-like particle moves freely in a domain with elastic reflections at the boundary. Depending on the shape of the boundary the systems shows a variety of dynamical behaviors ranging from integrable to fully chaotic. Billiard-like solid-state devices are studied in the field of mesoscopic physics [58–60]. These devices operate at the border between classical and quantum mechanics, i.e., in the so-called semiclassical (short-wavelength) regime, where quantum-classical correspondence becomes relevant. Studies of this correspondence belong to the field of quantum chaos [61–65].

In recent years the focus of the field of quantum chaos has shifted from closed to open systems. Optical microcavities are ideal candidates for such open systems and allow for a direct comparison with experiments. Of particular interest are deformed microdisks – quasi-two-dimensional cavities with a non-circular cross section, some examples are shown in Fig. 1.3. Deformed microdisks can be regarded as open billiards [66, 67], replacing the classical particle and the quantum mechanical wave function by light rays and the electromagnetic field. One practical issue which has strongly driven this research area is “the quest for unidirectional light emission” [68] from such non-circular microdisks. Unidirectional emission has been reported for spiral-shaped cavities [69], however, a degradation of the  $Q$ -factor and, thus, the lifetime of the mode, spoils the usability of this approach. Another application of deformed microdisks is the use as filters [70]. In some cases, as for the microcrystals shown in Fig. 1.3(b), the cross-sectional shape of the cavities is inherently non-circular.

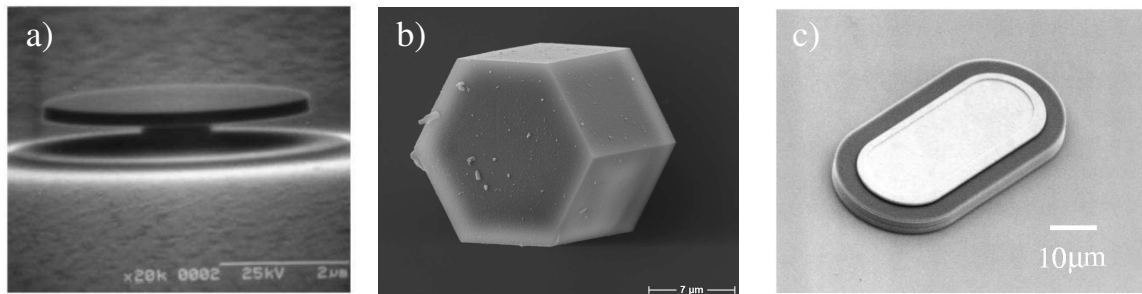


**Figure 1.3:** Some examples of ideal and “deformed microdisks”: (a) circular InGaAs/InGaAsP microdisk [71], (b) AlPO<sub>4</sub> – 5 microcrystal [72, 73], and (c) GaAs-microstadium [74].

## Purpose of this work and overview

In this Habilitation thesis, we study nonlinear dynamics, quantum chaos, and light-matter interaction in semiconductor nanostructures and optical microcavities. We begin with an analysis of the optical properties of microcavities in Chapter 2. Two different types of cavities are considered: deformed microdisks and VCSEL-micropillar cavities. Deformed microdisks are discussed in the context of quantum chaos. It is our intention to show that on the one hand deformed microdisks are ideal systems to further develop the field of quantum chaos in open systems. On the other hand, nonlinear dynamics and quantum chaos provide new concepts beyond the traditional approaches in optics which can be exploited for novel cavity designs. To do so, we first introduce the boundary element method which allows for an efficient computation of highly-excited modes in deformed microdisks. Based on ideas from quantum chaos we derive two independent schemes to solve the longstanding problem of unidirectional light emission from high quality modes of microdisks. Subsequently, we derive for a class of cavity geometries analytical approximations of mode properties based on ray dynamics and ray-wave correspondence. Moreover, we contribute to the understanding of wave localization in open systems by showing the

---

formation of such localized states in optical microcavities. Finally, we discuss optical modes in micropillar cavities for various different material systems and compare them to experimental data.

The goal of Chapter 3 is to develop a systematic microscopic description of light-matter interaction in semiconductor QDs including many-body and quantum-optical effects. First, we review several aspects of the general approach including the equation-of-motion technique for photon and carrier operators [75] and the cluster expansion truncation scheme [76]. We use these methods to derive the semiconductor luminescence equations (SLE) for semiconductor QDs. The SLE can be regarded as generalization of the well-known semiconductor Bloch equations [77]. In contrast to the latter equations the SLE treat the light field in the incoherent regime fully quantum mechanically. Using the SLE we study the influence of Coulomb correlation effects on spectral and dynamical properties of the photoluminescence from semiconductor QDs in free space and from QDs embedded into optical microcavities. The mode characteristics computed in Chapter 2 enter here as input parameters. The SLE are also capable of describing laser action in semiconductor QDs. We derive an extended version of the SLE, which incorporates carrier-photon correlations. This gives direct access to the photon autocorrelation function and, thereby, to the photon statistics of the laser emission. Moreover, we analyze the first-order coherence of the emitted light.

Chapter 4 is devoted to a discussion of nonlinear dynamics and quantum chaos in the context of charge transport in nanostructures. We present studies for various types of nanostructures. First, we consider the magnetoresistance of a two-dimensional electron gas with an additional periodic potential. Second, we analyze transport properties of nanoelectromechanical charge shuttles. Here, the mechanical degree of freedom of the device allows to shuttle electrons between the electrodes leading to low-noise transport. We consider the more general case of a pair of charge shuttles which are coupled by tunneling. The formalism of single electron tunneling [78] is briefly explained. Finally, we discuss multi-walled carbon nanotubes. These systems show peculiar transport properties [79–81]. In order to understand the origin of this behavior we investigate the electronic DOS of double-walled carbon nanotubes using a tight-binding model.



## 2 Optical properties of microcavities

The possibility to confine photons in all three spatial directions using microcavities has triggered intense basic and applied research in physics over the past decade [19], e.g., research on ultralow threshold lasing [38, 39], single-photon emitters [82, 83], and solid-state cavity quantum electrodynamics [3, 5, 84]. A prerequisite for performing such studies is the knowledge of the relevant optical eigenmodes of the microcavities. An optical mode is defined as a solution of Maxwell's equations with resonance frequency  $\omega$ , in the same way as a quantum mechanical eigenstate is a solution of the Schrödinger equation with given eigenenergy. However, microcavities are always open systems as light leaks out of the cavity. Hence, an optical mode is a quasi-bound state decaying exponentially in time with lifetime  $\tau$ . In the optics community this is expressed in terms of the dimensionless quality factor  $Q = \omega\tau$ . A further important property of an optical mode is its spatial mode structure, consisting of the near-field and the far-field pattern.

In general, the optical modes in microcavities cannot be computed analytically. Over the last decades, several numerical schemes have been developed for this purpose. Finite-difference time-domain (FDTD) methods [85] are well suited to model light propagation through microstructures [86]. However, the computation of optical modes with high  $Q$ -factors requires extremely long computation times. For this reason it is more convenient to work directly in the frequency domain. Another advantage is that a frequency-dependent index of refraction can be easily included. Available methods are wave matching [87], boundary element methods [88–90] and volume element methods [91–94]. Figure 2.1 shows as an example a mode in a “deformed microdisk” computed with the boundary element method.

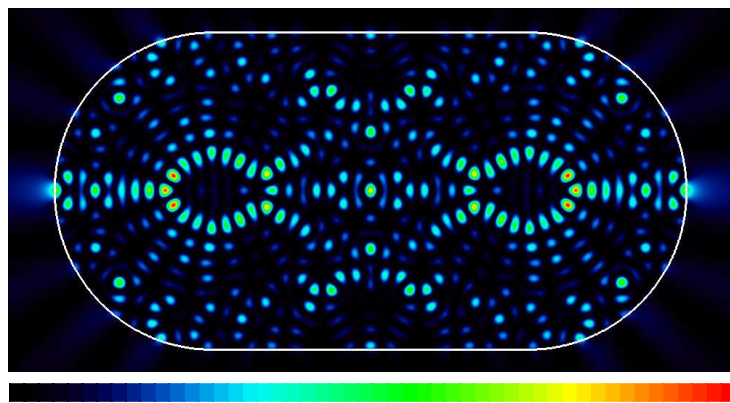


**Figure 2.1:** Calculated near-field intensity pattern of an optical mode in a semiconductor microstadium. Intensity is higher for redder colours, and vanishes in the dark regions. The refractive index inside the cavity is  $n = 3.3$ . Note the light intensity outside the cavity.

From the complex spatial mode pattern in Fig. 2.1 it becomes apparent that it is desirable to not only compute the modes but also to understand their relevant features. This is of high practical value for the development of novel cavity designs. It turns out that much understanding about the wave dynamics in microcavities can be gained by studying the wave-ray correspondence [66, 95]. This is in analogy to studying the quantum-classical correspondence in the field of quantum chaos [61–64].

A frequently studied class of model systems in nonlinear dynamics and quantum chaos are planar billiards, see, e.g., Refs. [55–57, 96–102]. In a classical billiard a point-like particle moves freely in a two-dimensional plane domain with elastic reflections at a hard boundary. The character of the dynamics is controlled by the shape of the boundary curve. Figure 2.2 illustrates as an example the stadium billiard given by two semicircles and two parallel segments [103]. A typical pair of trajectories with very similar initial conditions is shown. After a few reflections the two trajectories have completely separated. This sensitive dependence on initial conditions obviously destroys the long-term predictability. Fully chaotic systems, such as the stadium billiard, exhibit this sensitivity for almost all pairs of initial conditions. The other extreme case is the class of integrable billiards, such as the circular billiard, which show regular dynamics without sensitive dependence on initial conditions. Generic billiards are partially chaotic, i.e., chaotic and regular motion coexist in phase space [55]. These systems are often referred to as “systems with mixed phase space”.

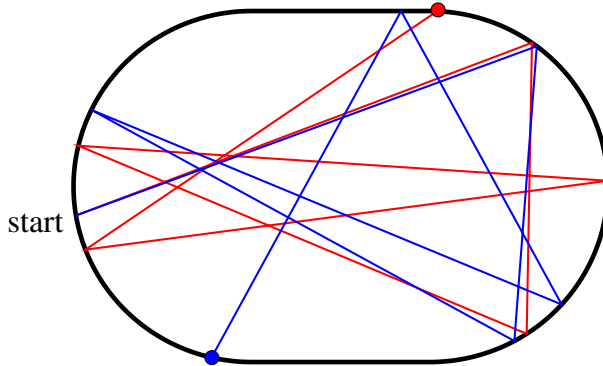


**Figure 2.2:** Chaos in the stadium billiard: two classical trajectories starting at the same position but with slightly different initial direction separate after a few elastic reflections at the boundary.

For a classical billiard the associated quantum billiard is defined by the free single-particle Schrödinger equation with wave functions that vanish on and outside the boundary of the same domain. In general, such an infinite-potential-well problem cannot be solved by means of separation of variables. Note that as the Schrödinger equation is linear, it cannot possess exponential instability in time as do the classical equations of motion. Understanding the quantum mechanical implications of classical chaos is the main issue in the field of quantum chaos [61–64]. A fundamental tool used in this field to study the quantum-classical correspondence of fully and partially chaotic systems is the so-called semiclassical approximation, which is an expansion in terms of the small but finite

---

wavelength divided by a characteristic length scale. The semiclassical approximation still contains quantum effects like interference.

As it will be demonstrated in Section 2.1 the mode equation for a microdisk corresponds to the time-independent Schrödinger equation of a quantum billiard with the same boundary curve if the electromagnetic field is identified with the quantum mechanical wave function. Correspondingly, light rays can be identified with classical trajectories. However, there is a fundamental difference between an optical microdisk and a quantum billiard. The boundary conditions of a dielectric cavity imply leakage of light. Hence optical microdisks represent a realization of open billiards [66, 87]. These systems offer the possibility to investigate the *ray-wave correspondence of open systems* in connection with experiments and applications. Such an investigation requires a highly efficient numerical method to compute the optical modes. For this purpose, we introduce in Section 2.2 the boundary element method. It is worth to mention that not only deformed microdisks are interesting for quantum chaos but also other cavity geometries such as vertical-cavity surface-emitting lasers (VCSELs) [104, 105] and deformed microspheres [106, 107].

In the first experiments on microdisks, circular-shaped disks had been studied [20–22] because they provide the largest quality factors. Figure 2.3(a) illustrates a ray trajectory in a circular microdisk with radius  $R$  trapped by total internal reflection. The corresponding modes are called whispering-gallery modes named after the whispering gallery at the St. Paul’s Cathedral in London. There, Lord Rayleigh analyzed propagation of acoustic waves [108].

The rotational symmetry of a circular microdisk results in an uniform far-field emission pattern, which is a considerable disadvantage for most applications, in particular for microlasers. Breaking the rotational symmetry, e.g., by deforming the boundary, leads in almost every case to an open billiard with partially or fully chaotic ray dynamics and an improved far-field emission pattern [66, 67, 109–111]. To illustrate the ray dynamics in a deformed microcavity, we consider a specific boundary curve, the limaçon of Pascal which reads in polar coordinates  $(\rho, \phi)$

$$\rho(\phi) = R(1 + \varepsilon \cos \phi) . \quad (2.1)$$

The limiting case of vanishing deformation parameter  $\varepsilon$  is the circle. The corresponding family of closed cavities is known as “limaçon billiards” [57, 96]. Figure 2.3(c) shows a trajectory in the limaçon cavity for  $\varepsilon = 0.43$ . Initially, the ray fulfills the condition for total internal reflection  $\sin \chi > 1/n$ ,  $\chi$  is the angle of incidence measured from the surface normal. After some time the condition is not satisfied anymore and the ray escapes refractively according to Snell’s and Fresnel’s laws.

A deeper understanding of the ray dynamics in microdisks can be acquired through a study of the phase space of the corresponding closed billiard system. The phase space is four dimensional consisting of two spatial degrees of freedom and two conjugate momenta. But due to conservation of energy, the motion actually takes place on a three-dimensional surface. A powerful tool in the field of nonlinear dynamics to investigate the dynamics on such a surface is the so-called Poincaré surface of section (SOS) [112]. It is a plot of the intersection points of a set of trajectories with a surface in phase space. For the trivial

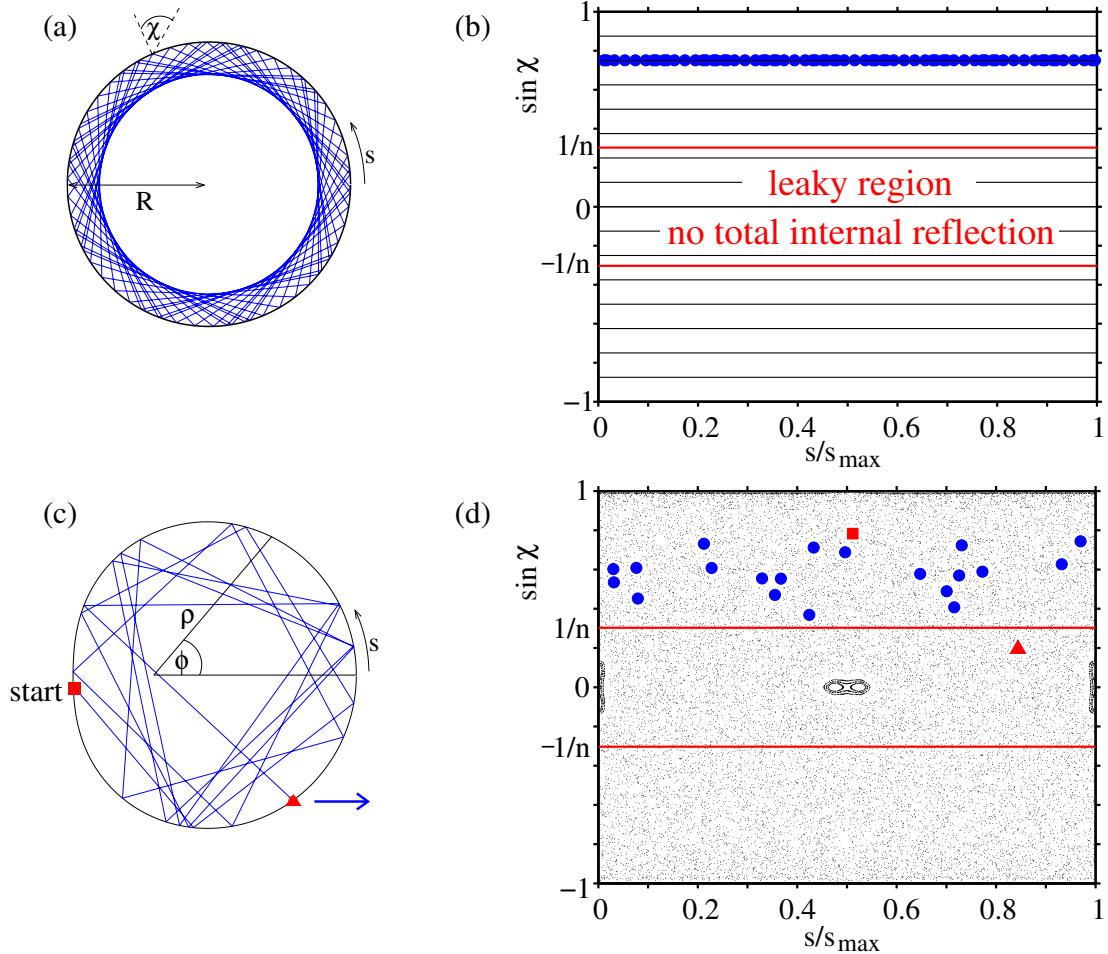


**Figure 2.3:** (a) Whispering-gallery ray trajectory in the circular microdisk. (b) Poincaré surface of section showing the trajectory (blue dots) in phase space;  $s$  is the arclength coordinate and  $\chi$  is the angle of incidence. The critical lines  $\sin \chi_c = \pm 1/n$  (red) enclose the leaky region. Typical trajectories in the circular billiard fill a line of constant  $\sin \chi$  (black lines). (c) Chaotic ray trajectory in the limaçon cavity defined in Eq. (2.1) with  $\varepsilon = 0.43$ . (d) Poincaré surface of section for the trajectory starting above the critical line (red square) and refractively escaping after only 20 bounces (red triangle). The black dots represent a typical trajectory in the limaçon billiard.

case of the circular billiard the SOS is illustrated in Fig. 2.3(b). Starting with a given trajectory, its position in terms of the arclength coordinate along the circumference  $s$  and the quantity  $\sin \chi$  is recorded always directly after the particle is reflected at the billiard's boundary. With the total momentum being normalized to unity,  $\sin \chi \in [-1, 1]$  can be interpreted as tangential momentum component with respect to the boundary curve at the position  $s \in [0, s_{\max}]$ . We adopt the convention that  $\sin \chi > 0$  means counterclockwise rotation and  $\sin \chi < 0$  means clockwise rotation. The so-called Birkhoff coordinates  $(s, \sin \chi)$  are the most natural representation of a Poincaré SOS for billiard systems as the map from bounce to bounce,  $(s_i, \sin \chi_i) \rightarrow (s_{i+1}, \sin \chi_{i+1})$ , is area-preserving [55].

In the case of the integrable circular billiard, the conserved angular momentum is pro-

---

portional to  $\sin \chi$ . Hence rays are confined to two-dimensional surfaces of constant  $\sin \chi$  and constant energy. The topology of such invariant surfaces is that of a two-dimensional torus [113]. The confinement on lower-dimensional surfaces has important consequences for the open circular microdisk. Consider a ray that initially fulfills the condition for total internal reflection  $|\sin \chi| > 1/n$ , see blue dots in Fig. 2.3(b). Since the ray does not leave the invariant torus  $\sin \chi = \text{const}$ , it cannot enter the leaky region between the two critical lines for total internal reflection  $\sin \chi_c = \pm 1/n$ . Hence, such a ray never leaves the cavity as long as wave effects like evanescent leakage, the optical analogue of tunneling, are ignored.

The transition from integrability to chaos in Hamiltonian mechanics is often described by the Kolmogorov-Arnol'd-Moser (KAM) theorem [114–116]. It states that for a sufficiently smooth perturbation of an integrable system some of the invariant tori survive, while others are destroyed giving rise to partially chaotic dynamics. The limaçon billiard with small perturbation parameter  $\varepsilon$  obeys the KAM scenario [57,117,118]. Figure 2.3(d) shows the case of strong perturbation where most of the invariant tori are already destroyed. The trajectory diffuses in phase space in a chaotic fashion as indicated by the small black dots. Remaining invariant tori with whispering-gallery trajectories are restricted to the tiny region  $|\sin \chi| \gtrsim 0.99$  not visible by the naked eye. Some new invariant tori have been created in the billiard system around  $\sin \chi \approx 0$  where they form so-called “regular islands in the chaotic sea”. The centre points of these islands can host stable periodic trajectories. Unstable periodic ray trajectories exist throughout the chaotic region.

The discussed phase-space structure of the closed billiard has consequences for the ray dynamics of the open microcavity. The typical ray trajectory shown in Fig. 2.3(c) and (d) starting with an initial  $\chi$  well above the critical line, follows the chaotic diffusion such that it rapidly enters the leaky region where it escapes according to Snell's and Fresnel's laws. From this observation one would conclude that modes in chaotic microdisks have low- $Q$  factors. This “ $Q$  spoiling” [87,117] would limit the possible applications of deformed microdisks considerably. However, wave localization effects discovered in the field of quantum chaos provide the possibility of high- $Q$  modes in chaotic cavities. For example, wave packets mimic to some extend the chaotic ray diffusion. However, destructive interference suppresses the chaotic diffusion on long time scales [119,120]. This phenomenon is called “dynamical localization” to place emphasis on the dynamical aspect. As a side remark we mention that dynamical localization is closely related to Anderson localization in disordered solids [119]. Dynamical localization has been demonstrated for microdisks with enhanced surfaces roughness [121,122]. Another wave localization phenomenon is “scarring” [123]. It refers to the existence of a small fraction of quantum eigenstates with strong concentration along unstable periodic trajectories of the underlying classical system. In optical microcavities, this localization of wave intensity has been observed in theory and experiment [124–128].

In cavities with a mixed phase space, diffusion can be significantly less pronounced than in fully chaotic systems. This is due to the presence of dynamical barriers in phase space. Examples are regular regions, which cannot be penetrated by chaotic ray trajectories. Here, wave effects like “dynamical tunneling” can effectively enhance the diffusion. Dynamical tunneling is a generalization of conventional tunneling which allows one to pass

not only through an energy barrier but also through other kinds of dynamical barriers in phase space [129]. The effect of dynamical tunneling in microcavities has been discussed in Refs. [107,130]. Tunneling between regular islands that are separated in phase space by a chaotic sea is called “chaos-assisted tunneling” [100,131,132]. It has been demonstrated that the  $Q$ -factors and the directionality of the light emission from microcavities can be strongly influenced by chaos-assisted tunneling [133].

This zoo of ray and wave dynamical effects is itself interesting enough to be studied. In addition, it may allow for useful applications. For example, one of the main goals in this research field is to achieve unidirectional light emission from microdisks, i.e., emission into a single direction with narrow angular divergence. However, all previous attempts had suffered from small  $Q$ -factors [69,134,135]. We present in Section 2.3 a novel, general applicable scheme which overcomes this problem. It is demonstrated that unidirectional emission from high quality modes can be obtained by exploiting enhanced dynamical tunneling near avoided resonance crossings [136], the generalization of avoided level crossings in closed systems.

Another beneficial aspect of the ray-wave correspondence is that it allows to compute mode characteristics in an approximate manner based on ray dynamics and first corrections to the ray dynamics. To demonstrate this, we consider in Section 2.4 as an example microcrystals with hexagonal-shaped cross section [137,138]. We show that the spatial mode structure, the resonance frequencies and the quality factors can be understood not only qualitatively but also quantitatively on the basis of semiclassical approximations.

The originally discovered scars in closed chaotic systems are exceptional states [123]. In open chaotic systems, however, many long-lived (i.e. high- $Q$ ) modes are scarred. Section 2.5 gives an explanation of this fact based on the finding that avoided resonance crossings can produce long-lived modes with scarlike features [139].

In Section 2.6 we explain the concept of “unstable manifolds” in the context of optical microcavities [140–142]. Very recently, it has become an important topic when it was realized that the far-field characteristics of optical modes in cavities with predominantly chaotic ray dynamics can be strongly influenced by the unstable manifolds [143–145]. We show how the unstable manifolds can be exploited to achieve unidirectional light emission from deformed microdisks. In combination with scarring it permits also high  $Q$ -factors [146].

Finally, in Section 2.7 we discuss optical modes in micropillar cavities for various different material systems. In this case, we are not interested in quantum chaos aspects, but instead in a quantitative comparison to experiments which is essential for the realistic modelling of light-matter interaction in Chapter 3.

## 2.1 Mode equations

As the basis of our analysis we first discuss the well-known equations which determine the optical modes in microcavities. We start from Maxwell's equations in CGS units [147] without free charges and currents

$$\nabla \times \mathbf{E} = -\frac{1}{c} \frac{\partial \mathbf{B}}{\partial t}, \quad \nabla \mathbf{D} = 0, \quad (2.2)$$

$$\nabla \times \mathbf{H} = \frac{1}{c} \frac{\partial \mathbf{D}}{\partial t}, \quad \nabla \mathbf{B} = 0, \quad (2.3)$$

with the electric field  $\mathbf{E}$ , the magnetic field  $\mathbf{H}$ , the electric displacement field  $\mathbf{D}$ , the magnetic flux density  $\mathbf{B}$ , and the speed of light in vacuum  $c$ . For linear materials we have  $\mathbf{B} = \mu \mathbf{H}$  and  $\mathbf{D} = \epsilon \mathbf{E}$  with the magnetic permeability  $\mu$  and the electric susceptibility  $\epsilon$ . The materials we are interested in are non-magnetic, i.e.,  $\mu = 1$ . The geometry of the cavity is solely determined by the spatial dependence of the refractive index  $n(\mathbf{r}) = \sqrt{\epsilon(\mathbf{r})}$ . The eigenmodes of the electromagnetic field are given by

$$\mathbf{E}(\mathbf{r}, t) = \mathbf{E}(\mathbf{r}) \exp(-i\omega t), \quad (2.4)$$

$$\mathbf{H}(\mathbf{r}, t) = \mathbf{H}(\mathbf{r}) \exp(-i\omega t), \quad (2.5)$$

where  $\omega$  is the angular frequency. With this factorization Maxwell's equations (2.2) and (2.3) yield partial differential equations for the complex-valued fields  $\mathbf{E}(\mathbf{r})$  and  $\mathbf{H}(\mathbf{r})$

$$\nabla \times \mathbf{E}(\mathbf{r}) = i \frac{\omega}{c} \mathbf{H}(\mathbf{r}), \quad \nabla[n^2(\mathbf{r}) \mathbf{E}(\mathbf{r})] = 0, \quad (2.6)$$

$$\nabla \times \mathbf{H}(\mathbf{r}) = -i \frac{\omega}{c} n^2(\mathbf{r}) \mathbf{E}(\mathbf{r}), \quad \nabla \mathbf{H}(\mathbf{r}) = 0. \quad (2.7)$$

For most solid-state microcavities the refractive index  $n(\mathbf{r})$  is a piece-wise constant function of the coordinates  $\mathbf{r}$ . In that case, we can apply the identity  $\nabla \times (\nabla \times \mathbf{a}) = \nabla(\nabla \cdot \mathbf{a}) - \nabla^2 \mathbf{a}$  for any vector field  $\mathbf{a}$  to rewrite the equations (2.6) and (2.7) as

$$\left( \nabla^2 + n^2(\mathbf{r}) \frac{\omega^2}{c^2} \right) \begin{pmatrix} \mathbf{E}(\mathbf{r}) \\ \mathbf{H}(\mathbf{r}) \end{pmatrix} = 0 \quad (2.8)$$

provided that  $\mathbf{r}$  is not a boundary point. If  $\mathbf{r}$  is on a boundary separating two regions 1 and 2 the fields are subject to the continuity relations

$$\boldsymbol{\nu}(\mathbf{r}) \times [\mathbf{E}_1(\mathbf{r}) - \mathbf{E}_2(\mathbf{r})] = 0, \quad \boldsymbol{\nu}(\mathbf{r}) \cdot [n_1^2 \mathbf{E}_1(\mathbf{r}) - n_2^2 \mathbf{E}_2(\mathbf{r})] = 0, \quad (2.9)$$

$$\boldsymbol{\nu}(\mathbf{r}) \times [\mathbf{H}_1(\mathbf{r}) - \mathbf{H}_2(\mathbf{r})] = 0, \quad \boldsymbol{\nu}(\mathbf{r}) \cdot [\mathbf{H}_1(\mathbf{r}) - \mathbf{H}_2(\mathbf{r})] = 0, \quad (2.10)$$

where  $\boldsymbol{\nu}(\mathbf{r})$  is the local normal vector. Appropriate boundary conditions at infinity are outgoing-wave conditions, which we will introduce below in more detail. Together with these boundary conditions, Eqs. (2.8)–(2.10) define the optical modes in a microcavity.

### 2.1.1 Reduction of Maxwell's equations

In this work, we restrict ourselves to cavity geometries where the  $(x, y)$ - and the  $z$ -dependence of the electromagnetic field effectively decouple. Inserting the ansatz

$$\mathbf{E}(x, y, z) = \mathbf{E}(x, y) \exp(-i\gamma z), \quad (2.11)$$

$$\mathbf{H}(x, y, z) = \mathbf{H}(x, y) \exp(-i\gamma z) \quad (2.12)$$

with the propagation constant in  $z$ -direction  $\gamma$  into the mode equations (2.8) gives

$$(\nabla_{x,y}^2 + \alpha^2) \begin{pmatrix} \mathbf{E}(x, y) \\ \mathbf{H}(x, y) \end{pmatrix} = 0 \quad (2.13)$$

with  $\nabla_{x,y} = (\partial/\partial x, \partial/\partial y)$ ,  $\alpha^2 = n^2 k^2 - \gamma^2$  and the vacuum wave number  $k = \omega/c$ . The position dependence of the piece-wise constant index of refraction  $n$  is suppressed. Next, we decompose the electromagnetic field into its longitudinal and transversal components

$$\mathbf{E}(x, y) = E_z(x, y) \hat{\mathbf{z}} + \mathbf{E}_t(x, y) \quad (2.14)$$

$$\mathbf{H}(x, y) = H_z(x, y) \hat{\mathbf{z}} + \mathbf{H}_t(x, y) \quad (2.15)$$

where  $\hat{\mathbf{z}}$  is the unit vector in  $z$ -direction. Using Eqs. (2.6) and (2.7) one finds

$$\mathbf{E}_t(x, y) = \frac{i}{\alpha^2} [\gamma \nabla_{x,y} E_z(x, y) - k \hat{\mathbf{z}} \times \nabla_{x,y} H_z(x, y)], \quad (2.16)$$

$$\mathbf{H}_t(x, y) = \frac{i}{\alpha^2} [\gamma \nabla_{x,y} H_z(x, y) + k n^2 \hat{\mathbf{z}} \times \nabla_{x,y} E_z(x, y)], \quad (2.17)$$

i.e., the transversal components  $\mathbf{E}_t$  and  $\mathbf{H}_t$  are fully determined by the longitudinal components  $E_z$  and  $H_z$ . Hence,  $E_z$  and  $H_z$  contain all information on the optical modes.

Solutions with  $H_z = 0$  for all positions  $(x, y)$  are called transversal magnetic (TM) polarized. Solutions with  $E_z = 0$  are called transversal electric (TE) polarized. In general, pure TE and TM polarizations do not exist, since the continuity conditions (2.9) and (2.10) mix both kinds of polarization.

### 2.1.2 Deformed microdisks

In the case of a microdisk, the light propagates predominantly in the  $(x, y)$ -plane, i.e.,  $|\gamma| \ll nk$ . In that case, the first term on the r.h.s. of Eqs. (2.16) and (2.17) can be ignored. It follows then from the continuity conditions (2.9) and (2.10) that  $H_z$ ,  $E_z$ ,  $\frac{1}{\alpha} \partial_\nu H_z$ , and  $\partial_\nu E_z$  must be continuous across boundaries, with  $\partial_\nu$  being the normal derivative. Thus, TE and TM polarization effectively decouple.

As a result, for microdisks the vectorial mode equations (2.8) reduce to two scalar equations

$$-\nabla^2 \psi(\mathbf{r}) = n^2(\mathbf{r}) k^2 \psi(\mathbf{r}), \quad (2.18)$$

with from now on  $\mathbf{r} = (x, y)$ ,  $\nabla = (\partial/\partial x, \partial/\partial y)$ , and wave function  $\psi(\mathbf{r}) = E_z(\mathbf{r})$  for TM polarization and  $\psi(\mathbf{r}) = H_z(\mathbf{r})$  for TE polarization. The continuity relations (2.9) and (2.10) simplify to

$$\psi_1 = \psi_2, \quad \partial_\nu \psi_1 = \partial_\nu \psi_2 \quad \text{TM polarization} \quad (2.19)$$

$$\psi_1 = \psi_2, \quad \frac{\partial_\nu \psi_1}{n_1^2} = \frac{\partial_\nu \psi_2}{n_2^2} \quad \text{TE polarization.} \quad (2.20)$$

Note that even in the case of finite but small  $|\gamma|/nk$  the wave equation (2.18) and the continuity relations (2.19)–(2.20) hold in good approximation, provided that an effective index of refraction  $n_{\text{eff}} = n\sqrt{1 - (\gamma/nk)^2}$  is used.

### 2.1.3 Boundary conditions at infinity

The boundary conditions at infinity are determined by the experimental situation. In a scattering experiment the wave function is for example composed of an incoming plane wave with wave vector  $\mathbf{k}$  and an outgoing scattered wave as illustrated in Fig. 2.4(a). The wave function in 2D has the asymptotic form

$$\psi \sim \psi_{\text{in}} + \psi_{\text{out}} = \exp(i\mathbf{k}\mathbf{r}) + f(\theta, \mathbf{k}) \frac{\exp(ikr)}{\sqrt{r}}, \quad (2.21)$$

where  $k = |\mathbf{k}|$  and  $f(\theta, \mathbf{k})$  is the angle-dependent differential amplitude for elastic scattering. In lasers, however, the radiation is generated within the cavity without incoming wave, see Fig. 2.4(b),

$$\psi \sim \psi_{\text{out}} = h(\theta, k) \frac{\exp(ikr)}{\sqrt{r}}. \quad (2.22)$$

This situation can be modelled in a naive way by a dielectric cavity with complex-valued refractive index  $n$ , leading to steady-state solutions of the wave equation (2.18). We use, however, a real-valued  $n$ , leading to states that are exponentially decaying in time. The lifetime  $\tau$  of these quasi-bound or resonant states is given by the imaginary part of the wave number, as  $\tau = -1/[2c \text{Im}(k)]$  with  $\text{Im}(k) < 0$ . The quality factor is related to the lifetime  $\tau$  by  $Q = \text{Re}(\omega)\tau$ . The quasi-bound states are connected to the peak structure in scattering spectra; see Ref. [148] for an introduction. Quasi-bound states have been introduced by Gamow [149] and by Kapur and Peirles [150].

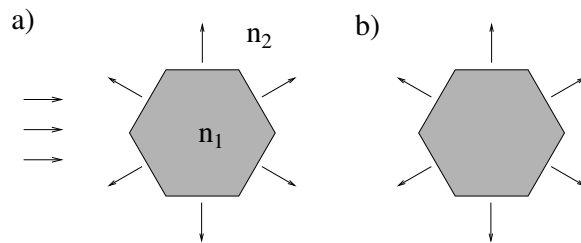


**Figure 2.4:** (a) Incoming and outgoing wave leading to a real frequency. (b) Purely outgoing component giving a complex frequency.

## 2.2 Boundary element method

The theoretical studies of optical modes of deformed microdisks are mainly based on numerical computations. The numerical calculations of highly-excited modes are computational rather challenging. We therefore have developed an efficient method based on Green's functions [90] which is nowdays used by several groups.

### 2.2.1 Introduction

The mode equation (2.18) with the outgoing-wave condition (2.22) can be solved analytically by means of separation of variables only for special geometries, like the isolated circular cavity (see, e.g., Ref. [151]) and the symmetric annular cavity [152]. In general, numerical methods are needed. Frequently used are wave-matching methods [87]. The wave function is usually expanded in integer Bessel functions inside the cavity and in Hankel functions of first kind outside, so that the outgoing-wave condition (2.22) is fulfilled automatically. The Rayleigh hypothesis asserts that such an expansion is always possible. However, it can fail for geometries which are not sufficiently small deformations of a circular cavity [153]. It should be mentioned that for a different kind of boundary conditions at infinity, the wave-matching method can work well for special strongly noncircular geometries, e.g., rectangular integrated microresonators [70].

More flexible are, for example, finite-difference methods; see, e.g., Ref. [88]. These methods involve a discretization of the two-dimensional space, which is a heavy numerical task for highly-excited states. An even more severe restriction is that it is impossible to discretize to infinity. One has to select a cut-off at some arbitrary distance from the cavities and implement there the outgoing-wave condition (2.22). For these reasons, finite-difference methods are not suitable for computing highly-excited resonances in dielectric cavities.

A class of flexible methods with better numerical efficiency are boundary element methods (BEMs). The central idea is to replace two-dimensional differential equations such as Eq. (2.18) by one-dimensional boundary integral equations (BIEs) and then to discretize the boundaries. BEMs have been widely applied to geometries with Dirichlet boundary conditions (wave function vanishes), Neumann boundary conditions (normal derivative vanishes) and combinations of them [88, 89, 154, 155]. Bounded states have been calculated in the context of quantum chaos; for an introduction see Refs. [156, 157]. For scattering problems consider, for example, Ref. [158]. Resonances have been computed for scattering at three disks by Gaspard and Rice [159].

The boundary conditions for dielectric cavities, however, are of a different kind: the wave function and its (weighted) normal derivative are continuous across a cavity boundary. An analogous quantum problem in semiconductor nanostructures has been treated by Knipp and Reinecke [160]. Their BEM is for bounded and scattering states only. The aim of the present section is to extend their approach to resonances in dielectric cavities for TM and TE polarization, including a discussion of spurious solutions, treatment of cavities with symmetries and cavities with corners.

## 2.2.2 Boundary integral equations

First we derive the BIEs for the general case of  $J-1$  optical cavities in an outer unbounded medium. As illustrated in Fig. 2.5, the space is divided into  $J$  regions  $\Omega_j$ ,  $j = 1, 2, \dots, J$ , in each of which the index of refraction  $n(\mathbf{r}) = n_j$  is uniform. Without loss of generality  $n_J$  is set to unity, i.e., the environment is vacuum or air. We first concentrate on TM polarization where both the wave function  $\psi$  and its normal derivative are continuous across an interface separating two different regions.

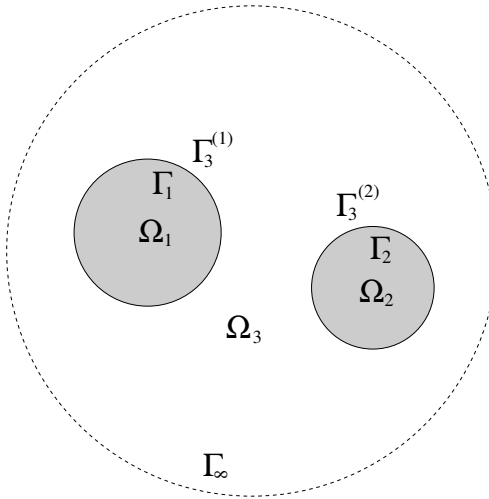


**Figure 2.5:** Geometry and notation for the BIEs. The cavity with domain  $\Omega_1$  is bounded by the curve  $\Gamma_1$ , the one with domain  $\Omega_2$  is bounded by  $\Gamma_2$ . The domain  $\Omega_3$  is “bounded” by  $\Gamma_3^{(1)} = \Gamma_1$ ,  $\Gamma_3^{(2)} = \Gamma_2$  and by a circle  $\Gamma_\infty$  at a large distance.

To reduce the two-dimensional differential equation (2.18) to one-dimensional integral equations, we first introduce the Green’s function, which is defined as solution of

$$[\nabla^2 + n_j^2 k^2]G(\mathbf{r}, \mathbf{r}'; k) = \delta(\mathbf{r} - \mathbf{r}') , \quad (2.23)$$

where  $\delta(\mathbf{r} - \mathbf{r}')$  is the two-dimensional Dirac  $\delta$ -function,  $\mathbf{r}$  and  $\mathbf{r}'$  are arbitrary points within  $\Omega_j$ . The outgoing solution for the Green’s function is

$$G(\mathbf{r}, \mathbf{r}'; k) = -\frac{i}{4}H_0^{(1)}(n_j k |\mathbf{r} - \mathbf{r}'|) . \quad (2.24)$$

$H_0^{(1)}$  is the zeroth order Hankel function of first kind [161].

Multiplying the  $\psi$ -equation (2.18) by  $G(\mathbf{r}, \mathbf{r}'; k)$  and subtracting the resulting equation from the  $G$ -equation (2.23) multiplied by  $\psi(\mathbf{r})$  gives

$$\begin{aligned} \psi(\mathbf{r})\delta(\mathbf{r} - \mathbf{r}') &= \psi(\mathbf{r})\nabla^2 G(\mathbf{r}, \mathbf{r}'; k) - G(\mathbf{r}, \mathbf{r}'; k)\nabla^2 \psi(\mathbf{r}) \\ &= \nabla[\psi(\mathbf{r})\nabla G(\mathbf{r}, \mathbf{r}'; k) - G(\mathbf{r}, \mathbf{r}'; k)\nabla\psi(\mathbf{r})] . \end{aligned}$$

Integrating this equation over the region  $\Omega_j$  yields on the l.h.s.  $\psi(\mathbf{r}')$  since  $\mathbf{r}' \in \Omega_j$ . Applying Green’s theorem, the integral on the r.h.s. can be expressed by a line integral

along the boundary curve  $\Gamma_j = \partial\Omega_j$ , such that

$$\psi(\mathbf{r}') = \oint_{\Gamma_j} ds [\psi(s) \partial_\nu G(s, \mathbf{r}'; k) - G(s, \mathbf{r}'; k) \partial_\nu \psi(s)] . \quad (2.25)$$

Note that the boundary curve may consist of a number of disconnected components  $\Gamma_j = \Gamma_j^{(1)} \cup \Gamma_j^{(2)} \cup \dots$  as depicted in Fig. 2.5. Each component is assumed to be oriented counterclockwise, smooth, and not to be a part of  $\Omega_j$  itself, i.e.,  $\Omega_j$  is an open set.  $\partial_\nu$  is the normal derivative defined as  $\partial_\nu = \boldsymbol{\nu}(\mathbf{r}) \nabla |_{\mathbf{r}}$ ;  $\boldsymbol{\nu}(\mathbf{r})$  is the outward normal unit vector to  $\Gamma_j$  at point  $\mathbf{r}$ ;  $s = s(\mathbf{r})$  is the arclength along  $\Gamma_j$  at  $\mathbf{r}$ . The derivative of the Green's function is given by

$$\partial_\nu G(\mathbf{s}, \mathbf{r}'; k) = \frac{i n_j k}{4} \cos \alpha H_1^{(1)}(n_j k |\mathbf{r} - \mathbf{r}'|) , \quad (2.26)$$

where  $H_1^{(1)}$  is the first order Hankel function of first kind [161] and

$$\cos \alpha = \boldsymbol{\nu}(\mathbf{r}) \frac{\mathbf{r} - \mathbf{r}'}{|\mathbf{r} - \mathbf{r}'|} . \quad (2.27)$$

The limit  $\mathbf{r}' \rightarrow \Gamma_j$  in Eq. (2.25) is not trivial since both the Green's function and its normal derivative are singular at  $\mathbf{r}' = \mathbf{r}$ . However, it can be shown that these singularities are integrable for smooth boundaries. This is obvious for the second part of the integral kernel in Eq. (2.25) since for small arguments  $z = n_j k |\mathbf{r} - \mathbf{r}'|$

$$H_0^{(1)}(z) \sim \frac{2i}{\pi} \ln z . \quad (2.28)$$

The first part is also integrable. At first glance, this seems to be surprising because for small arguments

$$H_1^{(1)}(z) \sim -\frac{2i}{\pi z} . \quad (2.29)$$

However, this singularity is compensated by

$$\cos \alpha \sim \frac{1}{2} \kappa |\mathbf{r} - \mathbf{r}'| , \quad (2.30)$$

where  $\kappa$  is the curvature of the curve  $\Gamma_j$  at  $\mathbf{r}(s)$ , which is finite for a smooth boundary. The limit  $\mathbf{r}' \rightarrow \Gamma_j$  in Eq. (2.25) can be performed in the sense of Cauchy's principal value, see, e.g., Ref. [156], giving

$$\frac{1}{2} \psi(\mathbf{r}') = \mathcal{P} \oint_{\Gamma_j} ds [\psi(s) \partial_\nu G(s, \mathbf{r}'; k) - G(s, \mathbf{r}'; k) \partial_\nu \psi(s)] . \quad (2.31)$$

Comparing the l.h.s of Eqs. (2.25) and (2.31) shows that  $\mathbf{r}' \in \Gamma_j$  gives the “average” of the results for  $\mathbf{r}' \in \Omega_j$  and  $\mathbf{r}' \in \Omega_i$  with  $i \neq j$ .

For each region  $\Omega_j$  there is an equation as Eq. (2.31). Special attention has to be paid to the unbounded region  $\Omega_J$ . It is convenient to consider instead a finite region bounded by

a circle  $\Gamma_\infty$  with a very large radius  $r$  as sketched in Fig. 2.5. We distinguish three cases in the following paragraphs.

The case of bounded states in the quantum analogue has been studied by Knipp and Reinecke [160]. Then,  $n_j k$  has to be replaced by  $[2m(E - V_j)]^{1/2}/\hbar$ , where  $E$  is the energy,  $V_j$  with  $j = 1, \dots, J$  is a piece-wise constant potential, and  $\hbar$  is Planck's constant divided by  $2\pi$ . The wave function and its normal derivative (weighted with the inverse of the effective mass  $m$ ) are continuous at domain boundaries. If  $E < V_J$  then the state is bounded, the wave function and its gradient vanish exponentially as  $r \rightarrow \infty$ . Moreover, with  $\text{Im}(k) = 0$  the Green's function (2.24) vanishes as either  $\mathbf{r}$  or  $\mathbf{r}'$  goes to infinity. As a result  $\Gamma_\infty$  does not contribute to any of the BIEs. Note that Eq. (2.18) does not permit bounded states since  $n_j^2 k^2 > 0$ .

Using the same notation as Knipp and Reinecke [160] we reformulate Eq. (2.31) as a linear homogeneous BIE

$$\oint_{\Gamma_J} ds [B(s', s)\phi(s) + C(s', s)\psi(s)] = 0 , \quad (2.32)$$

with  $B(s', s) = -2G(s, s'; k)$ ,  $C(s', s) = 2\partial_\nu G(s, s'; k) - \delta(s - s')$ , and  $\phi(s) = \partial_\nu \psi(\mathbf{r})$ . The entire set of BIEs can be written in a symbolic way as

$$\begin{pmatrix} B_1 & C_1 \\ B_2 & C_2 \\ \vdots & \vdots \\ B_J & C_J \end{pmatrix} \begin{pmatrix} \phi \\ \psi \end{pmatrix} = M \begin{pmatrix} \phi \\ \psi \end{pmatrix} = 0 , \quad (2.33)$$

where  $B_j$  and  $C_j$  represent the integral operators in region  $\Omega_j$ . The lower half of the vector  $(\phi, \psi)^t$  contains the values of the wave function on the boundaries, and the upper half contains the values of the normal derivative. Note that each boundary curve has two contributions to Eq. (2.33) with identical  $\psi, \phi$  (which are continuous across the boundary) but different  $B_j, C_j$ .

The scattering states in the related quantum problem have been discussed again by Knipp and Reinecke [160]. In contrast to the case of bounded states, their results also apply to dielectric cavities.

In region  $\Omega_J$  the wave function has the asymptotic form as in Eq. (2.21). The incoming wave  $\psi_{\text{in}}$  satisfies Eq. (2.18). Thus,  $\psi$  can be replaced by  $\psi - \psi_{\text{in}}$  in Eq. (2.25) giving

$$\psi(\mathbf{r}') = \exp(i\mathbf{k}\mathbf{r}') + \oint_{\Gamma_J} ds \{ [\psi(s) - \psi_{\text{in}}(s)]\partial_\nu G(s, \mathbf{r}'; k) - G(s, \mathbf{r}'; k)[\phi(s) - \phi_{\text{in}}(s)] \} , \quad (2.34)$$

where  $\psi_{\text{in}}(s) = \exp(i\mathbf{k}\mathbf{r})$  and  $\phi_{\text{in}}(s) = i\mathbf{k}\nu(\mathbf{r}) \exp(i\mathbf{k}\mathbf{r})$  at  $\mathbf{r} = \mathbf{r}(s)$ . The circle at infinity does not contribute to the BIE (2.34) as in the case of bounded states. The reason, however, is different as we shall see in greater detail in the following paragraphs when considering resonances.

If  $\mathbf{r}'$  is taken from the boundary then Eq. (2.34) can be written as inhomogeneous integral equation

$$\oint_{\Gamma_J} ds [B(s', s)\phi(s) + C(s', s)\psi(s)] = \oint_{\Gamma_J} ds [B(s', s)\phi_{\text{in}}(s) + C(s', s)\psi_{\text{in}}(s)] . \quad (2.35)$$

Together with the other  $J - 1$  BIEs, which are of the same form as in Eq. (2.32), the resulting inhomogeneous system of equations is

$$M \begin{pmatrix} \phi \\ \psi \end{pmatrix} = M_0 \begin{pmatrix} \phi_{\text{in}} \\ \psi_{\text{in}} \end{pmatrix} \quad (2.36)$$

with

$$M_0 = \begin{pmatrix} 0 & 0 \\ \vdots & \vdots \\ 0 & 0 \\ B_J & C_J \end{pmatrix}. \quad (2.37)$$

Having determined the solutions  $\psi$  and  $\phi$  we can compute the differential scattering amplitude by evaluating Eq. (2.34) for large  $r'$  and comparing the result with Eq. (2.21) giving

$$f(\theta, \mathbf{k}) = \frac{1+i}{4\sqrt{\pi k}} \oint_{\Gamma_J} ds \exp[-i\mathbf{k}_f \mathbf{r}(s)] \{i\mathbf{k}_f \boldsymbol{\nu}(s)[\psi(s) - \psi_{\text{in}}(s)] + \phi(s) - \phi_{\text{in}}(s)\}, \quad (2.38)$$

where  $\mathbf{k}_f = (k \cos \theta, k \sin \theta)$  and  $\theta$  is the detection angle. Here,  $|f(\theta, \mathbf{k})|^2$  is the differential scattering cross section. The total cross section  $\sigma(\mathbf{k}) = \int d\theta |f(\theta, \mathbf{k})|^2$  can be easily calculated from the forward-scattering amplitude,  $\mathbf{k}_f = \mathbf{k} = (k \cos \phi, k \sin \phi)$ , with the help of the optical theorem (see, e.g., Ref. [148])

$$\sigma(\mathbf{k}) = 2\sqrt{\frac{\pi}{k}} \text{Im}[(1-i)f(\theta = \phi, \mathbf{k})]. \quad (2.39)$$

We now turn to the BIEs for resonances. Comparing the scattering boundary condition (2.21) and the outgoing-wave condition (2.22) indicates that we possibly can use the scattering approach neglecting the incoming wave, that is Eq. (2.36) with  $M_0 = 0$ . Apart from the fact that  $k$  is now a complex number, this is then identical to Eq. (2.33) for bounded states. There is, however, one problem. The circle at infinity,  $\Gamma_\infty$ , may give a nonvanishing contribution

$$I_\infty(\mathbf{r}') = \oint_{\Gamma_\infty} ds [\psi(s) \partial_\nu G(s, \mathbf{r}'; k) - G(s, \mathbf{r}'; k) \partial_\nu \psi(s)] \quad (2.40)$$

to the r.h.s. of Eq. (2.25) because with  $\text{Im}(k) < 0$  neither the wave function (2.22) nor the Green's function (2.24) vanish at infinity. Gaspard and Rice [159] have shown for a Dirichlet scattering problem that nonetheless  $I_\infty(\mathbf{r}') = 0$  if  $\mathbf{r}'$  is at one of the scatterers' boundaries or if  $\mathbf{r}'$  is at a large distance from these boundaries. We have to extend their result because (i) the problem of dielectric cavities involves a different kind of boundary conditions; (ii) we are interested in the wave function  $\psi(\mathbf{r}')$  also in the near-field. We start with recalling that the circle at infinity,  $\Gamma_\infty$ , is defined by  $r = \text{const}$  with  $r \rightarrow \infty$ . Using the asymptotical behaviour of Hankel functions of first kind [161]

$$H_m^{(1)}(z) \sim \sqrt{\frac{2}{\pi z}} \exp[i(z - m\pi/2 - \pi/4)] \quad (2.41)$$

as  $z = k|\mathbf{r} - \mathbf{r}'| \rightarrow \infty$ , it can be shown that the Green's function in Eq. (2.24) is asymptotically given by

$$G(\mathbf{r}, \mathbf{r}'; k) \sim g(\theta - \theta', r') \frac{\exp(ikr)}{\sqrt{r}} , \quad (2.42)$$

with

$$g(\theta - \theta', r') = -\frac{1+i}{4\sqrt{\pi k}} \exp[-ikr' \cos(\theta - \theta')] . \quad (2.43)$$

Equation (2.42) has the same  $r$ -dependence as the outgoing-wave condition (2.22). With  $G$  and  $\psi$  appearing in Eq. (2.40) in an antisymmetric way it follows  $I_\infty(\mathbf{r}') = 0$  for all  $\mathbf{r}' \in \Omega_J \cup \Gamma_J$ . The fact that  $I_\infty(\mathbf{r}')$  vanishes for  $\mathbf{r}' \in \Gamma_J$  means that the BIEs (2.33) can indeed be used to determine the resonant wave numbers  $k$ . Moreover, since  $I_\infty(\mathbf{r}') = 0$  also for  $\mathbf{r}' \in \Omega_J$  Eq. (2.25) can be used to compute the corresponding wave functions in the entire domain.

Having established that the resonances are solutions of the BIEs (2.33) with complex-valued  $k$ , we now demonstrate that the BIEs (2.33) posses additional solutions which do not fulfil the outgoing-wave condition (2.22). We study this in an elementary way for a single cavity of arbitrary shape. Outside this cavity sufficiently far away from its boundary, a solution of wave equation (2.18) can be expressed as

$$\psi(r, \theta) = \sum_{m=-\infty}^{\infty} [\alpha_m^{(1)} H_m^{(1)}(kr) + \alpha_m^{(2)} H_m^{(2)}(kr)] \exp(im\theta) , \quad (2.44)$$

with Hankel functions of first and second kind [161] and with unknown complex-valued parameters  $\alpha_m^{(1)}$  and  $\alpha_m^{(2)}$ . Without boundary conditions at infinity, solutions as in Eq. (2.44) exist for all values of  $k$ . Boundary conditions that fix all parameters  $\alpha_m^{(2)}$  give rise to a discrete spectrum of  $k$ ; for instance, the outgoing-wave condition (2.22) requires  $\alpha_m^{(2)} = 0$  for all  $m$ . Inserting the expansion (2.44) into Eq. (2.40) leads to

$$I_\infty(\mathbf{r}') = 2 \sum_{m=-\infty}^{\infty} \alpha_m^{(2)} J_m(kr') \exp(im\theta') . \quad (2.45)$$

Hence,  $I_\infty(\mathbf{r}')$  vanishes identically for all  $\mathbf{r}' \in \Omega_J \cup \Gamma_J$  only in the case of a resonance, where  $\alpha_m^{(2)} = 0$  for all  $m$ .

However, the circle at infinity does not contribute to the BIEs (2.33) already if the weaker condition  $I_\infty(\mathbf{r}') = 0$  for  $\mathbf{r}' \in \Gamma_J$  is satisfied. We insert this condition into the l.h.s. of Eq. (2.45) and note that the r.h.s. is an expansion of a solution of wave equation (2.18) inside the cavity with “wrong” index of refraction  $n = n_J = 1$ . The result is that the BIEs (2.33) possess undesired solutions, namely bounded states of an interior Dirichlet problem, in addition to the resonances. As one consequence, the solutions of the scattering BIEs (2.36) are not unique whenever  $k$  is a solution of the interior Dirichlet problem. Note that this nonuniqueness has not been discussed by Knipp and Reinecke [160].

A related problem is known for cases with Dirichlet or Neumann conditions; see, e.g., Refs. [88, 155]. There have been several attempts to modify the BIEs in order to get rid of these “spurious solutions”. Some of these modifications could be applied to the present

case, but this would result in singular integrals which are hard to deal with numerically. Fortunately, the spurious solutions are not a severe problem for our purpose. We can distinguish them, in principle, from the resonances in which we are interested in. The former have  $\text{Im}(k) = 0$  whereas the latter have  $\text{Im}(k) < 0$ .

In the case of TE polarization, Eq. (2.18) is valid with  $\psi$  representing the magnetic field  $H_z$ . The wave function  $\psi$  is continuous across the boundaries, but its normal derivative is not, in contrast to the case of TM polarization. Instead,  $n(\mathbf{r})^{-2}\partial_\nu\psi$  is continuous [147], see Eq. (2.20). This new boundary condition can be easily incorporated in the BEM by defining  $\phi = n^{-2}\partial_\nu\psi$ ,  $B(s', s) = -2G(s, s'; k)n^2$  and  $\phi_{\text{in}}$  accordingly in equations like Eqs. (2.32) and (2.35). We remark that the spurious solutions are not affected by this change of boundary conditions.

Many dielectric cavities studied in the literature possess discrete symmetries. For example, the elliptical cavity in Fig. 2.6 is symmetric with respect to the  $x$  and  $y$  axes. In such a case, the wave functions can be divided into four symmetry classes

$$\psi_{\zeta\xi}(-x, y) = \zeta\psi_{\zeta\xi}(x, y), \quad (2.46)$$

$$\psi_{\zeta\xi}(x, -y) = \xi\psi_{\zeta\xi}(x, y), \quad (2.47)$$

with the parities  $\zeta \in \{-, +\}$  and  $\xi \in \{-, +\}$ . The normal derivative obeys the same symmetry relations.

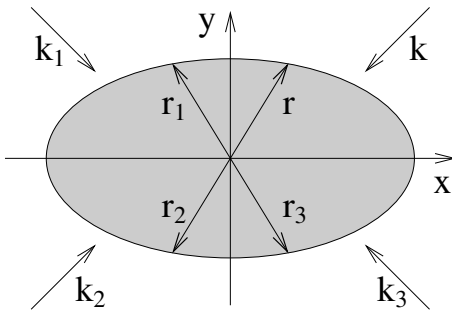


**Figure 2.6:** Symmetric cavity.

For systems with symmetries the BIEs can be reduced to a fundamental domain if a modified Green's function is used. This decreases the numerical effort considerably. Let us restrict our discussion to the case in Eqs. (2.46) and (2.47); other symmetries can be treated in a similar way. The BIEs (2.31) reduce to integrals along the boundaries restricted to the quadrant  $x, y \geq 0$  if the Green's function  $G(\mathbf{r}, \mathbf{r}')$  is replaced by

$$G(\mathbf{r}, \mathbf{r}') + \zeta G(\mathbf{r}_1, \mathbf{r}') + \zeta\xi G(\mathbf{r}_2, \mathbf{r}') + \xi G(\mathbf{r}_3, \mathbf{r}') \quad (2.48)$$

with  $\mathbf{r} = (x, y)$ ,  $\mathbf{r}_1 = (-x, y)$ ,  $\mathbf{r}_2 = (-x, -y)$ ,  $\mathbf{r}_3 = (x, -y)$ ; see Fig. 2.6. The derivative  $\partial_\nu G(s, \mathbf{r}')$  is modified in the same way with the normal unit vector  $\nu$  changing as  $\mathbf{r}$ .

The scattering problem as formulated above does not allow the symmetry reduction because the incoming plane wave in general destroys the symmetry;  $\phi_{\text{in}}$  and  $\psi_{\text{in}}$  in Eq. (2.36) do not fulfil the conditions (2.46) and (2.47). There are certain incoming directions which

do not spoil the symmetry, but using only these special directions is dangerous because possibly not all resonances are excited. A better approach is to consider a different physical situation illustrated in Fig. 2.6. Four plane waves are superimposed to a symmetric incoming wave

$$\psi_{\text{in}} = \exp(i\mathbf{k}\mathbf{r}) + \zeta \exp(i\mathbf{k}_1\mathbf{r}) + \zeta \xi \exp(i\mathbf{k}_2\mathbf{r}) + \xi \exp(i\mathbf{k}_3\mathbf{r}) \quad (2.49)$$

where  $\mathbf{k} = (k_x, k_y)$ ,  $\mathbf{k}_1 = (-k_x, k_y)$ ,  $\mathbf{k}_2 = (-k_x, -k_y)$ ,  $\mathbf{k}_3 = (k_x, -k_y)$ . With this incoming wave, the scattering problem can be symmetry reduced. A more general formulation for an arbitrary symmetry can be found in Ref. [162].

### 2.2.3 Boundary element method

The most convenient numerical strategy for solving BIEs as in Eqs. (2.32) and (2.35) is the BEM. The boundary is discretized by dividing it into small boundary elements. Along such an element, the wave function and its normal derivative are considered as being constant (for linear, quadratic, and cubic variations see, e.g., Refs. [89, 155]). Equation (2.32) is therefore approximated by a sum of  $N_j$  terms

$$\sum_{l=1}^{N_j} (B_{il}\phi_l + C_{il}\psi_l) = 0 \quad (2.50)$$

where  $B_{il} = \int_l ds B(s_i, s)$ ,  $C_{il} = \int_l ds C(s_i, s)$ ,  $\phi_l = \phi(s_l)$ ,  $\psi_l = \psi(s_l)$ , and  $\int_l$  denotes the integration over a boundary element with midpoint  $s_l$ . The entire set of BIEs is approximated by an equation as in Eq. (2.33), but for which  $B_j$  and  $C_j$  are  $N_j \times N$  matrices,  $M$  is a  $2N \times 2N$  (non-Hermitian complex) matrix,  $\phi$  and  $\psi$  are  $N$ -component vectors with  $2N = \sum_{j=1}^J N_j$ . Note that each boundary element belongs to two different regions. In the same way the scattering problem is approximated by an equation as in Eq. (2.36) with  $M_0$  being a  $2N \times 2N$  matrix,  $\phi_{\text{in}}$  and  $\psi_{\text{in}}$  being  $N$ -component vectors.

In the literature several levels of approximation are used for the matrix elements  $B_{il}$  and  $C_{il}$ . The crudest approximation is to evaluate such an integral only at the corresponding midpoint  $s_l$ . While this is sufficient for the calculation of bounded states in quantum billiards [157], in our case the small imaginary parts of  $k$  require a more accurate treatment. We therefore do perform the numerical integration of the matrix elements  $B_{il}$  and  $C_{il}$ , using standard integration routines like, for example, Gaussian quadratures [163]. The number of interior points in the range of integration should be chosen large if the boundary elements  $s_i$  and  $s_l$  are close to each other and small if they are far away. Moreover, our experience is that the results are considerably more accurate if the boundary elements are not approximated by straight lines but, instead, the exact shape of the boundary elements is used for all interior points in the range of integration.

Due to the almost singular behaviour of the integral kernels at  $\mathbf{r}' = \mathbf{r}$ , the diagonal elements  $C_{ll}$  and  $B_{ll}$  require special care. Inserting the limiting cases for small boundary-element length  $\Delta s_l$  in Eqs. (2.29) and (2.30) into Eq. (2.26) gives

$$C_{ll} = -1 + \frac{\kappa_l}{2\pi} \Delta s_l , \quad (2.51)$$

where  $\kappa_l$  is the curvature at point  $s_l$ . To approximate  $B_{ll}$  accurately, more higher order terms than in Eq. (2.28) are needed:

$$H_0^{(1)}(z) \sim \frac{2i}{\pi} \ln \frac{z}{2} + 1 + \frac{2i}{\pi} \gamma , \quad (2.52)$$

where  $\gamma = 0.577215\dots$  is Euler's constant. Integration yields

$$B_{ll} = \frac{\Delta s_l}{\pi} [1 - \ln \frac{n_j k \Delta s_l}{4} + i \frac{\pi}{2} - \gamma] . \quad (2.53)$$

Dielectric corners are numerically difficult to treat because certain components of the electric field can be infinite at the corner (see the discussion in Ref. [164] in the context of dielectric waveguides). In the BEM, a corner leads to a second problem. The integral kernel of  $C_{ll}$  has a singularity caused by a diverging curvature  $\kappa$ ; see Eq. (2.30). To circumvent these difficulties, we smooth the boundary as sketched in Fig. 2.7. The curvature  $\kappa$  and the electric field are then everywhere bounded.

The minimum value of the radius of curvature,  $\rho = 1/\kappa$ , along such a rounded corner should be much larger than the typical distance between discretization points, so that the boundary is locally smooth. However, in order to ensure that the rounding does not influence the result,  $\rho$  should be much smaller than the wavelength  $\lambda$ . Clearly, these requirements can be met most efficiently by using a nonuniform discretization with a relatively large density of discretization points at corners as illustrated in Fig. 2.7. Since the results do not depend on the particular selected rounding and discretization we do not give explicit formulae.

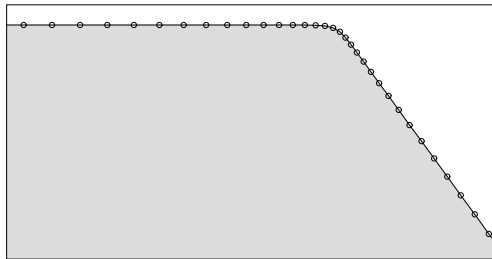


**Figure 2.7:** Rounded corner. The number of discretization points (circles) is enhanced at the corner.

The scattering problem provides us with first approximations to the wave numbers of the resonances. Let us fix  $\phi$  to an appropriate value and plot the total cross section in Eq. (2.39) as function of  $k$  in the range of interest. Resonances can be identified as peaks. The peak position  $\alpha$  and the width  $\gamma$  determine the resonant wave number as  $k_{\text{res}} \approx k_1 = \alpha - i\gamma/2$ . It might be difficult to resolve numerically very broad and very narrow peaks, because they are hidden either in the background or between two consecutive grid points. For microlaser operation, however, these two extreme cases are not relevant. Too short-lived resonances (broad peaks) fail to provide a sufficient long lifetime for the light to accumulate the gain required to overcome the lasing threshold, whereas too long-lived resonances (narrow peaks) do not supply enough output power.

The spurious solutions of the interior Dirichlet problem occasionally appear in the scattering spectrum as extremely narrow peaks. The reason is that numerical inaccuracies broaden the  $\delta$ -peaks to peaks of finite width. However, choosing a sufficiently fine boundary discretization and/or an appropriate, not too fine discretization in  $k$  reduces the probability of observing them. Moreover, they can be removed with a simple trick: use  $k$  with a small negative imaginary part in Eq. (2.39).

The discretized version of Eq. (2.33) has a nontrivial solution only if  $\det M(k_{\text{res}}) = 0$ . Using a first approximation  $k_1$  from the scattering problem as starting value, we find a much better approximation to  $k_{\text{res}}$  in the complex plane with the help of Newton's method

$$k_{l+1} = k_l - \frac{g(k_l)}{g'(k_l)} \quad (2.54)$$

with  $l = 1, 2, \dots$  and  $g(k) = \det M(k)$ . The derivative  $g'(k) = \partial g(k)/\partial k$  can be approximated by

$$g'(k) \approx \frac{g(k + \Delta) - g(k)}{2\Delta} - i \frac{g(k + i\Delta) - g(k)}{2\Delta}, \quad (2.55)$$

where  $\Delta$  is a small real number. Equation (2.54) is repeated iteratively until a chosen accuracy is achieved.

Newton's method in Eq. (2.54) is very efficient close to an isolated resonance where  $\det M \propto k - k_{\text{res}}$ . For  $q$ -fold degenerate resonances the determinant behaves like  $(k - k_{\text{res}})^q$ . The resulting problem of slow convergence can be eliminated by choosing  $g = (\det M)^{1/q}$ .

A slightly different approach for finding resonances can be gained by rewriting Newton's method in Eq. (2.54) with the help of the matrix identity  $\ln \det M = \text{tr} \ln M$  as

$$k_{l+1} = k_l - \frac{q}{\text{tr}[M^{-1}(k_l)M'(k_l)]}, \quad (2.56)$$

where  $\text{tr}$  denotes the trace of a matrix. The derivative  $M'(k)$  can be calculated as in Eq. (2.55). It turns out that the numerical algorithm corresponding to Eq. (2.56) is a bit faster than the original Newton's method in Eq. (2.54).

Having found a particular wave number  $k_{\text{res}}$ , the vector components  $\phi_l$  and  $\psi_l$  are given by the null eigenvector of the square matrix  $M(k_{\text{res}})$ . This eigenvector can be found with, for instance, singular value decomposition [163]. The wave function in each domain  $\Omega_j$  is then constructed by discretizing Eq. (2.25)

$$\psi(\mathbf{r}') = \sum_l \psi_l \int_l ds \partial_\nu G(s, \mathbf{r}'; k_{\text{res}}) - \sum_l \phi_l \int_l ds G(s, \mathbf{r}'; k_{\text{res}}), \quad (2.57)$$

where  $l$  runs over all boundary elements of  $\Gamma_j$ .

How fine must be the discretization of the boundary in order to obtain a good approximation of a resonance at  $k_{\text{res}}$ ? The local wavelength  $\lambda = 2\pi/n\text{Re}(k_{\text{res}})$  is the smallest scale on which the wave function and its derivative may vary. Hence the minimum number of boundary elements along each wavelength,  $b = \lambda/\Delta s$ , should be larger or equal than at least 4;  $\Delta s$  is the maximum value of all lengths  $\Delta s_i$ . We have verified the BEM using different values of  $b$ . Taking  $b = 16$ , we find good agreement with the separation-of-variables

solution of the circular cavity (see, e.g., Ref. [151]) and to results of the wave-matching method obtained for the quadrupolar cavity [66]. Only for extremely long-lived resonances larger  $b$  are necessary to determine the very small imaginary parts of  $k$  accurately (recall that this is important for distinguishing spurious solutions from real resonances).

### 2.2.4 Summary

We have introduced a boundary element method (BEM) to compute TM and TE polarized quasi-bound modes in effectively two-dimensional microcavities. We have discussed spurious solutions, the treatment of cavities with symmetries and cavities with corners.

If compared to finite-difference methods and related methods the BEM is very efficient since the wave function and its derivative are only evaluated at the boundaries of the cavities. In contrast to the wave-matching method, the BEM can be applied to complex geometries, such as cavities with corners and coupled cavities,

The BEM is especially suitable for computing phase space representations of wave functions such as the Husimi function which also only requires the wave function and its normal derivative on the domain boundaries [165].

## 2.3 Unidirectional light emission from high- $Q$ modes

We introduce a scheme to design optical microcavities supporting high- $Q$  modes with unidirectional light emission. This is achieved by coupling a low- $Q$  mode with unidirectional emission to an isotropic high- $Q$  mode. The coupling is due to the presence of an avoided resonance crossing. Numerical results for a microdisk with a suitably positioned air hole demonstrate the feasibility and the potential of this concept.

### 2.3.1 Introduction

A key quantity characterizing a cavity mode is its quality factor  $Q = \omega/\Delta\omega$ , where  $\omega$  is the mode frequency and  $\Delta\omega$  is the linewidth. A large  $Q$ -factor is a basic requirement for low threshold lasing, high sensor sensitivity, narrow wavelength-selective filtering, and strong light-matter interaction. Whispering-gallery modes (WGMs) in microdisks [20], microspheres [23], and microrotori [24] have *ultra-high Q-factors*. For state-of-the-art semiconductor microdisks, the record  $Q$ -factor is  $> 6 \times 10^5$  [166]. The applicability of those cavities as microlasers and single-photon sources is, however, limited by isotropic light emission. The best directionality so far is provided by VCSEL-micropillars; see, e.g., Ref. [167]. The emission is *unidirectional* at the cost of a reduced  $Q$ -factor, typically below  $10^4$ . With present technology, there is a trade-off between  $Q$ -factor and directionality.

This dilemma remains when breaking the rotational symmetry of a microdisk. Shape deformation [66, 168] allows improved directionality of emission due to *refractive escape*, but the  $Q$ -factors are significantly spoiled. Unidirectional emission has been reported for rounded triangles [135] with  $Q \approx 35$  and for spiral-shaped disks [69]. In the latter case, a strong degradation of the cavity  $Q$  allows lasing operation only for spirals of the size of conventional edge emitting lasers.

Another approach is to break the symmetry by modifying the evanescent leakage (the optical analogue of tunneling) from WGMs, thereby keeping the high  $Q$ -factor. In Ref. [169] unidirectional lasing from a vertical double-disk structure has been reported. Unfortunately, the study was restricted to the near-field pattern. Another suggestion has been to introduce a linear defect into the evanescent inner region of WGMs [170]. Nearly spherical, high- $Q$  fused-silica cavities showed emission into four directions explained by *dynamical tunneling* from a WGM to the exterior of the cavity [107].

In this section, we overcome the trade-off between  $Q$ -factor and directionality by combining dynamical tunneling and refractive escape. We couple a uniform high- $Q$  mode (HQM) and a directional low- $Q$  mode (LQM) using enhanced dynamical tunneling near *avoided resonance crossings* (ARCs). ARCs appear in open systems, where a complex frequency  $\omega - i\Delta\omega/2$  is assigned to each mode. ARCs are generalizations of avoided frequency (or energy level) crossings. Avoided level crossings in closed or conservative systems are discussed in textbooks on quantum mechanics. They occur when the curves of two energy eigenvalues, as function of a real parameter  $\Delta$ , come near to crossing but then repel each

other [171]. This behavior can be understood in terms of a  $2 \times 2$  Hamiltonian matrix

$$H = \begin{pmatrix} E_1 & V \\ W & E_2 \end{pmatrix}. \quad (2.58)$$

For a closed system this matrix is Hermitian, thus the energies  $E_j$  are real and the complex off-diagonal elements are related by  $W = V^*$ . The eigenvalues of the coupled system,

$$E_{\pm}(\Delta) = \frac{E_1 + E_2}{2} \pm \sqrt{\frac{(E_1 - E_2)^2}{4} + VW}, \quad (2.59)$$

differ from the energies of the uncoupled system  $E_j$  only in a narrow parameter region where the detuning from resonance,  $|E_1(\Delta) - E_2(\Delta)|$ , is smaller or of the size of the coupling strength  $\sqrt{VW}$ . The parameter dependence of  $V$  and  $W$  can often be safely ignored.

The matrix (2.58) also captures features of avoided *resonance* crossings (ARCs) in open or dissipative systems if one allows for complex-valued energies  $E_j$ . The imaginary part determines the lifetime  $\tau_j \propto 1/\text{Im}(E_j)$  of the quasi-bound state far away from the avoided crossing  $|E_1 - E_2|^2 \gg VW$ , where the off-diagonal coupling can be neglected. Keeping the restriction  $W = V^*$  allows for two different kinds of ARCs [172]. For the strong coupling situation  $2|V| > |\text{Im}(E_1) - \text{Im}(E_2)|$ , there is an avoided crossing in the real part of the energy and a crossing in the imaginary part upon which the eigenstates interchange their identity. Correspondingly, all spatial mode characteristics such as, e.g., the far-field patterns switch their identity. At resonance  $\text{Re}(E_1) = \text{Re}(E_2)$  the eigenvectors of the matrix (2.58) are symmetric and antisymmetric superpositions of the eigenvectors of the uncoupled system. If one of the latter corresponds to a localized state then such an ARC leads to delocalization and lifetime shortening [173]. For the weak coupling situation  $2|V| < |\text{Im}(E_1) - \text{Im}(E_2)|$ , there is a crossing in the real part and an avoided crossing in the imaginary part. Here, the eigenstates, and also the spatial mode characteristics, do not interchange but only intermix near the crossing point. Moreover, the  $Q$ -factors are maintained.

Our idea is to exploit the weak coupling scenario to slightly "hybridize" a HQM and a directional LQM to a mode with high  $Q$ -factor and the directed far-field pattern of the LQM. This idea can be realized in three steps. First, take a cavity with HQMs, e.g., a microdisk. Second, introduce a one-parameter family of perturbations such that at least one HQM is almost unaffected and at least one HQM turns into a LQM having directed emission via refractive escape. Third, vary the parameter such that an ARC occurs between the HQM and the LQM. This scheme allows the systematic design of modes with high  $Q$ -factors and highly directed emission.

### 2.3.2 The system

We demonstrate the applicability of this scheme by a theoretical study of a semiconductor microdisk with a circular air hole as illustrated in Fig. 2.8. Different versions of such an

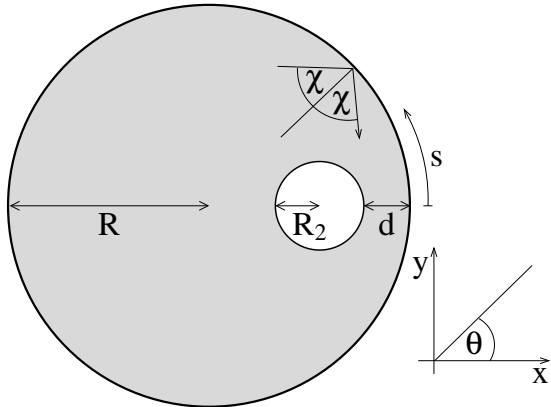


**Figure 2.8:** Schematic top view of the annular cavity with radius  $R$ . The radius of the hole is  $R_2$ , the distance to the disk's circumference is  $d$ . The direction of the outgoing light is characterized by the angle  $\theta$ .

annular cavity have been studied in the context of quantum chaos [152], optomechanics [174], and dynamical tunneling [130]. The closed system with perfectly reflecting walls has been used as model for dynamical tunneling [175, 176].

Holes with radii  $\geq 100$  nm can be pierced through the disk surface by techniques currently applied to photonic crystal membranes [177]. In Ref. [178], square-shaped holes had been introduced into a GaAs disk to reduce the laser threshold by perturbing the nonlasing modes. Our calculations apply to a small GaAs microdisk of radius  $R = 1\ \mu\text{m}$ . Similar disks have been used recently to demonstrate strong coupling between excitons and photons in single quantum dots [5]. We choose a slab thickness of 375 nm, a temperature of 4 K and a free-space wavelength  $\lambda$  close to 900 nm. This results in an effective index of refraction  $n = 3.3$  for the transverse magnetic polarization with an electric field perpendicular to the disk plane. We focus on this polarization, the conclusions are the same for transverse electric polarization.

### 2.3.3 Numerical analysis

We use the boundary element method [90] as introduced in Section 2.2 and the  $S$ -matrix approach [152] to compute the spatial profile of the electromagnetic field, the  $Q$ -factors, and the normalized frequencies  $\Omega = \omega R/c$ ,  $c$  being the speed of light in vacuum. According to the discrete symmetry, the modes are divided into even and odd symmetry classes.

A WGM in a disk without hole is characterized by azimuthal and radial mode numbers  $(m, n)$ . The introduction of a hole modifies a  $\text{WGM}_{m,n}$  the stronger the larger  $n$  is. This can be seen from the mode in Fig. 2.9(a) which bears a faint resemblance to a  $\text{WGM}_{12,3}$  but is a LQM with directed emission due to refractive escape. In contrast, a  $\text{WGM}_{m,n}$  with  $n = 1$  is nearly unaffected, see Fig. 2.9(b). Such modes have high  $Q$ -factors and are expected to emit without any preferred direction [170]. Here, we encounter the trade-off between  $Q$ -factors and directionality in a single cavity.

We turn now to the realization of an ARC as we vary the parameter  $d$ , the minimal dis-

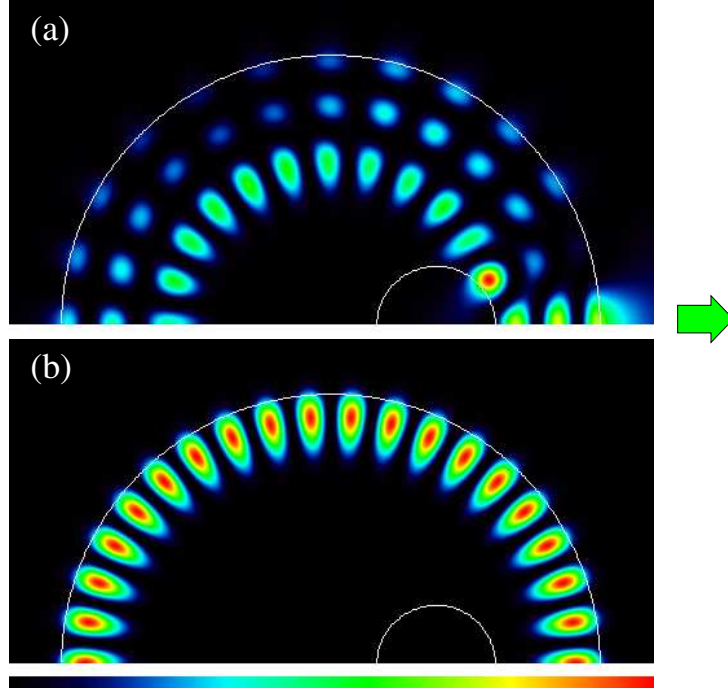


**Figure 2.9:** (a) Calculated near-field intensity pattern for LQM,  $\Omega = 7.0599$ ,  $Q \approx 300$ , even symmetry,  $R_2/R = 0.22$  and  $d/R = 0.389$ . The arrow shows the direction of light emission. (b) WGM<sub>19,1</sub>,  $\Omega = 7.0278$ ,  $Q \approx 553\,000$ .

tance of the hole to the disk's boundary. Figure 2.10(a) shows the normalized frequencies of all even-symmetry modes with  $\Omega \in [6.97, 7.05]$  corresponding to  $\lambda \approx 900$  nm. This figure reveals the typical scenario. For  $d/R > 0.35$ , WGMs such as WGM<sub>19,1</sub> (solid line) and WGM<sub>15,2</sub> (dotted) are much less affected by moving the hole than LQMs (dashed). With decreasing  $d/R$  all frequencies blueshift since dielectric material is effectively removed from the WGM region. This results in ARCs between WGMs and LQMs, see Figs. 2.10(a) and (b). At  $d/R \approx 0.24$ , a frequency repulsion together with a linewidth ( $Q$ -factor) crossing takes place. At  $d/R \approx 0.42$ , we observe a frequency crossing and a linewidth repulsion (cf. inset).

Figure 2.10(c) shows the directionality  $U$  versus  $d$ . We define  $U$  as the fraction of light emitted into an angular range of  $\pm 40^\circ$  around  $\theta = 0^\circ$ . Remarkably, near the frequency crossing at  $d/R \approx 0.423$ , the directionality of the WGM<sub>19,1</sub> and of the LQM behave in exactly the same way. Gradually decreasing  $d/R$ , the directionality of the WGM remains close to that of the LQM until it reaches the maximum at  $d/R \approx 0.389$ , where 90% of the light is emitted into a range of  $\pm 40^\circ$ . Figure 2.11 shows that at this value of  $d$  the angular emission pattern of the WGM and the LQM are almost identical. The far-field pattern has a narrow beam divergence angle of about  $57^\circ$  (full width at half maximum). The spectacular finding is that a WGM with ultra-high  $Q \approx 553\,000$  possesses highly directed emission. The explanation is the hybridization of modes near the ARC. Note that even a small contribution of the LQM to the WGM dominates the far-field pattern because of the strong leakiness of the LQM.

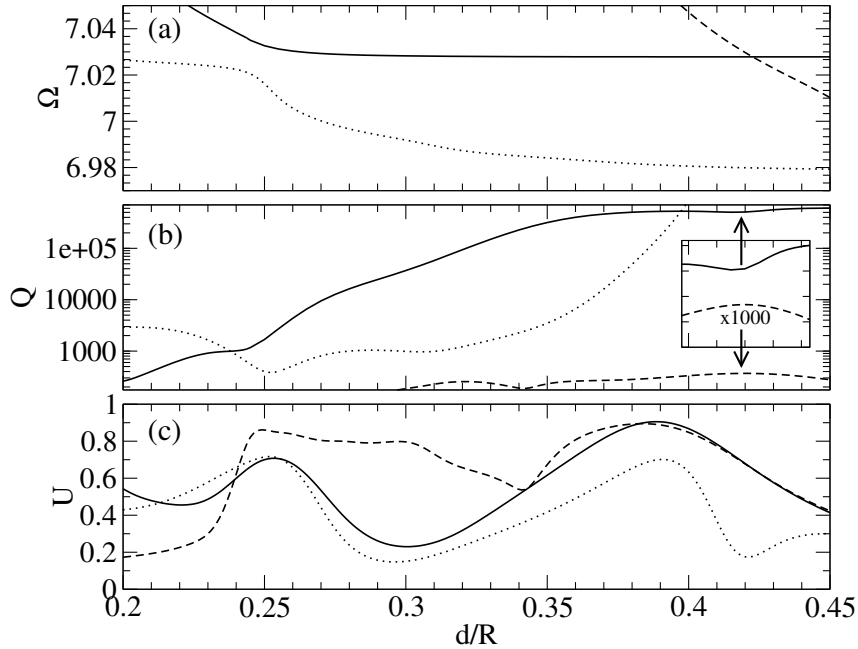
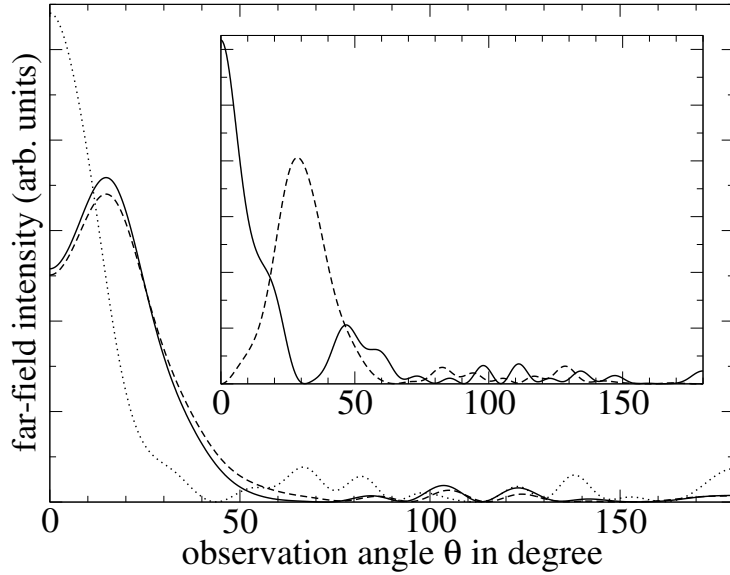


**Figure 2.10:** Normalized frequencies (a) and  $Q$ -factors (b) of even-symmetry modes vs.  $d$  at fixed  $R_2/R = 0.22$ . Inset,  $Q$ s in linear scale near the linewidth repulsion in the interval  $[0.4, 0.44]$ . The low- $Q$  branch (dashed) is multiplied by 1000. (c) Fraction  $U$  of emitted light into  $|\theta| \leq 40^\circ$  for the same modes as in (a) and (b).

Two additional features in Fig. 2.10(c) fit naturally into this scheme. First, the directionality of WGM<sub>15,2</sub>, a spectator of the ARC at  $d/R \approx 0.42$ , is less affected by the LQM. Second, near the ARC of the WGMs at  $d/R \approx 0.24$  the directionalities of both (strongly modified) WGMs are similar.

To see the relation to dynamical tunneling, we have to compare mode patterns with ray dynamics. A common approach in the field of quantum chaos is to superimpose the Husimi phase space projection (smoothed Wigner function) of a mode onto the Poincaré surface of section [165] as shown in Fig. 2.12. The Poincaré surface of section restricts the phase space of rays to the outer boundary of the cavity. The remaining variables are  $(s, \sin \chi)$ , where  $s$  is the arclength along the circumference of the disk and  $\chi$  is the angle of incidence measured from the surface normal; cf. Fig. 2.8. A good visualisation of the dynamics is achieved by reflecting the rays a finite number of times in the closed cavity with perfectly reflecting outer boundary [152]. The phase space of the annular cavity contains two regular regions defined by  $|\sin \chi| > 1 - d/R$ . A ray with such a large angle of incidence never encounters the hole. It rotates as whispering-gallery trajectory ( $\sin \chi = \text{const}$ ) clockwise,  $\sin \chi > 0$ , or counterclockwise,  $\sin \chi < 0$ . In particular, it cannot enter the region  $|\sin \chi| < 1 - d/R$ . For small  $R_2/R$ , this region is dominated by chaotic trajectories hitting the hole several times and thereby filling this phase space area in a pseudo-random fashion. Embedded into the chaotic region is the leaky region  $|\sin \chi| < 1/n$ . In the open cavity, a ray entering this region escapes refractively according to Snell's and Fresnel's laws.

The Husimi projection of the LQM is restricted to the chaotic part of phase space, see



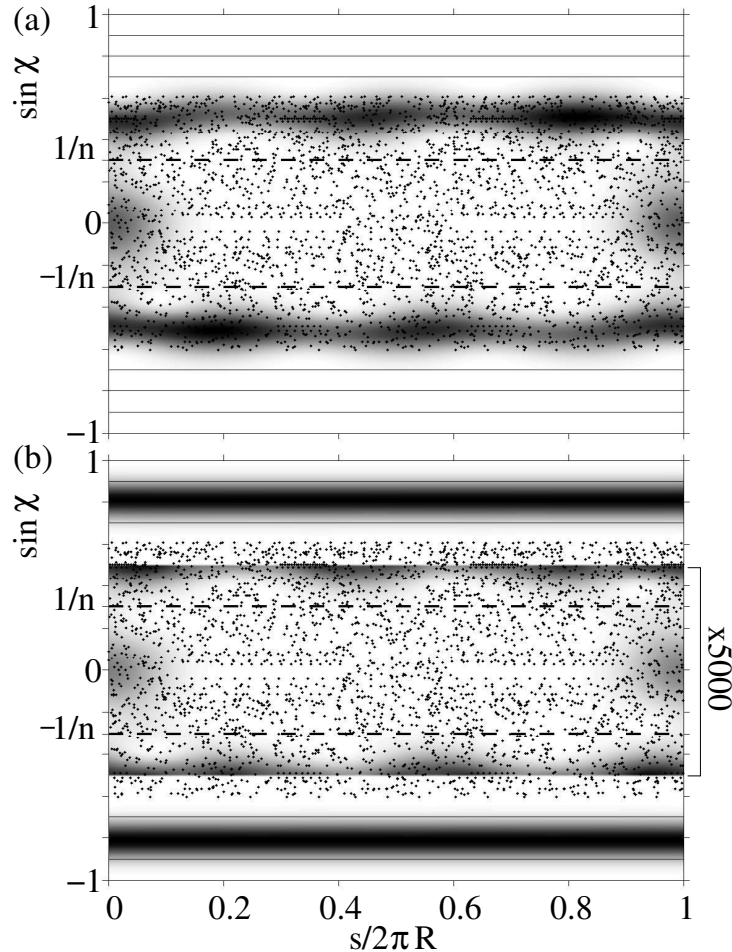
**Figure 2.11:** Angular dependence of the far-field intensity for  $\text{WGM}_{19,1}$  (solid line) and LQM (dashed) from Fig. 2.9. Dotted line marks  $\text{WGM}_{34,1}$ ,  $d/R = 0.399$ ,  $\Omega = 11.8833$ . Inset, even (solid) and odd (dashed) symmetry  $\text{WGM}_{36,1}$ ,  $d/R = 0.4478$ ,  $\Omega = 12.5241$ .

Fig. 2.12(a). The significant overlap with the leaky region explains the low  $Q$ -factor. In contrast, the WGM lives mainly in the regular region, see Fig. 2.12(b), far away from the leaky region ensuring a high  $Q$ . However, a small contribution exists in the chaotic region. To highlight this contribution, the intensity inside the region  $|\sin \chi| \leq 1/2$  is multiplied by 5000. The striking similarity to the LQM in Fig. 2.12(a) carries over to their far-field patterns in Fig. 2.11.

The role of tunneling is studied through the time evolution of a pure WGM which we define as a wave packet having no contribution in the chaotic region. Such a mode is a superposition of the real (hybridized) WGM and the LQM in Fig. 2.12 such that the LQM cancels the chaotic contribution of the real WGM. As time evolves, the initial cancellation vanishes since the LQM component in the superposition is short lived. In other words, a fraction of the initial pure WGM has tunneled from the regular to the chaotic region which allows for directed emission.

Figure 2.13(a) shows the directionality for various normalized frequencies  $\Omega$ . It illustrates that for lower (higher) frequency less (more) peaks appear. This is fully consistent with the fact that the larger the frequency the higher is the density of modes and therefore the larger the number of ARCs.

The best emission directionality we found for  $\text{WGM}_{34,1}$  with  $\Omega \approx 11.88$ , which corresponds to  $R = 1.7 \mu\text{m}$  at  $\lambda \approx 900 \text{ nm}$  or  $R = 1 \mu\text{m}$  at  $\lambda \approx 530 \text{ nm}$ . The maximum in  $U$  is at  $d/R = 0.399$ , see Fig. 2.13(a). The near-field pattern of this high- $Q$  mode and the corresponding low- $Q$  mode is depicted in Figs. 2.14(a) and (b), respectively. The far-field pattern of the high- $Q$  mode is shown in Fig. 2.11 as a dotted line. The emission is unidirectional with an angular divergence of  $28^\circ$  which is much smaller than the values reported for rounded triangles ( $90^\circ$ ) [135] and spiral-shaped disks ( $60^\circ$ ) [69], and only

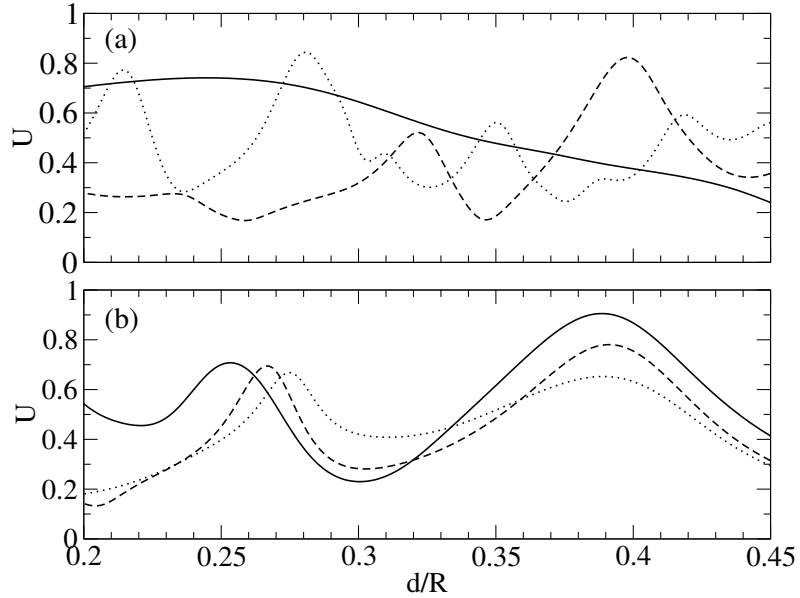


**Figure 2.12:** Poincaré surface of section (dots, solid lines) and Husimi projection (shaded regions) of modes in Fig. 2.9. (a) LQM. (b)  $WGM_{19,1}$ , the intensity inside  $|\sin \chi| \leq 1/2$  is multiplied by 5000 to allow for a comparison with the LQM. The dashed lines mark the leaky region.

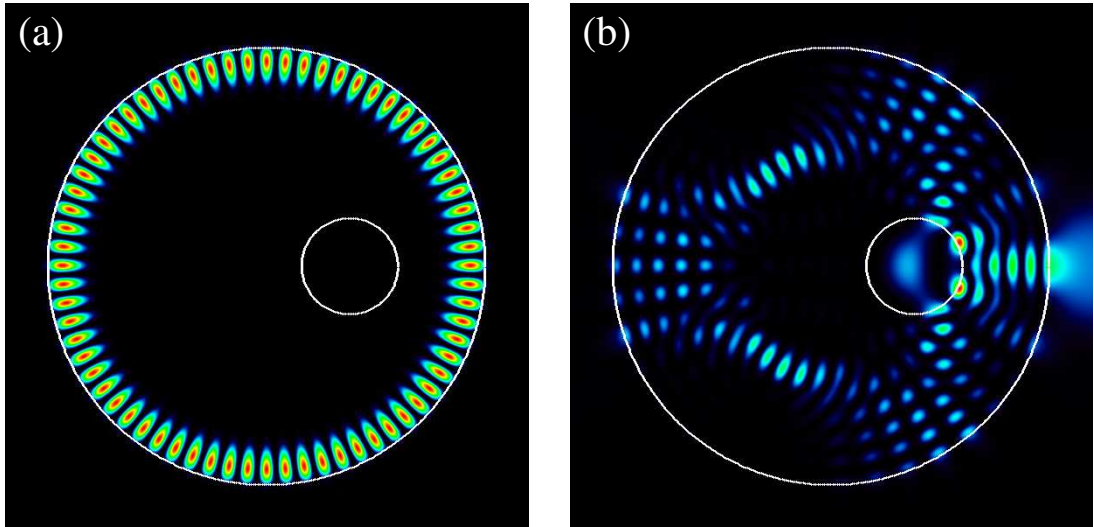
50% larger than that of a VCSEL-micropillar of the same radius [167]. The  $Q$ -factor is so huge that our numerics is pushed to the limit; as a conservative lower bound, we estimate  $Q \approx 10^8$ . In practice, this theoretical bound for the  $Q$ -factor is unreachable nowadays due to absorption [20] and surfaces roughness [179], i.e., the introduction of the hole does not affect the experimental  $Q$ -factor.

Figure 2.13(b) reveals that the directionality depends only weakly on the hole radius. This behavior allows rather large fabrication tolerances without compromising the directionality much.

Let us now briefly turn to the odd symmetry modes. Since the ARC scenario is different for even and odd symmetry, the respective far-field patterns will differ. For WGMs with low radial mode number  $n$ , the introduction of a hole only slightly lifts the even-odd degeneracy present in a perfect disk. Hence, a light emitter couples easily to both WGMs which possibly leads to less directed emission. This problem is resolved in the following cases: (i) In realistic microdisks, the degeneracy is lifted due to Rayleigh scattering from



**Figure 2.13:** (a) Directionality vs.  $d$  for various frequencies  $\Omega$  at fixed  $R_2/R = 0.22$ . WGM<sub>15,1</sub> with  $\Omega \approx 5.71$  (solid line), WGM<sub>34,1</sub> with  $\Omega \approx 11.88$  (dashed), WGM<sub>38,1</sub> with  $\Omega \approx 13.16$  (dotted). (b) WGM<sub>19,1</sub> for various hole radii:  $R_2/R = 0.22$  (solid), 0.28 (dashed), and 0.315 (dotted).



**Figure 2.14:** Calculated near-field intensity pattern for (a) even symmetry WGM<sub>34,1</sub>,  $\Omega \approx 11.88$ ,  $Q \approx 10^8$  and (b) corresponding LQM,  $\Omega \approx 11.93$ ,  $Q \approx 170$ .  $R_2/R = 0.22$  and  $d/R = 0.399$ .

the boundary [180]. (ii) For a single-photon source, it is desirable to place a single emitter, e.g., a quantum dot, on an antinode of an optical mode in order to enhance light-matter interaction. In such a case, the emitter does not couple to the other-symmetry mode which has zero intensity there. (iii) It is possible to find pairs of ultra-high- $Q$  WGMs showing simultaneously highly directed output, see inset in Fig. 2.11. In this particular case, the far-field maxima are displaced from each other which is interesting for applications, such

as all-optical switches and sensors.

Finally, the angular divergence of the output beam in vertical direction can be estimated to be  $2/\sqrt{m}$  as in the case of an ideal disk [181]. For our examples with  $m = 19$ , 34, and 38 follow angular divergences of  $26.3^\circ$ ,  $19.7^\circ$ , and  $18.6^\circ$ .

### 2.3.4 Summary

We presented a new and general concept to achieve unidirectional light emission from high- $Q$  modes in microcavities. The scheme is based on an avoided resonance crossing of an isotropic long-lived mode and a short-lived mode with unidirectional emission. As an example, we discussed a pierced microdisk. Here, the coupling of modes near the avoided resonance crossing can be interpreted as dynamical tunneling from a regular region in phase space containing long-lived whispering-gallery rays to a chaotic region containing short-lived rays. The corresponding modes show unidirectional light emission with narrow angular divergence and ultra-high quality factors,  $Q > 10^8$ .

## 2.4 Microcrystals

In this section, we analyse the properties of optical modes in zeolitic microcrystals [72] with hexagonal-shaped cross section, see Fig. 1.3(b). Hexagonally shaped cavities appear naturally also in other systems, such as ZnO nanoneedles [182], ZnO nanodisks [183], mesoporous silica [184] and ice columns [185]. We will see in the following that many features of the long-lived modes in hexagonal shaped microcavities can be successfully described by semiclassical approximations.

### 2.4.1 Introduction

We will compare our analysis to recent experiments on microlasers based on nanoporous molecular sieve host-guest systems [72]. Organic dye guest molecules were put into the channel pores of a zeolitic microcrystal AlPO<sub>4</sub> – 5 host. The aluminophosphate crystals grow with natural hexagonal boundaries with a high degree of perfection.

Microlasers and microresonators are not only relevant for experiments and applications but they are also of great interest from a theoretical point of view because they are *open* and they can be *mesoscopic*. In our case, the latter depends on the lasing dye and on the crystal size. Both introduce a characteristic length scale: the wavelength  $\lambda$  ranging from 600 nm to 800 nm, and the side length  $R$  of the hexagonal cross section of the crystal ranging from 2.6  $\mu\text{m}$  to 4.6  $\mu\text{m}$  in Refs. [72, 73]. In current experiments, larger crystals with  $R$  up to 20  $\mu\text{m}$  are under investigation. Only the ratio of these two length scales is relevant. It can be expressed by the dimensionless size parameter  $20 \leq kR \leq 190$ , where  $k = 2\pi/\lambda$  is the free-space wave number. For small  $kR$  the wavelength and the cavity size are of the same order. The system is microscopic. For large but finite  $kR$  the system is mesoscopic.

In Ref. [73] preliminary numerical computations of the full wave equations have been restricted to the near-field intensity pattern. We present a systematic numerical analysis of the hexagonally shaped dielectric resonator with  $20 \leq kR \leq 60$ , including resonance positions and lifetimes, near-field intensity patterns, far-field emission patterns, and effects of rounding of corners. To avoid convergence problems at corners, which had been a problem in Ref. [73], we will employ the boundary element method (BEM) as introduced in Section 2.2.

To study the deep mesoscopic regime  $kR > 60$ , we will introduce a semiclassical ray model. The semiclassical (short-wavelength) approximation is applied in the field of quantum chaos to relate quantum (wave) dynamics to their underlying classical (ray) dynamics. Most research efforts have been focused on closed resonators, i.e., billiards, where the dielectric interface is replaced by a hard wall on which the wave function vanishes. The regular hexagon belongs to the class of rational polygonal billiards. All angles  $\phi_j$  between sides are rationally related to  $\pi$ , i.e.,  $\phi_j = m_j\pi/n_j$ , where  $m_j, n_j > 0$  are relatively prime integers. If all  $m_j$  are equal to unity, for example in the case of the rectangle, then the dynamics is integrable. In the presence of *critical corners* with  $m_j > 1$ , the dynamics is not integrable but instead *pseudointegrable* [186]. As for integrable systems the phase

space is foliated by two-dimensional invariant surfaces [187, 188]. However, there are some peculiar features that distinguish these billiards strongly from integrable ones (and also from fully or partially chaotic billiards): (i) an invariant surface does not have the topology of a torus but instead that of a surface of higher genus [186], roughly speaking, a torus with additional handles; (ii) the dynamics is not quasiperiodic. This is reflected, for example, by multifractal Fourier spectra of classical observables [101, 189]; (iii) the quantum-classical correspondence is exotic [65]; (iv) the quantum spectrum obeys critical statistics [190]. To compute the quantum spectrum of a pseudointegrable billiard with a semiclassical treatment is extremely difficult, if possible at all. In this section, we will demonstrate that for a *sufficiently open* hexagonal dielectric resonator the spectrum and the eigenmodes can be computed semiclassically. As a byproduct, we gain an intuitive understanding of the numerical results.

## 2.4.2 The system

In the experiments on the microcrystals it has been shown that the electromagnetic field is TM polarized [72, 73]. Maxwell's equations reduce to a two-dimensional wave equation (2.18) with outgoing-wave condition (2.22). The index of refraction is  $n = 1.466$  inside the cavity and 1 outside. The origin of the coordinate system  $\mathbf{r} = (x, y) = (r \cos \theta, r \sin \theta)$  is located in the center of the hexagonal cavity. The complex-valued wave function  $\psi$  represents the  $z$ -component of the real-valued electric-field vector  $E_z(\mathbf{r}, t) = \text{Re}[\psi(\mathbf{r}) \exp(-i\omega t)]$  with angular frequency  $\omega = ck$ . We are here only interested in long-lived modes that provide a sufficiently long lifetime for the light to accumulate the gain required to overcome the lasing threshold.

Figure 2.15 shows the eight symmetry classes of the hexagon; see, e.g., Ref. [191]. In the notation  $-+a, \dots$ , the first sign is + if the wave function is even with respect to  $x \rightarrow -x$ , and - otherwise. Correspondingly, the second sign refers to  $y \rightarrow -y$ . The letter  $a$  indicates two symmetry lines, whereas the letter  $b$  indicates six symmetry lines.

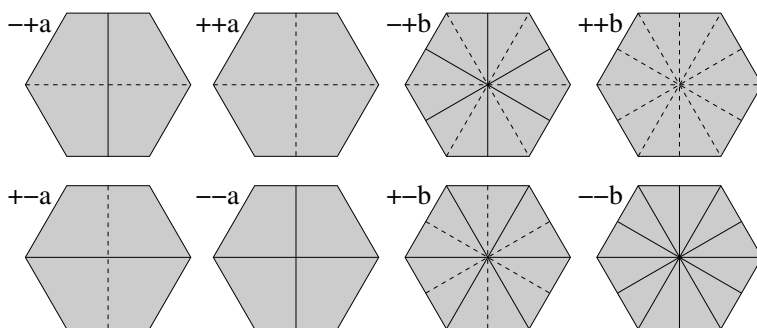


**Figure 2.15:** The eight symmetry classes of the hexagon. Odd (Even) symmetry is marked by solid (dashed) lines.

The  $+ - a$  and the  $- + a$ -modes have exactly the same complex  $k$ . The reason is that a  $+ - a$ -mode can be converted to a  $- + a$ -mode and vice versa in the following way. Take two copies of a single  $+ - a$ -mode. Rotate the first copy by  $60^\circ$  clockwise around the

origin of the coordinate system and the second copy by the same angle counterclockwise. Subtracting the two gives a  $-+a$ -mode with the same  $k$ . The way from  $-+a$  to  $+ - a$ , from  $++a$  to  $--a$ , and from  $--a$  to  $++a$  is analog. Hence,  $a$ -modes always appear in degenerate pairs having the same  $k$ .

Each linear superposition of such a pair of degenerate  $a$ -modes, we denote them by  $\psi_1$  and  $\psi_2$ , is also a solution of the wave equation (2.18). Because of the 6-fold symmetry of the system, we can find always two superpositions  $\psi_{\pm} = \psi_1 + p_{\pm}\psi_2$  with the property that the corresponding intensities  $|\psi_{\pm}|^2$  and  $|\psi_{\mp}|^2$  are invariant under  $60^\circ$ -rotations. That means  $\psi_+$  and  $\psi_-$  change only by a phase factor  $\exp i\Omega_{\pm}$  when rotated in real space by  $60^\circ$ . A full rotation about  $360^\circ$  does not change the wave function. Hence,  $\Omega_{\pm} = \pi q/3$  with  $q = -2, -1, 0, 1, 2, 3$ . Yet,  $q = 0$  and  $q = 3$  are not allowed because the intensities of  $a$ -modes are not invariant under  $60^\circ$ -rotations. A rotation about  $180^\circ$  is identical to  $(x, y) \rightarrow (-x, -y)$ . From this we find  $\Omega_{\pm} = \pm\pi/3$  for  $\psi_{\pm}$  formed by  $a$ -modes of type  $+-$ ,  $-+$  and  $\Omega_{\pm} = \pm 2\pi/3$  for  $\psi_{\pm}$  formed by  $a$ -modes of type  $++$ ,  $--$ . These requirements lead to

$$p_{\pm} = -\frac{\exp(i\Omega_{\pm})\psi_1(\mathbf{r}) - \psi_1(\tilde{\mathbf{r}})}{\exp(i\Omega_{\pm})\psi_2(\mathbf{r}) - \psi_2(\tilde{\mathbf{r}})}, \quad (2.60)$$

where  $\mathbf{r} \neq (0, 0)$  is an arbitrary point and  $\tilde{\mathbf{r}}$  is  $\mathbf{r}$  rotated by  $60^\circ$  counterclockwise. Formula (2.60) is valid for any relative phase of  $\psi_1$  and  $\psi_2$ .

The  $b$ -modes cannot be converted into each other since each  $b$ -mode is invariant under  $60^\circ$ -rotations up to a phase. Hence,  $b$ -modes do not form degenerate pairs.

For our numerics, it will be necessary to round the corners of the resonator slightly as depicted in Fig. 2.16. In terms of polar coordinates the parametrization of the boundary reads

$$r^s = \frac{2R^s}{(\cos \theta - \frac{1}{\sqrt{3}} \sin \theta)^s + (\frac{2}{\sqrt{3}} \sin \theta)^s + (\cos \theta + \frac{1}{\sqrt{3}} \sin \theta)^s}, \quad (2.61)$$

where  $s$  is the rounding parameter, a positive even integer.  $s = 2$  gives the circle, whereas  $s \rightarrow \infty$  gives the hexagon with flat sides and sharp corners. The parametrization in Eq. (2.61) preserves the full symmetry of the problem. Note that the parametrization used in Ref. [73] is different.

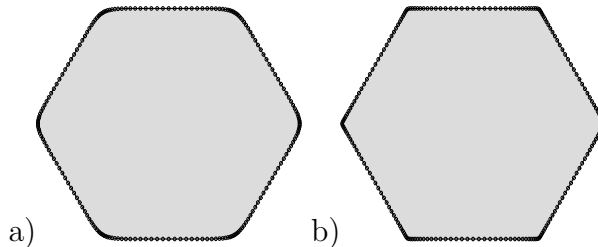


**Figure 2.16:** Shape and discretization (circles) of the resonator with (a)  $s = 20$ , (b)  $s = 200$  and  $\eta = 0.1$ . For illustrational reasons only  $N = 200$  discretization points are used.

It is easy to show that the maximum curvature for the rounded hexagon in Eq. (2.61) is given by  $(s - 1)/3R$  for  $s \geq 6$ . The radius of curvature  $\rho$  per wavelength  $\lambda = 2\pi/\text{Re}(k)$

is, therefore, given by

$$\frac{\rho}{\lambda} = \frac{3}{2\pi} \frac{\operatorname{Re}(kR)}{s} \quad (2.62)$$

for large  $s$ .

### 2.4.3 Numerical analysis

To solve wave equation (2.18) with outgoing-wave condition (2.22) we use the BEM. The boundaries are discretized by dividing them into  $2N$  small boundary elements. For the boundary (2.61), we choose the following discretization:

$$\theta = \xi + \eta \sin [6(\xi + \pi/2)] . \quad (2.63)$$

The discretization points on the circle  $\xi \in [0, 2\pi]$  are chosen to be spaced equidistantly. The parameter  $\eta$  determines the distribution of points on the cavity, the shape of which is completely determined by the rounding parameter  $s$ .  $\eta = 0$  gives an uniform density of points, while  $\eta > 0$  gives an enhancement near the corners as illustrated in Fig. 2.16. We always use  $\eta = 0.1$ .

Figure 2.17 shows the total cross section  $\sigma$  as function of the dimensionless wave number  $kR$  [ $\operatorname{Im}(kR) = 0$ ] for plane-wave scattering with incidence angle  $\theta = 15^\circ$ . We observe a *single-mode spectrum*, a series of roughly equidistant peaks. Note that the fine structure around  $kR \approx 24.5$  is an artifact of the BEM, which can be removed by increasing the number of discretisation points [90]. We will count the peaks by the *mode index*  $m$  according to increasing  $kR$  starting with  $m = 0$  at  $kR = 0$ . The first peak at  $kR \approx 20.5$  in Fig. 2.17 is then labeled by  $m = 23$ . The position of a given peak  $kR$  and its width  $\Gamma$  in Fig. 2.17 are related to the complex value of  $kR_{\text{mode}}$  of the corresponding resonant mode by means of  $kR_{\text{mode}} \approx kR - i\Gamma/2$ . The subscript ‘‘mode’’ will be dropped from now on.

The BEM not only solves the scattering problem but it also can compute the resonant modes. In Fig. 2.18, we plot the real and imaginary part of  $kR$  of a resonance as function of the rounding parameter  $s$ .  $\operatorname{Re}(kR)$  saturates around  $s = 55$ , whereas  $\operatorname{Im}(kR)$  saturates at  $s \geq 100$ . We take  $s = 100$  translating to  $\rho/\lambda \approx 0.11$ . It is surprising that one has to decrease  $\rho$  to values one order of magnitude smaller than the wavelength. In the following, we will fix  $\rho/\lambda \approx 0.11$ , that means when we change  $\operatorname{Re}(kR)$ , we have to change  $s$  accordingly.

Figure 2.19 shows the long-lived resonances in the complex plane inside the strip  $20 \leq \operatorname{Re}(kR) \leq 60$ . Our numerics cannot cover the full regime of the microlaser experiments [72, 73]  $20 \leq \operatorname{Re}(kR) \leq 190$ . Small values of  $|\operatorname{Im}(kR)|$  correspond to long-lived modes and, correspondingly, large values correspond to short-lived modes. Four features in Fig. 2.19 are striking: (i) the *a*-modes are two-fold degenerated as predicted from the symmetry considerations. (ii) The *b*-modes come in quasi-degenerated pairs with slightly different  $kR$  (differences in  $\operatorname{Re}(kR)$  and  $\operatorname{Im}(kR)$  are of the same order which cannot be seen in Fig. 2.19). It is not possible to resolve these small splittings in the scattering cross

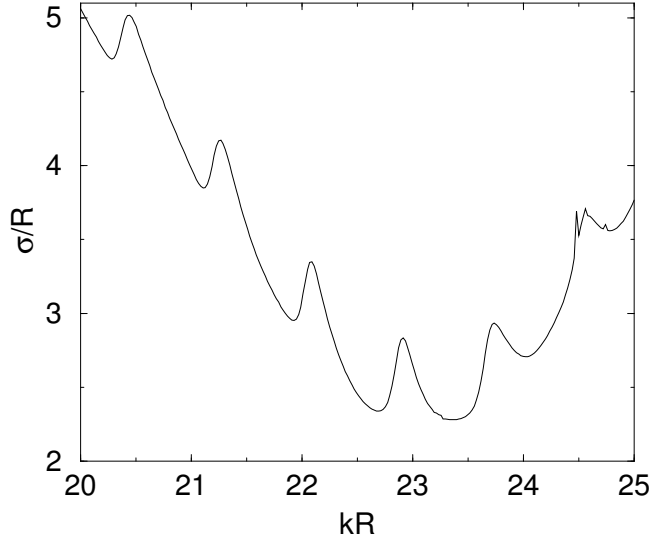


**Figure 2.17:** Calculated total scattering cross section  $\sigma/R$  vs.  $kR$  for a hexagonal resonator. The plane wave is incidence at  $15^\circ$  to the horizontal side faces.  $s = 100$ , and  $2N = 2000$ .

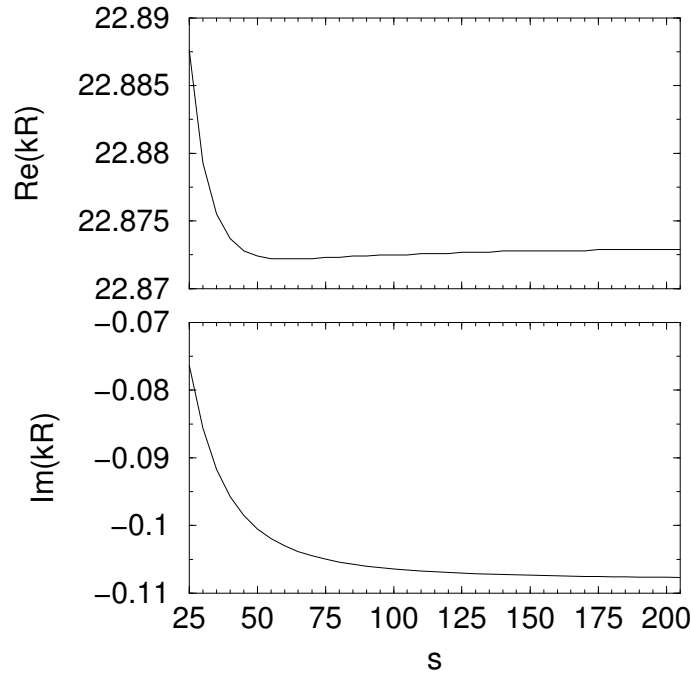


**Figure 2.18:** Real and imaginary part of  $kR$  as function of the rounding parameter  $s$ .  $2N = 2000$ ,  $m = 26$ ,  $kR = 22.8725 - i0.1064$  for  $s = 100$ .

section in Fig. 2.17. (iii) The values of  $\text{Re}(kR)$  are approximately equidistantly spaced. (iv) Highly-excited resonances with  $\text{Re}(kR) \geq 34$  lie approximately on a smooth curve.

The equidistant spacing of  $\text{Re}(kR)$  can be seen more clearly in Fig. 2.20(a). Pairs of (quasi-) degenerated modes are labeled by the mode index. We see that all pairs lie extremely close to a line  $\text{Re}(kR) = \nu(m + m_0)$  with mode spacing  $\nu$  and shift  $m_0$ . Linear regression gives  $\nu \approx 0.8238$  and  $m_0 \approx 1.7516$ . The same mode spacing can be observed

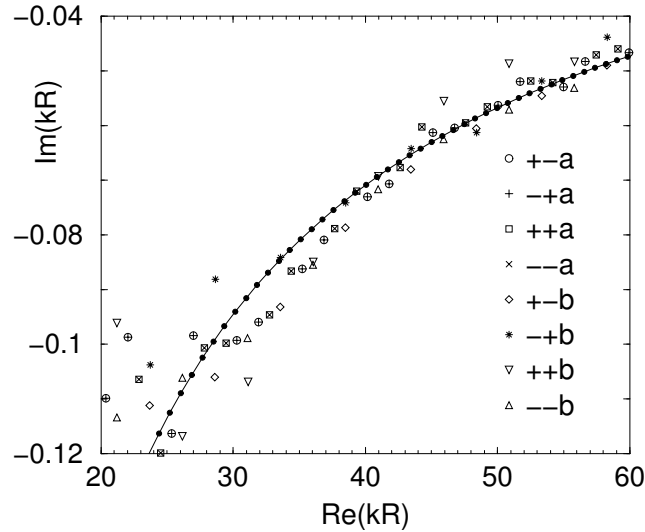


**Figure 2.19:** Long-lived resonances in the complex plane, cf. Fig. 2.15. Filled circles on the solid line are the semiclassical solutions in Eqs. (2.66) and (2.73).

in Fig. 2.17. The corresponding free spectral range  $\Delta\lambda = \nu\lambda^2/2\pi R$  is in agreement with the experiments [72, 73].

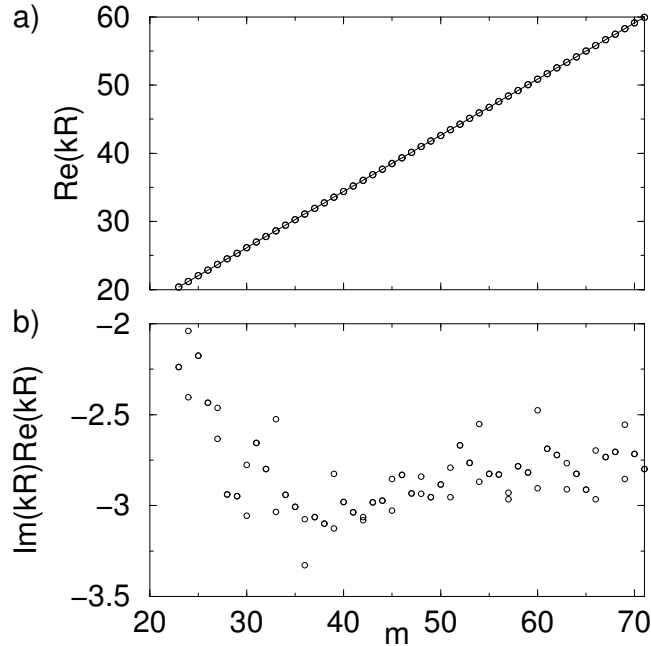


**Figure 2.20:** (a) Wave number  $\text{Re}(kR)$  vs. mode index  $m$ . The data can be approximated by a straight line  $\text{Re}(kR) = \nu(m + m_0)$  with  $\nu \approx 0.8238$  and  $m_0 \approx 1.7516$ . (b)  $\text{Im}(kR)\text{Re}(kR)$  vs.  $m$ . For  $m \geq 34$ , the data is well approximated by the mean value  $\approx -2.87$ .

From Fig. 2.20(b), we can infer that the product of real and imaginary part of  $kR$  for

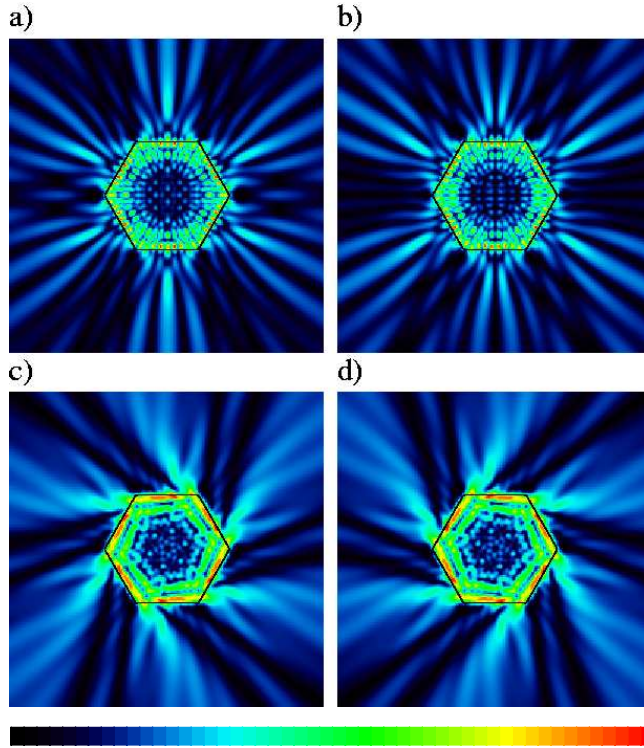
highly-excited modes does not depend on the mode index  $m$ . We find

$$\text{Im}(kR)\text{Re}(kR) \approx -2.87 \quad (2.64)$$

for  $n = 1.466$ . Later, we will see that this remarkable relation is a good approximation not only in the numerical accessible regime but also in the full experimental regime. Relation (2.64) implies that the lifetime is proportional to  $\text{Re}(k)R^2$  and the quality  $Q$  is proportional to  $\text{Re}(kR)^2$  ( $Q$  ranges from roughly 70 to 6400). This finding is relevant for the future experiments on microcrystal lasers, it implies that the laser threshold decreases as the size of the resonator is increased.

Due to the qualitative change in behavior around  $\text{Re}(kR) \approx 34$  in Figs. 2.19 and 2.20(b), we distinguish the regions  $\text{Re}(kR) < 34$  and  $\text{Re}(kR) > 34$ . We refer to the former one as the microscopic regime and to the latter as the mesoscopic regime.

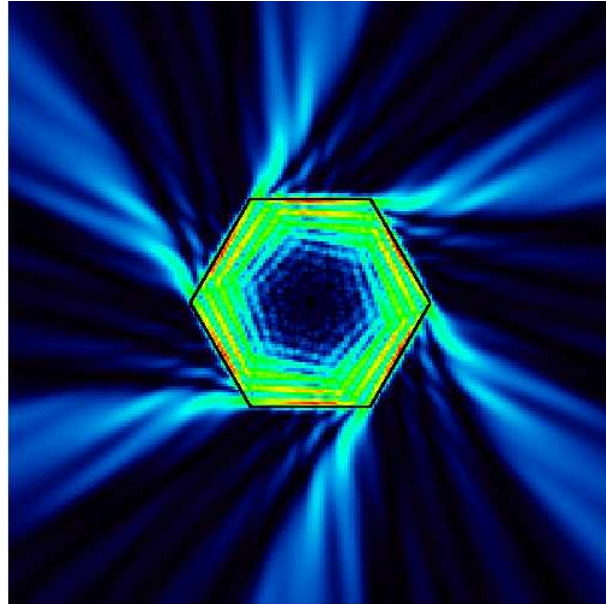
Figures 2.21(a) and (b) show the near-field intensity pattern of the modes  $26++a$  and  $26--a$  (mode index  $m = 26$ ), respectively. While these two modes are standing waves, the corresponding superpositions  $\psi_+$  and  $\psi_-$  in Figs. 2.21(c) and (d) are unidirectional traveling waves. We call them chiral modes. Such a mode is specified by its mode index  $m$  and a label + (traveling counterclockwise) or - (traveling clockwise). In the following, we will deal only with these chiral modes which are more straightforward to compare to the ray dynamics.



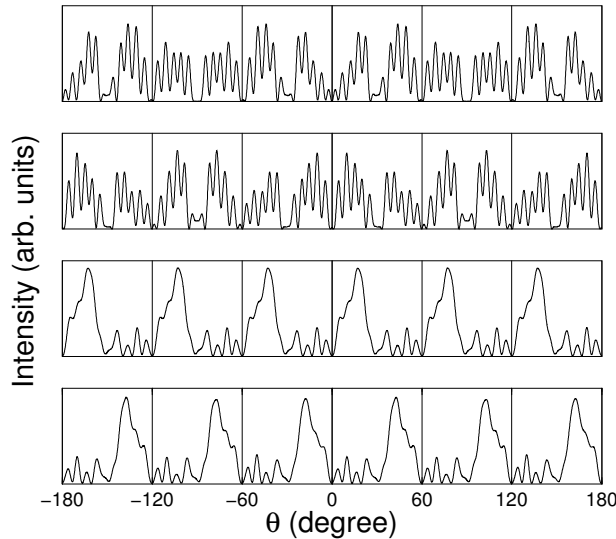
**Figure 2.21:** Calculated near-field intensity pattern  $|\psi(\mathbf{r})|^2$  of two-fold degenerated modes. (a)  $26++a$  and (b)  $26--a$  with well-defined parity. (c)  $26+$  and (d)  $26-$  with well-defined chirality. Intensity is higher for redder colours, and vanishes in the dark regions.  $kR = 22.8725 - i0.1064$ ,  $s = 100$ ,  $2N = 2000$ .

Figure 2.22 shows a higher-excited superposition  $\psi_-$ . The following properties can be

observed: (i) the intensity is concentrated along the boundary of the cavity, resembling *whispering-gallery modes* in circular or weakly deformed circular cavities. (ii) The wave pattern looks regular. An approximate nodal-line structure with a peculiar twist is visible. (iii) The *emission is predominantly at the corners*. This is in agreement with the laser emission measured in the experiments in Refs. [72, 73]. (iv) Outside the cavity the light propagates along certain directions *not parallel to the facets*. The latter fact can be seen more clearly in the far-field distribution shown in Fig. 2.23. There are six emission peaks with angular width of  $\approx 14^\circ$  and angular distance to the nearest facet of  $\approx 17^\circ$ .



**Figure 2.22:** Chiral mode  $50-$ .  $kR = 42.6318 - i0.06766$ ,  $s = 200$ ,  $2N = 4000$ .



**Figure 2.23:** Far-field emission pattern,  $|\psi(r, \theta)|^2$  for large  $r$ , of (from above)  $50--a$ ,  $50++a$ ,  $50-$ , and  $50+$  modes; cf. Fig. 2.22. Vertical lines mark the directions parallel to the edges.

The *sensitivity to rounding* found for the resonance positions in the complex plane, see Fig. 2.18, also shows up in the mode structure. Figure 2.24 shows the near-field intensity pattern of a rounded hexagon with  $s = 20$ , i.e.,  $\rho \approx \lambda$ . The emission is again at the corners, but it is reduced. Moreover, the directionality has decreased and the high-intensity directions are now parallel to the edges. The latter fact can be seen better in the far-field emission pattern in Fig. 2.25.

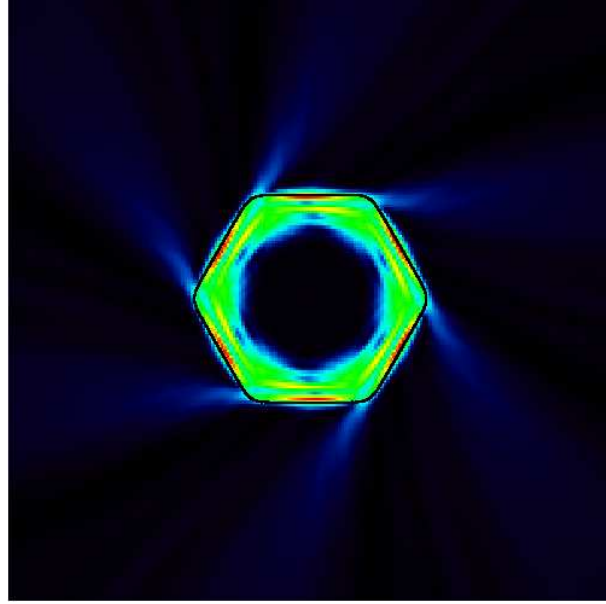


**Figure 2.24:** Mode 50 $-$  in a rounded hexagon with  $s = 20$ , cf. Fig. 2.22.  $kR = 42.7099 - i0.01836$ ,  $2N = 4000$ .

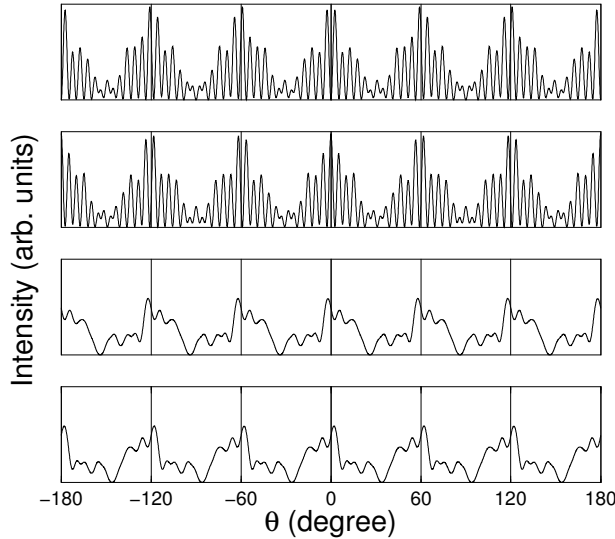


**Figure 2.25:** Far-field emission pattern of the mode (from above) 50 $--a$ , 50 $++a$ , 50 $-$ , and 50 $+$  in the rounded hexagon; cf. Fig. 2.24.

#### 2.4.4 Semiclassical analysis

Having computed numerically the long-lived modes in the regime  $20 \leq \text{Re}(kR) \leq 60$ , we now introduce a semiclassical ray model in order to see what happens in the deep mesoscopic regime  $\text{Re}(kR) > 60$ . So far, semiclassical approximations of dielectric resonators have been discussed only for the case of smooth boundaries [66, 87, 192]. Our heuristic approach is divided into three steps: geometric optics, semiclassical quantization, and emission mechanisms.

Geometric optics follows from wave equation (2.18) in the limit  $\text{Re}(kR) \rightarrow \infty$  neglecting all interference effects. In the following, we focus on low-index materials with  $n_{\min} < n < n_{\max}$  where  $n_{\min} = 1/\sin 60^\circ \approx 1.16$  and  $n_{\max} = 1/\sin 30^\circ = 2$ . The lower bound guarantees that a six-bounce periodic ray with angle of incidence  $\theta_i = 60^\circ > \theta_c$  (with  $\sin \theta_c = 1/n$ ) is trapped within the hexagonal resonator by total internal reflection at the facets; see Fig. 2.26. Some aspects of the much simpler case  $n < n_{\min}$  have been studied in Ref. [193]. The periodic ray is marginally stable with respect to shifting it along the boundary. In this way, we obtain a whole family of periodic rays with identical length and angle of incidence.

The upper bound  $n_{\max} = 2$  ensures that triangular-shaped periodic rays with  $30^\circ$  angle of incidence are not totally reflected. The periodic-ray family with  $\theta_i = 60^\circ$  is then the only long-lived family of short period. Yet, since periodic rays are dense in phase space, we cannot exclude the possibility that there are also long-lived periodic rays of high period.

It should be emphasized at this point that the (infinite) long lifetime of the rays is relevant for our purpose, whereas the periodicity of the rays is not relevant. The latter comes in here simply because periodic rays (and their neighborhood) can be long-lived. We will not apply methods from semiclassical periodic-orbit theory [61].

The periodic rays are unstable with respect of changing the angle of incidence. Figure 2.26 shows a ray with slightly different initial angle of incidence. The ray is slowly diverging from the central one. After some time, it reaches the corner on its other side at (almost) normal incidence. Consequently, it then escapes refractively with probability close to 1.

As long as the ray does not escape from the cavity it behaves as if it were in a closed resonator, i.e., in a billiard. It is illuminating to examine the ray dynamics of the open system in terms of the invariant surface of the hexagonal billiard. The genus of the invariant surfaces is given by the general formula [186]

$$g = 1 + \frac{\mathcal{N}}{2} \sum_j \frac{m_j - 1}{n_j} \quad (2.65)$$

where the sum is over all corners with angles  $\phi_j = m_j \pi / n_j$  and  $\mathcal{N}$  is the least common multiple of the  $n_i$ . For the hexagon  $m_j = 2$  and  $n_j = 3$  for all  $j$ ; hence,  $\mathcal{N} = 3$  and finally,  $g = 4$ . The surface of genus four is shown schematically in Fig. 2.27. The topology is the same for all initial conditions. First, we consider the special case where the surface is foliated by periodic orbits. Each periodic ray with  $\theta_i = 60^\circ$  appears here as two disjoint circles with different sense of rotation. These two circles correspond to the two unidirectional traveling waves. In the following, we will focus on the circle with clockwise

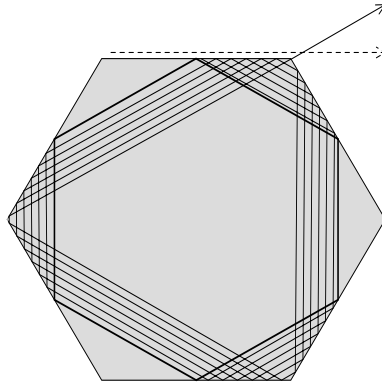


**Figure 2.26:** Semiclassical ray model. Thick line marks a member of the family of long-lived rays, other members are obtained by shifting the ray along the boundary (not shown). The thin line marks a ray with slightly different angle of incidence. Arrows indicate emission due to pseudointegrable dynamics (thin) and boundary waves (dashed).

rotational sense. On the same invariant surface we also find periodic rays of “bouncing-ball” type with angle of incidence  $\theta_i = 0^\circ$ . In the open system, the bouncing-ball rays are not long-lived since they are not totally reflected.

The dynamics on a generic invariant surface in the neighborhood of the special surface discussed above is as follows. A nonperiodic ray starting near the central periodic ray with slightly different initial angle of incidence stays in the vicinity of the central ray by winding around the handle many times. Finally, it has to leave the vicinity of the periodic ray since pseudointegrable motion is ergodic on generic invariant surfaces [194]. Before the ray can reach another handle (in the gray region in Fig. 2.27) and perform complicated dynamics, it escapes refractively from the cavity. Hence, the sufficiently open resonator does not see the complicated topology of the full invariant surface but just two disjoint tori. In this sense, the openness moves the system closer to integrability. That is the reason why we can derive in the following paragraphs a practical semiclassical approximation for the open hexagonal resonator, whereas this is impossible for the hexagonal billiard.

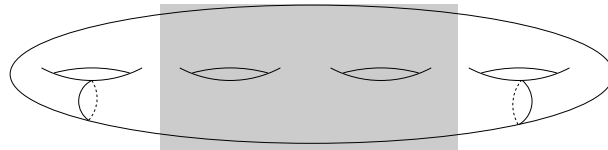


**Figure 2.27:** Invariant surface of the hexagonal billiard. The small circle on the left- (right-) hand side represents the central periodic ray in Fig. 2.26 cycling (counter) clockwise. In the gray region the condition for total internal reflection is not fulfilled.

Having identified the long-lived part of classical phase space, we now quantize it in a semiclassical approximation. This approximation is valid for small  $1/\text{Re}(kR)$  and it does include interference effects, in contrast to the geometric-optics limit.

Because of the absence of stability of the periodic rays the conventional approach in laser optics, the paraxial approximation (see, e.g., Ref. [195]), does not work. Nevertheless, the

semiclassical quantization is simple. The idea is that an integer number  $m = 1, 2, 3, \dots$  of wavelengths  $\lambda_{\text{inside}} = \lambda/n$  fits on the path length of the long-lived ray  $l = 3\sqrt{3}R$  shown in Fig. 2.26, taking into account the phase shifts at the dielectric boundary. As detailed in Appendix A we arrive at

$$\text{Re}(kR) = \frac{2\pi}{3\sqrt{3}n}(m + \beta) \quad (2.66)$$

with the total boundary phase shift  $\beta$  given by

$$\tan \frac{\pi}{6}\beta = \alpha \quad (2.67)$$

and

$$\alpha = \frac{\sqrt{n^2 \sin^2 \theta_i - 1}}{n \cos \theta_i}. \quad (2.68)$$

Note that the number  $m$  defined in this way is identical to the mode index  $m$  as used before. The quantization condition (2.66) explains the single-mode spectrum in Figs. 2.17 and 2.20(a). With  $n = 1.466$  the mode spacing is  $2\pi/3\sqrt{3}n \approx 0.8248$  in agreement with  $\nu = 0.8238$  obtained by fitting to the numerical data. However, the shift  $\beta \approx 1.562$  differs a bit from the numerically obtained shift  $m_0 \approx 1.7516$ . To understand this discrepancy, we plot in Fig. 2.28 the phase shifts  $\beta_m$  defined as  $\beta$  computed from Eq. (2.66) inserting the numerically computed values of  $\text{Re}(kR)$ . Clearly, going towards the semiclassical limit  $m \rightarrow \infty$  leaves the crude fitting value  $m_0 \approx 1.7516$  in favour of a smaller value  $\beta_\infty = \lim_{m \rightarrow \infty} \beta_m$  closer to our semiclassical prediction  $\beta \approx 1.562$ .

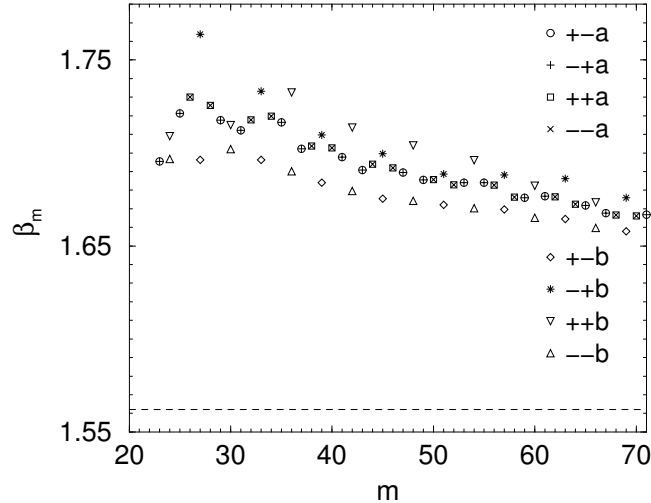


**Figure 2.28:**  $\beta_m$  vs. mode index  $m$ . Dashed line marks the semiclassical prediction  $\beta \approx 1.562$ .

Let us assume that  $\beta_m$  has the following form:

$$\beta_m = \gamma m^{-\delta} + \beta_\infty \quad (2.69)$$

and that  $\beta_\infty$  equals our semiclassical solution  $\beta \approx 1.562$ . Figure 2.29 shows  $\Delta\beta = \beta_m - \beta_\infty$  as function of  $m \geq 34$  in a log-log plot for fixed  $n = 1.466$ . Linear regression gives  $\gamma \approx 0.89$

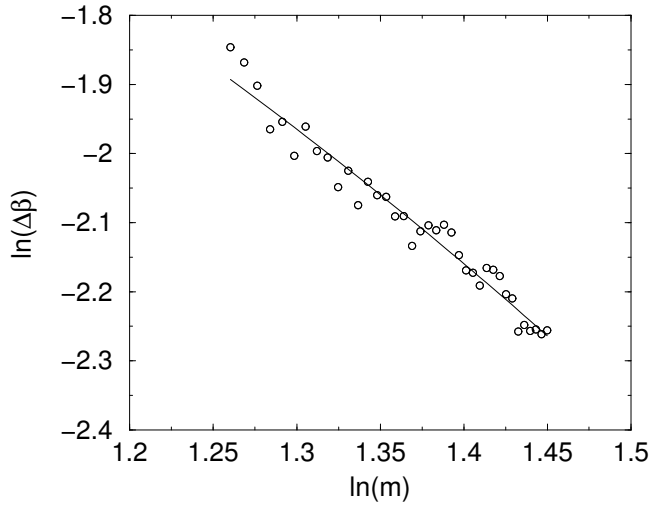


**Figure 2.29:**  $\ln \Delta\beta$  vs.  $\ln m$  with  $m \geq 34$ . For quasi-degenerate modes the arithmetic mean of  $\Delta\beta$  is taken.

and  $\delta \approx 0.5038$ . Based on this numerical finding, we conjecture that the next order in the semiclassical approximation (2.66) is of the form  $\gamma/\sqrt{m}$ .

Observation of Figs. 2.21(c) and (d) shows that the “nodal lines” close to the boundary of the cavity are not exactly parallel to the boundary but slightly tilted (about  $5^\circ$ ). This angular shift decreases as one goes to higher-excited modes. Specular reflection of a plane wave at the boundary leads always to nodal lines parallel to the boundary. Hence, it is reasonable to interpret the angular shift as a kind of *non-specular reflection*. The angular shift can be traced back to the fact that the wave function restricted to the boundary is a periodic function. Because of the periodicity, the Fourier spectrum of the wave function along the boundary is discrete. The discrete peaks can be related to a discrete set of allowed angles of incidence. The angle  $\theta_i = 60^\circ$  typically falls between two neighboring discrete angles. In Appendix A, we compute the angular shift analytically to first order as  $\Delta\theta = \theta_i - 60^\circ = \theta_i - \pi/3 \approx -\sqrt{3}\beta/m$  in agreement with the numerics (not shown). In the semiclassical limit  $m \rightarrow \infty$  the angular shift vanishes. Our angular shift is different from those cases discussed in the context of non-specular reflections (see, e.g., Ref. [196]), in that it happens above the critical angle of total internal reflection. Moreover, it has nothing to do with the angular Goos-Hänchen effect (see, e.g., Ref. [197]), which is the Goos-Hänchen shift at a curved interface.

The number of wavelengths fitting on a path length determines the symmetry class. Straightforward considerations give Table 2.1. The semiclassical quantization procedure neither distinguishes between  $+-$  and  $-+$  parties nor between  $++$  and  $--$  parties. Hence, within the semiclassical approximation these modes are exactly degenerated, regardless whether they are of type *a* or *b*. This explains the numerical finding of quasi-degenerate *b*-modes.

The fact that our model predicts a single-mode spectrum, a one-parameter  $m = 1, 2, \dots$  family of long-lived resonances, is related to the fact that there is only one long-lived family of periodic rays (with short period). There is no “transversal mode index” which

$m$	symmetry class
1	$+ - a, - + a$
2	$+ + a, - - a$
3	$+ - b, - + b$
4	$+ + a, - - a$
5	$+ - a, - + a$
6	$+ + b, - - b$

**Table 2.1:** Symmetry class and mode index  $m$ . The table is periodic in  $m$  with period 6.

would be expected if the paraxial approximation were applicable. Higher transverse modes correspond to rays with angle of incidence considerably different from  $60^\circ$ . They are much shorter lived which becomes clear in the following paragraphs when we discuss the emission mechanisms.

Having derived a semiclassical quantization condition for the real part of  $kR$ , we now compute its imaginary part. The temporal behavior of the intensity of a resonant mode is  $I \propto \exp[2 \operatorname{Im}(\omega)t]$ . The outgoing relative intensity per unit time is

$$\Delta I = -\frac{1}{I} \frac{dI}{dt} = -2 \operatorname{Im}(\omega) = -2c \operatorname{Im}(k). \quad (2.70)$$

What are the mechanisms for this decay of intensity? In the framework of ray optics, the periodic rays in Fig. 2.26 remain forever in the cavity. Hence, we have to include explicitly wave effects. We identify three candidates of such wave effects, all of which are related to the corners. The first one is *diffraction at corners*. Corner diffraction may be a emission mechanism since a wave with finite wavelength coming close to a corner is diffracted partly to the exterior and partly back into the interior with another spectrum of directions for which the condition of total internal reflection may not be fulfilled at the next reflection. We will argue that corner diffraction is important for the *emission directionality* but not for the *escape rate*. For the escape rate, we find two new relevant effects which are responsible for *transport to corners*. We call them *boundary-wave leakage* and *pseudointegrable leakage*.

The boundary-wave leakage is illustrated in Fig. 2.26. An evanescent boundary wave travels along an infinitely extended dielectric interface from  $-\infty$  to  $+\infty$ . We assume that at a finite interface the boundary wave fully separates from the interface at the corner. In Appendix A, we determine the outgoing relative intensity for any regular polygon (equilateral triangle, square, hexagon, ...) due to boundary waves. In particular, for the hexagon we find

$$\Delta I_{\text{bw}} = \frac{3c}{4 \operatorname{Re}(k) R^2} \frac{n^3}{\sqrt{3n^2/4 - 1}(n^2 - 1)}. \quad (2.71)$$

The pseudointegrable leakage is due to the fact that wave optics does not realize exactly  $\theta_i = 60^\circ$  as already mentioned and shown in Appendix A. Putting this small angular deviation  $\Delta\theta$  into the initial conditions gives rise to rays with finite lifetime due to the

pseudointegrable dynamics; see Fig. 2.26. In Appendix A, we estimate the outgoing relative intensity due to pseudointegrable leakage for the hexagon as

$$\Delta I_p = \frac{4\pi c}{3\text{Re}(k)R^2} \frac{\beta(n)}{n^2}. \quad (2.72)$$

The derivation can be easily extended to any regular polygon. Cavities with integrable internal dynamics, like the equilateral triangle and the square, have  $\Delta I_p = 0$ . That means the neighborhood of the long-lived family of periodic rays has roughly the same lifetime as the periodic rays. In such a case, we expect a multimode spectrum in the mesoscopic regime. Indeed, this has been found in scattering experiments on the dielectric square in Ref. [198].

Remarkably, both contributions in Eqs. (2.71) and (2.72) have the same dependence on  $\text{Re}(k)$ . In either case, the contribution vanishes in the limit  $\text{Re}(k) \rightarrow \infty$ , reflecting their wave nature. Adding both contributions,  $\Delta I = \Delta I_{bw} + \Delta I_p$ , gives the central result

$$\text{Im}(kR) \text{Re}(kR) = f(n) \quad (2.73)$$

with

$$f(n) = f_{bw}(n) + f_p(n), \quad (2.74)$$

$$f_{bw}(n) = -\frac{3n^3}{8\sqrt{3n^2/4 - 1}(n^2 - 1)}, \quad (2.75)$$

and

$$f_p(n) = -\frac{2\pi}{3} \frac{\beta(n)}{n^2}. \quad (2.76)$$

For  $n = 1.466$ , we find  $\text{Im}(kR) \text{Re}(kR) \approx -2.837$  in reasonable agreement with the numerical data in Figs. 2.19 and 2.20(b). Figure 2.30 compares the semiclassical result in Eqs. (2.73)–(2.76) to the numerical data as function of  $n$ . While some resonances are very well described by the semiclassical approximation, some are only roughly described. The latter cases correspond to the strong fluctuations around the semiclassical hyperbola (2.73) already visible in Fig. 2.19.

Our ray model also explains some aspects of the mode structure in Figs. 2.22 and 2.23. The whispering-gallery-like structure is related to the geometry of long-lived rays; see Fig. 2.26. The envelopes of the emission direction are described by the boundary-wave leakage and the pseudointegrable leakage; cf. Figs. 2.22, 2.23, and 2.26. The distribution within the envelopes is not predicted by our model. Here, corner diffraction is important because both the boundary waves and the pseudointegrable ray dynamics lead to escape arbitrarily close to the corner.

Our ray model gives a natural explanation for the sensitivity to rounding of corners. Let us assume that a sufficiently small rounding only slightly weakens the loss due to boundary waves, whereas it reduces corner diffraction strongly. Numerical simulations of ray dynamics in rounded hexagons show that the periodic rays, see Fig. 2.26, are stabilized. This statement is independent on the particular chosen boundary parametrization. Hence, there is no pseudointegrable leakage. This leads to considerably larger lifetimes and emission parallel to the facets; compare Figs. 2.22–2.25.

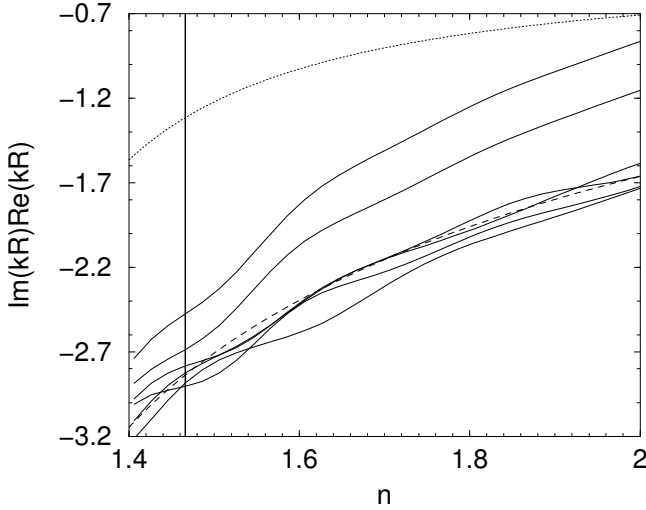


**Figure 2.30:**  $\text{Im}(kR)\text{Re}(kR)$  vs.  $n$  for several resonances with  $m \geq 50$  (solid curves). The contribution of the boundary waves, Eq. (2.75), is shown as dotted curve. The entire contribution, i.e. with pseudointegrable leakage, Eq. (2.76), is shown as dashed curve. The vertical line marks  $n = 1.466$ .

## 2.4.5 Conclusion

We have discussed the properties of long-lived modes in hexagonally shaped dielectric microcavities. These microcavities play an important role for experiments on a class of microcrystal lasers [72, 73]. The numerical analysis revealed the following facts: (i) The resonance positions in the complex plane are approximated by a hyperbola. This fact is relevant for future experiments on microcrystal lasers because it implies that the laser threshold is lower for larger crystals. (ii) The near-field intensity pattern show a whispering-gallery-like structure. (iii) The emission is at corners in agreement with the experiments. (iv) The emission is directed. The high-intensity directions are not parallel to the facets. (v) The lifetimes and the emission directionality are sensitive to rounding of the corners.

The numerical analysis does not cover the full experimental regime. To overcome this limitation, we have introduced a semiclassical approximation which can be easily extended to any cavity of regular polygonal geometry. Our semiclassical ray model contains two new emission mechanisms: leakage due to boundary waves and due to the pseudointegrable ray dynamics. Explicit expressions for the resonance positions can be given even though the system is not integrable. The semiclassical approximation explains all numerical findings (i)–(v) in an intuitive way, except the emission directionality. To describe the directionality properly it is necessary to consider corner diffraction in the future.

Our results are not only relevant for microcrystal lasers but also for other kinds of polygonal-shaped microlasers. To name a few, hexagonal lasers with attached optical waveguides based on semiconductor heterostructures [199], hexagonally shaped solid polymer dye microcavities [200], equilateral-triangular laser cavities fabricated from semiconductor heterostructures [201], and square laser micropillar cavities based on dye-doped polymers [202].

## 2.5 Formation of long-lived, scarlike modes

In Section 2.3 we have seen how avoided resonance crossings (ARCs) can be used to achieve unidirectional light emission from high- $Q$  modes. In this section, we discuss another interesting effect near ARCs, namely the formation of long-lived states [139]. For three different optical microcavities (rectangle, ellipse, and semi-stadium) we provide numerical evidence that these states are localized along periodic rays, resembling scarred states in closed systems. Our results shed light on the morphology of long-lived states in open mesoscopic systems.

### 2.5.1 Introduction

Understanding the properties of long-lived, quasi-bound states in open mesoscopic systems is of central importance for many research subjects, e.g., semiconductor ballistic quantum dots [203–206], photoionization of Rydberg atoms [207], microwave systems [64, 208], quantum chaos [209], and optical microcavities [66, 67, 104, 124–127, 210]. In several of these studies the long-lived states are *scarred*. The original scarring phenomenon has been discovered for closed systems in the field of quantum chaos [123]. It refers to the existence of a small fraction of eigenstates with strong localization along unstable periodic orbits of the underlying classical system. In open systems, however, scarred states seem to be the rule rather than the exception. The nature of the mechanism behind this scarlike phenomenon is not yet understood.

In Section 2.3 we have exploited ARCs to design optical microcavities with unidirectional light emission from long-lived modes. The two-level model (2.58) with eigenvalues (2.59) has been discussed for the case  $W = V^*$ . This case is called *internal coupling* since the only difference to the Hermitian coupling of two states in a closed system is that each state is *individually* coupled to the continuum. The latter is described by the imaginary part of the diagonal elements of matrix (2.58). The fully nonhermitian case  $W \neq V^*$  is more general; it permits an *external coupling* of the states *via* the continuum. Figure 2.31 illustrates that the real part undergoes an avoided level crossing as in the case of a closed system. The important feature is that one of the states has a considerably increased lifetime. The constraint of the conservation of the trace of the matrix in Eq. (2.58) simultaneously generates a state with short lifetime. The formation of fast and slowly decaying states is known as resonance trapping, see, e.g., Refs. [211, 212].

The aim of this section is to show that ARCs due to external coupling can have a strong impact on the localization properties of long-lived states in open systems. The symmetric or antisymmetric superpositions are more localized in real or phase space than the original states, so that important decay channels are blocked. A surprising finding is that these states can resemble scarred states which helps to explain the frequently observed scarring in open mesoscopic systems.

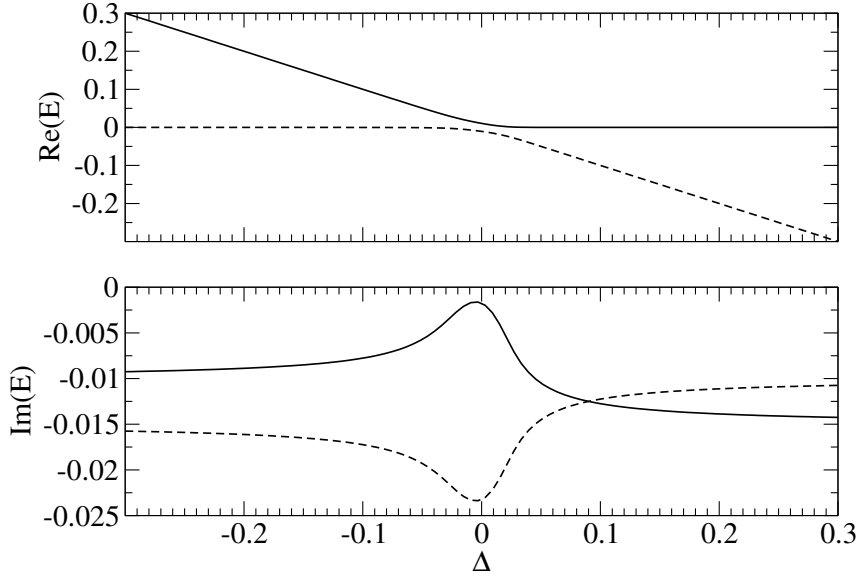


**Figure 2.31:** Avoided resonance crossing in the case of the matrix (2.58) with  $VW = i0.000225$ ,  $E_1 = -i0.015$ , and  $E_2 = \Delta - i0.01$ . Real (top) and imaginary (bottom) part of the energy vs. parameter  $\Delta$ .

## 2.5.2 The system

We examine optical microcavities, where the optical modes and their frequencies play the role of states and their energies. Light confinement in microcavities has attracted considerable interest in recent years due to the huge potential for various research fields and applications, for a review see Ref. [19]. For most applications, like low-threshold lasing, long-lived modes are required. We consider quasi-two-dimensional dielectric cavities with rectangular, elliptical and stadium-shaped cross section. We first focus on rectangles because of the following convenient properties: (i) the modes not close to an ARC can be computed analytically to a good approximation, including mode pattern and complex frequency; (ii) the internal ray dynamics is trivial, so localization effects related to chaotic ray dynamics [144] can be ruled out. Rectangular and square microcavities have already been studied both experimentally and theoretically [70, 198, 213]. However, ARCs in these systems have not been addressed so far.

We fix one side length to  $R = 2\text{ }\mu\text{m}$  and vary the aspect ratio  $0 < \varepsilon \leq 1$ . We choose the effective index of refraction to be  $n = 3.3$  inside and  $n = 1$  outside the dielectric for the transverse electric (TE) polarization with magnetic field  $\mathbf{H}$  perpendicular to the cavity plane. Maxwell's equations for the modes  $H_z(x, y, t) = \psi(x, y)e^{-i\omega t}$  reduce to the two-dimensional scalar wave equation (2.18). The wave function  $\psi$  and its normal derivative times  $n^{-2}$  are continuous across the boundary of the cavity. At infinity, outgoing wave conditions are imposed. Even though the geometry of the cavity is rather simple the wave equation cannot be solved analytically since the boundary conditions introduce diffraction at corners.

### 2.5.3 Numerical and analytical analysis

We compute the modes numerically using the boundary element method as introduced in Section 2.2. In order to apply this method each corner is replaced by a quarter of a circle with radius much smaller than the wavelength. We have carefully checked that the rounding does not influence the solutions in the studied frequency regime.

Before we discuss the numerical solutions of the open cavity we will briefly consider the corresponding closed cavity with vanishing wave intensity along the boundary. We expect that the solutions of the closed system approximate those modes in the open system which are confined by total internal reflection. The closed cavity is called an integrable billiard [64] since the modes can be computed analytically

$$\psi_{n_x, n_y}(x, y) = \sin\left(\frac{\pi n_x}{R} x\right) \sin\left(\frac{\pi n_y}{\varepsilon R} y\right) \quad (2.77)$$

if  $0 \leq x \leq R$  and  $0 \leq y \leq \varepsilon R$ ; otherwise  $\psi_{n_x, n_y}(x, y) = 0$ . The positive integers  $n_x, n_y$  count the number of maxima of  $|\psi|^2$  in  $x$ - and  $y$ -direction, respectively. The normalized frequency  $\Omega = \omega R/c$  belonging to such a mode is given by

$$\Omega_{n_x, n_y} = \frac{\pi}{n} \sqrt{n_x^2 + \frac{n_y^2}{\varepsilon^2}}. \quad (2.78)$$

As expected for an integrable billiard [64], this system shows frequency crossings instead of avoided crossings when the aspect ratio  $\varepsilon$  is varied. For example, for the modes  $(n_x, n_y) = (10, 7)$  and  $(12, 5)$  Eq. (2.78) yields the crossing point  $\varepsilon = \sqrt{6/11} \approx 0.739$  and  $\Omega \approx 13.12$  corresponding to a free-space wavelength of about 960 nm. Figure 2.32 shows that this accidental degeneracy is lifted in the open cavity. The associated ARC equals the case of the  $2 \times 2$  matrix in Fig. 2.31. We therefore conclude that diffraction at corners in rectangular cavities leads to an external coupling of modes.

It has been demonstrated in Section 2.4 that losses from a polygonal cavity due to diffraction at corners can be estimated by the boundary wave approach. Boundary waves travel along a flat interface between dielectric material and air. In the case of an infinitely extended interface, these waves are evanescent. In the case of a finite interface, however, these waves can leave the interface region at the corners. Following the treatment in Section 2.4 we have derived a formula describing the losses from a given mode  $(n_x, n_y)$  in the rectangular cavity due to boundary waves

$$\text{Im}(\Omega) = -\frac{2n}{\varepsilon \text{Re}(\Omega)} \sum_{j=1}^2 \frac{\sin \theta_j}{\sqrt{n^2 \sin \theta_j^2 - 1} (1 + \alpha_j^2)} \quad (2.79)$$

with  $\alpha_j = n \sqrt{n^2 \sin \theta_j^2 - 1} / \cos \theta_j$ ,  $\tan \theta_1 = \varepsilon n_x / n_y$ , and  $\theta_2 = \pi/2 - \theta_1$ . For a mode A with  $\varepsilon = 0.72$  and  $(n_x, n_y) = (10, 7)$  we find  $\text{Im}(\Omega) \approx -0.0048$  corresponding to a quality factor of  $Q = \text{Re}(\Omega) / [2\text{Im}(\Omega)] \approx 1380$ . For a mode B with  $\varepsilon = 0.72$  and  $(n_x, n_y) = (12, 5)$  we get  $\text{Im}(\Omega) \approx -0.0109$  and  $Q \approx 600$ . The boundary wave approach as developed in Section 2.4 can only compute the losses of individual modes, i.e., the diagonal elements of

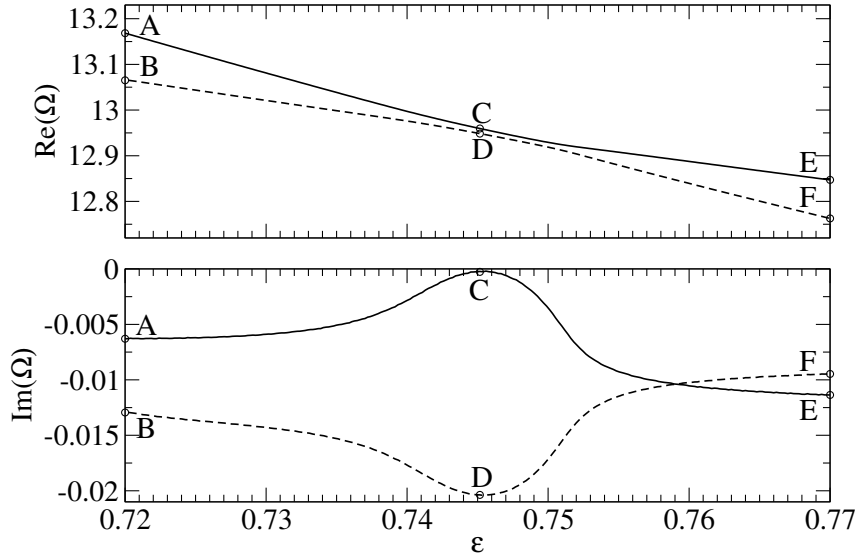


**Figure 2.32:** An avoided resonance crossing in the rectangular microcavity. Plotted are the complex frequencies  $\Omega$  as function of the aspect ratio  $\varepsilon$ .

the matrix (2.58). The off-diagonal part, i.e., the coupling of modes, cannot be determined within this approach. For a direct comparison to the exact results in Fig. 2.32 it is therefore useful to consider the mean value of  $\Omega_+$  and  $\Omega_-$  since here the ARC contributions cancel; cf. Eq. (2.59). The result of this procedure is shown in the bottom panel of Fig. 2.33. It can be seen that the averaged boundary wave result overestimates the averaged lifetimes of the modes by just 20 percent. Hence, leakage due to boundary waves is the dominant decay channel.

At the center of the ARC,  $\varepsilon \approx 0.7453$ , in Fig. 2.32 a fast mode D with  $\text{Im}(\Omega) \approx -0.02$  and a slow mode C with  $\text{Im}(\Omega) \approx -0.00028$  is formed. The slow mode has  $Q \approx 23\,200$  which is a dramatic increase by more than one order of magnitude if compared to the “normal” quality factor. In this frequency regime, the leakage due boundary waves limits the quality factor to roughly 1900. This indicates that possibly all long-lived modes (modes with, say,  $Q \geq 4000$ ) in this frequency regime are caused by ARCs. This conclusion is supported by extensive numerical studies on this system (not shown).

The spatial patterns of modes A, B, E, and F in Fig. 2.34 approximately match the solutions of the closed cavity in Eq. (2.77). Upon the avoided crossing the mode patterns exchange their character, i.e., mode B and E have roughly the same spatial profile but belong to different frequency branches; cf. Fig. 2.32. The same holds for mode A and F. The modes at the ARC, C and D, correspond to symmetric and antisymmetric superpositions of the mode A and B (or E and F). Now, we can identify the physical mechanism behind the increased quality factor of mode C: destructive interference reduces the light intensity at the corners and consequently the main decay channel, leakage due to boundary waves, is strongly suppressed. A closer inspection of the mode C in Fig. 2.34 reveals that its intensity is concentrated along a diamond-shaped periodic ray. The long-lived mode formed in the ARC therefore resembles a scarred mode. In the case of mode D, constructive interference at the corners spoils the quality factor. Mode D is localized

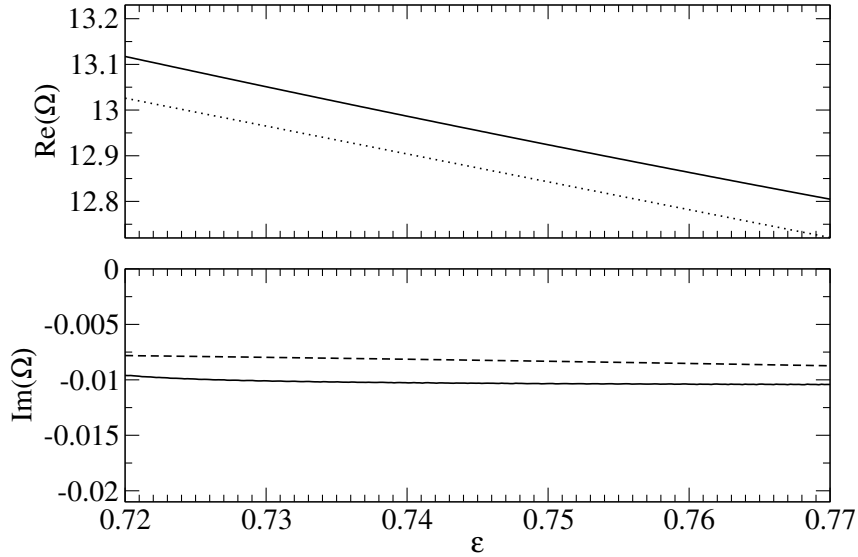


**Figure 2.33:** Mean value of real (top) and imaginary (bottom) part of frequencies (solid lines) near the avoided resonance crossing shown in Fig. 2.32. The dotted line is the scar approximation (2.80). The dashed line is the averaged result of the boundary wave approach (2.79).

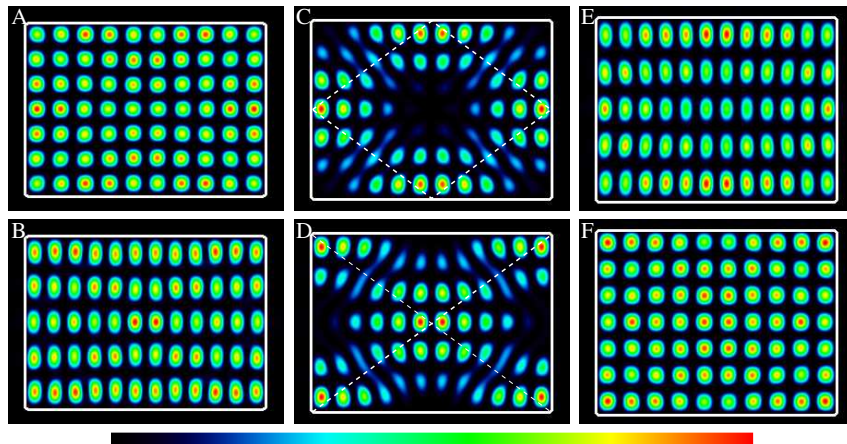


**Figure 2.34:** Calculated near field intensity of modes with the same labels as in Fig. 2.32. Mode C shows localization along a periodic ray (dashed line), mode D is localized along two rays connecting the corners (dashed lines).

along two symmetry-related rays connecting the corners of the cavity. Such kind of rays are called diffractive rays [208].

The spatial pattern of mode C is not a special feature of the chosen boundary conditions but is also observed in square cavities of very different types: (i) square quantum dots with leads attached at the corner region [203]; (ii) square billiards with magnetic flux [214]; (iii) vertical-cavity surface-emitting lasers with square-shaped cross section [104, 215].

The resemblance of mode C with the diamond-shaped periodic ray is apparent with the naked eye. In the following, it will be demonstrated that the relation is even deeper. To do so, we estimate the frequency of the mode by using the localization along the ray. We

stipulate that an integer number  $m$  of wavelengths fits onto the periodic ray with length  $l = 2R\sqrt{1 + \varepsilon^2}$ . The calculation is straightforward giving

$$\Omega_{\text{scar}} = \frac{\pi}{n\sqrt{1 + \varepsilon^2}}(m + \beta) \quad (2.80)$$

with

$$\beta = \frac{2}{\pi} \sum_j \arctan \alpha_j \quad (2.81)$$

being the total phase shift from the reflection at the dielectric boundary for TE polarization. The quantities  $\alpha_1$  and  $\alpha_2$  are the same as for Eq. (2.79) but with  $\tan \theta_1 = 1/\varepsilon$ , and  $\theta_2 = \pi/2 - \theta_1$ . The top panel of Fig. 2.33 demonstrates that the scar approximation with  $m = 15$  describes the mean behaviour of the modes involved in the ARC over a broad range of parameter values. The small frequency offset of about 0.086 can be traced back to the fact that the scar approximation assumes that the plane waves lying on the ray segments have no wave vector component in the transverse direction. However, the mode is restricted to an interval of length  $R$  ( $\varepsilon R$ ) in  $x$ -direction ( $y$ -direction). At least half a wavelength fits into these intervals for which the wave vector components give frequency contributions of approximately  $\pi/n$  and  $\pi/(\varepsilon n)$ . Summing up the squares of the frequency contributions gives the correction

$$\Delta\Omega \approx \frac{\pi^2 (1 + 1/\varepsilon^2)}{2n^2\Omega_{\text{scar}}} . \quad (2.82)$$

In the regime  $\varepsilon = [0.72, 0.77]$ , we get  $\Delta\Omega \approx 0.096..0.102$  which convincingly explains the discrepancy between  $\Omega_{\text{scar}}$  and the exact value of  $\Omega$ .

Coupling between two modes  $(n_x, n_y)$  and  $(m_x, m_y)$  occurs only for modes with the same symmetry with respect to the lines  $x = R/2$  and  $y = \varepsilon R/2$ . That implies that if  $n_x$  is even (odd)  $m_x$  must be even (odd) too. The same holds for  $n_y$  and  $m_y$ . Interestingly, this restriction ensures that for given allowed pair  $(n_x, n_y)$  and  $(m_x, m_y)$  cancellation at *all* corners is possible.

We can create a variety of scarlike modes near ARCs. Consider a periodic ray bouncing  $q$  times at the horizontal lines and  $p$  times at the vertical lines. A straightforward analysis shows that  $q = 2[(|n_x - m_x| + 1)/2]$  and  $p = 2[(|n_y - m_y| + 1)/2]$  where  $[ \dots ]$  denotes the integer part. Figure 2.35(a) depicts an example with  $q = 4$  and  $p = 2$ . This long-lived mode with  $\Omega \approx 16.306 - i0.00047$  ( $Q \approx 17500$ ) results from an ARC of modes  $(10, 7)$  and  $(14, 5)$  at  $\varepsilon = 0.4954$ .

The formation of long-lived, scarlike modes near ARCs with external coupling is not restricted to TE polarization nor to the rectangular geometry. Figures 2.35(b)–(e) show examples with transverse magnetic (TM) polarization in an elliptical and a (semi-) stadium-shaped resonator with refractive index  $n = 3.3$ . The shape parameter is the eccentricity  $e$  and the length of the horizontal straight lines  $L$ , respectively. The scenario is as in the cases shown in Figs. 2.31 and 2.32. At the ARC a short- and a long-lived mode is formed; see Fig. 2.35(c) and (e). The long-lived mode exhibits a localization along a periodic ray; see Fig. 2.35(b) and (d). This localization gradually disappears when the shape parameter is detuned from resonance (not shown). Note that elliptical billiards do not show

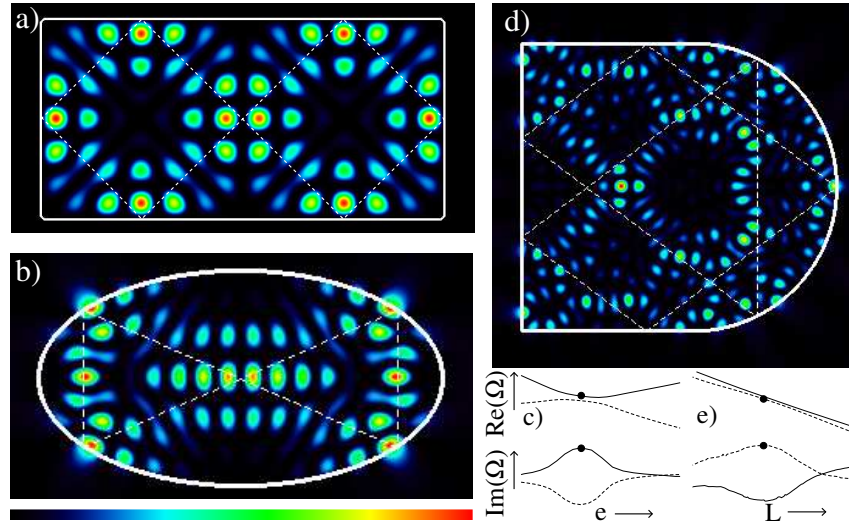


**Figure 2.35:** a) Near field intensity of a long-lived mode resulting from an ARC of modes  $(10, 7)$  and  $(14, 5)$ . The white dashed line is the periodic ray. b) and c) Long-lived TM mode formed at an ARC (marked by the dot) in an elliptical resonator with eccentricity  $e$ . d) and e) Long-lived TM mode at an ARC in a stadium resonator with horizontal lines of length  $L$ .

such scarring [99]. Let us mention that local maxima of quality factors as function of a shape parameter had already been exploited for minimizing losses from stadium-shaped cavities [127, 210]. However, the case in Refs. [127, 210] is not related to ARCs, but is an interference effect of unstable periodic rays [128].

#### 2.5.4 Summary

We demonstrated the formation of long-lived modes near avoided resonances crossings in optical microcavities. For a number of different types of cavities we observed strong localization of these modes, resembling scarred states in closed systems. We expect that this finding is highly relevant for understanding the localization properties of long-lived states not only in optical systems but in various fields of research.

## 2.6 Unidirectional light emission and unstable manifolds

In Section 2.3 we introduced a scheme to achieve unidirectional light emission without  $Q$ -spoiling. The advantage of this approach is that it is very general and not restricted to microdisk-like geometries. The drawback, however, is the existence of nearly degenerate modes which can have different far-field patterns (FFPs). If two such modes are excited simultaneously which is typical for present-day laser devices, the unidirectionality might be lost. Nearly degenerate modes with similar FFP do occur but to find them requires laborious numerical calculations and a sophisticated adjustment of geometry parameters depending on refractive index, wavelength and cavity size. Here we report another scheme which allows for unidirectional light emission and ultrahigh  $Q$ -factors without the above-mentioned drawback. The devices are especially well suited for multi-mode operation as all high- $Q$  modes possess similar FFPs. This surprising finding is explained by a combination of a wave phenomenon, namely scarring, i.e., wave localization along unstable periodic ray trajectories [123], and chaotic ray dynamics in open systems leading to universal emission directionality due to unstable manifolds [143–145].

### 2.6.1 The system

A microdisk is a quasi-2D geometry described by an effective index of refraction  $n$ . We assume  $n = 3.3$  (GaAs) both for transverse magnetic (TM) and transverse electric (TE) polarization. A slight polarization dependence of  $n$  is neglected; it could be adjusted in the fabrication process, e.g., by changing the slab thickness. For the boundary curve of the deformed microdisk we choose the limaçon of Pascal in Eq. (2.1). Figures 2.3(c) and (d) show a trajectory in the limaçon cavity for  $\varepsilon = 0.43$ .

### 2.6.2 Chaotic repeller and unstable manifold

While in the long-time limit the phase space of closed chaotic systems is essentially structureless, cf. Fig. 2.3(d), the phase space of open chaotic systems is structured by the so-called “chaotic repeller” [112]. It is the set of points in phase space that never visit the leaky region. A trajectory that starts close to the repeller does not escape the system for a long time. The stable (unstable) manifold of a chaotic repeller is the set of points that converges to the repeller in forward (backward) time evolution. The unstable manifold therefore describes the route of escape from the chaotic system. In the case of light, Fresnel’s laws impose an additional, polarization dependent weighting factor to the unstable manifold in the leaky region.

Figure 2.36 depicts the Fresnel weighted unstable manifolds for the limaçon cavity with  $\varepsilon = 0.43$ . It can be regarded as a survival probability distribution calculated from a huge number of rays starting uniformly in phase space. Note that (i) in the leaky region, the manifold is concentrated on only a few high-intensity spots. We therefore expect a highly directional FFP. (ii) While the TE polarization has one spot with  $\chi > 0$  (and another symmetry-related one at  $s \rightarrow s_{\max} - s, \chi \rightarrow -\chi$ ), the TM polarization possesses two of those.

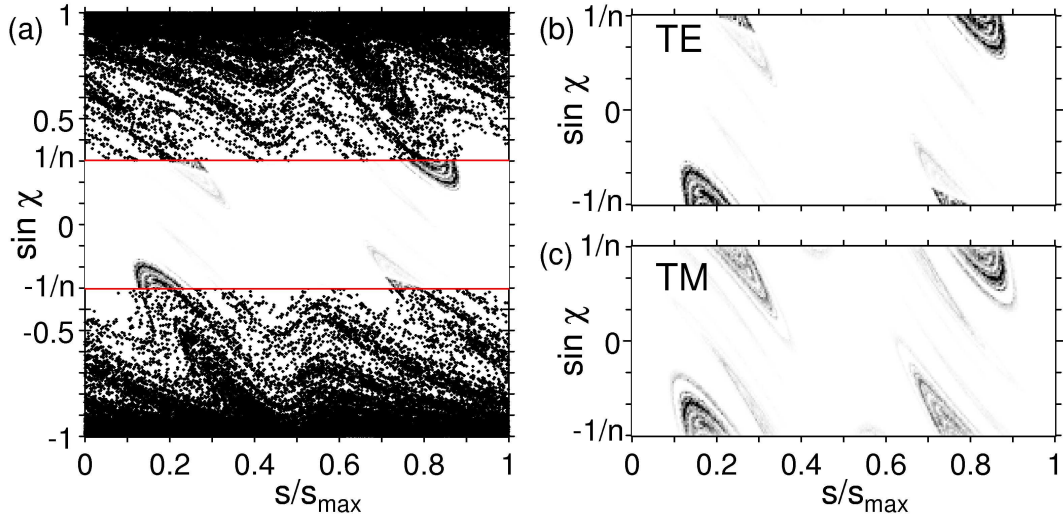


**Figure 2.36:** (a) Fresnel weighted unstable manifold of the limaçon cavity for TE polarization. Magnification reveals the differences between TE (b) and TM (c) polarization in the leaky region, which originate from Fresnel's law.

Figure 2.37 shows how these findings are translated into the FFP. For TE polarization, we find unidirectionality around  $\phi = 0$ , whereas in the TM case additional, smaller peaks occur. The orange ray in the left inset represents one typical trajectory emitting to  $\phi = 0$  (marked by orange arrows). The emitting bounce (marked 1, 1s is the symmetry-related counterpart), the three bounces before and the one after (marked 2, green) are shown. Whereas the trajectories are equal for both polarizations, their intensities are different: As visible in the right inset, the orange rays escaping at 1 hit the line of the Brewster angle

$$|\chi_B| = \arctan 1/n < \arcsin 1/n . \quad (2.83)$$

In the TE case, transmission is nearly complete and no intensity can reach the next bounce 2. This causes the sharp decrease in the intensity that is more clearly visible in Fig. 2.36(b).

The Fresnel law for TM polarization does not show the Brewster angle feature. Therefore, about 30 percent of the light is reflected towards bounce 2. Since bounce 2 emits into a different direction (green arrows), an appreciable amount of intensity collects in a second far-field peak.

### 2.6.3 Wave dynamics

To summarize up to this point, we have seen that chaotic ray dynamics can lead to unidirectional emission. However, the  $Q$ -factor is low since the light rays leave the cavity very quickly. Does this result of geometric optics carries over to the wave dynamics of the electromagnetic field?

It has been demonstrated that the FFP of optical modes can be strongly influenced by

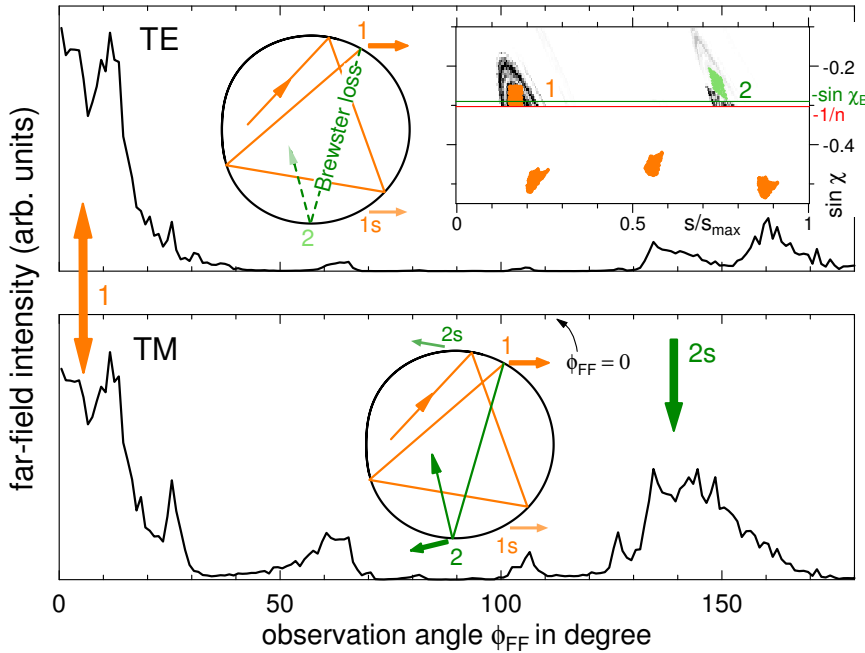


**Figure 2.37:** Far-field emission pattern calculated from ray dynamics. TE (top) and TM polarization (bottom); cf. Fig. 2.36(b) and c. Insets illustrate ray dynamics leading to directed emission. Right inset: 250 rays were started in the rectangular region at 1 and followed forwards and backwards.

the unstable manifold [143, 144]. A consequence is that the FFP can be universal, i.e., independent on the internal mode structure [145]. This raises the hope that the high directionality from the limaçon cavity observed above will survive in wave optics. To this end we solve Maxwell equations numerically using the boundary element method from Section 2.2. According to the discrete symmetry, even and odd modes are distinguished.

The top panel of Fig. 2.38 shows near- and far-field pattern of a high- $Q$  TE mode. The normalized frequency  $\Omega = \omega R/c = 26.0933$ ,  $c$  being the speed of light in vacuum, corresponds to, e.g., a free-space wavelength of about 900 nm for  $R = 3.75 \mu\text{m}$ . Indeed, as predicted by our ray dynamical analysis the mode exhibits unidirectional light emission around  $\phi = 0$ . The angular divergence of  $24^\circ$  is significantly smaller than the values reported for low- $Q$  disks [69, 135], and also less than in Section 2.3. Moreover, the FFP is universal, i.e., all high- $Q$  TE modes in this cavity have similar FFPs as exemplarily demonstrated in the upper panel of Fig. 2.38 for an odd-parity mode (dashed line) which is quasi-degenerate with the even-parity solution (solid line). For the high- $Q$  TM modes we also observe an universal FFP, now with some sidepeaks, see lower panel of Fig. 2.38.

Whereas the wave and ray based FFPs in Figs. 2.37 and 2.38 agree remarkably well, other wave properties seem to contradict the ray simulations: (i) the mode does not look chaotic but spatially rather well confined. (ii) the cavity  $Q$ s are too large if compared to the escape rate from the chaotic repeller, in fact their values reach, or even exceed, the present limit achievable for microdisks with low residual absorption and surface roughness [166].

To further investigate the character of these optical modes it is convenient to consider the

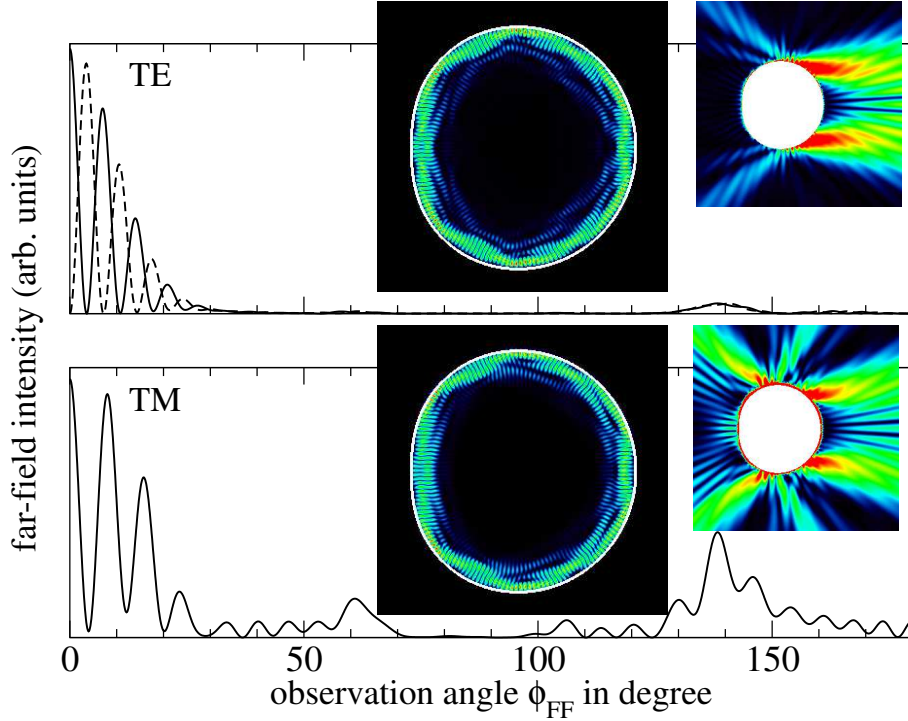


**Figure 2.38:** Angular dependence of the far-field electric field intensity for a TE mode of even (top, solid line) and odd parity (top, dashed) with  $\Omega = 26.0933$ ,  $Q \approx 185\,000$ , and a TM mode (bottom)  $\Omega = 25.8069$ ,  $Q \approx 10^7$ ; cf. Fig. 2.37. Insets contain near-field pattern of even-parity modes (middle) and their external structure (right).

Husimi phase space projection [165], representing the wave analogue of the Poincaré SOS. From ray-wave correspondence one would expect that the Husimi projection is distributed uniformly over the unstable manifold. However, Fig. 2.39(a) demonstrates that the TE mode is localized around  $|\sin \chi| \approx 0.86$  and has only exponentially small intensity in the leaky region which explains the high  $Q$ -factor. A closer inspection [216] reveals that the mode is scarred [123], i.e., the wave intensity is enhanced around an unstable periodic ray trajectory (dots and inset in Fig. 2.39(a)) which is part of the chaotic repeller. Note that the other high- $Q$  modes found in this system also exhibit localization along – in general other – unstable periodic ray trajectories. The Husimi projection of the TM mode in Fig. 2.38 looks similar (not shown). However, the localization is even stronger leading to a higher  $Q$ -factor.

Even though the Husimi projection has an exponentially small contribution in the leaky region, it is precisely this outgoing light that determines the FFP. Figures 2.39(b) and (c) show the Husimi projection in the leaky region. The convincing agreement with the unstable manifold in Figs. 2.36(b) and (c) demonstrates that the unstable manifold is responsible for the unidirectional emission, whereas scarring assures the high  $Q$ -factor.

So far we focused on a particular deformation parameter,  $\varepsilon = 0.43$ . This value is the optimum value for the discussed modes but highly localized FFP and high  $Q$ -factors can also be found for  $0.41 \lesssim \varepsilon \lesssim 0.49$  (not shown), i.e., fabrication tolerances are not crucial. Moreover, we tested that our results are robust against variations of the refractive index

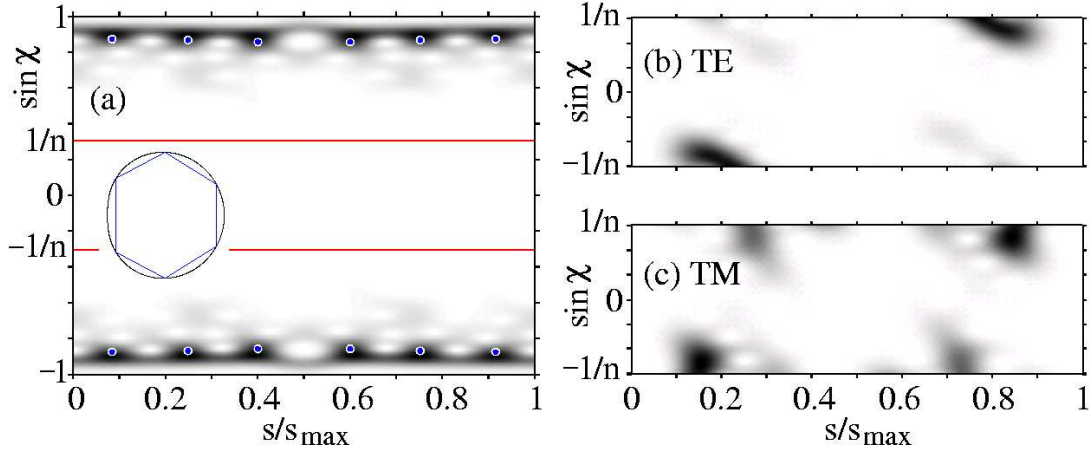


**Figure 2.39:** (a) Husimi projection of TE mode in Fig. 2.38, cf. Poincaré SOS in Fig. 2.3(d) and unstable manifold in Fig. 2.36(a). The red lines enclose the leaky region, the dots mark the periodic ray trajectory illustrated in the inset. Magnified Husimi projection in the leaky region for the TE (b) and TM (c) mode; cf. Fig. 2.36(b) and (c) for the ray simulation results.

and remain valid for  $2.7 \lesssim n \lesssim 3.9$ .

## 2.6.4 Summary

We have proposed a deformed microdisk as a novel cavity design for unidirectional light emission from high- $Q$  modes. No complicated adjustment of geometry parameters is necessary, and the emission directionality is universal, i.e., largely independent from wavelength, cavity size, refractive index, and the details of the interior mode structure. The latter finding is especially relevant for multi-mode lasing devices. We trace our counterintuitive results back to (i) wave localization along unstable periodic ray trajectories ensuring high  $Q$ -factors and (ii) escape of rays along the unstable manifold of the chaotic repeller leading to universal, unidirectional emission.

## 2.7 Micropillar cavities

This section deals with the optical properties of pillar microcavities [26], examples of which can be seen in Fig. 2.40. These cavities allow for highly-directed vertical light emission. However, for some material systems it is difficult to achieve  $Q$ -factors that can compete with those of other cavity types. Getting high  $Q$ -factors requires a sophisticated fabrication process, usually starting from a planar vertical-cavity surface-emitting laser (VCSEL) structure. In such a structure, the light emitters are located in a central cavity called the spacer, which is sandwiched between two distributed Bragg reflectors (DBRs). A DBR consists of layers with alternating high and low refractive indices. Each layer has a thickness of a quarter of the light wavelength in the material, yielding high reflectivities due to Bragg reflection. The lateral structuring provides optical confinement in the transverse direction perpendicular to the VCSEL structure by total internal reflection at the sidewalls of the pillar, caused by the refractive index contrast between the semiconductor material and the surrounding air.

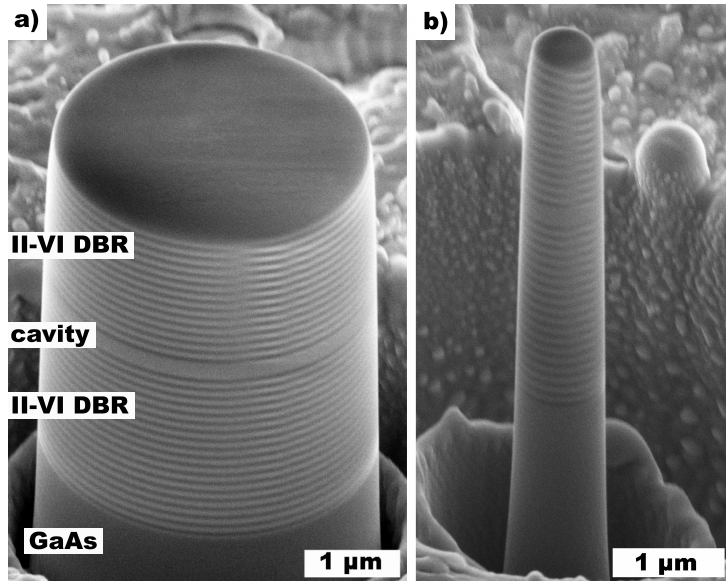


**Figure 2.40:** Scanning electron microscope pictures of II-VI micropillars on base of ZnSe and MgS with diameters of (a)  $3.5 \mu\text{m}$  and (b)  $700 \text{ nm}$ . The pillars have been fabricated by the research groups of D. Hommel and J. Gutowski in Bremen [17].

Several methods to compute the modes of pillar microcavities are used in the literature, such as finite-difference time-domain (FDTD) methods [217, 218], the Fourier modal method [219], and the vectorial transfer matrix approach (VTMA) [220–222]. We use the VTMA. For completeness, this well-known method is explained in Appendix B. In the following, we compare our numerical results obtained from this method to experimental data for various different material systems. These studies have been performed in collaboration with the groups of Prof. P. Michler (Stuttgart), Prof. A. Forchel (Würzburg), Prof. D. Hommel (Bremen), and Prof. J. Gutowski (Bremen).

### 2.7.1 AlAs/GaAs micropillars

Our first example are AlAs/GaAs micropillars studied in Refs. [223,224]. The investigated sample was grown by molecular beam epitaxy (MBE) on a GaAs substrate. A 260 nm GaAs spacer was sandwiched between the bottom and top DBRs, which consist of 23-period and 20-period AlAs/GaAs layer pairs, respectively. Each pair contains a 79 nm-thick AlAs and a 67 nm-thick GaAs layer. The refractive indices at the wavelength  $\lambda \approx 910$  nm and a temperature of 4 K are  $n \approx 2.92$  and  $n \approx 3.52$ , respectively. A 1.4 nm single layer of self-assembled (In,Ga)As/GaAs QDs is used as the active region and is inserted at the centre of the GaAs spacer at the antinode position of the optical mode. An array of different pillar diameters ranging from  $4\mu\text{m}$  up to  $6\mu\text{m}$  were fabricated by electron beam lithography and dry etching.

The larger-diameter pillars considered here contain many QDs. Due to the QD size distribution, the ensemble photoluminescence (PL) is inhomogeneously broadened. The ensemble PL can therefore be used as an internal light source to reveal the pillar mode structure [9,27]. For instance, the charge coupled device (CCD) image in Fig. 2.41 (b) provides an one-dimensional cross-section of the emitted intensity of the  $6\mu\text{m}$  pillar in the plane parallel to the mirror layers as a function of the emission wavelength. This CCD image experimentally accesses the transverse mode structure: the outermost right peak is identified as the fundamental mode having a field maximum in the centre and a simple Gaussian-like decay; other peaks correspond to higher order modes. A quality factor of  $Q \approx 10\,000$  is estimated for the fundamental mode. The dashed lines in Figs. 2.41 (c), (d), and (e) display the measured PL spectra of the  $6\mu\text{m}$ , the  $5\mu\text{m}$ , and the  $4\mu\text{m}$  diameter pillar, respectively. For decreasing pillar diameters, these spectra show well-known characteristic properties [225]: the wavelength of the fundamental mode decreases with diameter and the spacing between resonant wavelengths increases monotonically for decreasing diameter as one would expect for a stronger spatial confinement of light in the smaller pillars.

The solid lines in Fig. 2.41 (c)–(e) show the *transmission* spectra calculated with the VTMA for the same pillar diameters. Most of these modes are two-fold degenerate. It is the overall number of modes contributing to each peak that determines the peak height of the calculated transmission spectrum. For some peaks in Fig. 2.41 (c) (second, third and last from right) three, two and again two nearby modes with very similar resonance wavelengths contribute which are not experimentally resolved. For each of these modes the calculated transverse components of the electric field are shown in Fig. 2.41 (a), positioned above the corresponding CCD signal. The resonance wavelengths of the peaks agree well with the experiment, confirming their nature as different transverse modes in the pillar. The theoretical linewidths are by a factor of 3 smaller than the theoretical ones, i.e., the theoretical  $Q$ -factors are too large. We attribute this discrepancy to residual absorption and surface roughness at the sidewalls, which is not included in the calculations. Fig. 2.41 (f) shows the longitudinal mode structure being the same for all modes in the considered wavelength regime.

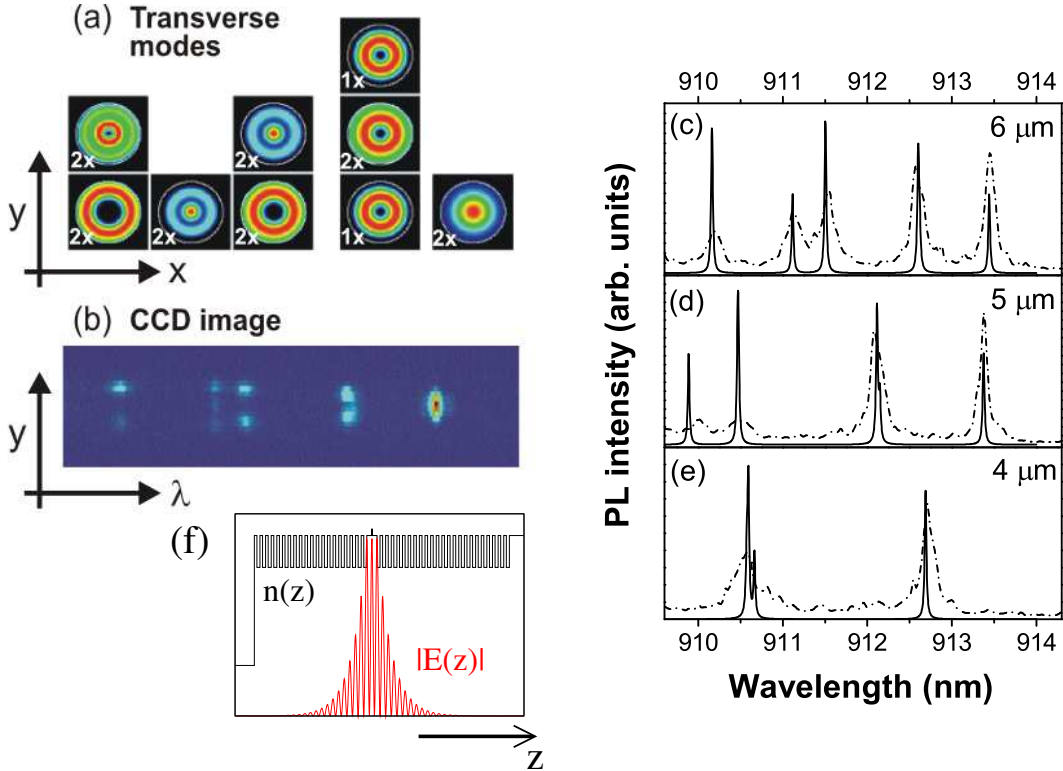


**Figure 2.41:** (a) Calculated 2-D transverse electric field patterns corresponding to various modes of the  $6\text{ }\mu\text{m}$  AlAs/GaAs pillar in the computed transmission spectrum (solid line) and experimental PL spectrum (dashed) in (c). The degeneracy of each mode (1x, 2x) is indicated. (b) Spectrally resolved 1-D CCD image of the  $6\text{ }\mu\text{m}$  pillar mode structures. (d) and (e) computed transmission spectrum (solid) and measured PL spectrum (dashed) for a diameter of 5 and  $4\text{ }\mu\text{m}$ . (f) Longitudinal mode structure and refractive index profile. The experiments have been performed in the labs of P. Michler [223, 224].

### 2.7.2 II-VI pillar microcavities

Wide bandgap II-VI semiconductors are candidates for optoelectronic applications in the blue-green spectral region. These materials are composed of elements of the II. and VI. group of the periodic table of elements. Compared to the (Al,Ga,In)As system, the II-VI system is technologically less developed, but significant progress has been made in recent years, e.g., single photon emission of CdSe QDs up to 200 K [226] as well as a green QD laser [227] has been demonstrated.

In this section, we discuss the modestructure of monolithic II-VI pillar [17]. The growth of the planar VCSEL structure was performed by MBE. The two DBRs of the VCSEL (18 periods bottom DBR, 15 periods top DBR) consist of 48 nm-thick  $\text{ZnS}_{0.06}\text{Se}_{0.94}$  high-refractive-index layers (refractive index  $n \approx 2.68$  at  $\lambda = 510\text{ nm}$  and  $4\text{ K}$ ), and  $\text{MgS}(1.9\text{ nm})/\text{ZnCdSe}(0.6\text{ nm})$  superlattices of 24.5 periods for the low-refractive index layers (effective index  $n \approx 2.08$ ). The  $\text{ZnS}_{0.06}\text{Se}_{0.94}$  spacer contains three ZnCdSSe QWs. The planar VCSEL structure shows a  $Q$ -factor exceeding 3 000. Pillars with various diameters were prepared from the planar VCSEL structure by focused ion beam (FIB)

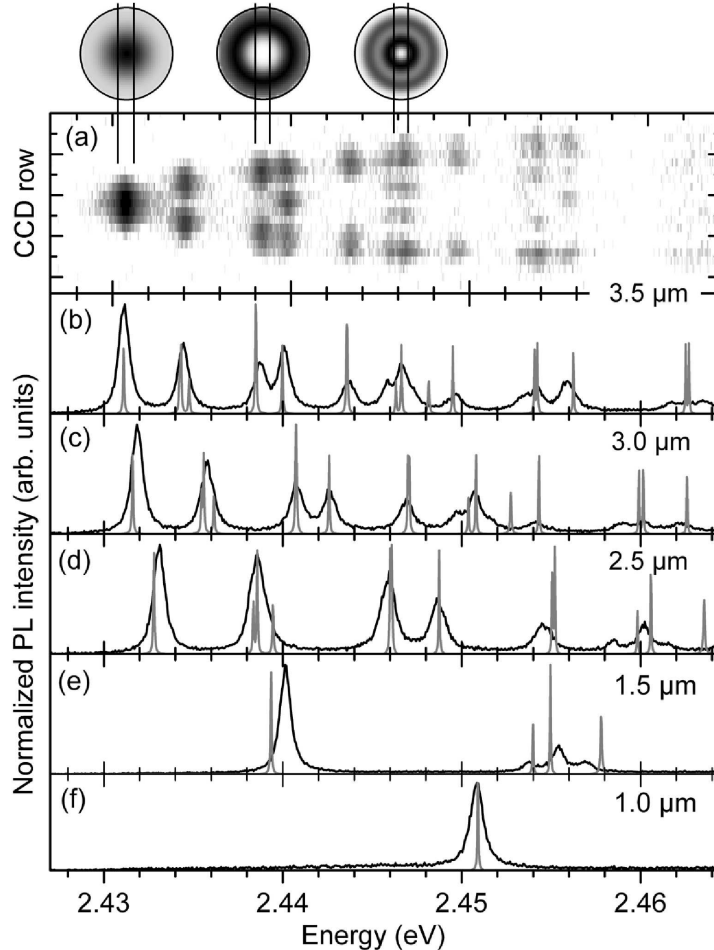


**Figure 2.42:** (a) Spectrally resolved 1-D CCD image of a II-VI pillar with a diameter of  $3.5 \mu\text{m}$ . Calculated transverse electric field patterns of the indicated modes are shown above. (b) Corresponding  $\mu$ -PL spectrum (dashed curve) and calculated transmission spectrum (solid). (c) to (f)  $\mu$ -PL spectra (dashed) and calculated transmission spectra (solid) of pillars with decreasing diameter. The experiments have been done by the groups of J. Gutowski and D. Hommel [17].

milling [18]. Figs. 2.40 (a) and (b) show scanning electron microscope (SEM) images of pillars with diameters of  $3.5 \mu\text{m}$  and  $700 \text{ nm}$ , respectively.

PL measurements at low excitation densities and a temperature of  $4 \text{ K}$  were performed on individual pillar structures using a microphotoluminescence ( $\mu$ -PL) setup.  $\mu$ -PL spectra of pillars with various diameters are shown in Figs. 2.42 (b) to (f). Series of sharp emission peaks which are blue-shifted with respect to the resonance of the planar cavity at normal incidence ( $2.43 \text{ eV}$ ) are observed. The relative intensities of the peaks decrease when going to higher energies away from the QW emission maximum. As for the AlAs/GaAs micropillars we observe the well-known trends for decreasing diameters: the energy position of the fundamental mode as well as the splitting between the individual modes increase monotonically.

Figure 2.42 (a) shows the CCD image corresponding to the  $\mu$ -PL spectrum in Fig. 2.42 (b).

The outermost left peak belongs to the fundamental mode of the pillar. For the following modes with higher energies an increasing number of intensity minima is observed, i.e., nodes of the transverse electric field pattern along the spatial cut through the pillar. The comparison with the CCD image for the AlAs/GaAs pillars in Fig. 2.41(b) (where the abscissa is the wavelength) reveals a qualitatively identical mode structure of the different kind of pillars.

To identify the observed cavity modes, we compute the modes using the VTMA incorporating the conical shape of the pillars, see Fig. 2.40, in the transfer matrix as discussed in Appendix B. We find that for the present structures the slight conical shape produces only negligible effects. In contrast, it turns out to be very important to include the frequency dependence of the refractive indices.

The solid lines in Figs. 2.42 (b) to (f) show the calculated transmission spectra. All features are qualitatively the same as in the case of the AlAs/GaAs micropillars discussed above. Again, it can be seen that to some experimental peaks several modes contribute, e.g., for the pillars with larger diameters in Fig. 2.42 (b) to (d) the second experimental peak (from the left) consist of three modes which are eventually experimentally resolved in the case of the  $1.5 \mu\text{m}$  pillar in Fig. 2.42 (e) due to increasing mode splitting. The calculated resonance wavelengths show a convincing agreement with the experiment. For illustration calculated transverse electric field patterns for the indicated modes of the  $3.5 \mu\text{m}$  pillar are exemplarily shown above Fig. 2.42 (a). The number of field maxima in radial direction corresponds to the experimentally observed intensity patterns.

For pillars with diameters larger than  $1.5 \mu\text{m}$  nearly constant and reproducible values  $Q \approx 3500$  are obtained for the fundamental mode. In this case, the  $Q$ -factor of the planar VCSEL cavity obviously limits the lifetime of the mode [228]. Our theoretically calculated  $Q$ -factor of 28 000 for the fundamental mode exceeds the experimental value considerably. Surface roughness cannot be the reason for this discrepancy since the experimental  $Q$ -factor of the microcavity and of the planar cavity are almost the same. Possibly, residual absorption spoils the  $Q$ -factor. For smaller pillars the measured  $Q$ -factor starts to decrease, e.g., for a pillar diameter of  $1 \mu\text{m}$  and  $700 \text{ nm}$   $Q \approx 1800$  and  $1100$  can be determined, respectively. The decrease of  $Q$  with decreasing pillar diameter has to be attributed mostly to scattering losses due to the residual roughness of the pillar sidewalls, an effect becoming more important for smaller pillars [229].

### 2.7.3 Nitride pillar microcavities

Similar to the II-VI material system there are only few reports in the literature concerning the realization of high- $Q$  and small-mode-volume cavities for the important nitride system emitting in the blue-violet spectral range. The successful fabrication and analysis of completely etched airpost pillar microcavities has been reported by us in Ref. [230]. In the following, we discuss the mode structure of this system.

The VCSEL structures were grown by plasma-assisted MBE on GaN/sapphire template layers. They consist of a 20.5-period bottom DBR, a spacer containing three InGaN QWs, and an 18-period top DBR. The high-refractive-index material of the DBRs is

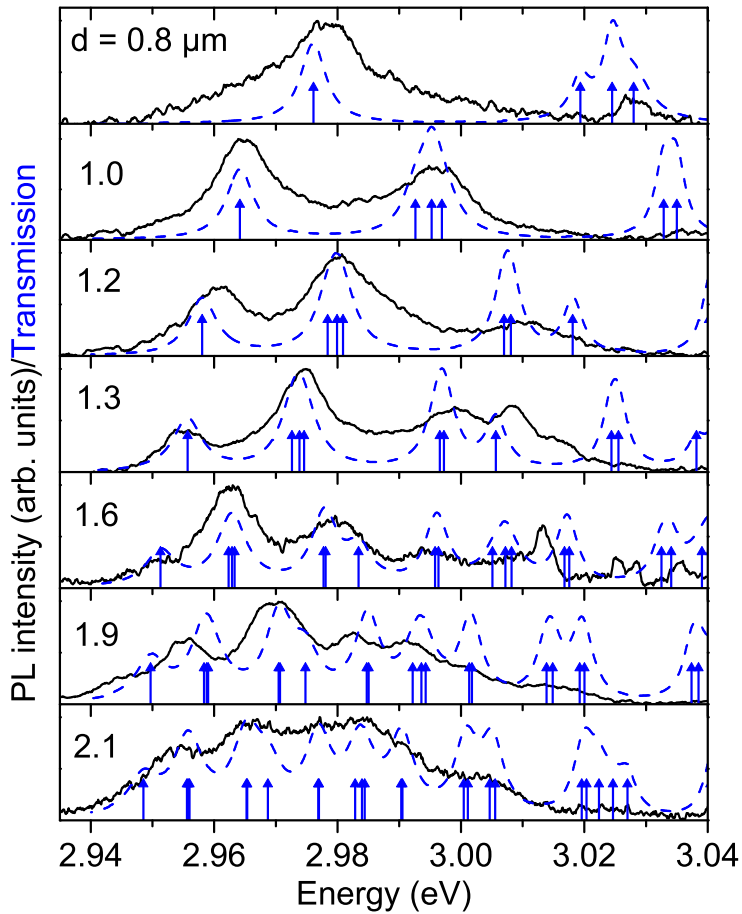


**Figure 2.43:** PL spectra of nitride pillars with the indicated diameters (solid lines) and the calculated transmission spectra (dashed). Arrows mark the calculated spectral position of the individual modes. Experiments were performed in the labs of J. Gutowski and D. Hommel [230].

formed by 42 nm thick GaN layers with  $n \approx 2.51$  at  $\lambda = 420$  nm, the low-index material by superlattices with effective index  $n \approx 2.3$  made of 19.5 periods AlN/In<sub>0.25</sub>Ga<sub>0.75</sub>N layers of 1.6 nm and 0.75 nm thickness, respectively. Pillars with various diameters were prepared from the planar samples by FIB etching.

$\mu$ -PL spectra at 4K of pillars with diameters between  $2.1 \mu\text{m}$  and 800 nm are shown in Fig. 2.43. To prove that the observed modulations are due to cavity modes, we calculated the transmission spectrum using the VTMA. The calculation predicts a  $Q$ -factor of about 500. This  $Q$ -factor, and correspondingly the reflectivity of the DBRs, is much lower than for the GaAs/AlAs and the II-VI pillars. This is due to the low refractive index contrast in the nitride DBRs. The spectral positions of the calculated resonances correspond very well to the measured spectra. As for the other material systems we observe for decreasing diameters a shift of the fundamental mode to higher energies and an increase of the mode splitting. For the fundamental mode of the  $1 \mu\text{m}$  pillar at 2.965 eV, a  $Q$ -factor of 240 can be determined that is comparable to the value measured for the planar structure. For the 800 nm pillar, a slight decrease of  $Q$  can be noticed.

In the next chapter, these kind of numerical results will be used as input for a semiconductor theory to describe light-matter interaction in optical microcavities.

# 3 Light-matter interaction in semiconductor nanostructures

In the previous chapter, it was shown how one can tailor the properties of the electromagnetic field by suitably designed optical microcavities. In an analog way, semiconductor nanostructures offer control over the charge carriers. Of particular importance are semiconductor quantum dots (QDs) since their tunable and narrow linewidths allow for the most significant modifications of the light-matter interaction. This is the reason why QDs are expected to play a major role in future developments in opto-electronics.

The ultimate control over light-matter interaction is achieved by inserting QDs into a microcavity. In the so-called strong coupling regime a cavity mode and a single QD exchange energy in a reversible manner. In solid-state devices this has been realized only recently [3–5]. In the weak coupling regime on the other hand the interactions are governed by the Purcell effect [28] with an enhancement of on-resonance transitions and a suppression of off-resonance transitions [11, 34–36, 231]. While an enhancement of the spontaneous decay is desired for many opto-electronic devices, like high-speed LEDs [34] and lasers [232], a suppression of spontaneous emission is needed in quantum information science [6, 7]. The Purcell effect also allows for lasers with a large spontaneous emission factor that leads to an ultralow laser threshold; see, e.g., Ref. [38]. In such a laser the spontaneous emission into the laser mode is enhanced, while spontaneous emission into nonlasing modes is suppressed. The photon statistics of the emitted light from such kind of device is of high topical interest [39, 233]. Lasers with large spontaneous emission factor are only one example of novel light sources based on QDs and microcavities. Other examples are single-photon sources [82, 83] and entangled-photons sources [234], which will have applications in quantum cryptography [235] and quantum teleportation [236, 237].

The quantification of the Purcell effect requires the study of the spontaneous emission *dynamics*. Experimentally this can be done in time-resolved photoluminescence (PL) measurements. The spontaneous emission lifetime is then usually extracted by fitting an exponential decay curve to the data. This procedure is based on the assumption that the PL decay can be described by a two-level scheme. However, in many cases a closer look at the experimental data reveals that the PL decay is non-exponential both in the presence of a microcavity [11, 84, 238, 239] and in the absence of a microcavity [240–242].

This chapter is devoted to the development and evaluation of a microscopic theory of light-matter interaction in semiconductor QDs that goes beyond the commonly used two-level model. First, a general scheme to investigate quantum properties of light in various sorts of semiconductor structures and photonic environments is discussed. The starting point is the Hamiltonian which treats both the carriers and the electromagnetic field fully

quantum-mechanically. To achieve a dynamical description of light-matter interaction in semiconductors, several approaches are possible, such as the nonequilibrium Green's functions [243, 244] and the equations-of-motion technique [75, 245]. The latter approach is the one we use and discuss in this work. In Section 3.2 the nanostructures are specified to be QD-wetting layer systems. We derive the semiconductor luminescence equations (SLE) for the QD-wetting layer system. These equations are generalizations of the semiconductor Bloch equations. Whereas the latter model coherent excitation dynamics with classical light fields [77], the SLE describe the incoherent regime with a quantized light field. This allows us to study spectral and dynamical properties of photoluminescence from QD ensembles in free space. The case of QDs embedded in optical microcavities is investigated in Section 3.3. Our studies give an explanation of the non-exponential spontaneous emission decay observed in recent experiments [84, 242]. In Section 3.4 we analyze QD-based microcavity lasers with particular emphasis on the photon statistics and the coherence properties of the emitted light.

## 3.1 Theoretical framework

### 3.1.1 Description of carrier confinement

The particular geometry of the nanostructure enters through the single-particle wave functions  $\langle \mathbf{r} | \nu, \lambda \rangle = \psi_\nu^\lambda(\mathbf{r})$  with band index  $\lambda$  and quantum number  $\nu$  containing the spin. The computation of single-particle states in realistic nanostructures is a research field of its own. For this purpose, nanodevices simulation packages are available, see, e.g., Ref. [246].

We restrict ourselves in the following to direct bandgap semiconductors that are well described by two bands  $\lambda = c, v$ , one conduction and one valence band. The generalization to a multi-band system is straightforward. Using the single-particle states as basis states, the Hamiltonian of non-interacting charge carriers can be written in second quantization as

$$H_{\text{carr}}^0 = \sum_\nu \varepsilon_\nu^c c_\nu^\dagger c_\nu + \sum_\nu \varepsilon_\nu^v v_\nu^\dagger v_\nu . \quad (3.1)$$

The fermionic operators  $c_\nu$  ( $c_\nu^\dagger$ ) annihilate (create) conduction-band electrons in the single-particle states  $|\nu, c\rangle$  of energy  $\varepsilon_\nu^c$ . The corresponding operators and single-particle energies for valence-band electrons are  $v_\nu$  ( $v_\nu^\dagger$ ) and  $\varepsilon_\nu^v$ , respectively.

### 3.1.2 Coulomb interaction between carriers

The many-body Hamiltonian which describes the Coulomb interaction of valence- and conduction-band electrons is given by

$$H_{\text{Coul}} = \frac{1}{2} \sum_{\alpha' \nu \nu' \alpha} \left[ V_{\alpha' \nu, \nu' \alpha}^{cc} c_{\alpha'}^\dagger c_\nu^\dagger c_{\nu'} c_\alpha + V_{\alpha' \nu, \nu' \alpha}^{vv} v_{\alpha'}^\dagger v_\nu^\dagger v_{\nu'} v_\alpha \right] + \sum_{\alpha' \nu \nu' \alpha} V_{\alpha' \nu, \nu' \alpha}^{cv} c_{\alpha'}^\dagger v_\nu^\dagger v_{\nu'} c_\alpha . \quad (3.2)$$

The explicit form of the single-particle wave function  $\psi_\nu^\lambda(\mathbf{r})$  enters the description via the Coulomb matrix elements

$$V_{\alpha'\nu,\nu'\alpha}^{\lambda\lambda'} = \int d^3r \int d^3r' \psi_{\alpha'}^{\lambda*}(\mathbf{r}) \psi_\nu^{\lambda*}(\mathbf{r}') V(\mathbf{r} - \mathbf{r}') \psi_{\nu'}^{\lambda'}(\mathbf{r}') \psi_\alpha^\lambda(\mathbf{r}) \quad (3.3)$$

with the Coulomb potential  $V(\mathbf{r}) = e^2/4\pi\epsilon_0\epsilon r$ . The dielectric constants of the vacuum and the background material are given by  $\epsilon_0$  and  $\epsilon$ , respectively.

Note that we omitted the electron-hole exchange interaction with corresponding matrix elements  $V_{\alpha'\nu,\nu'\alpha}^{cv,\text{exch}} = \int d^3r \int d^3r' \psi_{\alpha'}^{c*}(\mathbf{r}) \psi_\nu^{v*}(\mathbf{r}') V(\mathbf{r} - \mathbf{r}') \psi_\nu^v(\mathbf{r}) \psi_\alpha^c(\mathbf{r}')$ . This contribution has only a small effect for the problems studied in this work [247, 248]. In the envelope-function approximation [77], which we will employ later, these matrix elements are found to be exactly zero.

### 3.1.3 Description of optical confinement

We use a quantum mechanical description of the electromagnetic field to formulate the theory of light-matter interaction. The free electromagnetic field is given by the Hamiltonian [249]

$$H_{\text{ph}} = \sum_\xi \hbar\omega_\xi \left( b_\xi^\dagger b_\xi + \frac{1}{2} \right), \quad (3.4)$$

where  $\xi$  labels the mode,  $\hbar\omega_\xi$  is the photon energy, and the bosonic operators  $b_\xi^\dagger$  ( $b_\xi$ ) create (destroy) a photon in the mode  $\xi$ . In free space, the label  $\xi$  contains the wave vector  $\mathbf{q}$  and the polarization vector of the electromagnetic field  $\mathbf{e}_p(\mathbf{q})$ , with the index  $p = \pm$ . The mode frequencies are then given by  $\omega_\xi = c|\mathbf{q}|$ , with  $c$  being the speed of light in vacuum, and the explicit form of the modes is  $\mathbf{U}_\xi(\mathbf{r}) = \mathbf{e}_p(\mathbf{q})e^{i\sqrt{\epsilon}\mathbf{q}\cdot\mathbf{r}}$ .

In the case of a more complicated dielectric environment the mode functions  $\mathbf{U}_\xi(\mathbf{r})$  and frequencies  $\omega_\xi$  have to be determined by solving Maxwell's equations for the given geometry. For microcavities this has been discussed in detail in Chapter 2.

### 3.1.4 Light-matter interaction

The light-matter interaction Hamiltonian in dipole approximation reads

$$H_D = -i \sum_{\xi,\alpha\nu} \left( g_{\xi\alpha\nu}^{cv} c_\alpha^\dagger v_\nu b_\xi + g_{\xi\alpha\nu}^{vc} v_\alpha^\dagger c_\nu b_\xi \right) + \text{h.c.} \quad (3.5)$$

The matrix elements  $g_{\xi\alpha\nu}^{cv}$  and  $g_{\xi\alpha\nu}^{vc}$ , which describe the coupling between the mode  $\xi$  of the electromagnetic field and the carrier interband transition between states  $|\alpha, c\rangle$  and  $|\nu, v\rangle$ , are given by

$$g_{\xi\alpha\nu}^{cv} = E_\xi \int d^3r \psi_\alpha^{c*}(\mathbf{r}) e \mathbf{r} \mathbf{U}_\xi(\mathbf{r}) \psi_\nu^v(\mathbf{r}), \quad (3.6)$$

$$g_{\xi\alpha\nu}^{vc} = E_\xi \int d^3r \psi_\alpha^{v*}(\mathbf{r}) e \mathbf{r} \mathbf{U}_\xi(\mathbf{r}) \psi_\nu^c(\mathbf{r}), \quad (3.7)$$

where  $E_\xi = \sqrt{\hbar\omega_\xi/2\epsilon\epsilon_0V}$  and  $V$  is the normalization volume.

Note that we ignore the so-called dipole self-energy [250]. This contribution leads to an energetic shift of the optical spectra. For materials with large background refractive index, like GaAs, the shift is particularly small [251].

### 3.1.5 Equations-of-motion technique

The total Hamiltonian for the interacting carriers and photons is given by

$$H = H_{\text{carr}}^0 + H_{\text{Coul}} + H_{\text{ph}} + H_{\text{D}} . \quad (3.8)$$

Note that coupling to phonons, the quantized lattice vibrations in a solid, can be included in a similar way like the coupling to photons [251, 252]. We will later consider effects of phonons on a phenomenological level.

The equations-of-motion technique [75] is based on Heisenberg's equation of motion. In the Heisenberg representation the time evolution of an operator  $A$ , which does not explicitly depend on time, is given by

$$i\hbar \frac{d}{dt} A = [A, H] . \quad (3.9)$$

This equation can be used to compute the dynamics of operator averages, such as the electron occupation  $f_\alpha^e = \langle c_\alpha^\dagger c_\alpha \rangle$  of a given conduction-band state  $\alpha$ , or the number of photons  $\langle b_\xi^\dagger b_\xi \rangle$  in a given mode  $\xi$ . To illustrate the procedure we consider the time evolution of the number of photons  $\langle b_\xi^\dagger b_\xi \rangle$ . With

$$i\hbar \frac{db_\xi}{dt} = \hbar\omega_\xi b_\xi + i \sum_{\alpha\nu} (g_{\xi\nu\alpha}^{cv*} v_\nu^\dagger c_\alpha + g_{\xi\nu\alpha}^{vc*} c_\nu^\dagger v_\alpha) \quad (3.10)$$

and a similar equation for  $b_\xi^\dagger$  obtained by hermitian conjugation, we find

$$i\hbar \frac{d}{dt} \langle b_\xi^\dagger b_\xi \rangle = i\hbar \left\langle \frac{db_\xi^\dagger}{dt} b_\xi + b_\xi^\dagger \frac{db_\xi}{dt} \right\rangle \quad (3.11)$$

$$= i \sum_{\alpha\nu} \left( g_{\xi\nu\alpha}^{cv*} \langle b_\xi^\dagger v_\nu^\dagger c_\alpha \rangle + g_{\xi\nu\alpha}^{cv} \langle b_\xi c_\alpha^\dagger v_\nu \rangle + g_{\xi\nu\alpha}^{vc} \langle b_\xi v_\alpha^\dagger c_\nu \rangle + g_{\xi\nu\alpha}^{vc*} \langle b_\xi^\dagger c_\nu^\dagger v_\alpha \rangle \right) . \quad (3.12)$$

The so-called photon-assisted polarization  $\langle b_\xi^\dagger v_\nu^\dagger c_\alpha \rangle$  corresponds to the transition of an electron from the conduction-band state  $\alpha$  to the valence-band state  $\nu$  via emission of a photon into the mode  $\xi$ . Its complex conjugate  $\langle b_\xi^\dagger v_\nu^\dagger c_\alpha \rangle^* = \langle b_\xi c_\alpha^\dagger v_\nu \rangle$  corresponds to the inverse transition of an electron from the valence-band state  $\nu$  to the conduction-band state  $\alpha$  via absorption of a photon. The remaining two terms in Eq. (3.12) give a negligible contribution as they are nonresonant and violate energy conservation. We will employ the rotating-wave approximation (RWA) [47, 249] in which these nonresonant terms are discarded.

### 3.1.6 Hierarchy problem

In Eq. (3.12) we observe that the dynamics of a single-particle average couples in general to other operator averages for which equations of motion have to be derived as well. To illustrate the arising hierarchy problem, we consider the dynamics of the electron population in the conduction band generated by the Coulomb Hamiltonian  $H_{\text{Coul}}$ :

$$i\hbar \frac{d}{dt} \Big|_{H_{\text{Coul}}} \langle c_\alpha^\dagger c_\alpha \rangle = i\hbar \left\langle \frac{dc_\alpha^\dagger}{dt} \Big|_{H_{\text{Coul}}} c_\alpha + c_\alpha^\dagger \frac{dc_\alpha}{dt} \Big|_{H_{\text{Coul}}} \right\rangle \quad (3.13)$$

with

$$i\hbar \frac{d}{dt} \Big|_{H_{\text{Coul}}} c_\alpha = \sum_{\alpha'\nu\nu'} V_{\alpha\alpha',\nu\nu'}^{cc} c_\alpha^\dagger c_\nu c_{\nu'} + \sum_{\alpha'\nu\nu'} V_{\alpha\alpha',\nu\nu'}^{cv} v_\alpha^\dagger v_\nu c_{\nu'} . \quad (3.14)$$

Again, the equation for  $c_\alpha^\dagger$  is obtained by hermitian conjugation. With these equations we get

$$i\hbar \frac{d}{dt} \Big|_{H_{\text{Coul}}} f_\alpha^e = 2i\text{Im} \left( \sum_{\alpha'\nu\nu'} V_{\alpha\alpha',\nu\nu'}^{cc} \langle c_\alpha^\dagger c_\alpha^\dagger c_\nu c_{\nu'} \rangle + \sum_{\alpha'\nu\nu'} V_{\alpha\alpha',\nu\nu'}^{cv} \langle c_\alpha^\dagger v_\alpha^\dagger v_\nu c_{\nu'} \rangle \right) . \quad (3.15)$$

From this example we learn that the dynamics of this single-particle quantity couples to two-particle quantities via the Coulomb interaction. To determine the time evolution of the single-particle quantities, we also have to compute the evolution of the two-particle quantities. It is easy to see that the equation of motion for two-particle quantities are connected to three-particle quantities and so on. This is the well-known hierarchy problem of many-particle physics [77, 253]. It is important to mention that also the light-matter interaction leads to a hierarchy problem, as can be anticipated from Eq. (3.12). Only if the electric field can be treated classically, the expectation values containing photon and carrier operators factorize, for instance  $\langle b_\xi^\dagger v_\nu^\dagger c_\alpha \rangle = \langle b_\xi^\dagger \rangle \langle v_\nu^\dagger c_\alpha \rangle$  since  $b_\xi^\dagger$  can be treated as a complex number.

In practice, the hierarchy of differential equations has to be truncated. The simplest approach is the Hartree-Fock (HF) approximation that is widely used in condensed matter physics. It is based on the approximation that every electron moves in the potential created by the nuclei plus the average potential of all the other electrons. This assumption leads to an independent-particle model that essentially reduces the many-electron problem to the problem of solving a number of single-electron equations. In our case, it means that two-particle averages are replaced by all possible combinations of single-particle averages, e.g.,

$$\langle a_i^\dagger a_j^\dagger a_k a_l \rangle \approx \langle a_i^\dagger a_j^\dagger a_k a_l \rangle_{\text{HF}} = \langle a_i^\dagger a_l \rangle \langle a_j^\dagger a_k \rangle - \langle a_i^\dagger a_k \rangle \langle a_j^\dagger a_l \rangle . \quad (3.16)$$

The sign is determined by the number of permutations needed to reorder the product of fermionic operators into the original order in the two-particle average. If the number of permutations is odd, a  $-$  sign is obtained, otherwise one gets a  $+$  sign. In the HF approximation, the equations of motion close.

### 3.1.7 Cluster expansion method

Truncation schemes beyond the HF approximation are controlled by either the required order of the applied electric field (dynamics-controlled truncation scheme [245, 254]), the number of involved particles, or the order of correlation functions (cluster expansion scheme [76]). Within this work, we use the latter approach to truncate the many-particle hierarchy. This truncation procedure has previously been used to describe the luminescence dynamics of quantum wells [250, 252, 255]. In this approach, operator averages are classified into singlets, doublets, triplets, quadruplets, etc., according to the number of particles they involve. Considering interband transitions, it must be borne in mind that the excitation of one electron is described as the destruction of a valence-band carrier and the creation of a conduction-band carrier. For the corresponding interaction processes, a photon operator is connected to two carrier operators [256, 257]. This fact is used to classify mixed expectation values with photon and carrier operators. For example, the electron population  $f_\nu^e = \langle c_\nu^\dagger c_\nu \rangle$  is a singlet contribution, the photon number  $\langle b_\xi^\dagger b_\xi \rangle$  and the photon-assisted polarization  $\langle b_\xi^\dagger v_\nu^\dagger c_\nu \rangle$  are doublet terms.

In the following,  $N$ -particle averages, schematically denoted as  $\langle N \rangle$  and containing  $2N$  carrier operators or an equivalent replacement of photon operators, are factorized into all possible combinations of averages involving one up to  $N - 1$  particle averages. For the difference between the full operator average and this factorization, we introduce a correlation function of order  $N$ , denoted as  $\delta\langle N \rangle$ . Schematically the factorization of singlets, doublets, triplets, and quadruplets is given by

$$\langle 1 \rangle = \delta\langle 1 \rangle , \quad (3.17a)$$

$$\langle 2 \rangle = \langle 1 \rangle \langle 1 \rangle + \delta\langle 2 \rangle , \quad (3.17b)$$

$$\langle 3 \rangle = \langle 1 \rangle \langle 1 \rangle \langle 1 \rangle + \langle 1 \rangle \delta\langle 2 \rangle + \delta\langle 3 \rangle , \quad (3.17c)$$

$$\langle 4 \rangle = \langle 1 \rangle \langle 1 \rangle \langle 1 \rangle \langle 1 \rangle + \langle 1 \rangle \langle 1 \rangle \delta\langle 2 \rangle + \langle 1 \rangle \delta\langle 3 \rangle + \delta\langle 2 \rangle \delta\langle 2 \rangle + \delta\langle 4 \rangle . \quad (3.17d)$$

Looking at the last equation, the first four terms on the right hand side represent all possible combinations of singlets, singlets and doublets, singlets and triplets, and doublets, respectively. The last term is the remaining quadruplet correlation function. Continuing the series (3.17a)–(3.17d) leads to quintuplet terms and so on. Note that singlets cannot be factorized any further.

The essential idea in the cluster expansion method is to replace in the equations of motion all occurring operator expectation values  $\langle N \rangle$  according to the Eqs. (3.17) so that equations of motion for the correlation functions  $\delta\langle N \rangle$  are obtained. Then the hierarchy of correlation functions is truncated rather than the hierarchy of expectation values itself. This allows the consistent inclusion of correlations up to a certain order in all of the appearing operator expectation values. Here, the HF approximation in Eq. (3.16) is equivalent to the singlet level, i.e., considering only singlet contributions in Eq. (3.17b).

### 3.1.8 Open microcavities

Microcavities as investigated in Chapter 2 are open systems. Quasi-bound modes cannot be described by a Hamiltonian  $H_{\text{ph}}$  as in Eq. (3.4). In quantum optics, such nonhermitian problems are treated by the system-reservoir approach [249, 258]. The “system” consists of the eigenmodes of a fictitious closed cavity. The “reservoir” is the external field described by a continuous set of modes. This leads to a formulation in terms of a Liouvillian  $L$  and the density operator  $\rho$ . Its equation of motion reads in the Schrödinger representation

$$\dot{\rho}(t) = -iL\rho(t), \quad L = L_H + i\Lambda_R \quad (3.18)$$

with the internal dynamics

$$L_H \rho = \frac{1}{\hbar} [H, \rho] \quad (3.19)$$

and the coupling to the reservoir at zero temperature

$$\Lambda_R \rho = \sum_{\xi} \frac{\kappa_{\xi}}{\hbar} \{ [b_{\xi}\rho, b_{\xi}^{\dagger}] + [b_{\xi}, \rho b_{\xi}^{\dagger}] \}, \quad (3.20)$$

where  $2\kappa_{\xi}/\hbar$  is the cavity loss rate. This definition of  $\Lambda_R$  is equivalent to [259]

$$\text{tr}_R \left( b_{\xi}^{\dagger n} b_{\xi'}^m e^{\Lambda_R t} \rho \right) = e^{-(n\kappa_{\xi} + m\kappa_{\xi'})t/\hbar} \text{tr}_R \left( b_{\xi}^{\dagger n} b_{\xi'}^m \rho \right), \quad (3.21)$$

with  $\text{tr}_R$  being the trace over the reservoir states. From this equation it can be easily shown that the dynamics generated by  $\Lambda_R$  is given by

$$i\hbar \frac{d}{dt} \Big|_R \langle b_{\xi}^{\dagger n} b_{\xi'}^m \rangle = -i(n\kappa_{\xi} + m\kappa_{\xi'}) \langle b_{\xi}^{\dagger n} b_{\xi'}^m \rangle. \quad (3.22)$$

Together with

$$i\hbar \frac{d}{dt} \Big|_{H_{\text{ph}}} \langle b_{\xi}^{\dagger n} b_{\xi'}^m \rangle = -\hbar(n\omega_{\xi} - m\omega_{\xi'}) \langle b_{\xi}^{\dagger n} b_{\xi'}^m \rangle \quad (3.23)$$

follows that the loss rates can be incorporated into complex-valued frequencies. Replacing  $\omega_{\xi}$  by  $\omega_{\xi} - i\kappa_{\xi}/\hbar$  gives

$$i\hbar \frac{d}{dt} \Big|_{R, H_{\text{ph}}} \langle b_{\xi}^{\dagger n} b_{\xi'}^m \rangle = -\hbar(n\omega_{\xi}^* - m\omega_{\xi'}) \langle b_{\xi}^{\dagger n} b_{\xi'}^m \rangle. \quad (3.24)$$

This equation implies that in the free photonic part of the equations of motion we have to use the complex-valued frequency  $\omega_{\xi}$  whenever the annihilation operator  $b_{\xi}$  appears and its complex conjugate  $\omega_{\xi}^*$  whenever the creation operator  $b_{\xi}^{\dagger}$  appears.

In the following, we apply the general theory for light-matter interaction discussed in this and the previous sections to QD ensembles.

## 3.2 Luminescence from semiconductor quantum dots

QDs provide carrier confinement in all three directions with a discrete atomic-like single-particle density of states. Localized carriers in such “artificial atoms” are often described in terms of excitons, i. e., fully correlated electron-hole pairs. However, this simplified picture should be treated with care since the elementary quasi-particles in semiconductors are electrons and holes, and the degree of correlations between them depends on the many-body Coulomb interaction and on the carrier-photon interaction.

The influence of Coulomb-correlated multi-exciton states on optical spectra of QDs has been investigated by several groups [260–266]. Much less is known about the influence of correlations on the spontaneous recombination dynamics. Time-resolved photoluminescence (PL) measurements provide direct access to the efficiency of carrier scattering processes after optical excitation with short pulses [267] and to the modification of the spontaneous emission lifetime for QDs in optical cavities due to the Purcell effect [11, 240, 241].

Based on the general discussion in the previous section we derive in this section a microscopic theory to study photoluminescence of semiconductor QDs under the influence of Coulomb and carrier-photon correlation effects [84, 257]. We apply the cluster expansion method up to the singlet-doublet level. Our numerical results show that it is necessary to go beyond the singlet level in order to obtain well-defined luminescence spectra. Moreover, we demonstrate that the higher order correlations can have a strong impact on the luminescence decay dynamics.

This section is organized as follows: In Section 3.2.1 our model system is introduced. Then the equations of motion for the carriers in the QDs and the quantized light field are derived. The PL spectrum is studied in Section 3.2.3 and the PL decay is investigated in Section 3.2.4. Finally, a comparison to recent experimental results is given.

### 3.2.1 The system

We consider self-assembled QDs, where the localized states lie energetically below a quasi-continuum of delocalized states corresponding to the two-dimensional motion in a wetting layer (WL). A sketch of the energy levels is shown in Fig. 3.1. To study PL, the system may be off-resonantly excited by an optical pulse which creates carriers in the WL. From there the carriers relax quickly into the localized QD states [268, 269]. At low temperatures, the carriers populate solely the QD states. Then the WL states are mainly important for carrier-scattering processes if the excitation involves the quasi-continuum. For the recombination dynamics due to carrier-photon interaction, the unpopulated WL states are of negligible importance and are therefore not included in our calculation. Coulomb correlations between the discrete QD states and the energetically displaced quasi-continuum of the WL are much weaker than those between QD states.

Single-particle states in semiconductor QDs have been studied with pseudopotential theory [270, 271],  $\mathbf{k} \cdot \mathbf{p}$  models [272], tight-binding models [247, 266], and density functional theory [273]. Since the main physical effects discussed below arise from the many-body interaction, we consider a simple model for the single-particle states. It has been shown

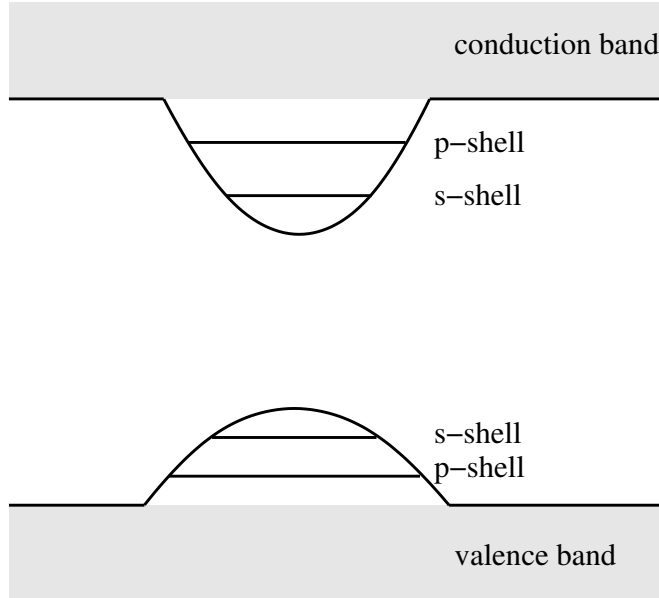


**Figure 3.1:** Schematic representation of energy levels in a quantum dot with two shells. The  $p$ -shell is two-fold degenerate. The quasicontinuum of the wetting layer is shown as shaded areas.

that in the case of flat, cylindrically symmetric QDs the single-particle bound-state wave functions in the plane of larger extension (perpendicular to the growth direction) are well approximated by those of a two-dimensional harmonic oscillator [274]. Due to the rotational symmetry around the QD axis, the corresponding angular momentum is a good quantum number. We consider the first two confined shells of such a system, which are denoted by  $s$  and  $p$  according to their in-plane symmetry. The  $s$ -shell is only spin-degenerate, while the  $p$ -shell has an additional angular-momentum two-fold degeneracy. To account for the strong confinement in growth direction, we use an infinite potential well to model the corresponding finite extension of the wave function. Only the energetically lowest state due to the confinement in growth direction will be considered. Further details of the QD model are discussed in [268] .

In envelope-function approximation [77] the wave function  $\psi_\alpha^c(\mathbf{r})$  and  $\psi_\nu^v(\mathbf{r})$  can now be decomposed into envelope parts  $\zeta_\alpha^c(\mathbf{r})$  and  $\zeta_\nu^v(\mathbf{r})$ , which vary only slightly over a unit cell, and the rapidly oscillating Bloch-factor  $u_{\mathbf{k} \approx 0}^{c,v}(\mathbf{r})$ . Inserting this factorization into Eq. (3.6) gives

$$g_{\xi\alpha\nu}^{cv} = E_\xi \mathbf{d}_{cv} \int d^3r \zeta_\alpha^{c*}(\mathbf{r}) \mathbf{U}_\xi(\mathbf{r}) \zeta_\nu^v(\mathbf{r}) , \quad (3.25)$$

with the dipole matrix element  $\mathbf{d}_{cv}$ . Here we do not consider  $g_{\xi\alpha\nu}^{vc}$  since terms containing this quantity drop out in the RWA. It can be shown that the matrix elements  $g_{\xi\alpha\nu}^{cv}$  are approximately diagonal in the carrier indices. This we demonstrate for two localized QD states  $|\alpha\rangle$  and  $|\nu\rangle$ . Taking into account that the electromagnetic field is approximately constant over the extent of a QD at position  $\mathbf{r}_0$  and considering equal envelopes for the conduction- and valence-band electrons, one finds from Eq. (3.25)

$$g_{\xi\alpha\nu}^{cv} = E_\xi \mathbf{d}_{cv} \mathbf{U}_\xi(\mathbf{r}_0) \delta_{\alpha\nu} \equiv g_{\xi\nu} \delta_{\alpha\nu} . \quad (3.26)$$

From Eq. (3.26) it follows that, within the envelope-function approximation, optical transitions occur only between the *s*-shells or the *p*-shells of electrons and holes.

### 3.2.2 QD semiconductor luminescence equations

The aim of our description is the calculation of the time-resolved PL and the corresponding emission spectrum. We first focus on QD ensembles in the absence of a microcavity. Following the general scheme in Section 3.1 we use Heisenberg's equations of motion together with the Hamiltonian of the interacting system and the RWA to obtain the time evolution of the carrier and photon operators. From this coupled equations, we derive equations of motion for operator averages, like the carrier population or photon number. To truncate the arising hierarchy, we use the cluster expansion scheme on the singlet-doublet level. We assume that the PL takes place in the incoherent regime where the influence of a coherent polarization can be neglected. Examples for such a situation are incoherent carrier excitations or coherent excitation of higher states with rapid dephasing and carrier relaxation. Since there is no coherent field,  $\langle b_\xi \rangle = 0$ , polarization-like averages of the form  $\langle v_\nu^\dagger c_\nu \rangle$  vanish [75, 250].

Using Heisenberg's equation of motion for the photon number, we find according to Eqs. (3.12) and (3.26) in the RWA

$$i\hbar \frac{d}{dt} \langle b_\xi^\dagger b_\xi \rangle = 2i \operatorname{Re} \sum_\nu g_{\xi\nu}^* \langle b_\xi^\dagger v_\nu^\dagger c_\nu \rangle , \quad (3.27)$$

which couples to the photon-assisted polarization amplitude  $\langle b_\xi^\dagger v_\nu^\dagger c_\nu \rangle$ . The corresponding equation of motion is given by

$$\begin{aligned} i\hbar \frac{d}{dt} \langle b_\xi^\dagger v_\nu^\dagger c_\nu \rangle &= (\tilde{\varepsilon}_\nu^c - \tilde{\varepsilon}_\nu^v - \hbar\omega_\xi - i\Gamma) \langle b_\xi^\dagger v_\nu^\dagger c_\nu \rangle + (f_\nu^c - f_\nu^v) \sum_\alpha V_{\nu\alpha\nu\alpha} \langle b_\xi^\dagger v_\alpha^\dagger c_\alpha \rangle \\ &\quad + i g_{\xi\nu} f_\nu^c (1 - f_\nu^v) + i \sum_\alpha g_{\xi\alpha} C_{\alpha\nu\nu\alpha}^x . \end{aligned} \quad (3.28)$$

The free evolution is determined by the renormalized energies  $\tilde{\varepsilon}_\nu^c = \varepsilon_\nu^c - \sum_\alpha V_{\nu\alpha\nu\alpha} f_\alpha^c$  and  $\tilde{\varepsilon}_\nu^v = \varepsilon_\nu^v - \sum_\alpha V_{\nu\alpha\nu\alpha} f_\alpha^v$ , the resonance frequency  $\omega_\xi$  of the optical mode  $\xi$ , and an introduced phenomenological dephasing  $\Gamma$  which broadens the spectral lines. The second term in the first line is analogous to the quantum well case, where it gives rise to the excitonic PL below the band gap [75]. Here it introduces the corresponding excitonic resonances for the QD states due to the interband Coulomb exchange interaction. The source term of spontaneous emission in the last line enters the theory naturally due to the quantization of the light field. We have omitted the term representing stimulated emission/absorption, which contributes for example if an external field is resonant with the considered transitions or if a resonator provides feedback for the emitted photons which will be considered in Section 3.3. Before evaluating the correlation term in the last

line of Eq. (3.28), we give the time evolution of the carrier population

$$i\hbar \frac{d}{dt} f_\nu^c = -2i \operatorname{Re} \sum_\xi g_{\xi\nu}^* \langle b_\xi^\dagger v_\nu^\dagger c_\nu \rangle + 2i \operatorname{Im} \sum_{\alpha\alpha'\nu'} V_{\nu\alpha'\alpha\nu'} (C_{\nu\alpha'\alpha\nu'}^c - C_{\alpha'\nu\alpha\nu'}^x) \quad (3.29)$$

$$i\hbar \frac{d}{dt} f_\nu^v = 2i \operatorname{Re} \sum_\xi g_{\xi\nu}^* \langle b_\xi^\dagger v_\nu^\dagger c_\nu \rangle - 2i \operatorname{Im} \sum_{\alpha\alpha'\nu'} V_{\nu\alpha'\alpha\nu'} (C_{\nu\alpha'\alpha\nu'}^v - C_{\alpha'\nu\alpha\nu'}^x) . \quad (3.30)$$

In the following, we consider  $s$ -states with zero angular momentum and  $p$ -states with angular momentum of  $\pm 1$ , which, as we now explain, allows us to take  $\langle a_\nu^\dagger a_{\nu'} \rangle = f_\nu^a \delta_{\nu\nu'}$ . Initially all expectation values but the population in the  $s$ - and  $p$ -shells are set to zero. The rotational symmetry of the system and the resulting conservation of angular momentum ensures that all off-diagonal terms  $\langle a_\nu^\dagger a_{\nu'} \rangle$  with  $\nu \neq \nu'$  describe forbidden transitions and remain zero during the time evolution. Therefore, in all equations expectation values of two carrier operators are restricted to populations. An inclusion of higher angular momentum states is straightforward, but unnecessary at low temperatures and left out for transparency.

The interband correlations are defined according to Eq. (3.17) as

$$\begin{aligned} C_{\alpha'\nu\nu'\alpha}^x &= \delta \langle c_{\alpha'}^\dagger v_\nu^\dagger c_{\nu'} v_\alpha \rangle \\ &= \langle c_{\alpha'}^\dagger v_\nu^\dagger c_{\nu'} v_\alpha \rangle - \langle c_{\alpha'}^\dagger v_\nu^\dagger c_{\nu'} v_\alpha \rangle_{\text{HF}} \\ &= \langle c_{\alpha'}^\dagger v_\nu^\dagger c_{\nu'} v_\alpha \rangle + f_{\nu'}^c f_\nu^v \delta_{\nu\alpha} \delta_{\nu'\alpha'} . \end{aligned} \quad (3.31)$$

The time evolution of the interband correlations is given by the equation of motion

$$\begin{aligned} i\hbar \frac{d}{dt} C_{\alpha'\nu\nu'\alpha}^x &= -(\varepsilon_{\alpha'}^c + \varepsilon_\nu^v - \varepsilon_{\nu'}^c - \varepsilon_\alpha^v) \langle c_{\alpha'}^\dagger v_\nu^\dagger c_{\nu'} v_\alpha \rangle \\ &\quad - \sum_{\nu_2\nu_3\nu_4} \left[ V_{\nu_1\nu_2\nu_3\alpha'} \langle c_{\nu_4}^\dagger (c_{\nu_2}^\dagger c_{\nu_3} + v_{\nu_2}^\dagger v_{\nu_3}) v_\nu^\dagger c_{\nu'} v_\alpha \rangle \right. \\ &\quad + V_{\nu_4\nu_2\nu_3\nu} \langle c_{\alpha'}^\dagger v_{\nu_4}^\dagger (c_{\nu_2}^\dagger c_{\nu_3} + v_{\nu_2}^\dagger v_{\nu_3}) c_{\nu'} v_\alpha \rangle \\ &\quad - V_{\nu'\nu_2\nu_3\nu_4} \langle c_{\alpha'}^\dagger v_\nu^\dagger (c_{\nu_2}^\dagger c_{\nu_3} + v_{\nu_2}^\dagger v_{\nu_3}) c_{\nu_4} v_\alpha \rangle \\ &\quad \left. - V_{\alpha\nu_2\nu_3\nu_4} \langle c_{\alpha'}^\dagger v_\nu^\dagger c_{\nu'} (c_{\nu_2}^\dagger c_{\nu_3} + v_{\nu_2}^\dagger v_{\nu_3}) v_{\nu_4} v_{\nu_4} \rangle \right] \\ &\quad - i \sum_\xi \left[ g_{\xi\alpha'}^* \langle b_\xi^\dagger v_{\alpha'}^\dagger v_\nu^\dagger c_{\nu'} v_\alpha \rangle - g_{\xi\alpha}^* \langle b_\xi^\dagger c_{\alpha'}^\dagger v_\nu^\dagger c_{\nu'} v_\alpha \rangle \right. \\ &\quad \left. + g_{\xi\nu'} \langle b_\xi c_{\alpha'}^\dagger v_\nu^\dagger v_{\nu'} v_\alpha \rangle - g_{\xi\nu} \langle b_\xi c_{\alpha'}^\dagger c_\nu^\dagger c_{\nu'} v_\alpha \rangle \right] \\ &\quad - i\hbar \frac{d}{dt} \langle c_{\alpha'}^\dagger v_\nu^\dagger c_{\nu'} v_\alpha \rangle_{\text{HF}} . \end{aligned} \quad (3.32)$$

Here, the first line is due to the free carrier Hamiltonian (3.1), the first sum due to the carrier Coulomb interaction (3.2), and the second sum due to the light-matter interaction (3.5). Note that the time derivative of the singlet factorization must be subtracted in order to obtain the pure four-operator correlation.

Evaluating Eq. (3.32) in singlet-doublet factorization leads to

$$\begin{aligned}
 i\hbar \frac{d}{dt} C_{\alpha'\nu\nu'\alpha}^x &= (\varepsilon_{\nu'}^c - \varepsilon_\nu^v - \varepsilon_{\alpha'}^c + \varepsilon_\alpha^v) C_{\alpha'\nu\nu'\alpha}^x \\
 &+ V_{\nu'\alpha\nu'\alpha'} [(1-f_\alpha^c)(1-f_\nu^v) f_{\nu'}^c f_\alpha^v - f_\alpha^c f_\nu^v (1-f_\nu^c)(1-f_\alpha^v)] \\
 &+ \sum_{\beta\beta'} \left\{ (f_\nu^v - f_\alpha^v) V_{\beta\alpha\nu\beta'} (C_{\alpha'\beta\nu'\beta'}^x + C_{\alpha'\beta\nu'\beta'}^c) + (f_{\alpha'}^c - f_{\nu'}^c) V_{\nu'\beta\beta'\alpha'} (C_{\beta\nu\beta'\alpha}^x + C_{\beta\nu\beta'\alpha}^v) \right\} \\
 &+ \sum_{\beta\beta'} \left\{ f_{\beta'}^c V_{\beta'\beta\beta'\alpha'} C_{\beta\nu\nu'\alpha}^x + f_{\beta'}^v V_{\beta'\beta\beta'\nu'} C_{\alpha'\beta\nu'\alpha}^x - f_\beta^c V_{\nu'\beta\beta'\beta} C_{\alpha'\nu\beta'\alpha}^x - f_{\beta'}^v V_{\alpha\beta\beta'\beta} C_{\alpha'\nu\nu'\beta'}^x \right\} \\
 &+ \sum_{\beta\beta'} (f_\beta^c + f_{\beta'}^v) [V_{\beta'\beta\beta'\alpha'} C_{\beta\nu\nu'\alpha}^x + V_{\beta'\beta\beta'\nu} C_{\alpha'\beta\nu'\alpha}^x - V_{\nu'\beta\beta'\beta} C_{\alpha'\nu\beta'\alpha}^x - V_{\alpha\beta\beta'\beta} C_{\alpha'\nu\nu'\beta'}^x] \\
 &+ \sum_{\beta\beta'} \left\{ (f_\alpha^v - f_{\alpha'}^c) V_{\beta\alpha\beta'\alpha'} C_{\beta\nu\nu'\beta'}^x - (f_\nu^v - f_{\nu'}^c) V_{\nu'\beta\nu\beta'} C_{\alpha'\beta\nu'\alpha}^x + (1-f_\alpha^v - f_{\nu'}^c) V_{\nu'\alpha\beta\beta'} C_{\alpha'\nu\nu'\beta'}^x \right. \\
 &\quad \left. + (f_{\alpha'}^c - 1 + f_\nu^v) V_{\beta\beta'\nu\alpha'} C_{\beta\nu\beta'\alpha}^x + (f_{\nu'}^c - f_{\alpha'}^c) V_{\nu'\beta\alpha'\beta'} C_{\beta\nu\beta'\alpha}^x + (f_\alpha^v - f_\nu^v) V_{\beta\alpha\beta\nu} C_{\alpha'\beta\nu'\beta'}^x \right\} \\
 &- i \sum_{\xi} \delta_{\alpha\alpha'} \delta_{\nu\nu'} [g_{\xi\alpha}^*(f_\alpha^v - f_\alpha^c) \langle b_\xi^\dagger v_\nu^\dagger c_\nu \rangle + g_{\xi\nu}^*(f_\nu^v - f_\nu^c) \langle b_\xi c_\alpha^\dagger v_\alpha \rangle] . 
 \end{aligned} \tag{3.33}$$

The first two lines of Eq. (3.33) correspond to a calculation of  $C^x$  in singlet approximation. A theory restricted to this level was used in [255, 275] for quantum wells and in [84] for QDs. Note that the singlet factorization of six-operator averages already goes beyond the Hartree-Fock (HF) approximation. The terms in the third line can be shown to provide screening according to the Lindhard theory for the Coulomb potential in Eq. (3.28). The next line contains exchange-like scattering terms, followed by one line of Hartree-like scattering terms, identified by the indices on the Coulomb matrix elements. The terms in the fourth sum are Coulomb renormalisations due to scattering between all possible states. The last line finally contains the contribution due to the light-matter interaction Hamiltonian (3.5).

Similar equations for the correlations  $C_{\alpha'\nu\nu'\alpha}^c = \delta \langle c_{\alpha'}^\dagger c_\nu^\dagger c_{\nu'} c_\alpha \rangle$  and  $C_{\alpha'\nu\nu'\alpha}^v = \delta \langle v_{\alpha'}^\dagger v_\nu^\dagger v_{\nu'} v_\alpha \rangle$ , obtained along the same lines, are provided in Appendix C. Note that all Coulomb correlations can only redistribute carriers without changing the total population  $\sum_\nu f_\nu^{c,v}$ . Therefore, the changes of the carrier densities in each band are determined only by the photon-assisted polarisation. From combination of Eqs. (3.27) and (3.29), one obtains

$$\frac{d}{dt} \left( \sum_\nu f_\nu^c + \sum_\xi \langle b_\xi^\dagger b_\xi \rangle \right) = 0 , \tag{3.34}$$

which reveals that a decrease (increase) of population in the conduction band is balanced by the increase (decrease) of the total photon number.

### 3.2.3 Photoluminescence spectrum

We now present results for the numerical solution of the equations derived in the previous section. The equations are solved in the time domain using a fourth order Runge-Kutta

method. The material parameters are those of [265] for an InGaAs QD system and we consider a density of QDs on the WL of  $3 \cdot 10^{10} \text{ cm}^{-2}$  and a gap energy of 1.52 eV. We assume that the excitation involves only carriers with one spin polarization, e.g., due to excitation with circular polarized light. It is not our purpose to study the dynamics of the carrier generation and relaxation. Since these processes are much faster than the recombination, we assume a quasi-equilibrium distribution of carriers with given carrier density and temperature as an initial state for our calculation. Within such an assumption, the initial values for the correlation functions  $C^x$ ,  $C^e$ , and  $C^v$  remain open. For an unexcited system, all correlation functions are zero and build up during the carrier generation process according to their equations of motion. Starting a calculation with quasi-equilibrium population and vanishing correlation functions can lead to an abrupt build-up of correlations, resulting in unphysical oscillations of the correlation matrix elements which carry over to the population dynamics. To avoid these unphysical results, we numerically determine the initial conditions for the correlation functions from their equations of motion. For this purpose, we perform a separate calculation, where the carrier populations are adiabatically ramped up to their equilibrium values. The resulting steady-state solutions of the equations of motion for the correlation functions provide the starting point of the time evolution discussed in the following. We define the time-dependent luminescence spectrum according to [250, 276] and consider the limit of high frequency resolution of a detector to obtain

$$I(\omega) = \frac{d}{dt} \sum_{\xi} \langle b_{\xi}^{\dagger} b_{\xi} \rangle \Big|_{|\mathbf{q}|=\frac{\omega}{c}} . \quad (3.35)$$

Here the mode label contains  $\xi = \{\mathbf{q}, \mathbf{e}_p\}$ . Using Eq. (3.27) leads to

$$I(\omega) = \frac{2}{\hbar} \sum_{\nu} |g_{q\nu}|^2 \operatorname{Re} \widetilde{\langle b_q^{\dagger} v_{\nu}^{\dagger} c_{\nu} \rangle} , \quad (3.36)$$

where  $\widetilde{\langle b_{\xi}^{\dagger} v_{\nu}^{\dagger} c_{\nu} \rangle} = \langle b_{\xi}^{\dagger} v_{\nu}^{\dagger} c_{\nu} \rangle / g_{\xi\nu}$  has been introduced. By means of this redefinition, the resulting quantity can be shown to depend only on the photon energy  $\hbar\omega = \hbar c q$  and neither on the direction nor on the polarization of the mode  $\xi$ . Then the angular part and the polarization can be integrated out in Eq. (3.35), yielding the quantity  $|g_{q\nu}|^2$  in Eq. (3.36) according to the Wigner-Weisskopf theory [249]. The total photon number is obtained from

$$I_{\text{tot}} = \int d\omega I(\omega) . \quad (3.37)$$

The PL spectrum after a time evolution of 50 ps is plotted in Fig. 3.2 for a temperature of 30 K and an initial carrier density of  $1.5 \cdot 10^{10} \text{ cm}^{-2}$ . Scaled relative to the bandgap, the two peaks correspond to the *s*-shell resonance at about -133 meV and the *p*-shell transition at about -79 meV. Both peaks are red shifted due to the Coulomb interaction from the non-interacting energies  $\varepsilon_p^c + \varepsilon_p^v = -111 \text{ meV}$  and  $\varepsilon_s^c + \varepsilon_s^v = -55.5 \text{ meV}$ , respectively. Furthermore, the peak height is increased due to the Coulomb interaction. The results of the calculation on the singlet-doublet level are compared to those obtained in HF approximation in Fig. 3.2. The PL at the *s*-shell is slightly enhanced, while the *p*-shell PL becomes negative. Contrary to an absorption spectrum, where a negative peak

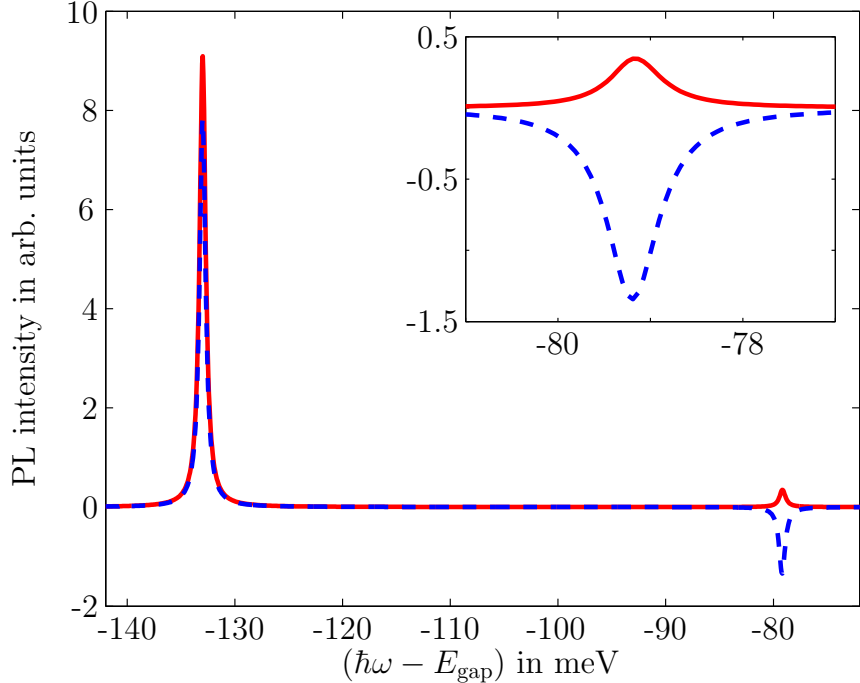


**Figure 3.2:** PL spectrum after 50 ps of time evolution. The solid line corresponds to the full calculation, the dashed line to the singlet (Hartree-Fock) factorisation. The inset shows a magnification of the intensity at the  $p$ -shell.

corresponds to gain, this result is unphysical and an artefact of the HF approximation at low temperatures. If the correlations (3.31) are factorized on singlet-doublet level, the spectrum is positive for all temperatures.

### 3.2.4 Time-resolved photoluminescence

In this section, we study the influence of the correlations on the time-resolved PL and on the corresponding population dynamics. Before we discuss the numerical results obtained by the solution of the full set of equations derived in Section 3.2.2, it is instructive to analyze the source term in Eq. (3.28) in more detail to gain a deeper understanding of the decay behavior of PL in a semiconductor. In the derivation of Eq. (3.28) the source term of spontaneous emission  $g_{\xi\nu}f_{\nu}^c(1-f_{\nu}^v) + \sum_{\alpha} g_{\xi\alpha}C_{\alpha\nu\nu\alpha}^x$  originates from the operator average  $\sum_{\alpha} g_{\xi\alpha}\langle c_{\alpha}^{\dagger}v_{\alpha}v_{\nu}^{\dagger}c_{\nu}\rangle$ . A simplified discussion is possible if one completely neglects the Coulomb interaction of carriers. Then the source term of spontaneous emission with the four-operator expectation value (resulting from the carrier-photon interaction) can be evaluated in two limiting cases. The first is the HF approximation, where correlations among the carriers are neglected. The second corresponds to the two-level approximation, where one assumes that the relevant physics is determined by one confined shell for electrons and for holes. The latter is of particular interest, since two-level models are frequently used in the discussion of QDs.

Within the HF approximation, the source term of spontaneous emission is solely deter-

mined by the product  $f_\nu^c(1-f_\nu^v)$ . In the absence of Coulomb interaction, one can formulate the stationary solution of Eq. (3.28) for the case of slowly varying populations to obtain

$$\frac{d}{dt} f_\nu^c = -\frac{2}{\hbar} \operatorname{Re} \sum_{\xi} \frac{i |g_{\xi\nu}|^2 f_\nu^c (1 - f_\nu^v)}{\varepsilon_\nu^c - \varepsilon_\nu^v - \hbar\omega_\xi - i\Gamma} = -\frac{f_\nu^c (1 - f_\nu^v)}{\tau_\nu}, \quad (3.38)$$

where  $1/\tau_\nu$  is the Wigner-Weisskopf rate of spontaneous emission for  $\Gamma \rightarrow 0$ . From this equation it is obvious that the decay of the population  $f_\nu^c$  is non-exponential, unless  $f_\nu^v$  is held constant by some mechanism, like background doping. Furthermore, the rate of decay depends on the carrier density and is higher for larger population. This behavior carries over to the PL according to Eq. (3.34). Due to the non-exponential PL decay a simple decay rate cannot be used to characterize the PL dynamics. This might appear surprising, since from a two-level atom an exponential decay behavior is known. Let us consider this two-level approximation as the second limiting case. Carrier indices are dropped as they are not needed if one restricts the population dynamics to one confined electron and hole level. In the de-excited (excited) state for this two-level system the electron is in the valence (conduction) band state. For the two spin polarizations, which are decoupled in the absence of Coulomb interaction, the independent processes then involve only the excitation of a single electron. This has a significant consequence for the evaluation of the source term of spontaneous emission. Within the two-level approximation, the successive application of more than one annihilation operator always yields zero, so that the source term  $\langle c^\dagger v v^\dagger c \rangle$  reduces to  $f^c$ . Along the same lines discussed above, instead of Eq. (3.38) one obtains

$$\frac{d}{dt} f^c = -\frac{f^c}{\tau}, \quad (3.39)$$

which corresponds to the exponential decay behavior known from the two-level system. In this case,  $1/\tau$  is the Wigner-Weisskopf rate for the considered two-level transition. From this analysis we deduce that the exponential decay within the two-level approximation stems from the fact, that the excitation of a QD conduction-band carrier is rigidly linked to the absence of a QD valence-band carrier. In the electron-hole picture, this corresponds to a fully correlated electron-hole pair. On the operator level this is expressed as  $c^\dagger v v^\dagger c = c^\dagger c$ . In a semiconductor, however, many carriers can be present and the correlations are subject to scattering and dephasing processes and must therefore be explicitly calculated.

Now we turn to the numerical results of the SLE including Coulomb interaction. In Fig. 3.3 we show the evolution of the time-resolved PL on a nanosecond timescale. Again, the initial carrier density is taken to be  $1.5 \cdot 10^{10} \text{ cm}^{-2}$ . For the solid line all correlations up to the singlet-doublet level have been included. The result of a calculation in the HF approximation, which corresponds to the discussed limiting case of uncorrelated carriers, is shown as a dashed line. In this case, the decay is clearly non-exponential in accordance with Eq. (3.38). Comparing these two results, it is obvious that carriers are correlated on the singlet-doublet level. However, our approach so far does not account for any kind of dephasing of the correlations. A physical mechanism for such dephasing is phonon scattering. Hoyer *et al.* have studied phonon scattering on a microscopic level for a quantum-well system. It is shown that dephasing of correlations is indeed provided, although this enters only via higher-order triplet terms [251, 252]. Extensions beyond the

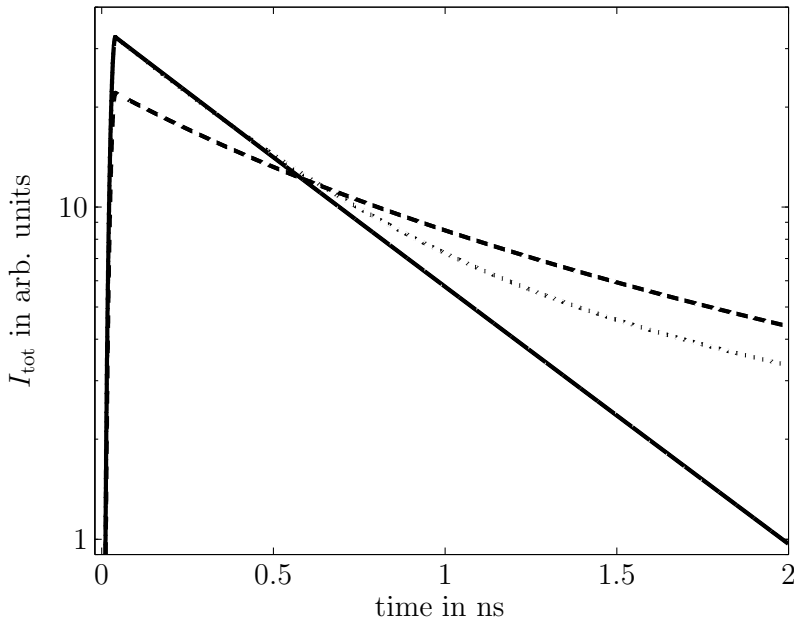


**Figure 3.3:** Logarithmic plot of the time evolution of the quantum dot photoluminescence. The dashed line corresponds to the calculation in singlet factorization and the solid line to the singlet-doublet level. For the dotted line the described phonon contributions were added to the singlet-doublet calculation.

singlet-doublet factorization are not within the scope of this work. Nevertheless, we can account for the main features of phonon scattering, which is dephasing of correlations and relaxation of the carrier population towards thermal equilibrium at the lattice temperature, on a phenomenological level. A constant dephasing term  $-i\gamma C_{\alpha'\nu\nu'\alpha}^x$  is added on the right-hand side of Eq. (3.33) and the scattering is treated within relaxation-time approximation by introducing

$$\frac{d}{dt} f_\nu^{c,v} \Big|_{\text{relax}} = -\frac{f_\nu^{c,v} - F_\nu^{c,v}(T)}{\tau_{\text{relax}}^{c,v}}, \quad (3.40)$$

in Eqs. (3.29) and (3.30), where  $F_\nu^{c,v}(T)$  is a Fermi-Dirac distribution at temperature  $T$ , evaluated for every timestep at the present carrier density.

Several recent experimental and theoretical investigations address the efficiency of carrier-phonon interaction in QDs. In the low-temperature regime, interaction of carriers with LA-phonons [277–279] provide the dominant dephasing mechanism while at elevated temperatures the interaction of carriers with LO-phonons leads to very efficient dephasing [269]. The temperature dependence of the dephasing has been studied, e.g., in four-wave experiments [280]. Even for the weakest dephasing values obtained there, we find that the influence of carrier correlations on the PL decay is strongly reduced.

To demonstrate the effect of a very weak constant dephasing rate,  $\gamma = 0.001$  meV has been used for the dotted line in Fig. 3.3. The correlations are drastically reduced so that a non-exponential signature of the decay is regained on longer timescales.

Our numerical analysis shows that the results presented here are rather insensitive to the exact value of the relaxation time  $\tau_{\text{relax}}^{c,v}$ . For the discussed example, typical values of  $\tau_{\text{relax}} = 1 \text{ ps}$  for electrons and holes are taken [269]. Hoyer *et al.* have shown that a constant dephasing  $\gamma$  causes unphysical heating of the system. However, this effect is only weak for a small value for the dephasing and, additionally, the scattering term (3.40) counteracts the heating.

Clearly such a phenomenological treatment of the dephasing via phonons cannot cover the spectral side-bands known from an interaction of the QD carriers with the continuum of acoustic phonons [278, 281, 282]. For this an inclusion of a microscopic description of the electron-phonon interaction would be necessary and is left for future work. Here the important point is that *any* kind of dephasing of the correlations will lead to deviations from an exponential decay.

Finally, we discuss the dependence of the PL decay on the excitation density that determines the initial carrier density. Figure 3.4 shows the PL for various initial carrier densities for the three different levels of approximation: singlet level (top panel), singlet-doublet level without dephasing (middle) and with dephasing (bottom). For the singlet level we find a strong dependence on the initial carrier density. This is in agreement with Eq. (3.38). In the case of the singlet-doublet level without dephasing, Fig. 3.4 demonstrates that the normalized intensity shows almost no dependence on the initial carrier density as we would expect for fully correlated carriers, cf., Eq. (3.39). As we have already seen, a very weak constant dephasing rate of  $\gamma = 0.001 \text{ meV}$  strongly reduces the correlations. We therefore expect to obtain in this case a dependence on the initial carrier density. This is confirmed by the bottom panel of Fig. 3.4, which shows a pronounced dependence on the initial carrier density. This result again demonstrates that the non-exponential decay and its dependence on excitation intensity are directly related.

### 3.2.5 Comparison to experiments

In this section, we compare our theory to recent experiments done in the research group of M. Bayer [242]. The self-assembled (In,Ga)As/GaAs QDs have been fabricated in the labs of A. Wieck. The QD parameters we use in our numerical simulations are the same as in the previous sections, except the QD density is  $N = 10^{10} \text{ cm}^{-2}$ , the dipole moment is  $16.8 e\text{\AA}$ , and the dephasing of the correlations is taken to be  $0.05 \text{ meV}$ . Even though the dephasing is weak it effectively destroys the correlations on a time scale of tens of ps.

Figure 3.5 shows results for undoped and n-doped QDs excited at the *p*-shell. For the undoped situation we pump the system with equal electron and hole density  $N_e = N_h = 0.35N$ . In the n-doped case, we assume in average one additional electron per QD, i.e.,  $N_e = N_h + N$  with again  $N_h = 0.35N$ . Apart from this difference in the initial conditions both curves are calculated with exactly the same parameters. An excellent agreement between theory and experiment can be observed in Fig. 3.5: (i) the doped QDs show an exponential decay, whereas the undoped ones show a non-exponential decay. (ii) the decay is much faster for the doped QD sample compared to the undoped QD sample.

To understand the origin of this behavior, it is illuminating to study the time evolution

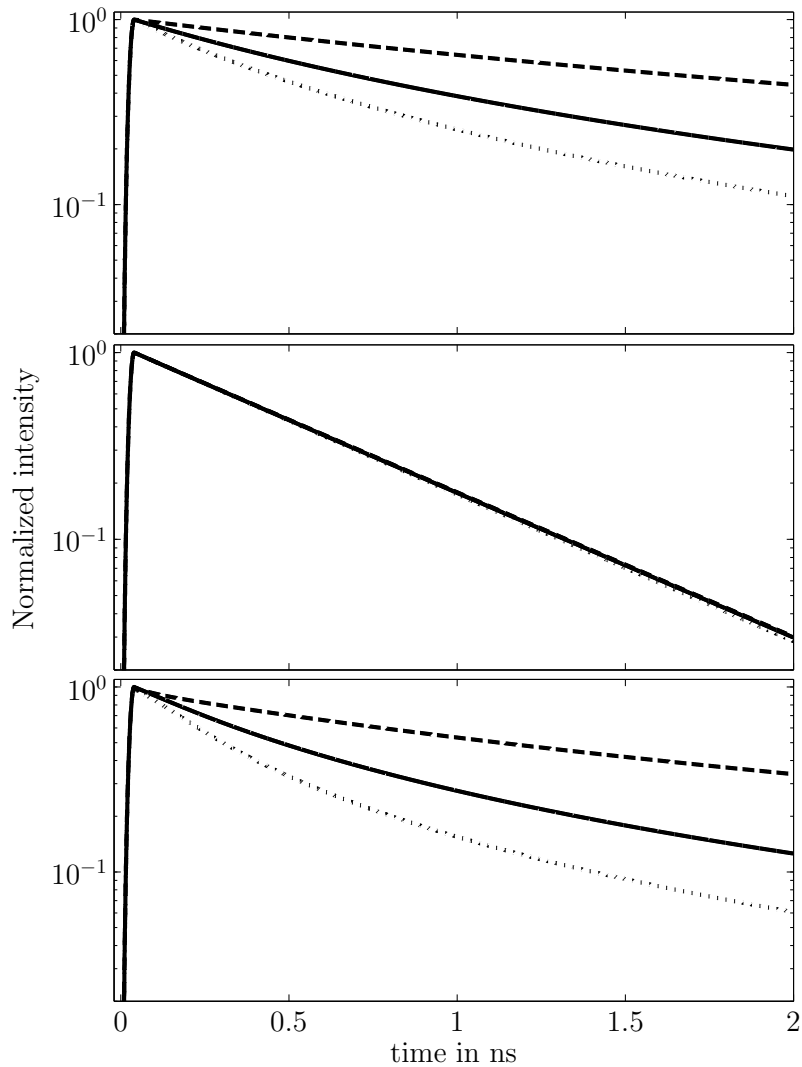


**Figure 3.4:** Time evolution of the photoluminescence calculated on singlet level (top panel), on singlet-doublet level without dephasing (middle), and on singlet-doublet level with small dephasing (bottom) for various initial carrier densities:  $0.6 \cdot 10^{10} \text{ cm}^{-2}$  (dashed line),  $1.5 \cdot 10^{10} \text{ cm}^{-2}$  (solid), and  $2.4 \cdot 10^{10} \text{ cm}^{-2}$  (dotted). For better comparison the curves are normalized.

of the  $s$ -shell populations,  $f_s^c = f^e$  and  $f_s^v = 1 - f^h$ , as depicted in Fig. 3.6 for one spin subsystem. In the undoped case, the  $s$ -shell populations are zero at first. Due to the pump process and the subsequent carrier scattering, the  $s$ -shell population increases temporarily and decays subsequently. In the n-doped case, the electron occupation in the  $s$ -shell starts with the finite value of 0.5 due to the doping. The temporal change of the electron population relative to the doping level is small. According to Eq. (3.38), a constant electron population  $f^e = f_s^c$  leads to an exponential decay of the hole population  $f^h = 1 - f_s^v$  and, hence, of the PL-intensity for the considered situation of strong suppression of excitonic correlations  $C^x$  due to dephasing.

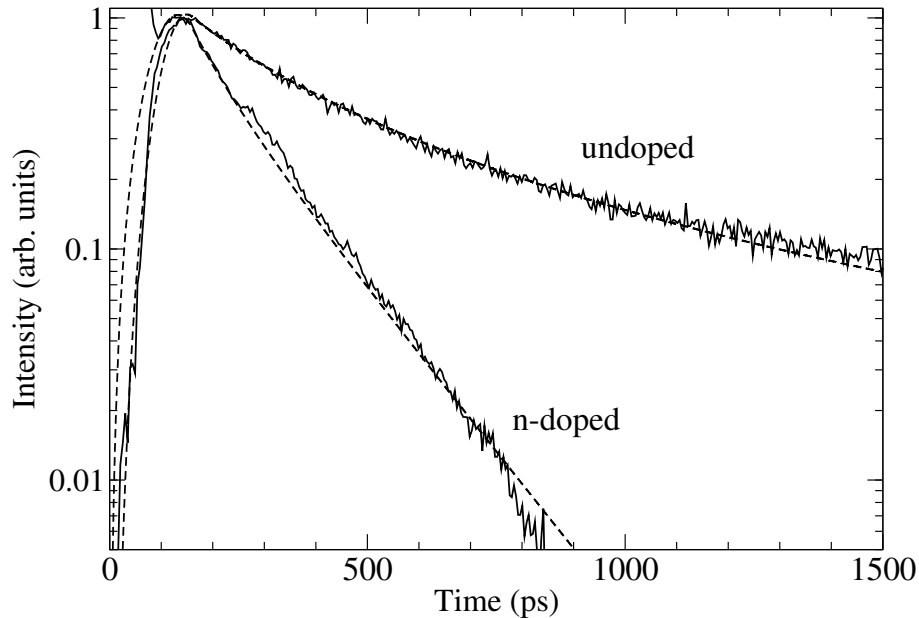


**Figure 3.5:** Calculated time-resolved PL intensity (dashed lines) for pumping into the  $p$ -shell. The solid lines represent experimental data of M. Bayer's group [242].

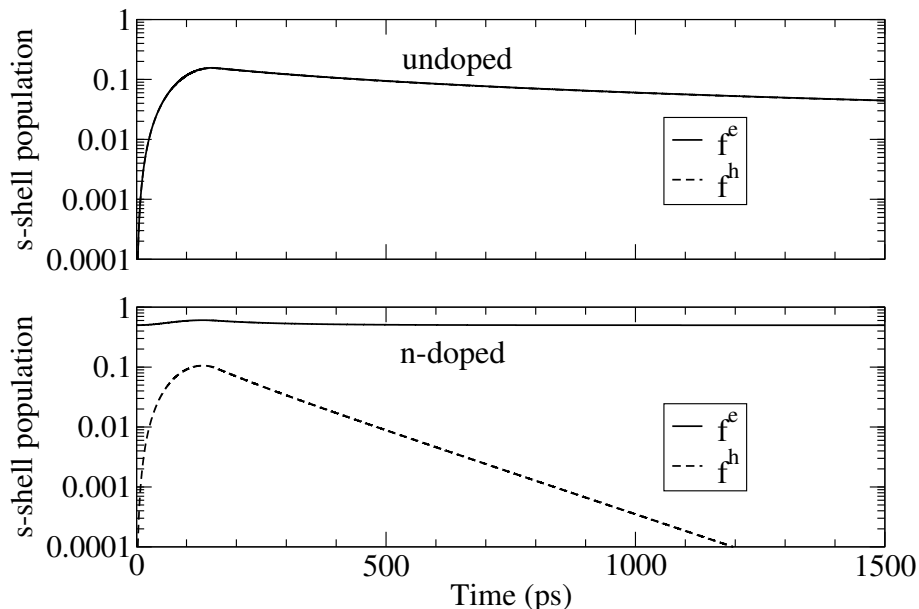


**Figure 3.6:** Time evolution of electron and hole populations in the  $s$ -shell of undoped (top) and n-doped (bottom) QDs.

### 3.2.6 Conclusion

A theory for semiconductor QDs in free space interacting with the quantized light field has been introduced to describe the spontaneous emission properties. The influence of carrier-carrier correlations due to Coulomb as well as carrier-photon interaction has been studied using the cluster-expansion technique on the singlet-doublet level. For the time-

resolved PL, we have discussed two limiting cases of (i) uncorrelated carriers (Hartree-Fock approximation), leading to a nonexponential decay, and (ii) fully-correlated carriers (two-level approximation), resulting in an exponential decay. Our numerical results reveal that correlations of the excited electrons and holes, treated on the singlet-doublet level, lead to an exponential PL decay, provided that dephasing of the correlations can be neglected. This indicates that with a theory where the fundamental quasi-particles are electrons and holes, the presented inclusion of correlations due to Coulomb and carrier-photon interaction allows to recover the limit of strongly correlated carriers, which are typically viewed as excitonic excitations. In turn, it is also shown that weak dephasing of the correlations leads to a clear departure from the exponential decay of the PL signal. This result provides a possible intrinsic explanation for experimental observations of non-exponential PL decay, which is in contrast to extrinsic effects like coupling to dark excitons or inhomogeneous broadening effects.

### 3.3 Time-resolved photoluminescence in microcavities

This section deals with time-resolved PL from semiconductor QDs in microcavities. We present a theory-experiment comparison which has been performed in a joint collaboration with the research groups of M. Bayer and P. Michler [84]. In these experiments the Purcell effect [28] is of particular interest. This effect refers to the modification of the spontaneous-emission time  $\tau$  of a emitter in the presence of a microcavity:

$$\frac{\tau_0}{\tau} = F_P \frac{\Delta\lambda_c^2}{4(\lambda_e - \lambda_c)^2 + \Delta\lambda_c^2} \frac{|\mathbf{E}(\mathbf{r})|^2}{|\mathbf{E}_{\max}|^2} \cos^2 \vartheta + \frac{\tau_0}{\tau_{\text{leak}}}, \quad (3.41)$$

where  $\tau_0$  is the decay time in a spatially homogeneous medium, determined by the Wigner-Weisskopf decay rate [249]. The application of Eq. (3.41) requires that the emitter linewidth  $\Delta\lambda_e$  is much smaller than the cavity linewidth  $\Delta\lambda_c$ . This is well fulfilled for QDs at cryogenic temperatures. The second term in Eq. (3.41) on the right-hand side models the emission into leaky modes. Leaky modes are very short-lived and spectrally broad modes that contribute to a nonresonant background of the optical density of states. The first term in Eq. (3.41) describes the QD emission at wavelength  $\lambda_e$  into a cavity mode at wavelength  $\lambda_c$ . An emitter at location  $\mathbf{r}$  is subject to an electric field  $\mathbf{E}(\mathbf{r})$  whose amplitude varies between the maximum value  $|\mathbf{E}_{\max}|$  and zero.  $\vartheta$  is the angle between the electric-field vector and the dipole moment of the electronic transition. The Purcell factor  $F_P$  gives the modification of the emission decay rate in the ideal coupling scenario

$$F_P = \frac{3\lambda^3}{4\pi^2 n^3} \frac{dQ}{V}, \quad (3.42)$$

with the quality factor  $Q$ , the effective mode volume  $V$ , the refractive index  $n$ , and the mode degeneracy  $d$ .

#### 3.3.1 Experiments

Figure 3.7(a) shows the decay of the time-resolved PL for detection at the energy of the respective fundamental optical mode of micropillars with different diameters. The excitation wavelength is 800 nm, corresponding to nonresonant creation of carriers in the GaAs barriers. The used low excitation power of  $5.5 \text{ W m}^{-2}$  guarantees that the observed PL occurs in the spontaneous emission regime. The faster decay for decreasing pillar diameter is a consequence of the Purcell effect. The reduction of the mode volume  $V$  leads to an increase of the Purcell factor because for the discussed range of diameters the mode volume decreases faster than the  $Q$ -factor. For the decay of the signal over the first order of magnitude, the deviation from an exponential decay is rather weak. However, on a larger time scale the decay clearly reveals a non-exponential character.

Figure 3.7(b) depicts the time-resolved PL of a  $5 \mu\text{m}$  pillar for different excitation power densities. With increasing power, the decay becomes faster. Even for the lowest excitation powers, for which a time-resolved signal could be recorded, no saturated, power-independent decay is found. For the highest excitation powers, rise and initial decay become more and more symmetric with respect to the signal maximum, indicating stimulated emission. Similar behaviors have been observed for pillars with other diameters.

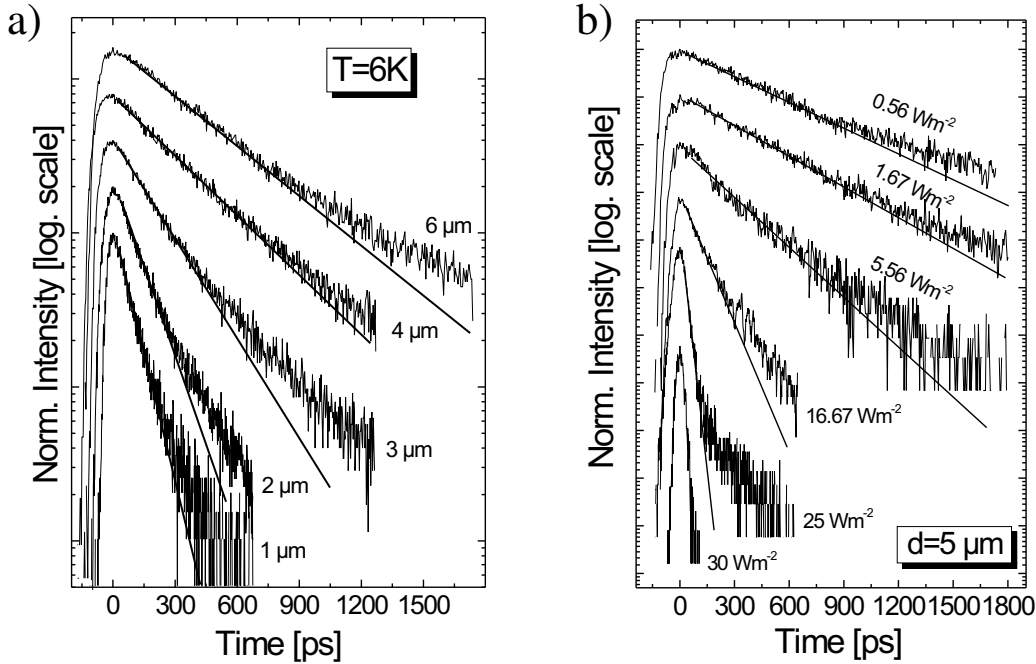


**Figure 3.7:** a) Low excitation time-resolved PL emission for micropillars with different diameters. The excitation power density is  $5.5 \text{ W m}^{-2}$ . The decay times corresponding to the single exponential fits shown by the solid lines are: 400 ps ( $6 \mu\text{m}$ ), 315 ps ( $4 \mu\text{m}$ ), 200 ps ( $3 \mu\text{m}$ ), 110 ps ( $2 \mu\text{m}$ ), and 80 ps ( $1 \mu\text{m}$ ). For clarity, the curves have been shifted vertically relative to each other. b) PL decay curves of a  $5 \mu\text{m}$  cavity at different excitation powers. The decay times corresponding to single exponential fits (solid lines) are: 550 ps ( $0.56 \text{ W m}^{-2}$ ), 475 ps ( $1.67 \text{ W m}^{-2}$ ), 265 ps ( $5.56 \text{ W m}^{-2}$ ), 120 ps ( $16.67 \text{ W m}^{-2}$ ), 30 ps ( $25 \text{ W m}^{-2}$ ), and 20 ps ( $30 \text{ W m}^{-2}$ ). The temperature is  $T = 6 \text{ K}$ . The measurements have been performed by the research groups of M. Bayer and P. Michler [84].

### 3.3.2 QD-microcavity luminescence equations

For the modelling of these experiments it is essential to realize that in high- $Q$  microcavities the reabsorption of photons can modify the results for the time-resolved emission even for weak excitation. Hence, the stimulated emission/absorption term in the photon-assisted polarization can no longer be neglected. In the electron-hole picture the equation of motion of the photon-assisted polarization is given by

$$i\hbar \frac{d}{dt} \langle \hat{b}_\xi^\dagger \hat{h}_\alpha \hat{e}_\alpha \rangle = (\tilde{\epsilon}_\alpha^e + \tilde{\epsilon}_\alpha^h - \hbar\omega_\xi^*) \langle \hat{b}_\xi^\dagger \hat{h}_\alpha \hat{e}_\alpha \rangle - (1 - f_\alpha^e - f_\alpha^h) \sum_\beta V_{\alpha\beta} \langle \hat{b}_\xi^\dagger \hat{h}_\beta \hat{e}_\beta \rangle - (1 - f_\alpha^e - f_\alpha^h) \sum_{\xi'} g_{\xi'\alpha} \langle \hat{b}_\xi^\dagger \hat{b}_{\xi'} \rangle + g_{\xi\alpha} f_\alpha^e f_\alpha^h + \sum_\nu g_{\xi\nu} C_{\nu\alpha\alpha\nu}^x . \quad (3.43)$$

To account for damped cavity modes the cavity loss rates  $\kappa_\xi$  are introduced via complex-valued frequencies  $\omega_\xi$  (and its complex conjugate  $\omega_\xi^*$ ) as discussed in Section 3.1.8. The

stimulated emission/absorption term contains coupling between modes described by  $\langle \hat{b}_\xi^\dagger \hat{b}_{\xi'} \rangle$  with  $\xi \neq \xi'$ . The equation of motion for these quantities is

$$i\hbar \frac{d}{dt} \langle \hat{b}_\xi^\dagger \hat{b}_{\xi'} \rangle = \hbar(\omega_{\xi'} - \omega_\xi^*) \langle \hat{b}_\xi^\dagger \hat{b}_{\xi'} \rangle - \sum_\alpha \left( g_{\xi'\alpha}^* \langle \hat{b}_\xi^\dagger \hat{h}_\alpha \hat{e}_\alpha \rangle - g_{\xi\alpha} \langle \hat{b}_\xi^\dagger \hat{h}_\alpha \hat{e}_\alpha \rangle^* \right). \quad (3.44)$$

To close the system of equations we need the equations for the populations

$$i\hbar \frac{d}{dt} f_\alpha^{(e,h)} \Big|_{\text{opt}} = 2i\text{Re} \sum_\xi g_{\xi\alpha}^* \langle \hat{b}_\xi^\dagger \hat{h}_\alpha \hat{e}_\alpha \rangle. \quad (3.45)$$

On the HF level (corresponding to uncorrelated carriers) the source term of spontaneous emission is given by  $g_{q\alpha} f_\alpha^e f_\alpha^h$ . Correlations due to Coulomb interaction of carriers are included in  $C^x$  and are evaluated on singlet level assuming sufficiently strong dephasing [255].

In order to correctly account for the effects of the size distribution of the QDs (different transition energies), their spatial distribution inside the cavity, and the different dipole orientations (different coupling matrix elements), it is not sufficient to analyze the equations for a single dot with averaged properties. Instead it is necessary to solve the SLE for an entire ensemble of different QDs. For our calculation we take only a fraction of the total number of QDs with a transition frequency close to that of the relevant cavity modes. Therefore, the effective density of QDs interacting with the cavity mode is assumed to be  $3 \cdot 10^9 \text{ cm}^{-2}$ , distributed in an interval of approximately 1.5 meV. The individual QDs are modeled with a harmonic confinement potential in the WL plane and a steplike confinement in growth direction. The strength of the harmonic confinement is varied for different QDs to account for the inhomogeneous broadening typically observed in this material system. We restrict our analysis to QDs with two confined shells for electrons and holes.

The transverse mode-pattern and resonance frequencies  $\omega_q^{\text{res}}$  of the optical modes are calculated using the vectorial transfer-matrix approach as discussed in Section 2.7 and Appendix B. The corresponding quality factors  $Q$  are obtained from the experiment. The complex resonance frequency is then given by  $\omega_q = \omega_q^{\text{res}}(1 + i/Q)$ . While it is sufficient to include only one resonant mode for the smaller pillar, the larger pillars have several modes within the spectral region of the QD emitters. These modes have to be taken into account. The coupling between different modes is neglected,  $\langle \hat{b}_q^\dagger \hat{b}_{q'} \rangle \approx \delta_{qq'} \langle \hat{b}_q^\dagger \hat{b}_q \rangle$ , since they are spectrally well separated. Besides the resonant modes, which are characterized by their large  $Q$ -values and pronounced peak structure in a transmission spectrum, there exists a background contribution formed by the continuum of leaky modes. In order to include their influence, we assume that the background contribution consists of a fraction of the continuum of modes of the homogenous space. The size of this fraction can be estimated by counting the plane waves that (i) either reach the sidewalls of the micropillar in an angle smaller than the critical angle of total internal reflection, or (ii) have a momentum component  $k_{||}$  along the pillar axis that lies outside the stopband of the DBR and can therefore immediately escape from the cavity.

### 3.3.3 Numerical results

In Fig. 3.8 we show the number of photons in the fundamental mode leaving the cavity per unit time. Different initial carrier densities are used to model the variation of the excitation power in the experiment. The non-exponential decay of the signal is clearly evident. Furthermore, the rapidness of the decay strongly depends on the initial carrier density, which corresponds to different pump intensities in the experiment. This shows that it is not meaningful to introduce a decay time that depends only on the optical density of states without including the influence of the carrier system. Instead, a thorough analysis of time-resolved PL signals has to take both the carrier system and the photonic system into account.

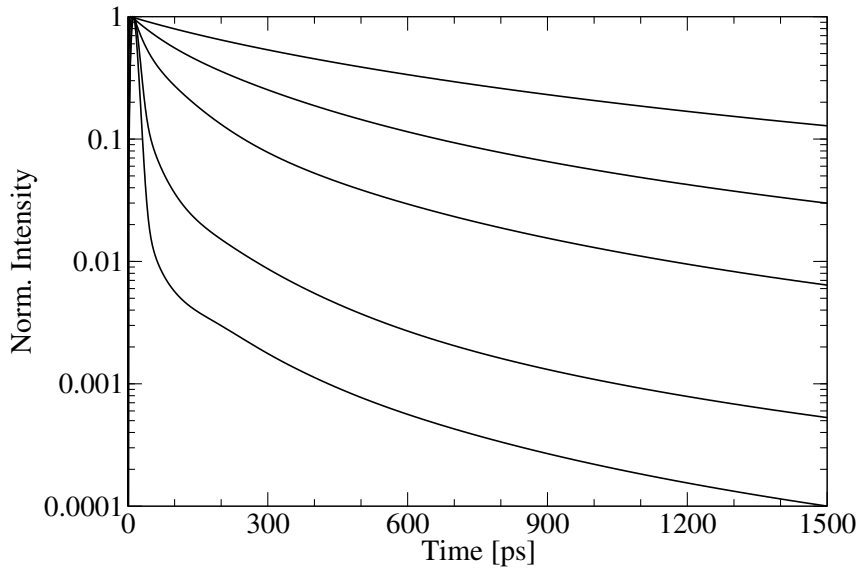


**Figure 3.8:** Calculated photoluminescence for an ensemble of QDs in a  $6\text{ }\mu\text{m}$  diameter pillar microcavity with initial carrier densities from  $1 \cdot 10^9 \text{ cm}^{-2}$  to  $5 \cdot 10^9 \text{ cm}^{-2}$  in equidistant steps from top to bottom. For better comparison the results are normalized.

The calculated PL for fixed initial carrier density but different diameters of the micropillar cavity is displayed in Fig. 3.9. The smaller pillars show a faster decay in connection with a larger Purcell factor, as is discussed above. The different heights of the curves can mainly be attributed to the fact that in larger pillars more carriers take part in the recombination dynamics.

Frequently it is argued, that the non-exponential decay observed in PL measurements stems from a superposition of many exponential PL signals of various emitters with different cavity positions. The role of an inhomogeneous distribution of QDs is analyzed in Fig. 3.10. The solid line represents the calculated decay of the time-resolved PL from an ensemble of QDs with various cavity positions and fluctuations of the transition energies and dipole moments. For comparison, the dotted line shows the result for identical QDs with averaged values for mode-strength, cavity field, transition energy, and dipole coupling. While the decay remains non-exponential, the decay rate is strongly underestimated. If identical QDs with maximum values for mode-strength, cavity field, and dipole

coupling as well as resonant transition energies are assumed (dashed line), the decay rate is slightly enhanced with practically the same shape as for the inhomogeneous QD distribution. The result shows that the QDs with efficient coupling to the cavity field dominate the emission properties. The non-exponential character of the decay is only weakly determined by inhomogeneous distribution effects. However, the variation of the decay with excitation density is to some extent influenced by the inhomogeneous broadening.

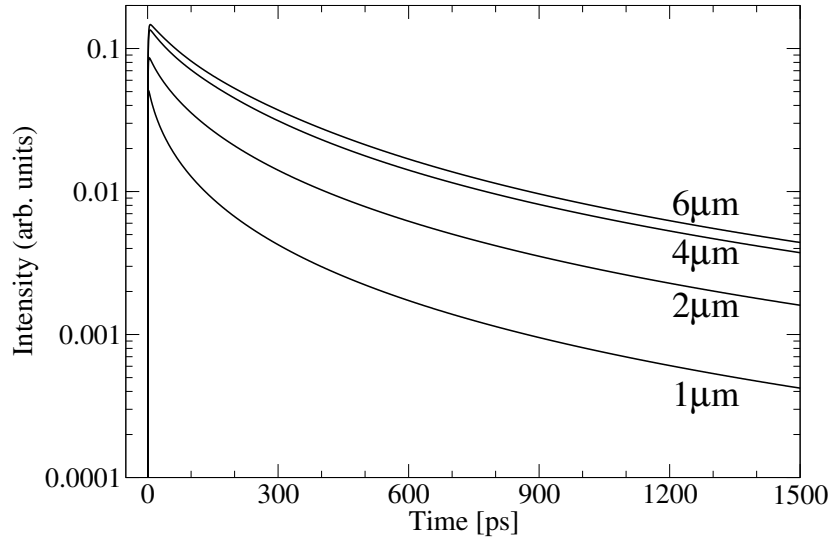


**Figure 3.9:** Calculated photoluminescence of QDs in a pillar microcavity with various diameters for an initial carrier density of  $2 \cdot 10^9 \text{ cm}^{-2}$ .

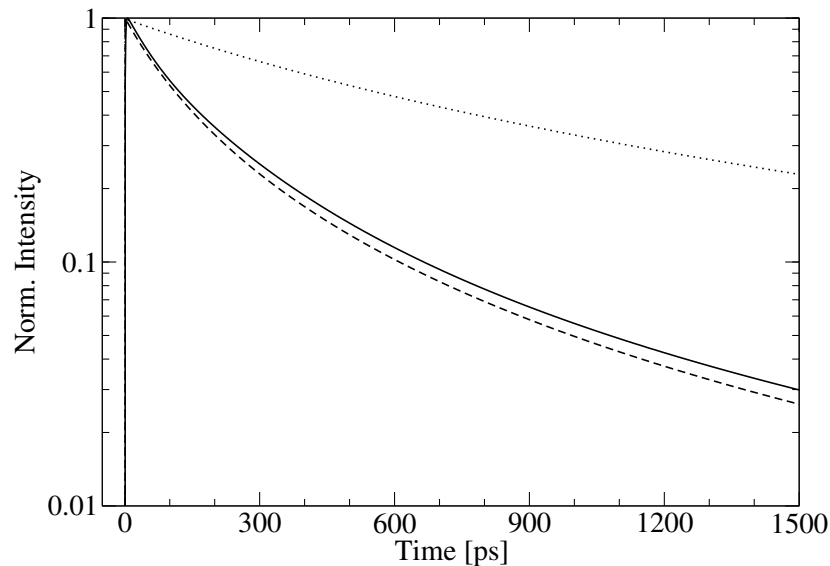


**Figure 3.10:** Calculated photoluminescence of an ensemble of QDs with inhomogeneous broadening (solid line), for identical QDs with maximum coupling strength and on-resonance transitions (dashed line), and for identical QDs with averaged coupling strength (dotted). The pillar diameter is  $6 \mu\text{m}$  and the initial carrier density is  $2 \cdot 10^9 \text{ cm}^{-2}$ .

### 3.3.4 Conclusion

We extended the microscopic description of QD emission to include the effects of the presence of a microcavity. The numerical results explain recent experiments on (In,Ga)As/GaAs QDs in GaAs-based pillar microcavities. The altered spontaneous emission due to the cavity is found to be accompanied by a non-exponential decay of the time-resolved photoluminescence where the decay rate strongly depends on the excitation intensity.

## 3.4 Quantum dot-based microcavity lasers

In the previous section, we have discussed spontaneous emission from QDs ensembles embedded in high- $Q$  microcavities. In this section, we study stimulated emission, i.e., lasing from such QD-microcavity systems. QD-microcavity lasers have been realized recently with microdisks [283–285], micropillars [39, 286], and photonic crystals [38, 233].

Quantum dots as gain material have in principle several advantages [1, 8], such as enhanced spectral purity, a small linewidth enhancement factor, high temperature stability, and ultralow threshold-current densities. The usage of microcavity resonators instead of conventional resonators offers additional advantages. First, the well separated resonance frequencies allow for the existence of a single high- $Q$  cavity mode within the gain spectrum of the QD ensemble. This leads to the possibility of genuine single-mode laser operation. Second, a high spontaneous emission factor can be achieved. In the case of single-mode operation, this factor is defined as

$$\beta = \frac{\text{spontaneous emission rate into the lasing mode}}{\text{spontaneous emission rate into all modes}}. \quad (3.46)$$

Conventional semiconductor lasers exhibit only very small  $\beta$ -factors, i.e., the vast majority of spontaneous emission is lost for the lasing action [40]. This results in a pronounced threshold in the input-output characteristic of the laser. Figure 3.11 illustrates this behavior using an atomic rate equation model for single-mode lasing [42, 44]. Such models predict that both the threshold pump rate and the height of the “jump” scales with a factor of  $1/\beta$ . The latter fact is often exploited for extracting the  $\beta$ -factor from experimental data.

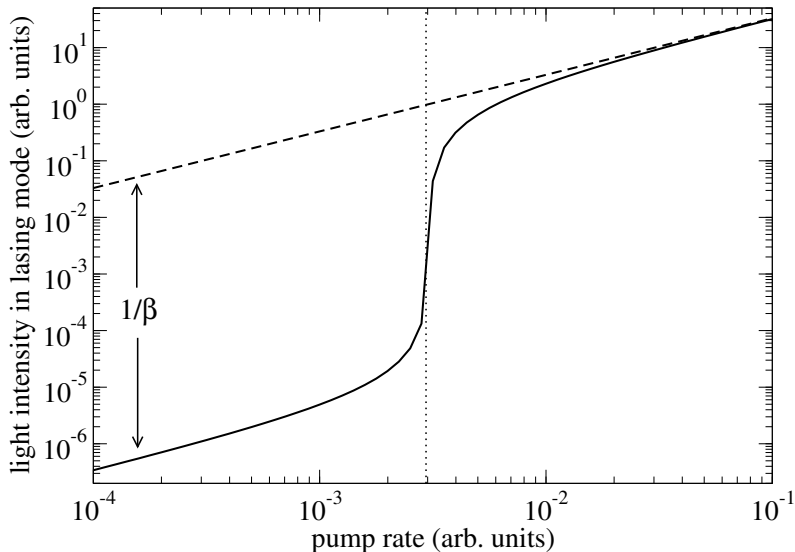


**Figure 3.11:** Double-logarithmic plot of the input-output curve (solid line) of a conventional atomic single-mode laser with  $\beta = 10^{-5}$ . The dashed line is a guide to the eye from which can be seen that the height of the “jump” from the lower to the upper branch is given by the factor  $1/\beta$ . The dotted line marks the threshold pump rate.

In order to reduce the threshold pump rate a large  $\beta$ -factor is desirable. Microcavities and QDs offer the possibility of a  $\beta$ -factor close to unity because of two effects. (i) Nonlasing high- $Q$  modes can be spectrally well separated from the spectral gain maximum of the QD ensemble. This suppresses the spontaneous emission into these modes. However, there is in general still a considerable amount of spontaneous emission into leaky modes, that are very low- $Q$  modes forming a nonresonant background in the optical density of states. (ii) For resonant QDs the Purcell effect, see Eqs. (3.41) and (3.42), can selectively enhance the spontaneous emission rate into the laser mode. In this way, one can in principle reach the limit  $\beta \rightarrow 1$  where all spontaneous emission goes into the lasing mode. In this case, the threshold in the input-output curve vanishes. Such a device is referred to as a “thresholdless laser” [41–44].

Even for a “thresholdless laser” one expects to have a transition from a region of spontaneous to a region of dominating stimulated emission. This transition can be revealed by investigating the photon statistics of the emitted light [44]. A convenient probe of the photon statistics is given by the intensity autocorrelation function (second-order coherence) at zero delay time [249, 287],

$$g^{(2)}(\tau = 0) = \frac{\langle n^2 \rangle - \langle n \rangle}{\langle n \rangle^2}, \quad (3.47)$$

where  $n$  is the photon number operator for the laser mode. This quantity can be measured, e.g., in a Hanbury-Brown and Twiss coincidence measurement setup [45]. The quantity  $g^{(2)}(0)$  allows to distinguish whether the light originates from a thermal source or a coherent source, or from a quantum source like a single atom or QD. A single atom can emit only one photon at a time. The probability of photon-pair emission is therefore strongly suppressed. The intensity correlation of such an “antibunched” stream of photons has  $g^{(2)}(0) = 0$ . This kind of light source is called a single-photon source [37]. A thermal light source, like a light bulb or a laser below threshold, shows “bunching” of photons with  $g^{(2)}(0) = 2$ . Here, the probability of photon-pair emission is enhanced. Finally, the photon statistics of a coherent light source, e.g., a laser above threshold, obeys the Poisson statistics with  $g^{(2)}(0) = 1$ . Hence, the transition from dominating spontaneous to dominating stimulation emission in a laser is accompanied by a transition from thermal light with  $g^{(2)}(0) = 2$  to coherent light with  $g^{(2)}(0) = 1$ .

In the literature, semiconductor QD-based laser devices are modeled almost without exception by considering atomic two- or multi-level systems, resulting either in a set of rate equations [42, 43], or a master equation for the reduced density matrix [44, 288, 289]. To describe the statistical properties of the light emission from the microcavity, such as the intensity correlation (3.47), the latter approach has been used. Alternatively, for two-level systems, the quantum regression theorem can be applied [249].

On the basis of underlying atomic models, it is, however, not possible to consider intrinsic semiconductor effects, such as a modified source term of spontaneous emission and Coulomb effects as discussed in the previous sections. Also, unlike conventional four-level gas lasers, QD-based microcavity lasers usually do not operate at full inversion, which leads to considerable differences in the input-output curve of these devices. Especially if characteristic values are derived from measured data, such as the  $\beta$ -factor, one must be

aware of the differences between an atomic and a semiconductor laser model. Therefore a semiconductor theory is desirable if QD-based devices are studied. A general semiconductor laser model based on a microscopic Hamiltonian has been previously used to study the influence of the carrier dynamics and many-body effects [47, 48], lasing without inversion [290], and noise spectra [291], but did not include correlations required to determine the photon statistics.

In this section, we introduce a microscopic theory to calculate both the light output and the intensity correlation of microcavity lasers with QDs as the active material [292]. Our semiconductor approach naturally includes a modified source term of spontaneous emission, Pauli-blocking effects of the occupied states, as well as many-body Coulomb effects.

The section is structured as follows: In Section 3.4.1 we show how the equations of motion follow from the Hamiltonian for the coupled carrier-photon system. In Section 3.4.2 the laser equations are derived and the atomic rate equation limit is discussed. Section 3.4.3 is concerned with higher order correlations needed to obtain the photon statistics in terms of the intensity correlation. A direct comparison of a reduced two-level version of our equations to the master equation is used in Section 3.4.4 to verify the validity of our approach. Results from the coupled equations for laser dynamics and photon correlations are presented in Section 3.4.5. Finally, a comparison to recent experiments is given.

### 3.4.1 Theoretical Model

As in Section 3.2 we start from the semiconductor Hamiltonian (3.8) for the interacting carrier-photon system, and derive coupled equations of motion for the relevant expectation values. The extensions of the SLE are twofold. By discriminating between the emission channels into the laser mode and the non-lasing modes and by explicitly considering the pump process, a semiconductor laser theory can be formulated, which contains the familiar rate equations for atomic systems as a limiting case. Furthermore, the hierarchy of coupled equations is extended to photon correlations in order to access the photon statistics of the light emission. In this context it is important to consider the correct terms for the spontaneous and stimulated emission in order to relate the  $\beta$ -factor to the threshold properties and especially to the height of the “jump” in the input-output curve. The correct source term already appears on the doublet level and is, therefore, part of a laser theory obtained from extending the SLE.

An important motivation for our work is the observation that for large  $\beta$  values typical for state-of-the-art microcavity systems the “jump” in the input-output curve broadens and cannot be used for a clear identification of the onset of coherent light emission. The statistical properties of the light emission can be described in terms of the autocorrelation function at zero delay time in Eq. (3.47). The photon number operator for the laser mode  $\xi_l$  can be written as  $n = b_{\xi_l}^\dagger b_{\xi_l} = b^\dagger b$ . By means of Eq. (3.17d), we can introduce  $\delta\langle b^\dagger b^\dagger b b \rangle = \langle b^\dagger b^\dagger b b \rangle - 2\langle b^\dagger b \rangle^2$ . Since  $\langle b \rangle = \langle b^\dagger \rangle = 0$  for a system without coherent excitation, only a factorization into doublets is possible. The factor of 2 arises from the two realizations for this factorization. Then the autocorrelation function can be written in terms of a

quadruplet correlation function:

$$g^{(2)}(\tau = 0) = 2 + \frac{\delta \langle b^\dagger b^\dagger b b \rangle}{\langle b^\dagger b \rangle^2}. \quad (3.48)$$

For the dynamical evolution of the photon number  $\langle b_\xi^\dagger b_\xi \rangle$  in the lasing and non-lasing modes  $\xi$  and the carrier populations  $f_\nu^e = \langle c_\nu^\dagger c_\nu \rangle$ ,  $f_\nu^h = 1 - \langle v_\nu^\dagger v_\nu \rangle$ , the contribution of the light matter interaction  $H_D$  in the Heisenberg equations of motion leads to

$$\left( \hbar \frac{d}{dt} + 2\kappa_\xi \right) \langle b_\xi^\dagger b_\xi \rangle = 2 \operatorname{Re} \sum_{\nu'} |g_{\xi\nu'}|^2 \langle b_\xi^\dagger v_{\nu'}^\dagger c_{\nu'} \rangle, \quad (3.49)$$

$$\hbar \frac{d}{dt} f_\nu^{e,h} \Big|_{\text{opt}} = -2 \operatorname{Re} \sum_{\xi} |g_{\xi\nu}|^2 \langle b_\xi^\dagger v_\nu^\dagger c_\nu \rangle. \quad (3.50)$$

Note that we have scaled  $\langle b_\xi^\dagger v_\nu^\dagger c_\nu \rangle \rightarrow g_{\xi\nu} \langle b_\xi^\dagger v_\nu^\dagger c_\nu \rangle$  to have the modulus of the coupling matrix elements appear. In Eq. (3.49) we have introduced the cavity loss rate  $2\kappa_\xi$  according to Section 3.1.8. For the laser mode, this is directly connected to the  $Q$ -factor of the fundamental cavity mode,  $Q = \hbar\omega/2\kappa$ . The dynamics of the photon number in a given mode is determined by the photon-assisted polarization  $\langle b_\xi^\dagger v_\nu^\dagger c_\nu \rangle$ . The sum over  $\nu'$  involves all possible interband transitions from various QDs. The dynamics of the carrier population in Eq. (3.50) is governed by contributions of photon-assisted polarizations from all possible modes  $\xi$ .

The dynamical equation for the photon-assisted polarization is given by

$$\begin{aligned} \left( \hbar \frac{d}{dt} + \kappa_\xi + \Gamma + i(\tilde{\varepsilon}_\nu^e + \tilde{\varepsilon}_\nu^h - \hbar\omega_\xi) \right) \langle b_\xi^\dagger v_\nu^\dagger c_\nu \rangle &= f_\nu^e f_\nu^h - (1 - f_\nu^e - f_\nu^h) \langle b_\xi^\dagger b_\xi \rangle \\ &\quad + i(1 - f_\nu^e - f_\nu^h) \sum_{\alpha} V_{\nu\alpha\nu\alpha} \langle b_\xi^\dagger v_\alpha^\dagger c_\alpha \rangle + \frac{1}{g_{\xi\nu}} \sum_{\alpha} g_{\xi\alpha} C_{\alpha\nu\nu\alpha}^x \\ &\quad + \delta \langle b_\xi^\dagger b_\xi c_\nu^\dagger c_\nu \rangle - \delta \langle b_\xi^\dagger b_\xi v_\nu^\dagger v_\nu \rangle. \end{aligned} \quad (3.51)$$

The free evolution of  $\langle b_\xi^\dagger v_\nu^\dagger c_\nu \rangle$  is determined by the detuning of the QD transitions from the cavity resonances and loss rates. In a semiconductor, the source term of spontaneous emission is described by an expectation value of four carrier operators  $\langle c_\alpha^\dagger v_\alpha v_\nu^\dagger c_\nu \rangle$ , see Section 3.2. For uncorrelated carriers, the Hartree-Fock factorization of this source term leads to  $f_\nu^e f_\nu^h$ , which appears as the first term on the right-hand side of Eq. (3.51). Corrections to this factorization are provided by the Coulomb and light-matter interaction between the carriers and are included in  $C_{\alpha\nu\nu\alpha}^x = \delta \langle c_\alpha^\dagger v_\nu^\dagger c_\nu v_\alpha \rangle$ .

A restriction of the source term of spontaneous emission to the factorization approximation is justified in certain situations, such as the laser applications considered here: High carrier densities efficiently screen the Coulomb interaction between the carriers and lead to strong dephasing that directly suppresses correlations [257]. Moreover, the feedback of the laser cavity can support strong carrier-photon correlations that dominate over carrier-carrier correlations. The calculation of carrier-correlation contributions  $C^x$  to the source

term of spontaneous emission is a central issue of Section 3.2, and a discussion about the sensitivity of  $C^x$  to dephasing can be found there. Note that in atomic systems, the spontaneous emission is always linear in the excited-state population. This difference to semiconductor systems is the origin of interesting new effects in QDs, which are unknown in atomic systems [84].

The stimulated emission/absorption term in Eq. (3.51), which is proportional to the photon number  $\langle b_\xi^\dagger b_\xi \rangle$  in the mode  $\xi$ , provides feedback due to the photon population in the cavity. Hartree-Fock (singlet) contributions of the Coulomb interaction lead to the appearance of renormalized energies  $\tilde{\varepsilon}$  and to the interband exchange contribution in Eq. (3.51) that couples the photon-assisted polarizations from different states  $\alpha$ . The last two terms in Eq. (3.51) are carrier-photon correlations that are discussed in Section 3.4.3. Carrier-carrier and carrier-phonon interaction lead to dephasing, which corresponds to a damping of the photon-assisted transition amplitude. This dephasing is here included via a phenomenological damping constant  $\Gamma$ .

### 3.4.2 Laser equations

To formulate the laser theory for QDs in optical microcavities, we have to specify the electronic structure of the system as well as the mode structure of the resonator. As in Section 3.2, we consider QDs with two confined shells, referred to as  $s$ - and  $p$ -shell, which appear energetically below a continuum of delocalized wetting layer (WL) states. The QDs are embedded in a microcavity, which provides one (potentially degenerate) fundamental mode with a large  $Q$ -factor that is in resonance with the QD  $s$ -shell emission. Higher cavity modes are assumed to be energetically well-separated from the fundamental mode, and a continuum of leaky modes is used to define the spontaneous emission coupling  $\beta$ , i. e. only a fraction of the spontaneous emission at the laser transition energy involves the laser mode.

In the following scheme, several assumptions are included, which lead to a convenient formulation of the theory. These assumptions are well justified by the experimental conditions that we consider in this section. They provide no principle limitations and can be circumvented at the cost of more complicated analytical and numerical formulations. (i) We assume that optical processes involving the laser mode (stimulated and spontaneous emission as well as photon reabsorption) are exclusively connected to the  $s$ -shell transitions. In this case, higher shells and WL states contribute only to the carrier dynamics. (ii) Ultrafast carrier scattering processes in QDs have been predicted in recent studies of carrier-carrier [268] and carrier-phonon [269] interaction. Thus, we assume that the carrier system is close to equilibrium, so that scattering processes can be described in relaxation-time approximation [268]. (iii) To include the simplest possible pump process, we consider carrier generation in the  $p$ -shell at a given rate  $P$ . This can be traced back either to resonant optical pumping in connection with rapid dephasing, or to carrier injection into the delocalized WL or bulk states and fast successive carrier capture and relaxation processes. (iv) For the non-lasing modes, stimulated emission and reabsorption of photons is neglected, which corresponds to a situation where photons spontaneously emitted into non-lasing modes rapidly leave the cavity. In the case of strong dephas-

ing (provided by efficient carrier scattering) it is then possible to analytically solve the equation for the corresponding photon-assisted polarization and to introduce a rate of spontaneous emission into the non-lasing modes. (v) It has been shown in Section 3.3 that the major emission into the fundamental mode is due to resonant QDs, whereas slightly detuned dots hardly contribute. Therefore, in the following, we can consider to a good approximation only those emitters in resonance with the fundamental mode, rather than using an inhomogeneously broadened sample of QDs. Under the assumption of identical resonant dots, the occurring energy differences with the laser mode,  $\tilde{\varepsilon}_\nu^e + \tilde{\varepsilon}_\nu^h - \hbar\omega_{\xi_l}$ , drop out in the equations of motion.

So far we have derived the fundamental equations for the carrier and photon dynamics. In order to describe a pumped laser system, we must incorporate carrier generation and the  $\beta$ -factor into the theory, as well as deal with the correlations appearing in Eq. (3.51).

Regarding the treatment of many-body Coulomb effects, one can distinguish between two limiting cases. In the high-carrier density and high-temperature regime, the WL states accommodate a substantial carrier density that screens the Coulomb interaction between the QD carriers. At the same time, the Coulomb interaction between QD and WL carriers leads to broadening and energy shifts of the QD transitions. Calculations of QD gain spectra in this regime are the subject of Ref. [293]. Relaxation oscillations in this regime are calculated in Ref. [294]. In the low-temperature regime that was recently studied in several experiments [39, 84], the population of the WL states is expected to be marginal. The remaining Coulomb interaction between the QD carriers leads to intra- and interband interaction effects and will be summarized in an effective transition energy and oscillator strength for the coupling to the laser mode. Since dominantly QDs with transitions in resonance with the high- $Q$  laser mode contribute to the emission, possible line shifts are not explicitly included subsequently. The main focus of this section is on carrier-photon and photon-photon correlations in QD lasers. Assuming sufficiently strong dephasing, the carrier-carrier Coulomb correlations  $C^x$  are not included in the calculation.

Under the discussed conditions, the equation of motion for the photon-assisted polarization of the laser mode takes the form

$$\left( \hbar \frac{d}{dt} + \kappa + \Gamma \right) \langle b^\dagger v_s^\dagger c_s \rangle = f_s^e f_s^h - (1 - f_s^e - f_s^h) \langle b^\dagger b \rangle + \delta \langle b^\dagger b c_s^\dagger c_s \rangle - \delta \langle b^\dagger b v_s^\dagger v_s \rangle , \quad (3.52)$$

where, from now on, the index is omitted for the laser mode,  $\xi = \xi_l$ . In the equation of motion for the photon-assisted polarization of the non-lasing modes, the negligible photon population allows the omission of the feedback term and carrier-photon correlations,

$$\left( \hbar \frac{d}{dt} + \kappa_\xi + \Gamma + i(\tilde{\varepsilon}_s^e + \tilde{\varepsilon}_s^h - \hbar\omega_\xi) \right) \langle b_\xi^\dagger v_s^\dagger c_s \rangle \Big|_{\xi \neq \xi_l} = f_\nu^e f_\nu^h . \quad (3.53)$$

As a result, Eq. (3.53) can be solved in the adiabatic limit and the part  $\xi \neq \xi_l$  of the sum in Eq. (3.50) can be evaluated, yielding a time constant  $\tau_{nl}$  for the spontaneous emission into non-lasing modes according to the Weisskopf-Wigner theory [249],

$$\frac{2}{\hbar} \operatorname{Re} \sum_{\xi \neq \xi_l} \frac{|g_{\xi s}|^2}{\kappa_\xi + \Gamma + i(\tilde{\varepsilon}_s^e + \tilde{\varepsilon}_s^h - \hbar\omega_\xi)} = \frac{1}{\tau_{nl}} . \quad (3.54)$$

In a laser theory, one typically distinguishes between the rate of spontaneous emission into lasing and non-lasing modes,  $1/\tau_l$  and  $1/\tau_{nl}$ , respectively. Both rates add up to the total spontaneous emission rate  $1/\tau_{sp}$ . Then the spontaneous emission factor is given by

$$\beta = \frac{\frac{1}{\tau_l}}{\frac{1}{\tau_{sp}}} = \frac{\frac{1}{\tau_l}}{\frac{1}{\tau_l} + \frac{1}{\tau_{nl}}} \quad (3.55)$$

and the rate of spontaneous emission into non-lasing modes can be expressed according to

$$\frac{1}{\tau_{nl}} = \frac{1 - \beta}{\tau_{sp}}. \quad (3.56)$$

For a further discussion of the time constants, see Appendix E.

From Eq. (3.50) one can now determine the population dynamics in the  $s$ -shell. For the spontaneous emission into non-lasing modes, the adiabatic solution of Eq. (3.53) is used according to Eqs. (3.54) and (3.56). Furthermore, we introduce a transition rate of carriers from the  $p$ - to the  $s$ -shell in relaxation-time approximation,  $R_{p \rightarrow s}^{e,h} = (1 - f_s^{e,h}) f_p^{e,h} / \tau_r^{e,h}$ , and  $g \equiv g_{\xi_l,s}$  to obtain

$$\frac{d}{dt} f_s^{e,h} = -2 |g|^2 \operatorname{Re} \langle b^\dagger v_s^\dagger c_s \rangle - (1 - \beta) \frac{f_s^e f_s^h}{\tau_{sp}} + R_{p \rightarrow s}^{e,h}. \quad (3.57)$$

Here the first term describes the carrier dynamics due to the interaction with the laser mode, while the second term represents the loss of carriers via recombination into non-lasing modes. The blocking factor  $1 - f_s^{e,h}$  in  $R_{p \rightarrow s}^{e,h}$  ensures that the populations cannot exceed unity.

The carrier dynamics for the  $p$ -shell can be written as

$$\frac{d}{dt} f_p^{e,h} = P (1 - f_p^e - f_p^h) - \frac{f_p^e f_p^h}{\tau_{sp}^p} - R_{p \rightarrow s}^{e,h}, \quad (3.58)$$

where a carrier generation rate  $P$  due to pumping is included together with the Pauli-blocking factor  $(1 - f_p^e - f_p^h)$ . The second term describes spontaneous recombination of  $p$ -shell carriers and the third contribution is the above-discussed carrier relaxation.

The resulting set of equations (3.57) and (3.58), together with Eqs. (3.49) and (3.52) now allows for the calculation of the coupled dynamics for the photon number and the carrier population. It turns out that the new carrier-photon correlations do not change the results for the input-output characteristics that is shown below in Fig. 3.14. Neglecting the carrier-photon correlations in Eq. (3.52), the resulting set of equations corresponds to a truncation of the hierarchy on doublet level. Note, however, that the inclusion of these correlations in Eq. (3.52) is of critical importance if  $\langle b^\dagger v_\nu^\dagger c_\nu \rangle$  is used for the calculation of the intensity correlation  $g^{(2)}(0)$ , cf. Section 3.4.3.

In the following, we show how the frequently used atomic rate equation model [42, 44] can be obtained from the above developed semiconductor theory as a limiting case. (i) The semiconductor specific source term of spontaneous emission  $f_\nu^e f_\nu^h$  in Eqs. (3.52), (3.57) and (3.58) is replaced by the electron population  $f_e^e$ . This happens because successive

destruction of more than one carrier always yields zero in the case of a two-level system, where only one electron is present per independent emitter, in which case we use  $c_\nu v_\nu = 0$ . Then the source of spontaneous emission  $\langle c_\alpha^\dagger v_\alpha v_\nu^\dagger c_\nu \rangle$  arising in Eq. (3.51) reduces to  $\langle c_\alpha^\dagger c_\alpha \rangle = f_\alpha^e$ . (ii) Full inversion of the laser transition is assumed,  $1 - f_s^h = \langle v_s^\dagger v_s \rangle = 0$ , which is usually well-justified for atomic four-level laser systems (but not for QDs). (iii) The adiabatic solution of Eq. (3.52) is inserted into Eq. (3.49). Introducing the number of excited emitters  $\bar{N} = f_s^e N$ , where  $N$  is the total number of emitters that arises from the sum over all states in Eq. (3.49), we find

$$\frac{d}{dt} \langle b^\dagger b \rangle = -2\kappa \langle b^\dagger b \rangle + \frac{\beta}{\tau_{sp}} (1 + \langle b^\dagger b \rangle) \bar{N}. \quad (3.59)$$

The photon population is determined by the interplay of the cavity losses  $2\kappa$  and the photon generation due to spontaneous processes  $\propto \bar{N}$  and stimulated processes  $\propto \langle b^\dagger b \rangle \bar{N}$ . For the number of excited emitters we obtain

$$\frac{d}{dt} \bar{N} = -\frac{\beta}{\tau_{sp}} \langle b^\dagger b \rangle \bar{N} - \frac{1}{\tau_{sp}} \bar{N} + P, \quad (3.60)$$

where, for atomic laser systems quite common, a constant pumping  $NR_{p \rightarrow s}^{e,h} = P$  has been used. The carrier recombination is determined by the stimulated emission into the laser mode  $\propto \beta/\tau_{sp} = 1/\tau_l$ , and by the spontaneous emission  $\propto 1/\tau_{sp}$  into all available modes. For a direct comparison with the semiconductor model, results of the rate equations (3.59) and (3.60) for the input-output curves and various values of the  $\beta$ -factor are shown in Fig. 3.12. We use a typical set of parameters:  $\tau_{sp} = 50$  ps (spontaneous emission of QDs enhanced by the Purcell effect),  $N = \tilde{N}/\beta$  with  $\tilde{N} = 20$  (the number of emitters is increased with decreasing  $\beta$  in order to have the thresholds occur at the same pump rate), and  $\kappa = 20 \mu\text{eV}$ . The corresponding cavity lifetime is about 17 ps, yielding a  $Q$ -factor of roughly 30 000. The curves show the typical intensity jump  $\propto \beta^{-1}$  from below to above threshold. In the limit  $\beta = 1$ , the kink in the input-output curve disappears.

### 3.4.3 Photon statistics

Now we turn to the extended set of laser equations including carrier-photon and photon-photon correlation functions. To access intensity correlations, we must calculate the correlation function in Eq. (3.48), which is a quadruplet contribution. This implies that the treatment within the cluster expansion has to be extended to the quadruplet level. Only photons from the laser mode are assumed to build up correlations, and because we consider only QDs in resonance with the cavity, the free evolution energy terms drop out and are therefore not explicitly given in the following.

The time evolution of the intensity correlation function is given by

$$\left( \hbar \frac{d}{dt} + 4\kappa \right) \delta \langle b^\dagger b^\dagger b b \rangle = 4 |g|^2 \sum_{\nu'} \delta \langle b^\dagger b^\dagger b v_\nu^\dagger c_{\nu'} \rangle, \quad (3.61)$$

where the sum effectively runs over the resonant  $s$ -shell transitions of all QDs. In this equation another quadruplet function enters, which represents a correlation between the

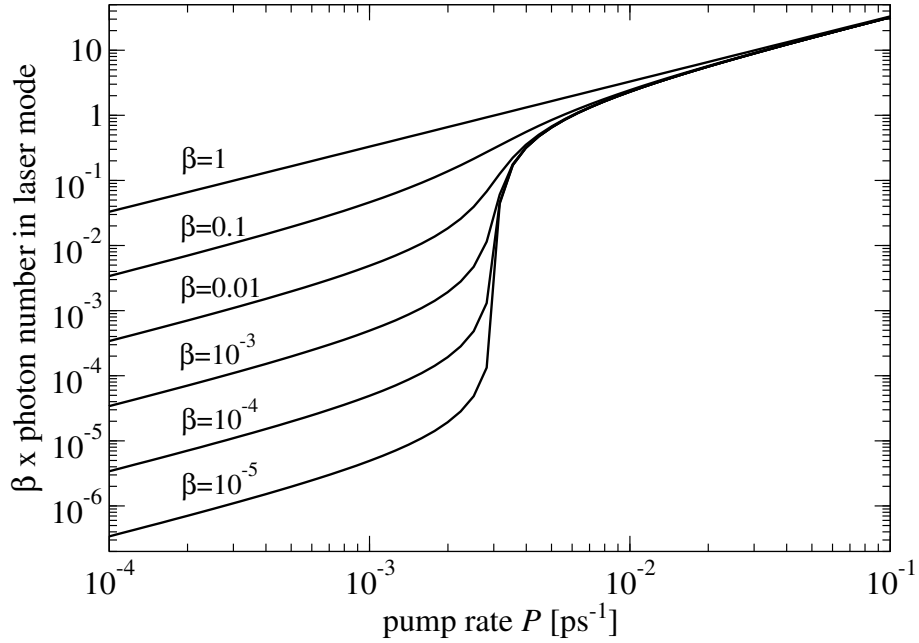


**Figure 3.12:** Calculated output curves for the atomic limit and various  $\beta$ -factors. For better comparison, the photon number is scaled with  $\beta$  in order to have the thresholds occur at equal pump intensities.

photon-assisted polarization and the photon number. For the corresponding equation of motion we obtain

$$\begin{aligned} \left( \hbar \frac{d}{dt} + 3\kappa + \Gamma \right) \delta \langle b^\dagger b^\dagger b v_\nu^\dagger c_\nu \rangle &= -2 |g|^2 \langle b^\dagger v_\nu^\dagger c_\nu \rangle^2 - (1 - f_\nu^e - f_\nu^h) \delta \langle b^\dagger b^\dagger b b \rangle \\ &\quad + 2 f_\nu^h \delta \langle b^\dagger b c_\nu^\dagger c_\nu \rangle - 2 f_\nu^e \delta \langle b^\dagger b v_\nu^\dagger v_\nu \rangle \\ &\quad - 2 \delta \langle b^\dagger b c_\nu^\dagger v_\nu^\dagger c_\nu v_{\nu'} \rangle + \sum_{\nu'} \delta \langle b^\dagger b^\dagger v_{\nu'}^\dagger v_\nu^\dagger c_\nu c_{\nu'} \rangle . \end{aligned} \quad (3.62)$$

Here we have again scaled  $\delta \langle b^\dagger b^\dagger b v_\nu^\dagger c_\nu \rangle \rightarrow g \delta \langle b^\dagger b^\dagger b v_\nu^\dagger c_\nu \rangle$  with the light-matter coupling  $g$  for the laser mode. The triplet photon-carrier correlations in the second line are the same as in Eq. (3.52), and their evolution is given by

$$\begin{aligned} \left( \hbar \frac{d}{dt} + 2\kappa \right) \delta \langle b^\dagger b c_\nu^\dagger c_\nu \rangle &= -2 |g|^2 \operatorname{Re} \left[ \delta \langle b^\dagger b^\dagger b v_\nu^\dagger c_\nu \rangle \right. \\ &\quad \left. + \sum_{\nu'} \delta \langle b^\dagger v_{\nu'}^\dagger c_\nu^\dagger c_{\nu'} c_\nu \rangle + (\langle b^\dagger b \rangle + f_\nu^e) \langle b^\dagger v_\nu^\dagger c_\nu \rangle \right] , \end{aligned} \quad (3.63)$$

$$\begin{aligned} \left( \hbar \frac{d}{dt} + 2\kappa \right) \delta \langle b^\dagger b v_\nu^\dagger v_\nu \rangle &= 2 |g|^2 \operatorname{Re} \left[ \delta \langle b^\dagger b^\dagger b v_\nu^\dagger c_\nu \rangle \right. \\ &\quad \left. - \sum_{\nu'} \delta \langle b c_{\nu'}^\dagger v_\nu^\dagger v_{\nu'} v_\nu \rangle + (\langle b^\dagger b \rangle + f_\nu^h) \langle b^\dagger v_\nu^\dagger c_\nu \rangle \right] . \end{aligned} \quad (3.64)$$

The correlation functions in the sum, which have been also scaled as  $\delta\langle b^\dagger v_\nu^\dagger c_\nu^\dagger c_{\nu'} c_\nu \rangle \rightarrow g \delta\langle b^\dagger v_\nu^\dagger c_\nu^\dagger c_{\nu'} c_\nu \rangle$ ,  $\delta\langle b c_{\nu'}^\dagger v_\nu^\dagger v_{\nu'} v_\nu \rangle \rightarrow g \delta\langle b c_{\nu'}^\dagger v_\nu^\dagger v_{\nu'} v_\nu \rangle$ , obey the equations of motion

$$\left( \hbar \frac{d}{dt} + \kappa + \Gamma \right) \delta\langle b c_{\nu'}^\dagger v_\nu^\dagger v_{\nu'} v_\nu \rangle = (1 - \delta_{\nu\nu'}) \left[ (1 - f_{\nu'}^e - f_{\nu'}^h) \delta\langle b^\dagger b v_\nu^\dagger v_\nu \rangle - |g|^2 \langle b^\dagger v_\nu^\dagger c_\nu \rangle^* \langle b^\dagger v_{\nu'}^\dagger c_{\nu'} \rangle^* \right], \quad (3.65)$$

$$\left( \hbar \frac{d}{dt} + \kappa + \Gamma \right) \delta\langle b^\dagger v_\nu^\dagger c_\nu^\dagger c_{\nu'} c_\nu \rangle = (1 - \delta_{\nu\nu'}) \left[ (1 - f_{\nu'}^e - f_{\nu'}^h) \delta\langle b^\dagger b c_\nu^\dagger c_\nu \rangle + |g|^2 \langle b^\dagger v_\nu^\dagger c_\nu \rangle \langle b^\dagger v_{\nu'}^\dagger c_{\nu'} \rangle \right]. \quad (3.66)$$

In the following, we give arguments why the correlation functions, which are determined by Eqs. (3.65) and (3.66), and the last term of Eq. (3.62) only contribute if correlations between *different* QDs exist, i.e. superradiant coupling plays a role in the system. The effect of superradiance is known to rely on weak dephasing, which is difficult to realize under the considered high-excitation conditions. In order to see the relation to superradiance, we refer to the dipole selection rules in cubic crystals, where optical transitions with a given circular light polarization are coupled to a particular electron spin and the corresponding hole total angular momentum. Specifically, the *s*-shell states for electrons are spin degenerate and the two spin states are coupled to different light polarizations. If we consider correlations between photons with the same circular polarization, we find that they are linked to states for which only one electron or hole per *s*-shell and QD are available. In other words, annihilating two valence-band electrons in the case of  $\langle b c_{\nu'}^\dagger v_\nu^\dagger v_{\nu'} v_\nu \rangle$  and two conduction-band electrons in the case of  $\langle b^\dagger v_{\nu'}^\dagger c_\nu^\dagger c_{\nu'} c_\nu \rangle$  is only possible if these carriers belong to different QDs. Hence for  $\nu = \nu'$  these expectation values, and according to their definition

$$\langle b c_{\nu'}^\dagger v_\nu^\dagger v_{\nu'} v_\nu \rangle = -\langle b c_{\nu'}^\dagger v_\nu \rangle f_\nu^v (1 - \delta_{\nu\nu'}) + \delta\langle b c_{\nu'}^\dagger v_\nu^\dagger v_{\nu'} v_\nu \rangle, \quad (3.67)$$

$$\langle b^\dagger v_{\nu'}^\dagger c_\nu^\dagger c_{\nu'} c_\nu \rangle = -\langle b^\dagger v_{\nu'}^\dagger c_{\nu'} \rangle f_\nu^c (1 - \delta_{\nu\nu'}) + \delta\langle b^\dagger v_{\nu'}^\dagger c_\nu^\dagger c_{\nu'} c_\nu \rangle, \quad (3.68)$$

also the corresponding correlation functions  $\delta\langle b c_{\nu'}^\dagger v_\nu^\dagger v_{\nu'} v_\nu \rangle$  and  $\delta\langle b^\dagger v_{\nu'}^\dagger c_\nu^\dagger c_{\nu'} c_\nu \rangle$  vanish exactly. The correlation functions referring to different QDs  $\nu \neq \nu'$  are related to superradiant coupling. The same applies to the expectation value

$$\langle b^\dagger b^\dagger v_{\nu'}^\dagger v_\nu^\dagger c_\nu c_{\nu'} \rangle = 2\langle b^\dagger v_\nu^\dagger c_\nu \rangle \langle b^\dagger v_{\nu'}^\dagger c_{\nu'} \rangle (1 - \delta_{\nu\nu'}) + \delta\langle b^\dagger b^\dagger v_{\nu'}^\dagger v_\nu^\dagger c_\nu c_{\nu'} \rangle, \quad (3.69)$$

which also vanishes together with the corresponding correlation function for  $\nu = \nu'$ . Under the assumption that superradiance is weak in the system, the discussed correlation functions are neglected. If, however, the phenomenon of superradiant coupling itself is to be studied, the correlation functions must be included via their own equations of motion. Finally, the term  $\delta\langle b^\dagger b c_{\nu'}^\dagger v_\nu^\dagger c_\nu v_{\nu'} \rangle$  in Eq. (3.62) is a generalization of the correlations to the source term of spontaneous emission  $C_{\alpha'\nu\nu\alpha}^x = \delta\langle c_\alpha^\dagger v_\nu^\dagger c_\nu v_\alpha \rangle$ . For consistency reasons, this contribution is neglected in accordance with the above discussed omission of  $C^x$ .

Effects due to the Coulomb interaction of carriers can be included along the same lines as discussed in Sections 3.4.1 and 3.4.2. The contributions to Eq. (3.62), that remain on the quadruplet level, are given by

$$i\hbar \frac{d}{dt} \delta \langle b^\dagger b^\dagger b v_\nu^\dagger c_\nu \rangle \Big|_{\text{Coul}} = -2 \sum_\alpha \left[ (1 - f_\nu^e - f_\nu^h) V_{\nu\alpha\nu\alpha} \delta \langle b^\dagger b^\dagger b v_\alpha^\dagger c_\alpha \rangle - 2(f_\alpha^e + f_\alpha^h) V_{\nu\alpha\nu\alpha} \delta \langle b^\dagger b^\dagger b v_\nu^\dagger c_\nu \rangle \right]. \quad (3.70)$$

The result shows an analogous structure like the Hartree-Fock Coulomb terms for  $\langle b^\dagger v_\nu^\dagger c_\nu \rangle$  in Eq. (3.51) and can be interpreted accordingly as a renormalization of the single-particle energies and as interband exchange interaction causing additional renormalizations of the transition energies as well as a redistribution of oscillator strength between different QD transitions.

Coulomb interaction contributions to  $\delta \langle b^\dagger b c_\nu^\dagger c_\nu \rangle$  and  $\delta \langle b^\dagger b v_\nu^\dagger v_\nu \rangle$  are analogous to those contributing to the carrier dynamics of  $f_\nu^e$  and  $f_\nu^h$  discussed in detail in Ref. [257]. Their inclusion is, however, beyond the scope of this work and will be the subject of future investigations.

### 3.4.4 Verification of the treatment of correlations: Comparison with the Master Equation model

In Section 3.4.2 we have shown that the developed laser model can be reduced to the well-known atomic rate-equations, if the semiconductor is replaced by two-level systems. In the extended laser model derived in the first part of this section, the calculation of photon correlations is based on the cluster expansion that provides a truncation of the hierarchy of correlation functions. The aim of this section is to verify that such a truncation on the quadruplet level provides correct results for the photon-intensity correlations, described by the intensity correlation  $g^{(2)}$ .

In quantum optics, access to photon-intensity fluctuations can either be obtained by invoking the quantum regression theorem [249], or by using a master equation to calculate the diagonal density matrix for the coupled atom-photon system [44, 288, 289]. Both methods are *not* directly applicable in semiconductors due to the presence of many-body effects and the modified source term of spontaneous emission. However, our semiconductor model can be reduced to a description of two-level systems. This provides a verification method for our approach and the possibility to study how well the truncation of correlations within the cluster expansion scheme works, as carrier-photon correlations are treated on an exact level in the master equation within the two-level approach.

We have shown in Section 3.4.2 that the source term of spontaneous emission reduces to  $f_\nu^e$  under the assumption that only one electron is present in each two-level system. Additionally, the equation of motion (3.62) changes to

$$\left( \hbar \frac{d}{dt} + 3\kappa + \Gamma \right) \delta \langle b^\dagger b^\dagger b v_\nu^\dagger c_\nu \rangle = -4 |g|^2 \langle b^\dagger v_\nu^\dagger c_\nu \rangle \operatorname{Re} \langle b^\dagger v_\nu^\dagger c_\nu \rangle - (1 - f_\nu^e - f_\nu^h) \delta \langle b^\dagger b^\dagger b b \rangle + 2 \delta \langle b^\dagger b c_\nu^\dagger c_\nu \rangle, \quad (3.71)$$

again neglecting the quadruplet-level correlation functions appearing on the right-hand side and scaling with the light-matter coupling strength. All other used equations of motion for the correlations remain unmodified under the two-level assumptions. In order to quantitatively compare to the master equation given in Ref. [44], we must once more assume a fully inverted system, which is done by setting  $1 - f_\nu^h = 0$  in Eqs. (3.52) and (3.71). Due to the coupling to the correlation functions in Eq. (3.52), an adiabatic solution in the spirit of the rate equations (3.59) and (3.60) is no longer possible. Nevertheless, the numerical steady-state solution can be directly compared to the results of the master equation.

To remain as close as possible to the semiconductor model, we solve the atomic two-level version of Eqs. (3.49) and (3.52) together with Eqs. (3.57) and (3.58) for the population dynamics of the laser and pump level (with  $f_\nu^e f_\nu^h$  replaced by  $f_\nu^e$  for the spontaneous emission). This allows us to avoid the introduction of a number of excited two-level systems. For the direct comparison with the master equations,  $R_{p \rightarrow s}$  is used as a measure for the carrier generation rate at the laser transition level.

Figure 3.13 shows numerical results from our truncated cluster expansion model applied to two-level systems, in comparison to results obtained from the master equation in the formulation of Rice and Carmichael [44]. The values for the parameters  $\kappa$ ,  $\tilde{N}$ , and  $\tau_{sp}$  were taken from Section 3.4.2 and are the same as for Fig. 3.12. Additionally relaxation rates entering  $R_{p \rightarrow s}^{e,h}$  for both electrons and holes of 1 ps, and a dephasing  $\Gamma = 1.36$  meV, corresponding to a time of approximately 500 fs, were used. The upper part of the figure shows the second order correlation function atop the input-output curve for various values of the  $\beta$ -factor. Looking at the input-output curves, we see that the equation of motion approach agrees extremely well with the results from the master equation for all values of  $\beta$ . Regarding the autocorrelation function in the top panel, there is excellent agreement for small values of the  $\beta$ -factor. A deviation of roughly 5% becomes apparent as  $\beta$  is increased to unity, and the results are in good agreement regarding the onset and the end of the transition from thermal to coherent light emission.

We point out that the deviation between lines and symbols in Fig. 3.13 is a measure for the applicability of the cluster expansion method that is here used to truncate the equations of motion at the quadruplet level. Clearly one has to consider the tradeoff between deviations due to this truncation and the possibility to include semiconductor effects. The influence of the latter will be discussed below. The agreement between the truncated (cluster expansion) and non-truncated (master equation) description of atomic two-level systems depends on parameters like the cavity lifetime and the spontaneous emission rate. As long as the semiconductor theory is used for parameters where its two-level version is in agreement with the master equation, we are reassured that the truncation of the cluster expansion can be applied with respect to the photonic correlations. The cluster expansion also well describes the carrier-carrier correlations. In fact, the cluster expansion was developed to treat many-body effects of carriers [76]. Successful applications include the photoluminescence of QDs [257, 295] as we have seen in Section 3.2 and exciton formation in quantum wells [252].

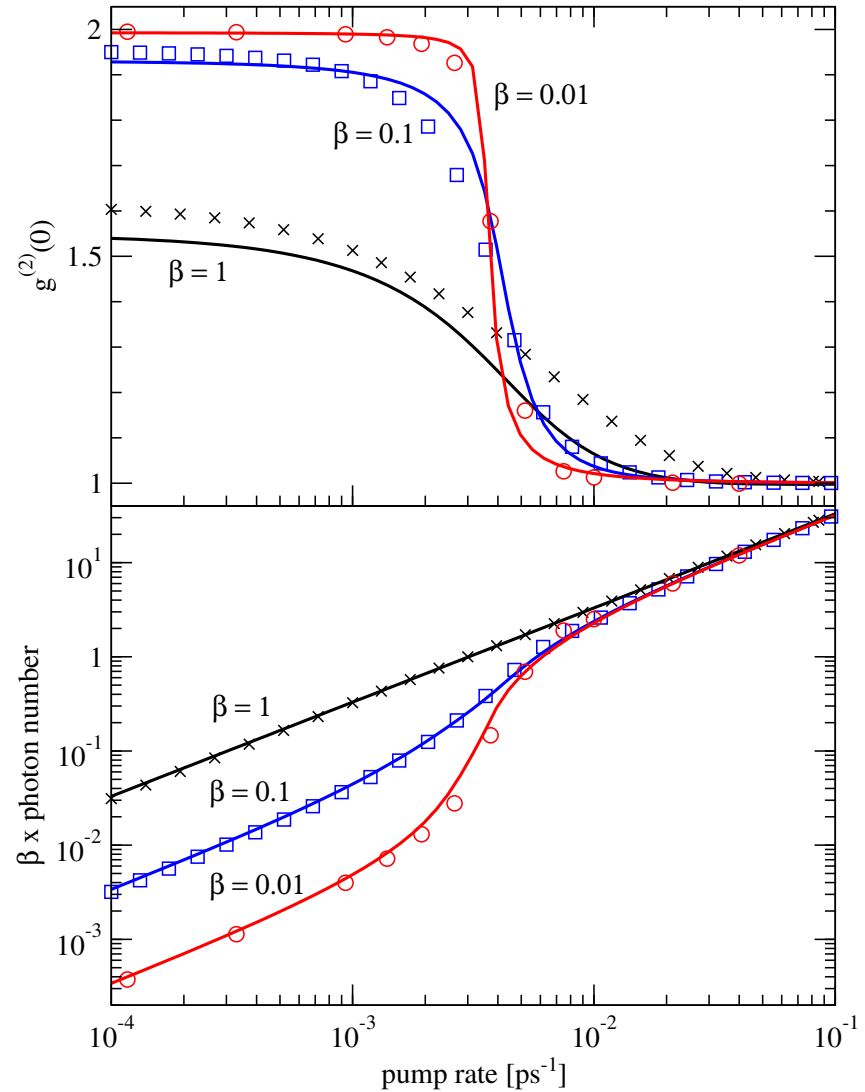


**Figure 3.13:** Autocorrelation function (top) and input-output curve (bottom) for a fully inverted two-level system. Comparison between the master equation (symbols) and the two-level version of the semiconductor theory (solid lines) for  $\beta = 1$ , 0.1, and 0.01. On the  $x$ -axis the pump rate into the laser level is given. For the modified semiconductor theory, this corresponds to an effective carrier generation rate in the  $s$ -shell.

### 3.4.5 Numerical results

We now present numerical solutions of the extended semiconductor laser theory including carrier-photon correlations based on Eqs. (3.49), (3.52), (3.57), (3.58), and (3.61)–(3.64). Again, we use the same parameters as in the previous sections, but different relaxation times for electrons and holes are taken:  $\tau_r^e = 1 \text{ ps}$ ,  $\tau_r^h = 500 \text{ fs}$ .

In Fig. 3.14 the autocorrelation function is shown atop the input-output curve for various values of  $\beta$ . There are several striking features: (i) The jump of the intensity curve from below to above threshold is no longer determined by  $1/\beta$ , as in Figs. 3.12 and 3.13, obtained from a laser theory for two-level systems. This is of particular importance since measurements of the input-output characteristics are often used to experimentally deduce the  $\beta$ -factor according to the predictions of the two-level models. If the atomic  $1/\beta$ -behavior would be used to extract the  $\beta$ -factors from the curves in Fig. 3.14, one would obtain 0.017 instead of 0.1, 0.0017 instead of 0.01, and 0.00017 instead of 0.001. (ii) For small  $\beta$  values, the s-shaped intensity jump is accompanied by a decrease of the second-order coherence from  $g^{(2)}(0) = 2$  for thermal light to the Poisson value  $g^{(2)}(0) = 1$  for coherent laser light. Using larger  $\beta$  values, the abrupt drop of the autocorrelation function becomes smoother, and below threshold  $g^{(2)}$  remains smaller than two. This decrease in the autocorrelation function is already a result of the relatively high cavity quality (long cavity lifetime). For a shorter cavity lifetime and a large number of emitters, also at  $\beta = 1$  a value of  $g^{(2)}(0) = 2$  is obtained in the sub-threshold regime, see below. (iii) At high pump intensities saturation effects due to Pauli blocking become visible in the input-output curve, effectively limiting the maximum output that can be achieved.

In Appendix D we derive analytical solutions of the semiconductor model for the intensity correlation  $g^{(2)}(0)$ . Well above threshold we find the result for coherent light  $g^{(2)}(0) = 1$  as expected. Below threshold in the “bad cavity” limit [44]  $\kappa^2 \gg |g|^2 N$  we get

$$g^{(2)}(0) = 2 - \frac{2}{N} . \quad (3.72)$$

In Fig. 3.15 this result (solid line) is compared to numerical solutions of the extended semiconductor laser model (open symbols) for  $\beta = 1$  and various values of  $\kappa$ . All other parameters are the same as those used in Fig. 3.14. If  $\kappa = 200 \text{ meV}$ , the condition for the analytical solution is fulfilled and perfect agreement between analytical and numerical results is obtained. In this case, the thermal emission  $g^{(2)}(0) = 2$  below the laser threshold is approached for a large number of emitters  $N$ . In the limit of one single QD, the antibunching signature  $g^{(2)}(0) = 0$  is numerically obtained. On the other hand, in the theoretical limit of an infinitely good cavity  $\kappa \rightarrow 0$ , a constant value of  $g^{(2)}(0) = 1$  is expected for atomic models [44]. The case of larger cavity lifetimes is displayed (circles and squares) and the trend of a decrease of the subthreshold value is observed. For the case of a small number of emitters in a very good cavity, photon correlations become so strong that the truncation on quadruplet order becomes insufficient.

In this section, we have developed a theory for the photon statistics in QD-microcavity lasers including semiconductor specific effects. In the next section, we will demonstrate that our theory is indeed capable to describe recent experiments.

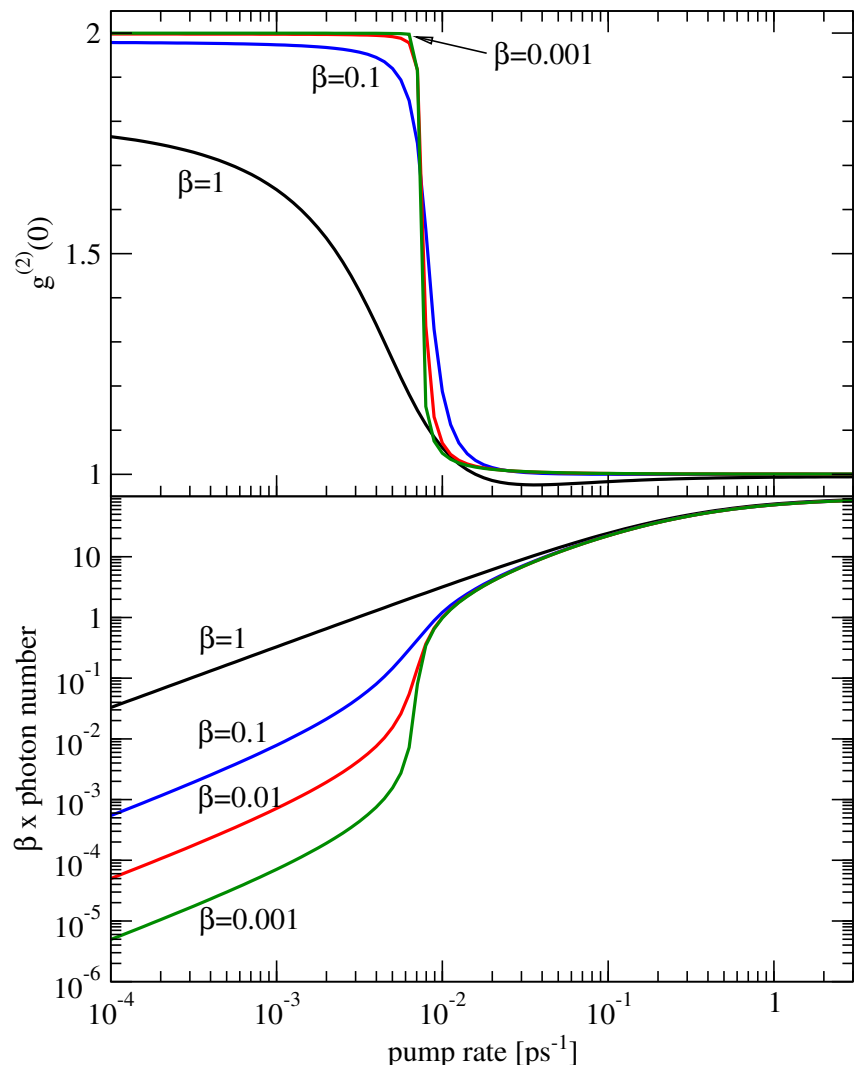


**Figure 3.14:** Calculated output curve (lower panel) and autocorrelation function  $g^{(2)}(\tau = 0)$  (upper panel) for  $\beta = 1, 0.1, 0.01$ , and  $0.001$ . The main parameters are the same as in Fig. 3.13 and also correspond to those in Fig. 3.12.

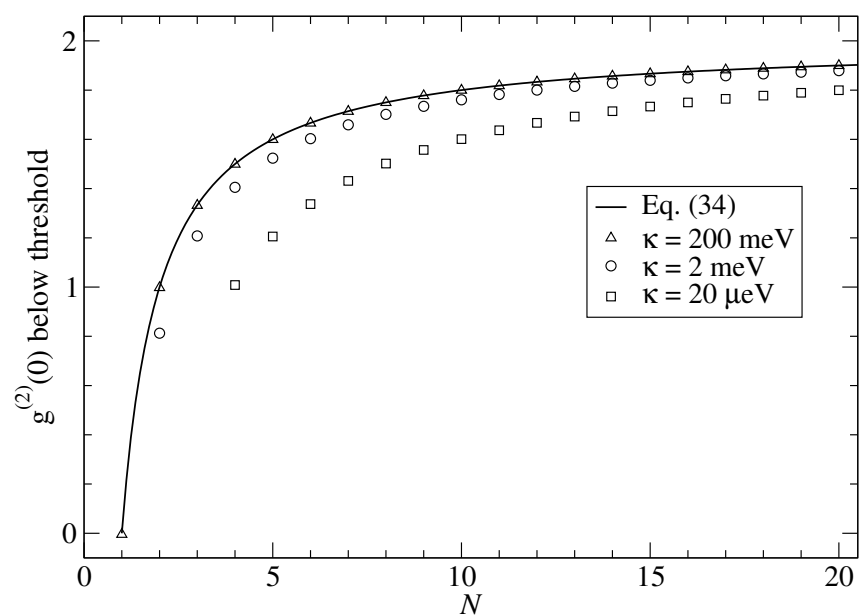


**Figure 3.15:** Sub-threshold values of  $g^{(2)}(0)$  for  $\beta = 1$  obtained from the extended semiconductor laser model. The analytical approximation in the “bad cavity” limit, Eq. (3.72), is compared to numerical results obtained with different values for the inverse cavity lifetime  $\kappa$ .

### 3.4.6 Comparison to experiments

In this section, we present a theory-experiment comparison for lasing of QDs embedded in pillar microcavities [39]. The micropillars were fabricated in the laboratory of A. Forchel in Würzburg. The planar cavity structure consists of 27 (bottom) and 23 (top) DBR periods of alternating AlAs (76 nm)/GaAs (66 nm) layer pairs of  $\lambda/4$  thickness. The DBRs are separated by two 130 nm GaAs spacer layers to form a  $\lambda$ -cavity, centered around a single layer (thickness 4.5 nm) of self-assembled  $\text{In}_{0.30}\text{Ga}_{0.70}\text{As}$  QDs with an average density of about  $6 \cdot 10^9 \text{ cm}^{-2}$ .

The measurements were performed by P. Michler *et al.* on two selected 3 and 4  $\mu\text{m}$  diameter pillars. In the bottom panels of Figs. 3.16 (a) and (b), the input-output curves of the fundamental mode in the 3  $\mu\text{m}$  and 4  $\mu\text{m}$  pillar samples under pulsed excitation are shown. In either case, a characteristic s-shaped smooth transition [296, 297] appears at intermediate excitation levels of  $\sim 200 \mu\text{W}$  ( $\sim 500 \mu\text{W}$ ) for the 3 ( $4 \mu\text{m}$ ) pillar, respectively. As is depicted in Fig. 3.16 (d) for the 3  $\mu\text{m}$  pillar, an equivalent trend is also found in the continuous-wave (cw) input-output curves, where the s-shaped threshold region is not fully developed due to experimental limitations.

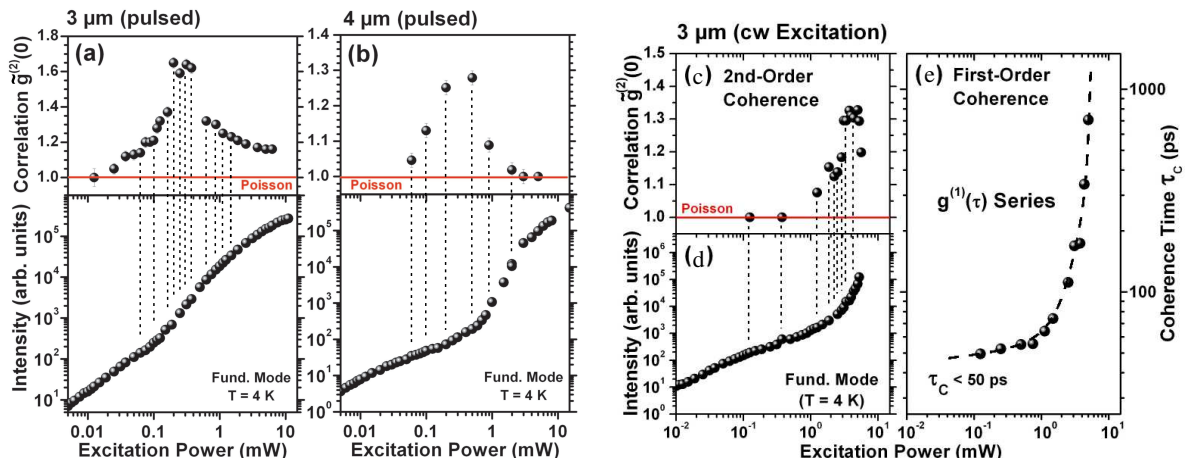


**Figure 3.16:** (a) and (b) Input-output curves (bottom) for the 3  $\mu\text{m}$  and 4  $\mu\text{m}$  pillars under non-resonant *pulsed* excitation. Strong photon bunching  $\tilde{g}^{(2)}(0) > 1$  is found from corresponding correlation measurements (top) over a broadened regime around “threshold”. (c)  $\tilde{g}^{(2)}(\tau = 0)$  for the 3  $\mu\text{m}$  pillar under *continuous-wave (cw)* excitation, together with the corresponding input-output curve (d); (e) Coherence time  $\tau_c$  from first-order coherence,  $g^{(1)}(\tau)$ , measurements in the low excitation limit. The experiments have been done by P. Michler *et al.* [39].

The intensity correlations have been measured with a Hanbury Brown and Twiss (HBT) setup [45]. We distinguish the experimental determined correlation function  $\tilde{g}^{(2)}(0)$  from the theoretical correlation function  $g^{(2)}(0)$  since the relation between the two quantities is nontrivial as we will see in the following. Figures 3.16 (a)–(d) indicate strong photon fluctuations over the full onset regions of stimulated emission. In the regime well below the threshold, the measured intensity correlations remain close to 1, in contrast to an expected thermal behavior with  $g^{(2)}(0) > 1$  discussed in the last sections. In order to

clarify this observation, the first-order coherence in terms of the correlation function

$$g^{(1)}(\tau) = \frac{\langle b^\dagger(t)b(t+\tau) \rangle}{\langle b^\dagger(t)b(t) \rangle} \quad (3.73)$$

and the coherence time

$$\tau_c = \int_{-\infty}^{\infty} |g^{(1)}(\tau)|^2 d\tau \quad (3.74)$$

have been measured by Michelson interferometry on the same  $3\mu\text{m}$  pillar under variable power cw excitation. As can be seen in Fig. 3.16 (e), the coherence time  $\tau_c$  decreases from 700 ps down to  $< 50$  ps from above to below the transition region. We therefore attribute the observed  $\tilde{g}^{(2)}(0) \rightarrow 1$  decrease for low excitation powers to the temporal detection limits of  $\Delta t \approx 600$  ps of the HBT setup, which fails to resolve the “real”  $g^{(2)}(\tau=0)$  result, but represents a convolution over extended time scales  $\tau \gg \tau_c$  with  $g^{(2)}(\tau > \tau_c) \approx 1$ .

The bottom panel of Fig. 3.17 provides a comparison of our theory with the pulsed measurements of the  $3\mu\text{m}$  pillar. As parameters we use  $\tau_{\text{cav}} = 13$  ps, a spontaneous emission time into the laser mode of  $\tau_{\text{lase}} = 250$  ps, and 42 resonant QDs. A fit with  $\beta = 0.12$  gives good agreement for the height of the output intensity jump. Saturation effects become visible in the high excitation regime, which occur due to blocking of the rapidly filled pump levels. Similarly,  $\beta = 0.04$  reproduces the  $4\mu\text{m}$  pillar results that we do not show here.

The calculated autocorrelation function is depicted in the upper panel of Fig. 3.17. To facilitate a direct comparison with our  $\tilde{g}^{(2)}$  experiments (limited by  $\Delta t$ ), we have adapted the measured coherence times  $\tau_c$  to our results in Fig. 3.17. Since the upper output intensity branch is not accessible for cw-pumping, this can only be done qualitatively. We approximate  $g^{(2)}(\tau)$  for each pump intensity from the calculated  $g^{(2)}(0)$  via

$$g^{(2)}(\tau) = 1 + [g^{(2)}(0) - 1] \cdot \exp(-2|\tau|/\tau_c) . \quad (3.75)$$

This relation is exact for thermal light [287]. The function (3.75) is convolved with a Gaussian apparatus function with width  $2\sigma = \Delta t$

$$\tilde{g}^{(2)}(\tau) = 1/\sqrt{2\pi\sigma^2} \int_{-\infty}^{\infty} d\tau' g^{(2)}(\tau - \tau') \exp(-\tau'^2/2\sigma^2) . \quad (3.76)$$

The  $\tau = 0$  value of this convolution for various pump rates is shown as a red line in Fig. 3.17, reproducing the measured  $\tilde{g}^{(2)}(0)$  correlation peak and its incomplete decay into full coherence, the latter being caused by saturation effects.

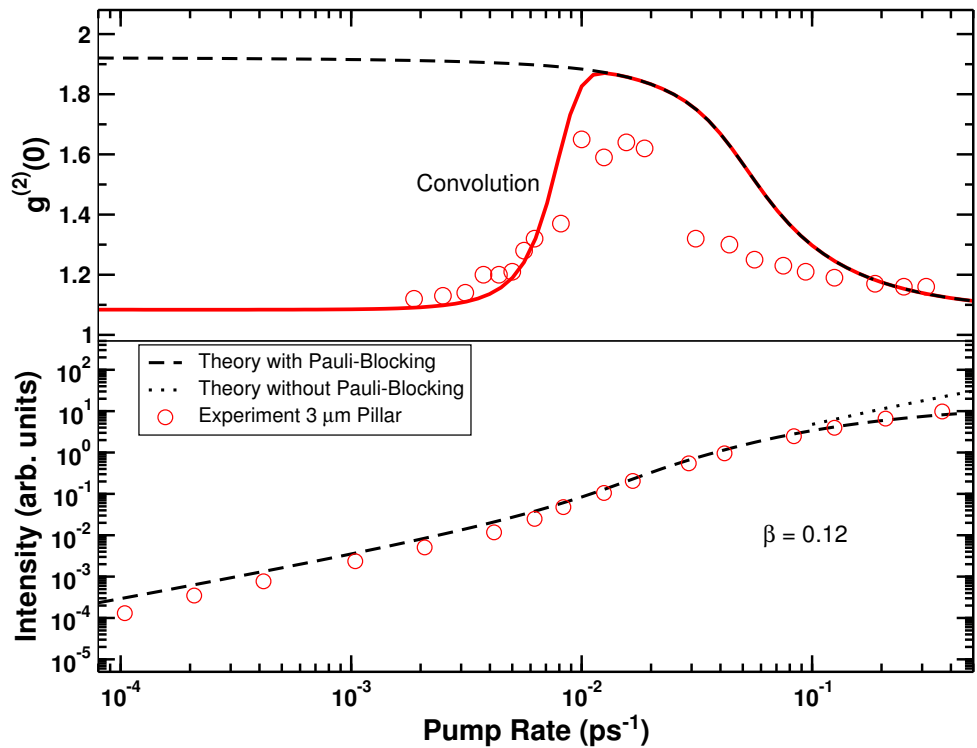


**Figure 3.17:** Calculated results vs. experimental data (red circles) for pulsed excitation for the 3 μm pillar from Fig. 3.16(a). The top panel shows the true  $g^{(2)}(0)$  (dashed line) and the convolution with the experimental temporal resolution  $\tau_c$  (red line). The bottom panel shows the corresponding input-output curves, indicating the effects of pump saturation.

### 3.4.7 Calculation of the first-order coherence

The aim of this section is to compute the first-order coherence (3.73) and the coherence time (3.74). We use the equation-of-motion technique as in the previous sections but now with respect to the delay time  $\tau$ . For convenience, we consider  $G(\tau) = e^{i\omega\tau}G^{(1)}(\tau)$  with the unnormalized first-order coherence  $G^{(1)}(\tau) = \langle b^\dagger(t)b(t+\tau)\rangle$ . Note that  $|G(\tau)| = |G^{(1)}(\tau)|$ . The equation of motion for  $G(\tau)$  is

$$\hbar \frac{d}{d\tau} G(\tau) = -\kappa G(\tau) + \sum_\nu g_\nu^* P_\nu(\tau) . \quad (3.77)$$

For the generalized polarization  $P_\nu(\tau) = e^{i\omega\tau}\langle b^\dagger(t)v_\nu^\dagger(t+\tau)c_\nu(t+\tau)\rangle$  we find

$$\hbar \frac{d}{d\tau} P_\nu(\tau) = i[\hbar\omega - (\tilde{\varepsilon}_\nu^c - \tilde{\varepsilon}_\nu^v) + i\Gamma]P_\nu(\tau) \quad (3.78)$$

$$+ e^{i\omega\tau} \sum_\xi g_{\xi\nu} \langle b^\dagger(t)b_\xi(t+\tau)c_\nu^\dagger(t+\tau)c_\nu(t+\tau)\rangle \quad (3.79)$$

$$- e^{i\omega\tau} \sum_\xi g_{\xi\nu} \langle b^\dagger(t)b_\xi(t+\tau)v_\nu^\dagger(t+\tau)v_\nu(t+\tau)\rangle . \quad (3.80)$$

The sums run over all modes  $\xi$  including the laser mode  $\xi_l$ . The dephasing rate  $\Gamma$  is introduced phenomenologically. Coulomb interaction between the QD carriers is again summarized in an effective transition energy and oscillator strength for the coupling to the laser mode.

As in the previous laser calculations we assume in the following that (i) coupling between the laser mode and other modes can be ignored. (ii) All  $N$  QDs are identical and exactly on resonance with the laser mode, i.e.,  $\tilde{\varepsilon}_\nu^c - \tilde{\varepsilon}_\nu^v = \hbar\omega$ ,  $f_\nu^{(c,v)} = f^{(c,v)}$ , and  $g_\nu = g$ . For the simplest nontrivial solution we restrict ourselves to the singlet-doublet level, which implies the semiclassical factorization

$$\langle b^\dagger b c_\nu^\dagger c_\nu \rangle \approx \langle b^\dagger b \rangle \langle c_\nu^\dagger c_\nu \rangle , \quad \langle b^\dagger b v_\nu^\dagger v_\nu \rangle \approx \langle b^\dagger b \rangle \langle v_\nu^\dagger v_\nu \rangle . \quad (3.81)$$

With these approximations and the abbreviation  $P = \sum_\nu P_\nu$  we obtain the differential equations

$$\hbar \frac{d}{d\tau} G(\tau) = -\kappa G(\tau) + g^* P(\tau) , \quad (3.82)$$

$$\hbar \frac{d}{d\tau} P(\tau) = -\Gamma P(\tau) + gN(f^c - f^v)G(\tau) . \quad (3.83)$$

In the last equation  $f^{(c,v)}(t+\tau) = f^{(c,v)}(t)$  since the occupations become stationary in the asymptotic regime. The differential equations (3.82) and (3.83) with initial conditions  $G(0) = \langle b^\dagger(t)b(t)\rangle$  and  $P(0) = N\langle b^\dagger(t)v^\dagger(t)c(t)\rangle$  have an *analytical solution*

$$G(\tau) = \frac{-\gamma_-}{\gamma_+ - \gamma_-} e^{-\gamma_+\tau} + \frac{\gamma_+}{\gamma_+ - \gamma_-} e^{-\gamma_-\tau} \quad (3.84)$$

with

$$\hbar\gamma_{\pm} = \frac{\kappa + \Gamma}{2} \pm \sqrt{|g|^2 N(f^c - f^v) + \frac{(\kappa - \Gamma)^2}{4}}. \quad (3.85)$$

The stationary values of the occupations  $f^c$  and  $f^v$  can be computed using the laser equations from the previous sections. From Eq. (3.84) and the general relation  $[g^{(1)}(-\tau)]^* = g^{(1)}(\tau)$  in the asymptotic regime for  $t$  follows

$$|g^{(1)}(\tau)| = \left| \frac{-\gamma_-}{\gamma_+ - \gamma_-} e^{-\gamma_+ |\tau|} + \frac{\gamma_+}{\gamma_+ - \gamma_-} e^{-\gamma_- |\tau|} \right|. \quad (3.86)$$

From Eqs. (3.74) and (3.85)–(3.86) one can calculate the coherence time according to

$$\tau_c = \frac{1}{\gamma_+} + \frac{1}{\gamma_-} + \frac{\hbar}{\kappa + \Gamma} = \hbar \frac{\kappa + \Gamma}{\kappa\Gamma - |g|^2 N(f^c - f^v)} + \frac{\hbar}{\kappa + \Gamma}. \quad (3.87)$$

Figure 3.18 shows the coherence time as a function of the pump rate. For the chosen parameters,  $\tau_c \approx 20$  ps well below threshold. In agreement with the experimental data in Fig. 3.16(e) we observe a strong increase of  $\tau_c$  near the threshold. Interestingly, the smaller the spontaneous emission factor  $\beta$  the faster the increase of the coherence time.

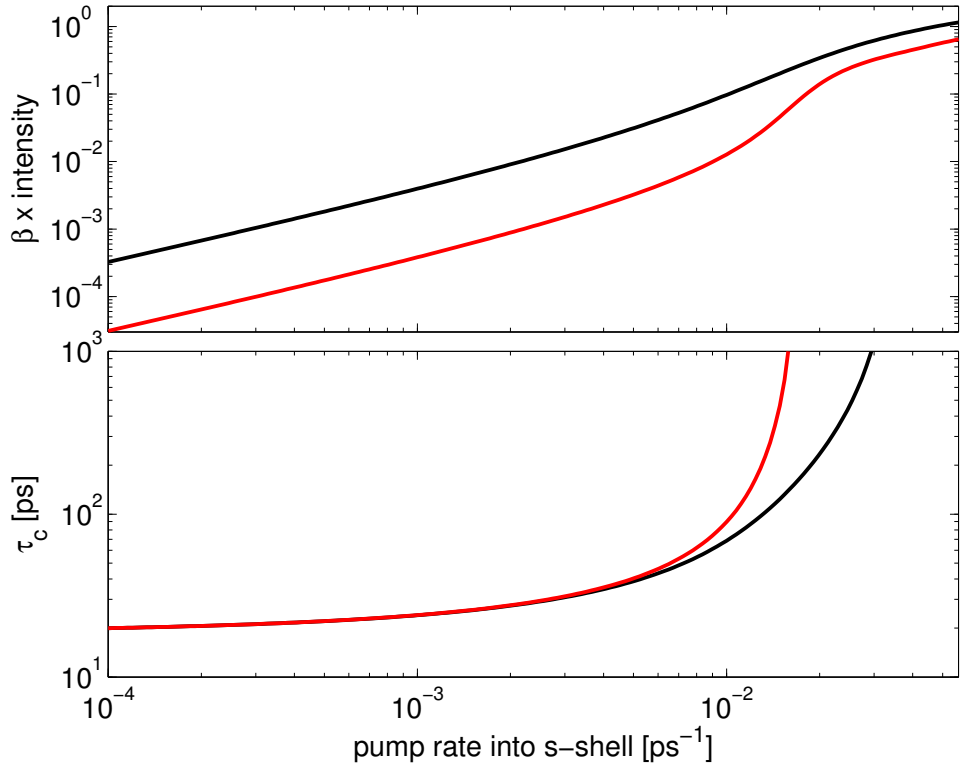


**Figure 3.18:** Calculated output curve (top) and coherence time  $\tau_c$  (bottom) for a  $3\text{ }\mu\text{m}$  pillar with  $\kappa = 20\text{ }\mu\text{eV}$ ,  $\Gamma = 160\text{ }\mu\text{eV}$  and  $\tau_{\text{spont}} = 50\text{ ps}$ . The number of QDs is  $N = 4/\beta$ . The black (red) curve corresponds to  $\beta = 0.1$  ( $0.01$ ).

Figure 3.19 displays  $g^{(1)}(\tau)$  according to Eq. (3.86). Below threshold a Gaussian-like behavior is found, which changes to an exponential behavior near threshold. The results

are consistent with recent experimental results [298]. Our theoretical analysis reveals that the Gaussian-like behavior results from the superposition of two exponentials with similar exponents.

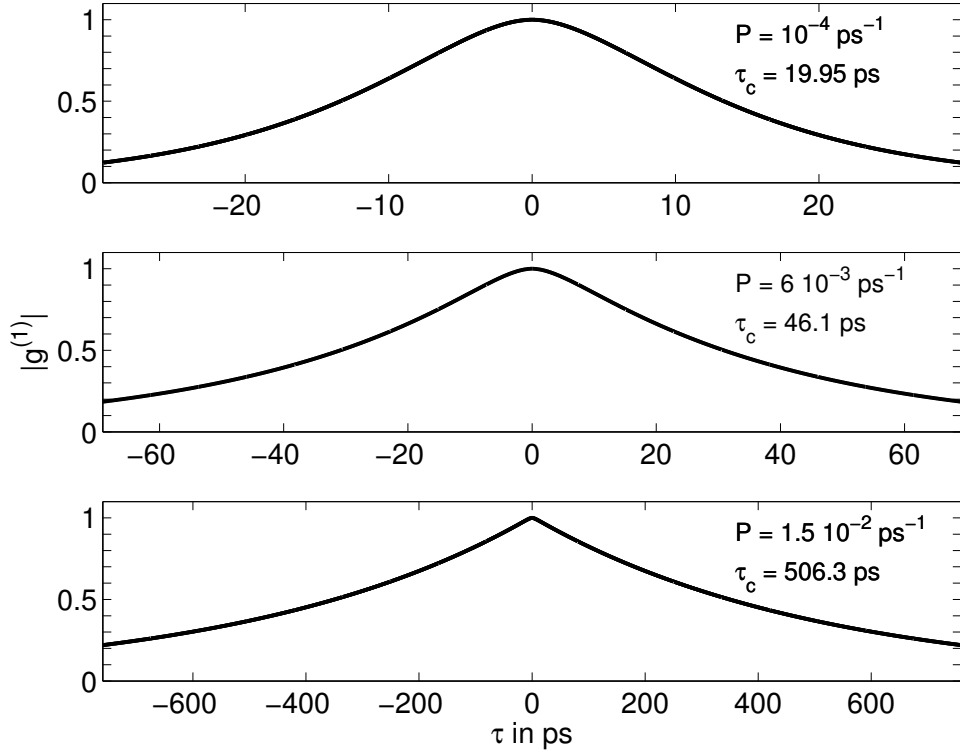


**Figure 3.19:** Calculated  $g^{(1)}(\tau)$  for various pump rates  $P$ ; parameters as for the red curves in Fig. 3.18. (Top) well below threshold, (middle) just below threshold, (bottom) at threshold.

### 3.4.8 Discussion

In conclusion, we have developed a novel semiconductor laser theory that includes carrier-photon correlations and allows one to determine the photon statistics of the light emission. The theory has been applied to describe microcavity lasers with QDs as active material. It has been demonstrated how (i) the model can be reduced to obtain the commonly used rate equations, and (ii) how the application of two-level assumptions makes it possible to compare the photon correlations to those obtained from a master equation. By these means, we have verified that the truncation method of the arising hierarchy of equations of motion can be applied in the considered parameter regime, which is typical for current state-of-the-art microcavity lasers.

Using a numerical evaluation of the theory, we have demonstrated modifications of the characteristic emission properties due to semiconductor effects. Especially the jump in the input-output curve from below to above threshold is found not to scale with  $1/\beta$ , as it does in the two-level case. Most importantly, our approach opens up the possibility to include the full spectrum of semiconductor effects in a consistent and well-defined manner. Besides

a more complete inclusion of Coulomb correlations beyond the singlet level, relaxation and dephasing processes can also be treated on a microscopic level. Furthermore, with respect to Coulomb and light-matter interaction-induced correlations between different QDs, effects of superradiant coupling can be studied.

We compared our theory to recent experimental results on QD-based microcavity lasers with large spontaneous emission coupling. In this regime, the statistical properties of the light emission are analyzed by photon-correlation measurements. A smooth transition from spontaneous emission with strong photon bunching to stimulated emission with a Poisson statistics of the photons is observed. Our results are in good agreement with calculations of the intensity and intensity fluctuations.

Finally, we extended our theory to calculate the coherence of first degree  $g^{(1)}(\tau)$  and the coherence time. Well below threshold we found small coherence times and a Gaussian-like behavior of  $g^{(1)}(\tau)$ . When approaching the laser threshold we observe a strong increase of the coherence time and a change to an exponential behavior of  $g^{(1)}(\tau)$ .



# 4 Nonlinear dynamics and quantum chaos in nanostructures

In this chapter, we discuss nonlinear dynamics and quantum chaos with respect to charge transport in nanostructures. Nonlinear dynamics and transport through semiconductor micro- and nanostructures has attracted considerable attention in the last decade [299–306]. While in Chapter 2 we have focused on Hamiltonian dynamics, we discuss here mainly nonlinear phenomena in *dissipative dynamics*, such as mode-locking [307, 308] and parametric instability [309]. We start our investigations with a two-dimensional electron gas in a uniform magnetic field subject to a periodic potential and an effective friction force. Of particular interest is the nonlinear response to an external electric field [310, 311]. Our numerical and analytical analysis shows that the ratio of transversal to longitudinal resistance forms a so-called Devil’s staircase due to mode-locking.

The coupling of electronic and mechanical degrees of freedom in nanoelectromechanical systems naturally leads to nonlinear phenomena. Section 4.2 deals with the nanoelectromechanical electron shuttle: a movable single-electron device [312], where the electron transport is assisted by the mechanical degree of freedom of the device itself. We extend this concept to a pair of tunnel-coupled charge shuttles [313]. A central result is that parametric instability can generate a direct net current even in the case of a fully symmetric configuration.

Quantum chaotic effects have been observed in several semiconductor micro- and nanostructures [204, 314–320]. A key subject in the field of quantum chaos which we have not addressed so far is the *statistical analysis of energy spectra* introduced by Wigner in an attempt to understand spectroscopic data in nuclear physics [321]. Wigner discovered that the level statistics of heavy nuclei could well be modeled by the statistics of eigenvalues of large matrices, drawn at random from some ensemble. The so-called random matrix theory [322] is now widely and successfully used in physics. It helps to understand quantum chaos [61–64], disordered [323, 324] and mesoscopic systems [60].

In the following paragraphs, we briefly discuss the statistical analysis of energy levels and review some important results for bound systems possessing time-reversal symmetry but no other discrete symmetries. The first step in the statistical analysis of energy levels lies in the “unfolding” of the spectrum, which separates a global smooth variation of the level density from the fluctuation structure of interest [325]. To this end, consider the integrated density of states  $N(E)$  which counts the number of levels  $E_1 \leq E_2 \leq E_3 \leq \dots$  below a given energy  $E$  as illustrated in Fig. 4.1. The staircase function  $N(E)$  can be written as a sum of a smooth part  $\bar{N}(E)$  and a fluctuating part  $N_{\text{fluc}}(E)$ . For billiard systems  $\bar{N}(E)$  is given by the generalized Weyl’s law [326]. In most cases, however,  $\bar{N}(E)$

has to be determined numerically [327]. The unfolding procedure consists of transforming the energies  $E_i$  into dimensionless levels  $e_i$  with unit mean level spacing. This can be achieved by the mapping  $e_i = \bar{N}(E_i)$ .

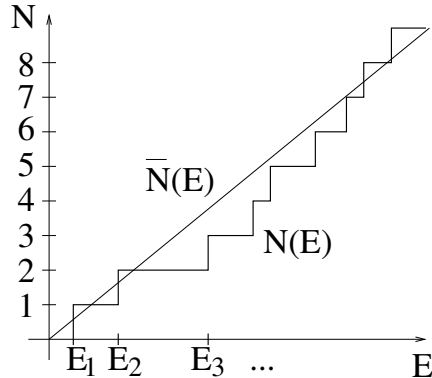


**Figure 4.1:** Sketch of the integrated density of states  $N(E)$  and its smooth part  $\bar{N}(E)$ .

With this unfolded sequence one performs a number of statistical analyses. An important statistical quantity is the nearest-neighbor spacing distribution  $P(s)$ . It is defined as the probability density of the spacing between adjacent levels  $s_i = e_i - e_{i-1}$ . While  $P(s)$  measures short-range level correlations, the number variance  $\Sigma(L)$  allows to study medium- and long-range level correlations. By construction, the mean number of levels in an interval of length  $L$  in the unfolded spectrum is  $L$ . The actual number, however, fluctuates about this value and  $\Sigma(L)$  is the variance of these fluctuations.

In a seminal article, Bohigas *et al.* [325] conjectured that the level statistics of quantum systems, which in the classical limit are fully chaotic, coincide with those of the so-called Gaussian orthogonal ensemble (GOE) of random matrices. This conjecture is nowadays strongly supported by experiments, numerical calculations, and analytical work based on semiclassical approximations [64, 328]. It is a remarkable fact that the level statistics has a universal form independent of the system at hand, provided that the underlying classical system is fully chaotic. This universality has been demonstrated not only for quantum billiards but also for atoms, molecules, and disordered systems in the diffusive metallic regime. For the GOE the distribution of level spacings  $P(s)$  is well fitted by the “Wigner-Dyson surmise”

$$P_{\text{GOE}}(s) \approx P_{\text{Wigner}}(s) = \frac{\pi}{2} s \exp\left(-\frac{\pi}{4}s^2\right) . \quad (4.1)$$

For large  $L$ , the number variance increases logarithmically

$$\Sigma_{\text{GOE}}(L) \approx \frac{2}{\pi^2} \ln L . \quad (4.2)$$

For integrable systems, there is also an universal distribution, the Poisson distribution, corresponding to uncorrelated levels [329]. Here,  $P(s)$  and  $\Sigma(L)$  are given by

$$P_{\text{P}}(s) = \exp(-s) , \quad (4.3)$$

$$\Sigma_{\text{P}}(L) = L . \quad (4.4)$$

The Poisson statistics also describes disordered systems in the insulating regime.

Another statistical distribution is the semi-Poisson (SP) distribution [190, 323]. This distribution is defined by removing every other level from an ordered Poisson sequence. For the nearest neighbor spacing distribution and the number variance follows in this case

$$P_{\text{SP}}(s) = 4s \exp(-2s), \quad (4.5)$$

$$\Sigma_{\text{SP}}(L) = \frac{L}{2} + \frac{1}{8}(1 - e^{-4L}). \quad (4.6)$$

It turns out that the SP distribution is important for the critical statistics of several disordered systems like the Anderson model at the mobility edge [330, 331], and systems without disorder such as pseudo-integrable billiards [190, 332–335].

Figure 4.2 shows the nearest neighbor spacing distribution  $P(s)$  and the number variance  $\Sigma(L)$  for the discussed distributions. An important feature is that  $P_{\text{GOE}}(s) \approx 0$  and  $P_{\text{SP}}(s) \approx 0$  for small spacings, i.e., the probability of observing nearly degenerate levels is reduced. In contrast to this “level repulsion”, the Poisson distribution exhibits “level clustering” with  $P_{\text{P}}(s) \approx 1$  for small spacings. From the number variance in the right panel of Fig. 4.2 it can be seen that the GOE is more “rigid” than the Poisson distribution. The number variance of the SP distribution lies in between those of the GOE and the Poisson distribution.

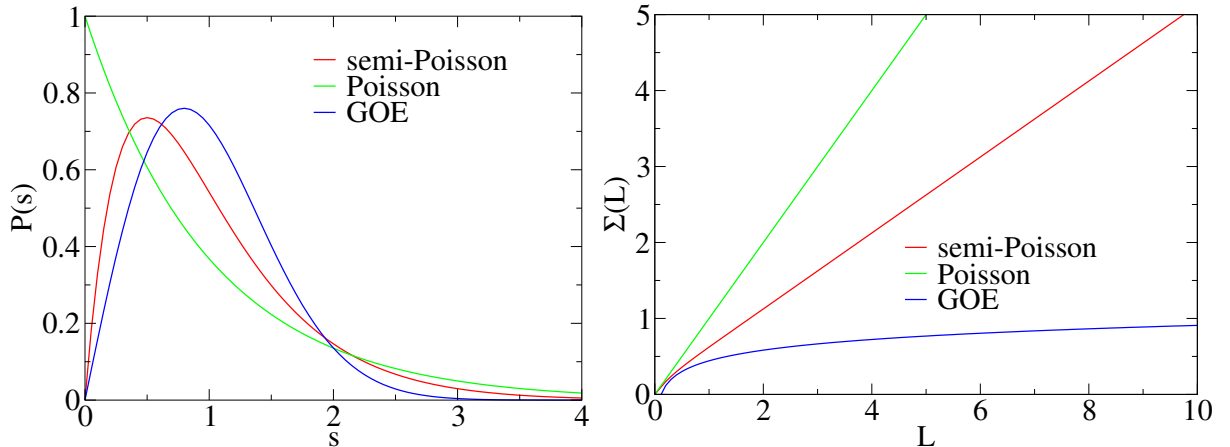


**Figure 4.2:** The nearest neighbor spacing distribution  $P(s)$  and the number variance  $\Sigma(L)$  of the semi-Poisson distribution, the Poisson distribution and the GOE.

In Section 4.3 we demonstrate that the level statistics shine light on the transport properties of nanostructures. We analyze the level statistics of incommensurate double-walled carbon nanotubes [336, 337] and find that the overall spectral properties are well described by the SP distribution. By restricting the statistics to a small region near the Fermi energy we can identify three different regimes characterized by GOE, Poisson, and SP distributions. This feature implies that the character of the electron transport in incommensurate multi-walled nanotubes depends on the position of the Fermi energy. This result provides a plausible explanation for seemingly contradictory experimental findings [79–81].

## 4.1 Two-dimensional electron gas

### 4.1.1 Introduction

The electron transport in two-dimensional periodic arrays of scatterers has been actively studied for the last decade. One of the most interesting feature is the plateau-like behaviour in the Hall resistance as well as peaks in the magnetoresistance [338, 339] at low magnetic fields below the quantum Hall regime. The peak structure in magnetoresistance has been attributed to the electron cyclotron orbits which enclose an *integer* number of scatterers [300, 339]. The cyclotron motion is important when the electron mean free path  $l$  ( $l$  is measured in the absence of periodic scatterers) is greater than the period  $a$  of the regular scatterers.

In this section, we present a theory for electron transport in the deeply *diffusive* regime  $l \ll a$  where cyclotron motion is not relevant. We predict a new and interesting effect where the structure in the magnetoresistance is associated with *fractional* numbers. We will show that the relative ratio between the transversal and longitudinal magnetoresistance forms a *Devil's staircase*. These fractal staircases originate from a dynamical phenomenon known as *mode-locking* which appears naturally in the context of *circle maps* [307]. Our prediction is based on the finding that the dynamics in a two-dimensional periodic array of scatterers with intrinsic momentum relaxation effectively reduces to a circle map.

### 4.1.2 The system

Let us consider first a particle of mass  $m$ , charge  $q$  in crossed electric ( $\mathbf{E} = E\hat{\mathbf{x}}$ ) and magnetic fields ( $\mathbf{B} = -B\hat{\mathbf{z}}$ ) with intrinsic momentum relaxation. The resulting drift motion  $\mathbf{x}(t) = [x(t), y(t)]$  can be described by adding a frictional force, proportional to the drift velocity  $\mathbf{v}$ , to the equations of motion yielding

$$\begin{aligned}\dot{x} &= v_x \quad , \quad m\dot{v}_x = -qBv_y + qE - mv_x/\tau \\ \dot{y} &= v_y \quad , \quad m\dot{v}_y = qBv_x - mv_y/\tau\end{aligned}\tag{4.7}$$

with  $\tau$  being the momentum relaxation time. Cyclotron motion only exists for a transient time; each trajectory finally converges to a straight line with the time-averaged velocity  $\langle \mathbf{v} \rangle = (m/\tau, qB)qE/(q^2B^2 + m^2/\tau^2)$ . With the charge density  $n$  and the current density  $\mathbf{J} = qn\langle \mathbf{v} \rangle$ , it is easy to calculate the resistivities defined by  $\mathbf{E} = \hat{\rho}\mathbf{J}$  and Onsager's relations  $\rho_{xx} = \rho_{yy}$  and  $\rho_{yx} = -\rho_{xy}$ : the diagonal resistivity  $\rho_{xx} = m/q^2n\tau$  is constant, whereas the off-diagonal resistivity  $\rho_{xy} = B/qn$  depends linearly on the magnetic field – no plateaus are present.

We now add a periodic potential  $V = V_0F(\mathbf{x})$  with  $|F|$  of order one to the equations of motion (4.7), assuming that the periodicity of the potential,  $a$ , is much larger than the length scale related to the intrinsic momentum relaxation. When we scale the coordinates  $\mathbf{x}$  with  $a$  and the time  $t$  with  $\tau$ , we get the same equations of motion for a given set of three dimensionless parameters:  $\tilde{B} = q\tau B/m$ ,  $\tilde{E} = q\tau^2 E/(ma)$ , and  $\tilde{V}_0 = V_0/(qEa)$ . We use the rescaled magnetic field  $\tilde{B}$  as a variable parameter and fix the rescaled electric field

and potential strength to  $\tilde{E} = 0.07$  and  $\tilde{V}_0 = 0.12$  if not otherwise stated. Though we could choose various sets of parameters ( $\tau, a, E$ , etc.) for the chosen values of  $\tilde{E}$  and  $\tilde{V}_0$ , for definiteness we will take  $\tau = 7.6 \cdot 10^{-14}$  s,  $E = -2.3 \cdot 10^4$  V/cm, and  $a = 0.5 \mu\text{m}$ , and fix these for the rest of the section. The particle is an electron in GaAs sample with  $q = -e$  and  $m = 0.067 m_e$ . By taking a typical value of Fermi velocity  $v_f \approx 3 \cdot 10^7$  cm/s, the mean free path of our system is  $l = v_f \tau \approx 0.02 \mu\text{m} \ll a$ .

### 4.1.3 Analytical results

First, we show how the particle's motion is related to a one-dimensional circle map through analytical considerations for sufficiently small potential strength. Note that our numerics do not rely on this requirement. Due to the periodicity of the potential it is sufficient to consider the unit cell of the potential with periodic boundary conditions, i.e., we can compactify the  $(x, y)$ -plane to a two-dimensional torus. A typical asymptotic solution for zero potential strength as discussed above appears here as a quasiperiodic trajectory filling densely a two-dimensional invariant torus  $\mathbf{v} = \text{const}$  in four-dimensional phase space. Trajectories starting away from the torus are attracted towards it and asymptotically converge onto it. For finite potential strength the torus is smoothly deformed or collapsed into lower-dimensional objects or broadened to a higher-dimensional object (loosely speaking, a torus with finite but very small thickness). The latter possibility can be ignored to a very good approximation as we will see later. A point on the torus (and on the lower-dimensional objects) is uniquely labelled by unit-cell coordinates  $(x_1 \bmod 1, x_2 \bmod 1)$  defined by  $\mathbf{x} = x_1 \mathbf{a}_1 + x_2 \mathbf{a}_2$ , with  $\mathbf{a}_1 = (a_{11}, a_{12})$ ,  $\mathbf{a}_2 = (a_{21}, a_{22})$  being the lattice vectors of the unit cell. The long-time behavior is therefore completely described by two-dimensional dynamics  $[x_1(t), x_2(t)]$ . As usual, such dynamics can be conveniently investigated by introducing *Poincaré surfaces of section* here defined by  $x_1(t_n) \bmod 1 = 0$ , where  $n$  is an integer and modulo 1 restricts the variable to the interval  $[0, 1)$ .

The discrete evolution of  $x_{2,n} \equiv x_2(t_n)$  is then governed by a one-dimensional map  $x_{2,n+1} = f(x_{2,n})$  where  $f$  is a smooth and monotonic function. Due to the periodicity of the potential the condition  $f(x_2) \bmod 1 = f(x_2 \bmod 1)$  holds. Such a map is called an *invertible circle map*. Its *rotation number*,

$$\rho \equiv \lim_{n \rightarrow \infty} \frac{x_{2,n} - x_{2,0}}{n}, \quad (4.8)$$

is well-defined and independent of the initial condition  $x_{2,0}$  [307]. A rational value of  $\rho = p/q$  ( $p$  and  $q$  are integers without common divisor) indicates periodic motion, whereas an irrational value indicates quasiperiodic motion; chaotic motion is not possible.

We now derive a simplified circle map valid in the limit  $\tilde{V}_0 \ll 1$ . If  $\tilde{V}_0 = 0$  then the asymptotic dynamics obeys  $\dot{v}_x = \dot{v}_y = 0$ , leading to  $f(x_2) = x_2 + \rho_0$  with the constant  $\rho_0(\tilde{B})$ ; here we have simply  $\rho = \rho_0$ , so  $\rho_0$  can be regarded as the unperturbed rotation number. The asymptotic dynamics for nonzero but sufficiently small  $\tilde{V}_0$  is overdamped, i.e.,  $|\dot{v}_x| \ll |v_x|/\tau$  and  $|\dot{v}_y| \ll |v_y|/\tau$ . As in the potential-free case the number of differential equations reduces to two, enabling us to determine  $f$  up to first order in  $\tilde{V}_0$

$$f(x_{2,n}; \rho_0, \tilde{E}, \tilde{V}_0) \approx x_{2,n} + \rho_0 + \tilde{V}_0 g(x_{2,n}; \rho_0) \quad (4.9)$$

with

$$g = \frac{\rho_0^2(a_{22}^2 + a_{21}^2) + 2\rho_0(a_{11}a_{21} + a_{12}a_{22}) + a_{12}^2 + a_{11}^2}{(a_{11}a_{22} - a_{21}a_{12})^2} \times \quad (4.10)$$

$$\int_0^1 \left( a_{21} \frac{\partial F}{\partial x_1} - a_{11} \frac{\partial F}{\partial x_2} \right) \Big|_{x_2=\rho_0 x_1 + x_{2,n}} dx_1 . \quad (4.11)$$

$g$  is a nontrivial periodic function of  $x_{2,n}$ . Note that  $f$  is independent of the parameter  $\tilde{E}$  in the present approximation. Using Stoke's theorem it can be shown that  $\int_0^1 g dx_2 = 0$ . For circle maps of the form given in Eq. (4.9) with the above-mentioned properties of  $g$  it is proven that for each  $\tilde{V}_0$  there exists a Devil's staircase, a monotonically increasing function  $\rho = \rho(\rho_0)$  with plateaus around each rational value of  $\rho_0$ . The width of the plateaus,  $\Delta\rho_0$ , is proportional to  $\tilde{V}_0$  [340]. Similarly, the widths of the plateaus,  $\Delta\tilde{B}$ , of the function  $\rho = \rho(\tilde{B})$ , are proportional to  $\tilde{V}_0$  since  $\Delta\tilde{B} \approx (d\tilde{B}/d\rho_0)\Delta\rho_0$ .

The rotation number  $\rho$  is directly related to the continuous-time dynamics. This can be seen by rewriting Eq. (4.8) with  $\mathbf{v} = v_1\mathbf{a}_1 + v_2\mathbf{a}_2$  as

$$\rho = \frac{\langle v_2 \rangle}{\langle v_1 \rangle} = \frac{-a_{12} + a_{11}\langle v_y \rangle/\langle v_x \rangle}{a_{22} - a_{21}\langle v_y \rangle/\langle v_x \rangle} = \frac{-a_{12} + a_{11}\sigma_{xy}/\sigma_{xx}}{a_{22} - a_{21}\sigma_{xy}/\sigma_{xx}} . \quad (4.12)$$

Hence,  $\rho$  is given by the ratio of the conductivities. In the case that the periodic potential is invariant under  $\pi/m$ -rotations,  $m = 2, 3, \dots$ , Onsager's relations show that  $\rho$  can also be expressed by the ratio  $\rho_{xy}/\rho_{xx}$ .

#### 4.1.4 Numerical results

We now present numerical evidence showing that for finite  $\tilde{V}_0 \lesssim 0.4$  the continuous-time dynamics is indeed given by a one-dimensional circle map and that the magnetoresistance shows a fractal structure. As an example of the periodic scatterers, we take a potential with hexagonal symmetry shown in Fig. 4.3(a),

$$\begin{aligned} V(x, y) = & V_0 \left\{ \left[ \cos\left(\frac{\pi}{3}(\sqrt{3}x - y)\right) \cos\left(\frac{2\pi}{3}y\right) \right]^\beta \right. \\ & + \left[ \cos\left(\frac{\pi}{3}(\sqrt{3}x + y)\right) \cos\left(\frac{\pi}{3}(\sqrt{3}x - y)\right) \right]^\beta \\ & \left. + \left[ \cos\left(\frac{2\pi}{3}y\right) \cos\left(\frac{\pi}{3}(\sqrt{3}x + y)\right) \right]^\beta \right\} , \end{aligned} \quad (4.13)$$

with  $\beta = 8$ . The lattice vectors are  $\mathbf{a}_1 = (\sqrt{3}, 0)$  and  $\mathbf{a}_2 = (-\sqrt{3}/2, -3/2)$ . We have used the Runge-Kutta method [163] with  $10^6$  time steps of variable size to integrate the equations of motion. We found that all initial conditions, for fixed parameters, lead to the same mean velocity  $\langle \mathbf{v} \rangle$ . So only one single orbit is needed to calculate the current density and the resistivities without employing the Kubo formula [341]. This already indicates the collapse to an invertible circle map. To show the reduction to the map explicitly,

we calculate a sequence of points  $(x_{2,n} \bmod 1, x_{2,n+1} \bmod 1)$  by solving the complete set of differential equations for different initial velocities from one Poincaré section to the next. Figures 4.4(a) and (b) show that these points indeed lie very close to a line, so  $x_{2,n+1}$  is to excellent approximation a function of  $x_{2,n}$  independent of the initial velocity. We have computed  $(x_{2,n+1} - x_{2,n} - \rho_0)/\tilde{V}_0$  for different parameters  $\tilde{V}_0$  and  $\tilde{E}$ . It can be seen from Fig. 4.4(c) that this quantity is roughly independent of  $\tilde{V}_0$ , even though small deviations indicate weak nonlinear behavior in  $\tilde{V}_0$ . Figure 4.4(d) shows that  $(x_{2,n+1} - x_{2,n} - \rho_0)/\tilde{V}_0$  does not change when  $\tilde{E}$  is varied over two orders of magnitude. Figures 4.4(a)–(d) therefore confirm the reduction to the circle map and its parameter dependence as predicted in Eq. (4.9).

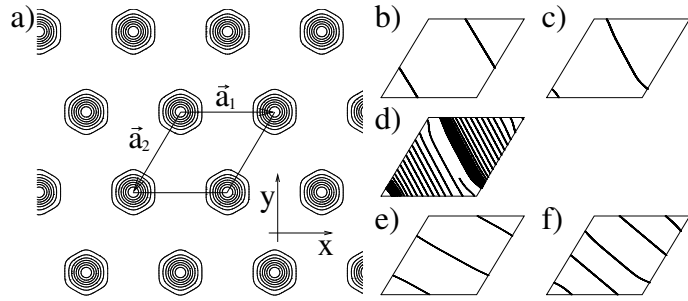


**Figure 4.3:** a) Contourplot of the potential in Eq. (4.13) with  $\beta = 8$ . b) Orbit with  $B = 8.7T$  and  $\rho = 1$  in the unit cell. c)  $B = 9.77T$  and  $\rho = 1$ . d)  $9.8T$  and  $\rho = 1.01407\dots$  e)  $2.9T$  and  $\rho = 1/2$ . f)  $4.4T$  and  $\rho = 2/3$ .

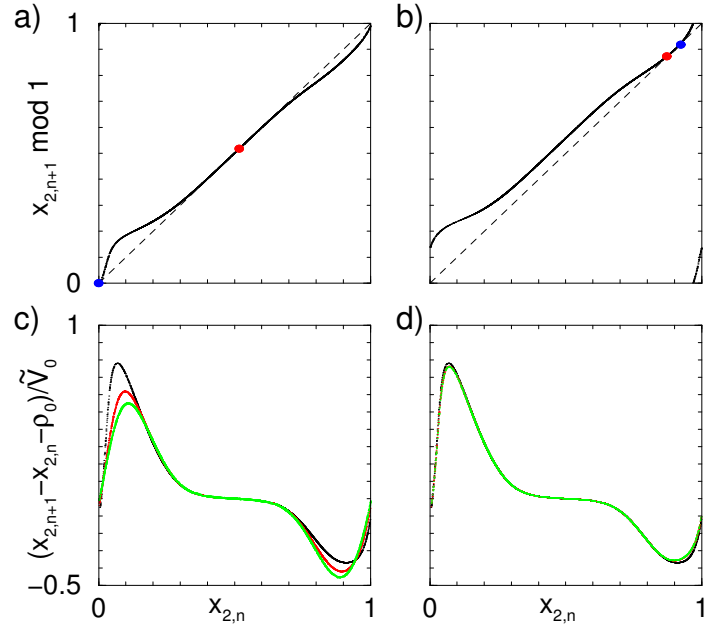


**Figure 4.4:** a)  $x_{2,n+1} \bmod 1$  vs.  $x_{2,n}$  for  $B = 8.7T$ . b)  $9.77T$ . c)  $(x_{2,n+1} - x_{2,n} - \rho_0)/\tilde{V}_0$  vs.  $x_{2,n}$  for  $B = 8.7T$ ,  $\tilde{V}_0 = 0.12$  and  $\tilde{E} = 0.07$  (black);  $\tilde{V}_0 = 0.06$  (red);  $\tilde{V}_0 = 0.03$  (green). d)  $\tilde{V}_0 = 0.12$  and  $\tilde{E} = 0.07$  (black);  $\tilde{E} = 0.007$  (red);  $\tilde{E} = 0.0007$  (green).

Figure 4.5 is our main result. It shows the Devil's staircase  $\rho$  vs.  $\rho_0$ . Both quantities are computed from the resistivities via the relations  $\rho = 2/(1 + \sqrt{3}\rho_{xx}/\rho_{xy})$  and  $\rho_0 = 2/(1 - \sqrt{3}/\tilde{B})$  from Eq. (4.12) with the lattice vectors of the rotational symmetric potential (4.13). Note the exactness of the plateaus. Let us discuss some features of the Devil's staircase in relation to the continuous and discrete-time dynamics. Figures 4.3(b) and (c) show two orbits moving in slightly different magnetic fields. Both have synchronized velocities  $\langle v_1 \rangle = \langle v_2 \rangle$ , i.e.,  $\rho = 1$ . Each orbit with  $\rho = 1$  is a stable fixed point  $x_2^* = f(x_2^*)$  in the corresponding map (red circles in Figs. 4.4(a) and (b); blue circles mark unstable fixed points). This synchronization phenomenon, usually called *mode-locking* in nonlinear dynamics, is therefore due to the robustness of fixed points under variation of a parameter, here  $\rho_0(B)$ . Orbits with  $\rho \neq 1$  are in a different *mode*; in particular, orbits with irrational rotation number are not periodic. In Fig. 4.3(d) we see an orbit with irrational  $\rho$  close to one. It stays for a long time near a periodic orbit with  $\rho = 1$  but from time to time it escapes, thereby filling the entire unit cell densely. This phenomenon is often called *intermittency* in nonlinear dynamics [342]. In terms of the circle map, the transition from  $\rho = 1$  to irrational  $\rho$  is a saddlenode bifurcation: as  $B$  is varied, stable and unstable fixed points come closer and closer as illustrated in Figs. 4.4(a) and (b), and finally destroy each other, yielding quasiperiodic motion. Varying  $B$  further can lead again to periodic motion. Figures 4.3(e) and (f) give two examples with  $\rho = 1/2$  and  $\rho = 2/3$ . The corresponding map has a stable fixed point of higher period, e.g., for  $\rho = 1/2$  the fixed point condition is  $x_2^* = f[f(x_2^*)]$ .

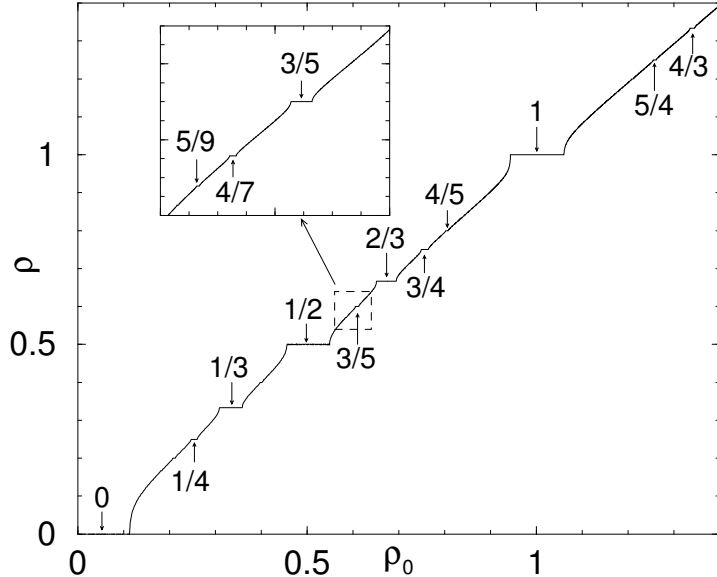


**Figure 4.5:** Rotation number  $\rho$  vs.  $\rho_0$ . Arrows assign the rational value of the rotation number  $\rho = p/q$  to each plateau. The inset highlights the fractal structure of the Devil's staircase.

We also observe a Devil's staircase-like function  $\rho_{xy}(B)$  in Fig. 4.6, which reminds one of the quantum Hall effects [343, 344], but here the “plateaus” are not perfectly flat. One may note also that the way  $\rho_{xx}$  varies for a number of  $\rho_{xy}$ -“plateaus” has similarities to the quantum Hall effects: going from the centre of a  $\rho_{xy}$ -“plateau” towards its border,

$\rho_{xx}$  increases and reaches its maximum exactly when the “plateau” ends. This can be explained qualitatively. First, note that an orbit from the centre of the  $\rho = 1$ -plateau (Fig. 4.3(b)) avoids the potential’s steep maxima at the corners of the unit cell. Hence, the diagonal resistivity roughly equals the potential-free value  $\rho_{xx} = m/q^2n\tau \approx 3.12 \text{ k}\Omega$ . We infer from Figs. 4.3(b) and (c) that the closer  $B$  is to the border of the plateau the closer is the orbit to the potential’s maxima. This effectively slows down the orbit, which explains the increase of  $\rho_{xx}$  (and  $\rho_{xy}$ ). Leaving the plateau finally reduces  $\rho_{xx}$  continuously because of the intermittency effect, which becomes less pronounced with increasing  $|\rho - 1|$ .

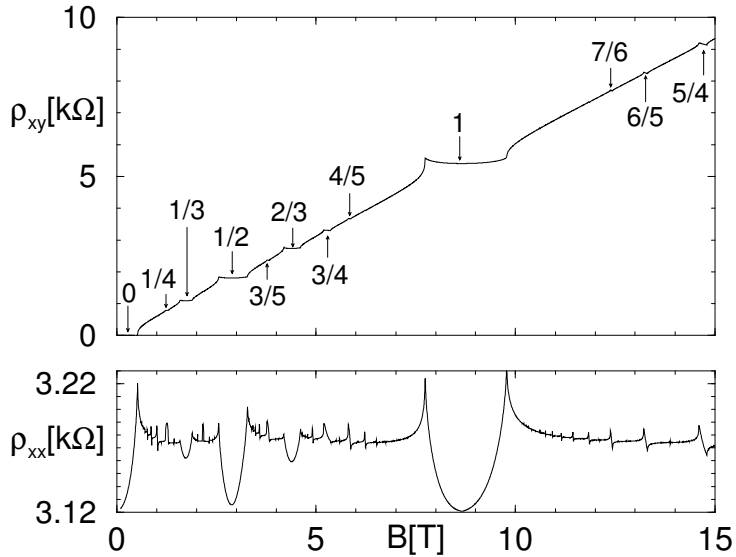


**Figure 4.6:** Off-diagonal resistivity  $\rho_{xy}$  and diagonal resistivity  $\rho_{xx}$  vs. magnetic field  $B$ . Arrows assign the rational value of the rotation number  $\rho = p/q$  to each “plateau”. We here have used  $n = 10^{12} \text{ cm}^{-2}$ .

The example in Fig. 4.7 confirms that the widths of the plateaus,  $\Delta B$ , is roughly proportional to  $\tilde{V}_0$  as predicted from the analysis of the simplified circle map in Eq. (4.9). By noting that  $\tilde{V}_0$  denotes the dimensionless potential strength we see an interesting analogy with the quantum Hall effect where the size of plateaus is sensitive to the disorder strength of the systems [345]. Here we have the advantage of the use of the simplified circle map to analyse the plateau size, although the overall structure of the hierarchy of the plateaus is also too complicated to be dealt with in an analytic fashion.

Since the particle can be trapped in the very flat local minima of the potential (4.13), a finite dc electric field is necessary to overcome the potential trap as in the experiment in Ref. [346]. The threshold value  $E_T$  of the electric field for the finite electrical current might be crudely estimated by  $E_T \sim V_0/(qa)$ , which is in agreement with our calculations (not shown). However, in reality the threshold electric field will be much smaller in the presence of the degenerate electron gas because the weak local trap potential will be screened. While we have chosen in our numerical calculation a large electric field ( $2.3 \cdot 10^4 \text{ V/cm}$ ) and a low mobility of the sample ( $\mu = e\tau/m \approx 2000 \text{ cm}^2/\text{Vs}$ ), the Devil’s staircase may be observed in a broad range of parameters. We also note that the specific

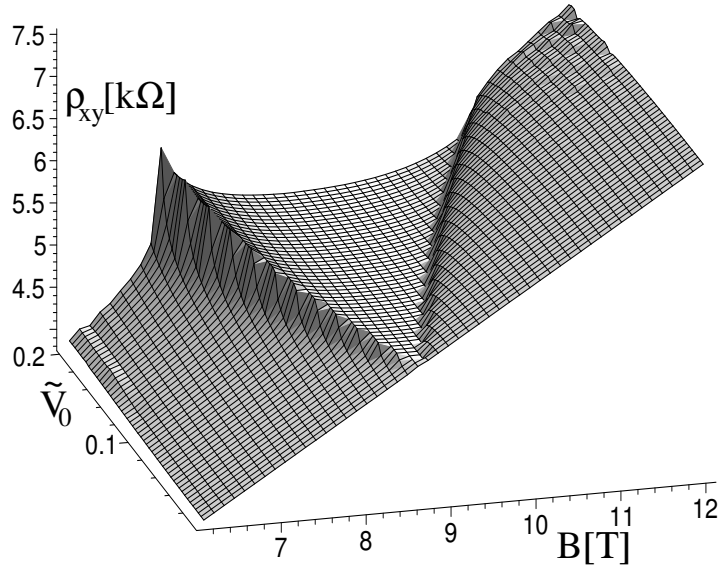


**Figure 4.7:** Dependence of the  $\rho = 1$ -plateau on  $\tilde{V}_0$ ; cf. Fig. 4.6.

form of the potential (4.13) is not relevant. However, the steepness of the potential influences the shape of the  $\rho_{xy}$ -“plateaus”. Large steepness (large  $\beta$ ) results in wide and curved  $\rho_{xy}$ -“plateaus”. It should be mentioned also that the Devil’s staircase will not be seen in the conventional Hall bar where the electrical current is fixed along the bar and the induced Hall voltage is measured. To measure the electrical current in two-dimensional samples for fixed applied voltages, one needs to use metallic leads which span the entire length of two opposite edges of the sample.

### 4.1.5 Summary

We have calculated the magnetoresistance of a lateral surface superlattice with strong momentum relaxation where the cyclotron motion is not involved. Our calculations show a fractal plateau structure in the magnetoresistance which stems from purely classical nonlinear dynamics. We have explained our calculational results in terms of the theory of circle maps where the Devil’s staircase is already well understood.

## 4.2 Coupled nanomechanical shuttles

### 4.2.1 Introduction

Recently, nanoelectromechanical systems (NEMS) have attracted great attention due to fundamental aspects in new electrical transport properties as well as new technology complementary to conventional microelectromechanical systems (MEMS) engineering [347]. A prototype of NEMS, single electron shuttle, was suggested by Gorelik *et al.* [312] which is a single electron transistor combined with its mechanical degree of freedom. The charge shuttles can be realized in two different ways in experiments. In a top-down approach, the charge shuttles can be realized by miniaturization of silicon structure [348, 349]. The other way is a bottom-up approach, where the charge shuttle is produced from molecules such as  $C_{60}$  [350].

In this section, we investigate the transport and the dynamical properties of tunnel-coupled double charge shuttles. The nonlinearity involved in this system shows an interesting bistable regime, where the electric current characteristics are of potentially great importance in NEMS applications. An interesting situation arises when the two shuttles are totally symmetric. In this case, through a dynamical symmetry breaking the system produces a net direct electric current. Symmetry-broken electric current under time-periodic perturbation has been an interesting topic of many theories and experiments [351] where a complete understanding is still necessary. We show that the double charge shuttle (DCS) allows for symmetry-broken DC current caused by parametric instability. This is in contrast to the single shuttle system where the DC current is vanishing in symmetric configuration.

### 4.2.2 The system

We start with the formalism of single electron tunneling [78] and classical dynamics which has been used for single charge shuttle [306, 312]. The drain lead is in the left side of the source lead where the ac voltage  $V(t) = V_0 \sin(\omega t)$  is applied to the source compared to the drain, see Fig. 4.8. The capacitance is supposed to be not sensitive to the displacement while the resistance is a function of displacements  $x_1$  and  $x_2$ :

$$\begin{aligned} R_1(x_1) &= R_1(0)e^{x_1/\lambda}, \\ R_2(x_1 - x_2) &= R_2(0)e^{(x_2-x_1)/\lambda}, \\ R_3(x_2) &= R_3(0)e^{-x_2/\lambda}. \end{aligned} \quad (4.14)$$

Here,  $\lambda$  is a phenomenological tunneling length. When the mutual capacitance of the  $j$ -th junction is  $c_j$ , the capacitance matrix is constructed as  $C_{kl} = c_k + c_{k+1}, -c_{k+1}, -c_k, 0$  for  $l = k, l = k + 1, l = k - 1$ , otherwise, respectively. The internal charging energy is given by

$$\epsilon(Q_1, Q_2) = \frac{1}{2} \sum_{k,l}^2 (C^{-1})_{kl} Q_k Q_l. \quad (4.15)$$

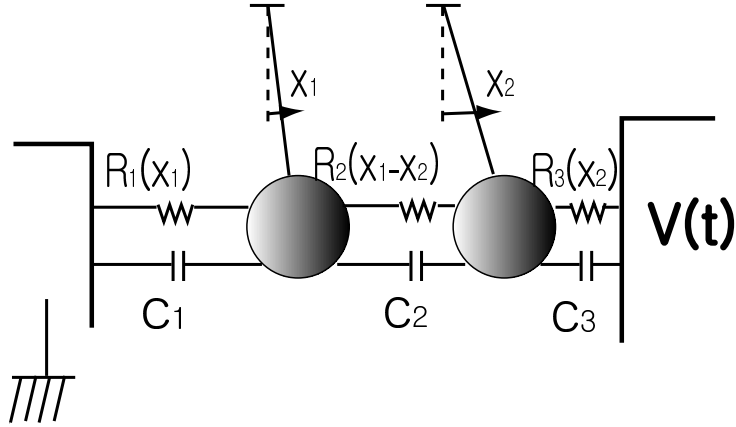


**Figure 4.8:** A schematic figure of the double charge shuttle.

The energy loss  $E_j$  of the  $j$ -th junction is

$$E_1 = \frac{c_{\text{tot}}}{c_1} eV + \epsilon(Q_1, Q_2) - \epsilon(Q_1 - e, Q_2), \quad (4.16)$$

$$E_2 = \frac{c_{\text{tot}}}{c_2} eV + \epsilon(Q_1, Q_2) - \epsilon(Q_1 + e, Q_2 - e), \quad (4.17)$$

$$E_3 = \frac{c_{\text{tot}}}{c_3} eV + \epsilon(Q_1, Q_2) - \epsilon(Q_1, Q_2 + e) \quad (4.18)$$

with the total capacitance  $c_{\text{tot}}$ . The rate of the tunneling from left to the right at the  $j$ -th junction at low temperature and environmental impedance is

$$\vec{\Gamma}_{n_1, n_2}^{(j)} = \frac{1}{e^2 R_j} E_j(V, Q_1, Q_2) \Theta[E_j(V, Q_1, Q_2)], \quad (4.19)$$

where the island charges  $Q_1, Q_2$  are integer multiple of  $-e$ ;  $Q_i = -n_i e$ . By replacing  $V, Q_1, Q_2$  with  $-V, -Q_1, -Q_2$  in the right-hand side of the above equation, one can get  $\overleftarrow{\Gamma}_{n_1, n_2}^{(j)}$ .

Now we come to the equations of motion. The time evolution of the probability  $P_{n_1, n_2}$  for the island charges  $Q_1 = -n_1 e, Q_2 = -n_2 e$  is given by the following rate equation

$$\frac{dP_{n_1, n_2}}{dt} = \vec{\Gamma}_{n_1-1, n_2}^{(1)} P_{n_1-1, n_2} + \overleftarrow{\Gamma}_{n_1+1, n_2}^{(1)} P_{n_1+1, n_2} \quad (4.20)$$

$$+ \vec{\Gamma}_{n_1-1, n_2+1}^{(2)} P_{n_1-1, n_2+1} + \overleftarrow{\Gamma}_{n_1+1, n_2-1}^{(2)} P_{n_1+1, n_2-1} \quad (4.21)$$

$$+ \vec{\Gamma}_{n_1, n_2-1}^{(3)} P_{n_1, n_2-1} + \overleftarrow{\Gamma}_{n_1, n_2+1}^{(3)} P_{n_1, n_2+1} \quad (4.22)$$

$$- \sum_{j=1}^3 (\overleftarrow{\Gamma}_{n_1, n_2}^{(j)} + \vec{\Gamma}_{n_1, n_2}^{(j)}) P_{n_1, n_2}. \quad (4.23)$$

At low temperatures the fluctuation of the displacements  $x_1, x_2$  are negligible compared to the charge fluctuations. While the charge fluctuations are important to the noise properties, we suppose  $1/\Gamma$  be much smaller than the typical time scale of displacement

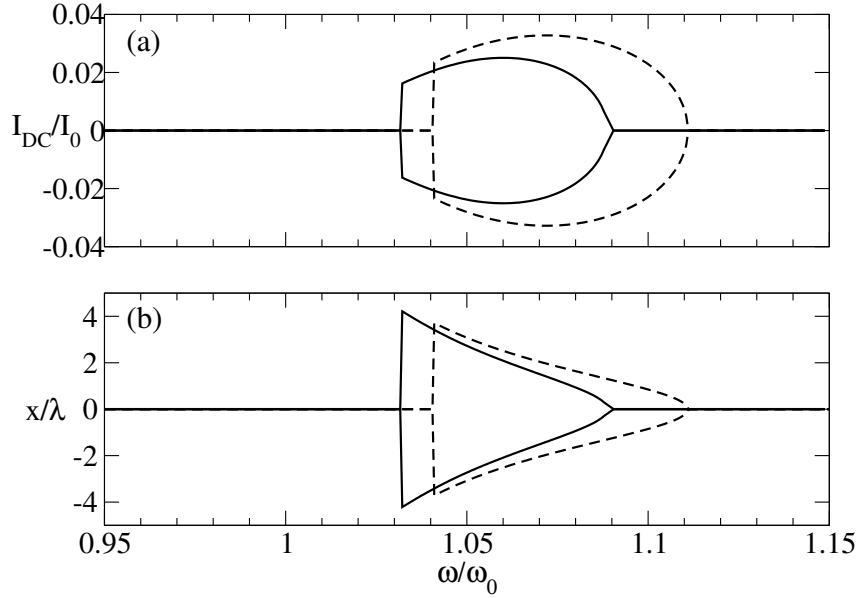


**Figure 4.9:** (a) The symmetry-broken DC current in units of  $I_0 = V_0/R$  vs. frequency of the applied AC voltage. The solid line refers to the result from the full calculations mentioned in the text and the dashed line refers to the result from the simplified calculation in the adiabatic limit. The parameters are fixed to  $c = 100 \text{ aF}$ ,  $R = h/e^2$ ,  $\lambda = 20 \text{ nm}$ ,  $L = 500 \text{ nm}$ ,  $\omega_0 = 50 \text{ MHz}$ ,  $\gamma = 0.025 \omega_0$ ,  $m = 1.1 \times 10^{-21} \text{ Kg}$ , and  $V_0 = 10.8 \text{ mV}$ . (b) The corresponding stroboscopic plot of  $x = x_1 - x_2$  obtained for a fixed phase of the oscillating voltage.

and investigate the mechanical motions using the mean island charge

$$\langle Q_i(t) \rangle = -e \langle n_i(t) \rangle = -e \sum_{n_1, n_2} n_i P(n_1, n_2, t) . \quad (4.24)$$

The island charges experience the force produced by the electric field  $-V(t)/L$ ;

$$\ddot{x}_i + \gamma_i \dot{x}_i + \omega_{0i}^2 x_i = -\frac{V(t)}{m_i L} \langle Q_i(t) \rangle, \quad i = 1, 2 \quad (4.25)$$

where  $L$  is the source-drain distance and  $\gamma_i$ ,  $\omega_{0i}$  denote the friction constant and the natural angular frequency of  $i$ -th shuttle. Note that the resonators are modeled as linear oscillators. The nonlinearity of the full system comes from the coupling via tunneling. The electric current from the source in the right-hand side to the drain in the left-hand side is computed as

$$I(t) = e \sum_{n_1, n_2} (\overrightarrow{\Gamma}_{n_1, n_2}^{(1)} - \overleftarrow{\Gamma}_{n_1, n_2}^{(1)}) P_{n_1, n_2}(t) . \quad (4.26)$$

### 4.2.3 Numerical and analytical results

In the following, we will consider a symmetric configuration:  $\omega_{0i} = \omega_0$ ,  $\gamma_i = \gamma$ ,  $m_i = m$ ,  $R_1(0) = R_3(0) = 0.5R_2(0) \equiv R$ , and  $c_1 = c_3 = 2c_2 \equiv c$ . In Fig. 4.9(a), we plot the

time-averaged current  $I_{\text{DC}} = \frac{\omega}{2\pi} \int_0^{2\pi/\omega} I(t)dt$ . From the symmetry of the configuration one would expect that the DC current computed according to Eq. (4.26) is zero for all frequencies of the applied AC voltage. Fig. 4.9(a), however, shows that in the vicinity of the natural frequency of the oscillators,  $\omega_0$ , the DC current can be negative or positive depending on the initial conditions. The initial conditions are specified by the initial position  $x_1, x_2$  and the velocities  $\dot{x}_1, \dot{x}_2$  at a given starting time. In the regime of zero current all initial conditions are attracted to an unique stable asymptotic solution (the so-called attractor). In the nonzero current case, two such attractors coexist and cause a *dynamical symmetry breaking*.

The global behaviour of the attractors can be conveniently represented on a stroboscopic section (a special case of a Poincaré section [307]) defined by a fixed value of the phase of the driving voltage. Fig. 4.9(b) shows the stroboscopic section at a fixed phase of the applied voltage. We find the center of mass coordinate does not move;  $X = (x_1 + x_2)/2 \approx 0$  for all frequencies  $\omega$ . Meanwhile in the regime of nonzero DC current we find two symmetry-related solutions for the relative coordinate  $x = x_1 - x_2$ .

Further insight can be obtained by investigating the adiabatic limit of the system. In Fig. 4.9 we plot the DC current and relative coordinates computed from the adiabatic approach using dotted lines. One can notice that the full numerical results are quite close to those obtained in the adiabatic limit. Therefore we may rely on the adiabatic approach for the analysis of the bistability.

In the adiabatic limit the electronic relaxation is much faster than the mechanical motion, i.e.,

$$\omega R c, \omega_0 R c \ll 1. \quad (4.27)$$

In this case, a classical circuit analysis of Fig. 4.8 on the charges  $q_j$  accumulated in each capacitor  $c_j$  gives

$$\begin{aligned} \frac{q_1}{R_1 c_1} - \frac{q_2}{R_2 c_2} &= \frac{q_2}{R_2 c_2} - \frac{q_3}{R_3 c_3} = 0 \\ \frac{q_1}{c_1} + \frac{q_2}{c_2} + \frac{q_3}{c_3} &= V(t). \end{aligned} \quad (4.28)$$

From the solutions of the above linear equations, the net charges of each islands  $Q_1 = q_1 - q_2$ ,  $Q_2 = q_2 - q_3$  are simply given by

$$Q_1 = Vc \frac{e^{x_1/\lambda} - e^{(x_2-x_1)/\lambda}}{e^{x_1/\lambda} + 2e^{(x_2-x_1)/\lambda} + e^{-x_2/\lambda}}, \quad (4.29)$$

$$Q_2 = Vc \frac{e^{(x_2-x_1)/\lambda} - e^{x_2/\lambda}}{e^{x_1/\lambda} + 2e^{(x_2-x_1)/\lambda} + e^{-x_2/\lambda}}. \quad (4.30)$$

Inserting these equations into the equation of motion for the mechanical degree of freedom (4.25) gives the equation of motion for the center of mass coordinate

$$\ddot{X} + \gamma \dot{X} + \omega_0^2 X = \left( -\frac{cV(t)^2}{2mL} \right) \frac{e^{X/\lambda} - e^{-X/\lambda}}{e^{X/\lambda} + 2e^{-3x/2\lambda} + e^{-X/\lambda}}, \quad (4.31)$$

where  $x = x_1 - x_2$  is the relative coordinate. Clearly,  $X = 0$  is a solution, in agreement with our numerical finding that the center of mass is not moving. Exploiting this fact, the equation of motion for the relative coordinate  $x$  can be derived as

$$\ddot{x} + \gamma\dot{x} + \omega_0^2 x = -\frac{cV_0^2 \sin^2 \omega t}{mL} \tanh \frac{3x}{4\lambda}. \quad (4.32)$$

From the above equation one can see that  $x = 0$  is a trivial solution. However, this solution can be unstable as we will prove in the following. Note that if a nontrivial solution of  $x(t)$  exists then  $-x(t)$  is also a solution. This is the pair of bistable solutions. Since the equation is invariant under the time-translation operation  $t \rightarrow t + \pi/\omega$ , a periodic solution should satisfy  $x(t + \pi/\omega) = \pm x(t)$ . As will be shown later, this parity is important for the nonzero DC current.

The electric current in the adiabatic limit can be expressed as

$$I(t) = \frac{q_1(t)}{R_1(x)c_1} = \frac{V(t)}{R_1(x) + R_2(x_1, x_2) + R_3(x_2)}. \quad (4.33)$$

Therefore the time-averaged DC current reads

$$I_{\text{DC}} = I_0 \frac{\omega}{4\pi} \int_{t_0}^{t_0+2\pi/\omega} \frac{\sin \omega t}{e^{x(t)/2\lambda} + e^{-x(t)/\lambda}} dt, \quad (4.34)$$

where  $I_0 = V_0/R$ . The dashed line in Fig. 4.9(a) was obtained using the above formula which also shows a clear bistability.

Now we are going to show that the origin of the symmetry-broken current and the bistability is parametric instability. By linearizing the term  $\tanh(3x/4\lambda)$  in the right-hand side of Eq. (4.32), we get

$$\ddot{x} + \gamma\dot{x} + \Omega_0^2 \left[ 1 - \frac{\mu^2}{1 + \mu^2} \cos(2\omega t) \right] x = 0, \quad (4.35)$$

where  $\mu = \frac{V_0}{\omega_0} \sqrt{\frac{3c}{8\lambda mL}}$  and  $\Omega_0$  is the dressed harmonic frequency of the relative motion;

$$\Omega_0 = \omega_0 \sqrt{1 + \mu^2} = \sqrt{\omega_0^2 + \frac{3cV_0^2}{8\lambda mL}}. \quad (4.36)$$

Equation (4.35) is called a damped Mathieu equation which is a paradigm for studying parametric resonance [309]. The stability analysis in Ref. [309] up to second order of  $M$  shows that the motion is unstable in the interval  $\omega_- < \omega < \omega_+$  where

$$\omega_{\pm} = \Omega_0 \left( 1 \pm \frac{1}{2} \sqrt{M^2 - \gamma^2/\Omega_0^2} + \frac{11}{16} M^2 \right), \quad (4.37)$$

with  $M = \frac{\mu^2}{2(1+\mu^2)}$ . This interval is called principal instability interval. Obviously, the interval has finite width only if  $M > \gamma/\Omega_0$ , i.e., the strength of the driving,  $V_0$ , must be sufficiently large in order to get parametric instability.

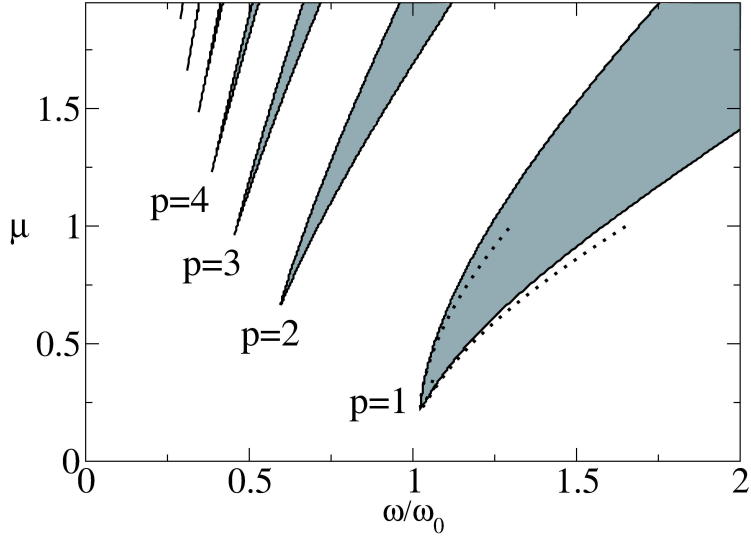


**Figure 4.10:** Bifurcation diagram  $\mu$  vs.  $\omega/\omega_0$  in the adiabatic limit for  $\gamma = 0.025\omega_0$ . Bistable regions (*Arnol'd tongues*) are mode-locked with  $p = 1, 2, 3, 4, \dots$ . The nonzero DC current arises only when  $p$  is odd. The dotted line denotes the boundary of the principal instability region obtained from the analytic formula (4.37).

From the above analysis and Fig. 4.9(b) we conclude that when entering the principal instability interval from the right-hand side the unique attractor turns into an unstable solution (a repeller) thereby creating two new attractors. This scenario leading to bistability is termed a supercritical pitchfork bifurcation. The bifurcation occurring when entering the principal instability interval from the left-hand side is different which can be seen from the abrupt change of the value of  $x$ . Here we have three attractors and two repellers (not shown). The repellers and the central attractor ( $x = 0$ ) merge in a subcritical pitchfork bifurcation creating a repeller at  $x = 0$ .

In Fig. 4.10, we plot the phase diagram of  $\mu$  and  $\omega/\omega_0$  which indicates the locations of the bistable regimes computed from Eq. (4.32). The dotted line denote the analytic results in Eq. (4.37) from the linearized equation (4.35). The reasonable agreement of the parameters showing the instability confirms that the parametric amplification causes the instability in the system. Beside the principal instability region there are higher-order regions in which the ratio of the frequency of the oscillators and the applied voltage is mode-locked to  $p = 2, 3, \dots$ . These regions, and also the principal instability region, are called *Arnol'd tongues* [352].

The second interval of instability denoted by  $p = 2$  in Fig. 4.10 arise from second harmonics of the system. The analytic formula for this region from the stationary solutions in Ref. [309] gives

$$\omega_{\pm} = \frac{1}{2}\Omega_0 \left( 1 + \frac{5}{12}M^2 \pm \frac{1}{8}\sqrt{M^4 - (4\gamma/\Omega_0)^2} \right). \quad (4.38)$$

The higher order bistable regions are found in our numerical calculations. The center of the intervals in each bistable regions are located where

$$\omega \approx \frac{\Omega_0}{p}; \quad p = 1, 2, 3, \dots \quad (4.39)$$

The main characteristics of the each bistable region is that the (unharmonic) frequency of the relative motion is given by  $p\omega$  even though there is a mismatch between the natural harmonic frequency and the frequency of the voltage, which is called *mode-locking* in the field of nonlinear dynamics [307]. In Fig. 4.11, we plot the time series of the relative coordinate  $x$  for various frequencies corresponding to different bistable regimes. One can clearly see the  $p$ -th order mode-locking. For instance, in spite of the large mismatch between  $\omega$  and  $\omega_0$  when  $p = 1$  ( $\omega = 1.45\omega_0$ ) the oscillation frequency is clearly given by  $\omega$ .

It is important to note that the rectified DC current arises only when  $p$  is an odd number of integer. When  $p$  is even, the periodic solution  $x(t)$  has even parity i.e.,  $x(t + \pi/\omega) = x(t)$ . In this case, the integration in Eq. (4.34) from  $t_0$  to  $t_0 + \pi/\omega$  is cancelled by the integration from  $t_0 + \pi/\omega$  to  $t_0 + 2\pi/\omega$ .

One may ask whether the parametric instability can cause symmetry breaking already in a single shuttle system. When we write the tunnel resistances as  $R_1(x) = R(0)e^{+x/\lambda}$  and  $R_2(x) = R(0)e^{-x/\lambda}$  where  $x$  is the coordinate of the shuttle, the equation of motion is given by

$$\ddot{x} + \gamma\dot{x} + \omega_0^2 x = -\frac{cV_0^2 \sin^2 \omega t}{mL} \tanh \frac{x}{\lambda} \quad (4.40)$$

similar to Eq. (4.32). Therefore, in the sense of the mechanical motion, the parametric resonance gives rise to the bistability and the bifurcation diagram is quite similar to Fig. 4.10. However, *the single shuttle systems does not allow a symmetry-broken DC current*. The absence of the DC current in the symmetric single shuttle is clear from the time-averaged current formula of the system

$$I_{DC} = I_0 \frac{\omega}{4\pi} \int_{t_0}^{t_0 + 2\pi/\omega} \frac{\sin \omega t}{\cosh x/\lambda} dt. \quad (4.41)$$

Note that the symmetry of the periodic solution  $x(t + \pi/\omega) = \pm x(t)$  always ensures

$$\cosh [x(t + \pi/\omega)/\lambda] = \cosh [x(t)/\lambda] \quad (4.42)$$

confirming that the above integral is zero.

In experimental systems, the charge and displacement fluctuations exist due to the discreteness of charges and finiteness of temperature. Noise properties of two colloidal particles in DC source-drain bias have been numerically investigated in Ref. [353] where the shot noise produces random telegraph noise. The noise properties in the presence of oscillating source-drain voltage are expected to contain interesting information on the mechanical properties, which is currently under study. For instance, the shuttles are expected to show enhanced noise power in the bistable regimes we studied in this work.

Our results are robust against the finite temperature effect which modifies the tunneling rate in Eq.(4.19). This is because the dynamical symmetry breaking appears as a classical

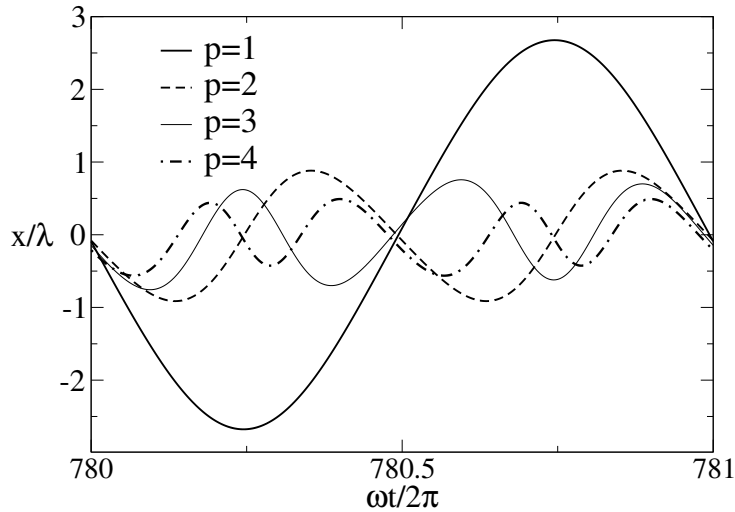


**Figure 4.11:** Time evolution of the relative coordinate  $x = x_1 - x_2$  for typical sets of values  $(\omega/\omega_0, \mu)$  belonging to the bistable regimes of  $p = 1, 2, 3, 4$ ;  $\omega/\omega_0 = 1.45, 0.79, 0.53, 0.415$  and  $\mu = 1.414$ .

effect. While the perfect left/right symmetry does not exist when the tunnel resistances differ by multiple of 5 or 10, we find the effects are still visible from the enhancement of the net current. The enhanced net current is also visible when the resonance frequencies and tunneling coefficients differ by 10 percents. This robustness comes from the nonlinear phenomenon, *mode-locking*, where the mechanical motions are locked to the driving voltage in spite of small variations of the system parameters. One may also note that the tunneling length  $\lambda$  enters the instability condition through  $\mu$ , so the net current can exist in a reasonable range of  $\lambda$  if  $\mu$  and  $\omega$  belongs to the Arnol'd tongue.

#### 4.2.4 Summary

The transport through two tunnel-coupled symmetric charge shuttles has been studied. We found that the oscillation frequencies of the two shuttles are mode-locked to the applied oscillating voltage. Moreover, we observed a dynamical bistability which allows for non-zero electric currents. The origin of this phenomenon has been traced back to parametric instability induced by the nonlinear coupling of the mechanical and electrical degree of freedom.

---

## 4.3 Multi-walled carbon nanotubes

### 4.3.1 Introduction

Carbon nanotubes have attracted great attention due to their remarkable electrical and mechanical properties [354]. Many theoretical and experimental studies have demonstrated that single-walled nanotubes (SWNTs) exhibit ballistic electron conduction [13, 355], and single-molecule devices utilizing semiconducting SWNTs have been realized [356, 357]. On the other hand, despite useful applications of multi-walled nanotubes (MWNTs) [358], the transport properties of MWNTs are not well understood and even controversial; conductance measurements using scanning probe microscope showed ballistic behavior [79], while magnetoresistances measured for MWNTs on top of metallic gate indicated diffusive conduction [80, 81].

In general, MWNTs have very complex electronic structure, so that a direct use of their transport properties is severely hindered. If concentric carbon shells are especially incommensurate, the Bloch theorem is no longer valid, and the Landauer formula for conductance is not directly applicable because it is difficult to count the number of conducting channels [359]. In fact, several experiments on MWNTs indicated that carbon shells have often different periodicities [2, 360]. However, electronic structure calculations have been mostly focused for commensurate multi-walled nanotubes so far. Here, instead of directly calculating conductances, we investigate the *spectral properties of energy levels* in clean incommensurate MWNTs.

### 4.3.2 The system

To study the spectral correlation, we consider double-walled carbon nanotubes (DWNTs), because the electrical conduction in MWNTs is believed to be governed by the outermost shells [81, 361]. We use a tight-binding model with one  $\pi$ -orbital per carbon atom, which successfully describes the electronic structure of DWNTs [362–364]. The tight-binding Hamiltonian is given by

$$H = \gamma_0 \sum_{i,j} c_j^\dagger c_i - W \sum_{i',j'} \cos(\theta_{i'j'}) e^{(a-d_{i'j'})/\delta} c_{j'}^\dagger c_{i'}, \quad (4.43)$$

where  $\gamma_0$  ( $= -2.75$  eV) is the hopping parameter between intra-layer nearest neighbor sites,  $i$  and  $j$ , and  $W$  ( $= \gamma_0/8$ ) is the strength of inter-wall interactions between inter-layer sites,  $i'$  and  $j'$ , with the distance of  $d_{i'j'}$  and the cut-off for  $d_{i'j'} > 3.9$  Å. Here  $\theta_{ij}$  is the angle between two  $\pi$  orbitals,  $c_{i'}$  is the annihilation operator of an electron on site  $i'$ ,  $a$  ( $= 3.34$  Å) is the distance between two carbon walls, and  $\delta = 0.45$  Å.

### 4.3.3 Spectral analysis

For the unfolding of the single-particle energy spectrum we use the Gaussian broadening scheme [327].

The two shells of DWNTs are incommensurate if the ratio of the unit cell lengths along the tube axis is irrational. We test many incommensurate DWNTs, where both the shells are metallic or semiconducting, a semiconducting shell is inside a metallic tube, and vice versa. The diameters of the inner and outer tubes are 1.5 and 2.2 nm, respectively, and the nanotube length is set to be about 53 nm. We find the spectral properties are similar for all the incommensurate DWNTs with different helicities. (See the nearest-neighbor spacing distribution  $P(s)$  in Figure 4.12). Since the spectral properties are similar for all the tubes considered here, from here on, we only present the spectral properties of the (16,5)/(23,8) DWNT where the semiconducting (16,5) single-walled tube is aligned inside the metallic (23,8) tube. In the inset of Figure 4.12, the number variance  $\Sigma(L)$  is also shown for the (16,5)/(23,8) nanotube. We find that  $P(s)$  and  $\Sigma(L)$  cannot be described by the Poisson distribution or GOE, but, they are well described by the semi-Poisson (SP) distribution [190, 332, 365], see Eqs. (4.5)–(4.6).

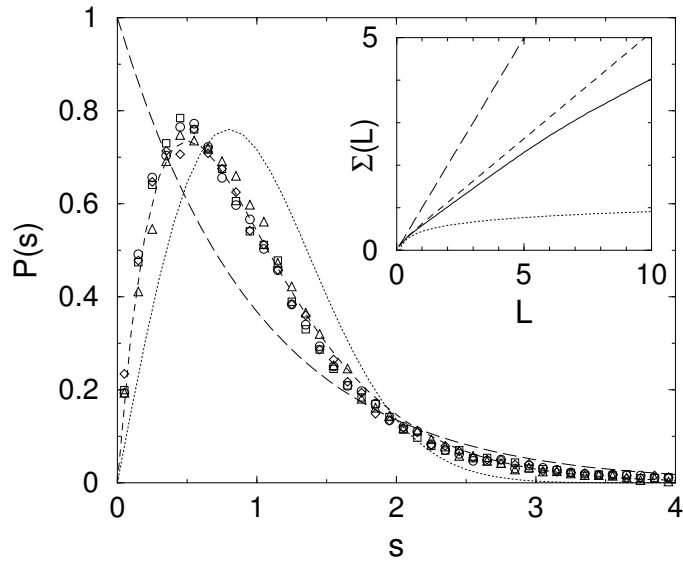


**Figure 4.12:** The nearest energy spacing distribution  $P(s)$  for energy levels between -7 and 7eV and different helicities (16,5)/(23,8) (triangle), (17,2)/(16,15) (circle), (16,5)/(17,15) (square), and (17,2)/(21,9) (diamond). The semi-Poisson (dashed), Poisson (long-dashed), and GOE (dotted) distributions were also plotted for comparison. The inset shows the number variance  $\Sigma(L)$  for (16,5)/(23,8) case. The number of considered levels for (16,5)/(23,8) case is 20220.

While  $P(s)$  carries information on short-range correlation in the energy spectra,  $\Sigma(L)$  contains rather long-range correlation. Usually  $\Sigma(L)$  indicates a deviation from the universal value for large  $L$ , thus, the particle dynamics becomes nonuniversal at short time scale. For large  $L$ , the spectral correlation is not universally SP but depends on the helicity of nanotubes. The deviation from the SP distribution gives useful information; the linear behavior for large  $L$ , i.e.,  $\Sigma(L)/L \rightarrow \chi$ , represents the level compressibility, and for disordered metals  $\chi$  was shown to be [366]

$$\chi = \frac{1}{2} \left( 1 - \frac{D_2}{d} \right), \quad (4.44)$$

where  $D_2$  is the multifractal exponent of the inverse participation ratio and  $d$  is the spatial dimension. Here  $D_2/d$  is related to the “probability of return” [367],

$$p(t) \propto t^{-D_2/d}. \quad (4.45)$$

Our incommensurate DWNT behave as a two-dimensional systems ( $d = 2$ ) with off-diagonal disorder, which has a mixed boundary between periodic and hard-wall conditions. From the inset in Fig. 4.12, we estimate  $D_2/d$  to be about 0.32 for the DWNT considered here. While  $p(t) \propto t^{-d/2}$  in normal diffusion, our system exhibits anomalous diffusion, which was also found by previous wavepacket spreading calculations [364].

The SP distribution in Fig. 4.12 is mostly contributed from the region of large  $|E|$ , where the density of states (DOS) is high, while the energy statistics is usually not independent of the energy regime. Since real electron conductances occur near the Fermi level, it is instructive to examine the energy-level statistics on various energy windows. Although we discuss the level statistics when the Fermi level increases, we find similar statistics for the downward shift of the Fermi level, which usually occurs in hole-doped tubes.

In the level statistics, we remove the states lying between 0 and 0.08 eV, which are associated with the localized states near the sample boundary due to the finite size of the system. In Fig. 4.13(a),  $P(s)$  is drawn for low energy states from 0.08 to 1.3 eV, and exhibits the Poisson distribution, indicating that the energy levels are uncorrelated. Single-wall nanotubes, which are constituents of the DWNT, are approximately described in terms of  $P_P(s)$  in Eq. (4.3) and  $\delta(s)$ . In this case, the delta-function peak results from the doubly degenerate states due to inversion symmetry. If inter-wall interactions are absent in the DWNT, a superposition of two independent spectra of the nanotube constituents is also described by the Poisson and delta functions.

When inter-wall interactions break the degeneracy, smearing out the delta-function peak,  $P(s)$  is still Poisson-like, as shown in Fig. 4.13(a), implying that the energy mixing between the two carbon shells is insignificant for low energies. In the low energy regime, it is useful to use the Landauer formula,

$$G = \frac{2e^2}{h} \sum_i T_i(E_F), \quad (4.46)$$

where  $T_i(E_F)$  is the transmission probability of the channel  $i$  obtained from the band structure calculations at the Fermi energy  $E_F$  [359]. Our results infer that quantized conductances observed in MWNTs [79] may be due to the fact that the Fermi level is close to the charge neutrality point,  $E_F \approx 0$ . However, it is usually very difficult to find experimentally the location of the Fermi level.

As the Fermi level is shifted further, since the mean level spacing becomes smaller and the inter-wall interaction matrix elements become more significant, the inter-wall interactions induce a more significant mixing of the energy levels between the carbon shells. For higher energy states, we find that  $P(s)$  follows the SP distribution, as shown in Figs. 4.13(b) and (d). The quantum conductance in this regime still remains a challenging problem. In particular, it is a nontrivial but important task to find the tube length dependence of

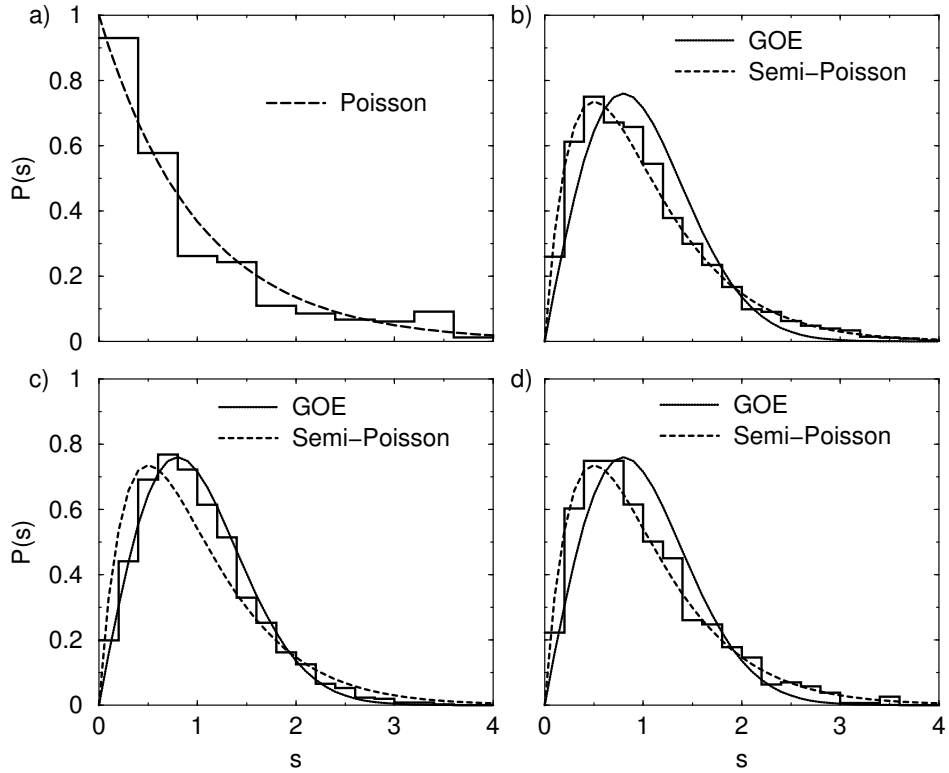


**Figure 4.13:** The nearest energy spacing distribution  $P(s)$  on the energy windows of (a) (0.08,1.3eV) with 511 levels, (b) (1.0,2.5eV) with 1872 levels, (c) (2.5,3.5eV) with 2696 levels, and (d) (3.5,4.0eV) with 888 levels.

quantum conductance in this regime. Recent calculations [368] showed negligible inter-wall tunneling currents for the tube length of  $1 \mu\text{m}$ , but it is questionable whether one can use the Bardeen's formalism for DWNTs where the coherent back-tunneling between carbon shells is non-negligible. According to the weak localization formula,  $\delta\sigma \propto -\int dt p(t)$ , with Eq. (4.45), conductances may depend on the tube length. However, the weak localization formula considers only the interference of the pair of time-reversal paths, which is not guaranteed in the critical regime.

In Fig. 4.13(c), one can see that the critical statistics evolves to the GOE as going to the higher energy region, where  $P(s)$  is quite close to the Wigner-Dyson surmise (4.1). We also find the GOE-like statistics for both  $P(s)$  and  $\Sigma(L)$  in all the incommensurate DWNTs tested here. The appearance of the GOE-like behavior indicates that all the symmetries except for time-reversal symmetry are effectively broken, and the corresponding electron motion is ergodic. In this regime, the conductivity of MWNTs may be described by the weak localization theory. One should also note that the weak localization theory is applicable for energies higher than those in the first critical regime, because the sequence of statistics with increasing energy is

$$\text{Poisson} \rightarrow \text{SP} \rightarrow \text{GOE} \rightarrow \text{SP}.$$

In MWNTs on top of metallic gates, the details of contacts, local excessive charges, and

depletion of charge carriers may change the position of the Fermi level [369]. Based on our results, we guess that in conductance measurements [13, 81, 356, 357], the Fermi level is shifted to the GOE regime or to the critical regime (close to the GOE) where conductivity is properly described by the weak localization formula. If the Fermi level lies in that critical regime, the small periodic oscillation observed by magnetoconductance measurements [81], which cannot be reconciled with the weak localization theory, might be a non-universal fingerprint of interferences between certain long trajectories in the critical regime. Further theoretical effort is needed for this issue.

The calculated variances over every 1000 consecutive levels are compared with the densities of states for two different DWNTs in Fig. 4.14. The size of fluctuations of the level spacing is dictated by the spectral statistics;

$$\langle(s - \langle s \rangle)^2\rangle = \int_0^\infty ds(s - 1)^2 P(s) = 1, \frac{1}{2}, \frac{4}{\pi} - 1 \quad (\text{Poisson, SP, GOE}). \quad (4.47)$$

It is expected that the effect of inter-wall interactions on the level spacing is most significant when the mean level spacing  $\Delta$  is minimum near  $E = \pm\gamma = \pm 2.75$  eV, where the maximum DOS occurs on a graphene sheet. One can see  $\langle(s - \langle s \rangle)^2\rangle = \frac{4}{\pi} - 1 \approx 0.27$  near  $E = \pm\gamma = \pm 2.75$  eV, which is a signature of GOE distribution. The variances larger than 1 near  $E = 0$  are due to the fact that  $P(s)$  is not completely Poisson-like because the degenerate levels of each nanotube layer are not completely lifted up.

We find that a transition from the Poisson-like to SP-like statistics occurs at lower energies as the diameter of nanotubes increases. One of the reasons for this trend seems that the DOS is enhanced for nanotubes with larger diameters. The transition energy is close to 1 eV in the (43,8)/(51,9) DWNT with the outer and inner diameters of 4.4 and 3.7 nm, respectively, while it is higher than 1 eV for the (16,5)/(23,8) tube with the diameters of 2.2 and 1.5 nm, as shown in Fig. 4.14. Since experimentally measured diameters of MWNTs are often in the range of 10 nm, we expect that the crossover of spectral statistics occurs at energies lower than 1 eV.

Very recently, Kociak and his co-workers [370] measured the conductance of a DWNT whose two tubes have a gap and showed linear conductance near the Fermi level. The linear conductance or a finite DOS near the Fermi level indicates that the Fermi level indeed can be shifted far from the charge neutral point. Further investigation on the relation between spectral statistics and  $I-V$  curves is necessary to understand the commensurability effects in DWNTs.

Finally, we point out that the spectral statistics might be probed through conductance measurements in the Coulomb blockade regime [371, 372]. The temperature should be low enough to ensure that  $k_B T < U, \Delta$ , where  $U$  is the charging energy of nanotube dot. In the resonant tunneling regime, where electron tunnels through one quantum level, if electron-electron interactions are not too strong [373], the conductance peak spacing with varying the gate voltage provides information on the single-particle energy spacing.

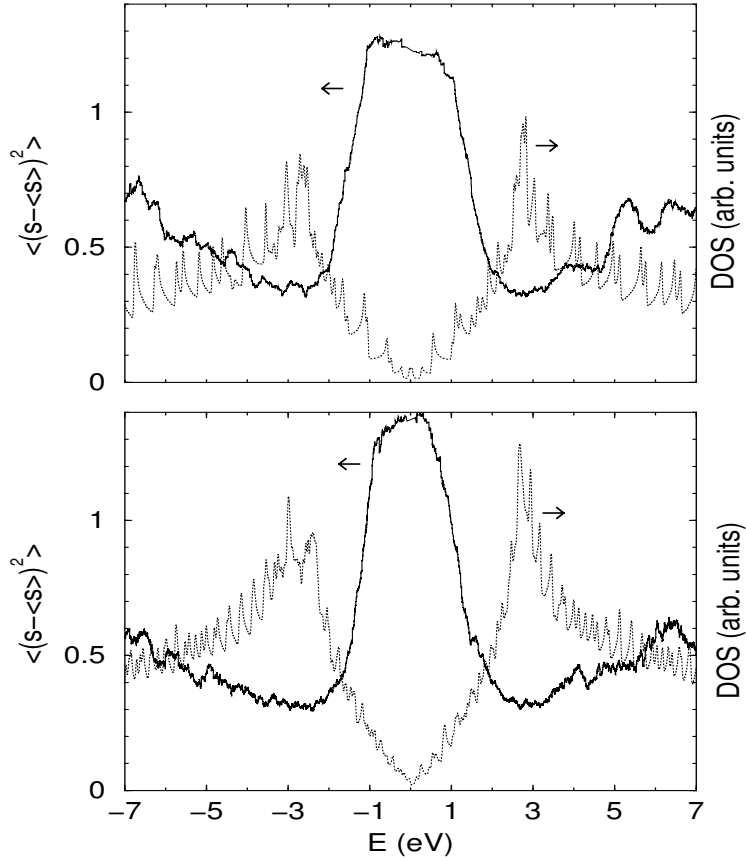


**Figure 4.14:** The variance of the level spacing (solid) in Eq. (4.47) and the density of states (dotted) in arbitrary units for the (16,5)/(23,8) (upper panel) and (43,8)/(51,9) (lower panel) double-walled tubes.

#### 4.3.4 Conclusion

We have shown that the spectral statistics of incommensurate double-walled nanotubes follows the Poisson, GOE, or SP distribution, depending on the energy window, while the overall states are well described by the SP distribution. This results indicate that the nature of electron transport in multi-walled nanotubes can be either ballistic, diffusive, or critical, depending on the position of the Fermi level. It is questioned whether the usual weak localization correction is relevant to existing experiments. The Coulomb blockade oscillation in nanotube dots is suggested to investigate the spectral statistics in this work.

## 5 Conclusions and future directions

In this Habilitation thesis, we have discussed nonlinear dynamics, quantum chaos, and light-matter interaction in semiconductor nanostructures and optical microcavities.

Deformed microdisks have been studied with particular emphasis on quantum chaos of open systems. One finding of utmost practical relevance is the existence of high quality modes with unidirectional light emission. We have demonstrated that this can be achieved by either exploiting avoided resonance crossings or by using the unstable manifolds of chaotic repellers. Another central finding is the formation of high- $Q$ , scarlike modes near avoided resonances crossings. It explains why long-lived states in open systems are often scarred, i.e., localized along unstable periodic ray trajectories. This is not only important for microcavities but also for other open mesoscopic systems. Moreover, we computed and discussed the optical properties of pillar microcavities. Excellent agreement with experimental spectra and CCD images of mode structures has been demonstrated.

The studies of quantum chaos in optical microcavities can be extended in several directions: (i) In recent years there have been exciting new developments in the field of quantum chaos in systems with mixed phase space, that are systems where chaotic and regular motion coexist. One can now study to what extent these findings for closed systems have to be modified in the case of open optical systems. One example for such a new development in quantum chaos is the concept of “hierarchical states” [374]. These states live in the hierarchical region between the regular and chaotic parts of classical phase space. Another example is “flooding of regular islands” [375, 376], which refers to the disappearance of regular states and the occupation of chaotic states in the corresponding regular region. (ii) Recently, a strong interest in the statistical properties of eigenenergies of open systems emerged. One active research subject is the study of so-called fractal Weyl’s laws [377, 378]. Optical microcavities are ideal systems for theoretical and experimental studies of this kind. (iii) Pattern formation in partially and fully chaotic microlasers due to nonlinearities induced by the gain material has attracted considerable attention [379–384]. It would be of great interest to study the proposed schemes for unidirectional light emission in this context.

The results of the mode calculations have been used as input in a microscopic theory of light-matter interaction in QD-microcavity systems including many-body and quantum-optical effects. The resulting semiconductor luminescence equations (SLE) can be used to study photoluminescence from an inhomogeneously broadened QD ensemble in free space or embedded into an optical microcavity. The numerical results show convincing agreement with recent experimental data. An important result is that semiconductor QDs may not always be considered as “artificial atoms”. The basic difference between simple few-level atoms and QDs are the nontrivial correlations between carriers due to

the Coulomb and light-matter interaction. A lack of full correlations in semiconductor QDs has experimental consequences: the time-resolved photoluminescence decay can be strongly nonexponential and excitation dependent. In such a case, the only way to extract the Purcell factor from the experimental data is the comparison to a microscopic theory. The introduced microscopic description of light-matter interaction in QD-microcavity systems can be systematically extended to study further physical effects. One such extension that we discussed in this work is the incorporation of carrier-photon correlations. This gives direct access to the photon statistics of laser emission. Our microscopic semiconductor theory shows important quantitative differences to theories based on atomic systems. For example, the jump in the input-output curves does not scale as  $1/\beta$ . This is highly relevant for the analysis of experiments, since often the spontaneous emission factor  $\beta$  is extracted from input-output characteristics. Another extension introduced in this work is the first-order coherence as function of the delay time. A central result here is the crossover from a Gaussian-like decay with a small coherence time below threshold to an exponential decay with strongly increased coherence time at threshold.

Future directions of research based on the introduced microscopic theory are the following: (i) Currently in progress are studies of superradiance from QD ensembles. Superradiance is a phenomenon of collective emission of an ensemble of light emitters [385]. First experimental evidence for superradiance from QDs has been reported only recently [386]. The theoretical analysis of this situation is still restricted to two-level emitters [387]. Our approach allows to overcome this limitation and to study, e.g., the influence of carrier-carrier correlations on the phenomenon of superradiance. Also one could investigate superradiant effects in QD-microcavity lasers. (ii) Moreover, the effect of inhomogeneous broadening on QD-microcavity lasers can be studied. (iii) We have discussed the autocorrelation function  $g^{(2)}(\tau)$  for vanishing delay time  $\tau$ . In very recent experiments on QD-microcavity lasers the autocorrelation function for  $\tau \neq 0$  has been measured [388]. Presently, we extend our semiconductor theory to compute the full  $g^{(2)}(\tau)$ . (iv) Another promising line of research is the investigation of single-QD lasing in microcavities. Single-atom lasing has been realized several years ago [389], revealing interesting photon statistics [390]. Single-QD lasing still faces severe experimental difficulties, but with improved microcavity and QD design this regime may be reached within the next few years.

Finally, the field of nonlinear dynamics and quantum chaos in nanostructures has been addressed. The focus has been on transport properties in various sorts of nanostructures. Using concepts from quantum chaos we have studied incommensurate double-walled carbon nanotubes. A statistical analysis of the energy levels shows that the nature of electron transport in such nanotubes can be either ballistic, diffusive, or critical, depending on the position of the Fermi level. As an example where nonlinear dynamics is important we studied a two-dimensional electron gas with an additional periodic potential. We found plateau-like structures in the magnetoresistance due to classical dynamics. These structures are organized as a “Devil’s staircase” originating from the dynamical phenomenon of mode-locking. We also observed mode-locking in a nanoelectromechanical system consisting of a pair of charge shuttles coupled by tunneling. However, more important was another nonlinear effect, namely a bistability due to parametric instability. This effect had a strong impact on the transport properties. It can generate a direct net current even

---

in a fully symmetric configuration. An interesting extension of this work is a nanoelectromechanical system containing many charge shuttles. This system would possibly allow for an observation of solitons in such nanostructures.



# Bibliography

- [1] Z. I. Alferov. Nobel Lecture: The double heterostructure concept and its applications in physics, electronics, and technology. *Rev. Mod. Phys.*, 73:767–782, 2001.
- [2] S. Iijima. Helical microtubules of graphitic carbon. *Nature (London)*, 354:56–58, 1991.
- [3] J.P. Reithmaier, G. Sek, A. Löffler, C. Hofmann, S. Kuhn, S. Reitzenstein, L.V. Keldysh, V.D. Kulakovskii, T.L. Reinecke, and A. Forchel. Strong coupling in a single quantum dot-semiconductor microcavity system. *Nature (London)*, 432:197–200, 2004.
- [4] T. Yoshi, A. Scherer, J. Hendrickson, G. Khitrova, H. M. Gibbs, G. Ruper, C. Ell, O. B. Shchekin, and D. G. Deppe. Vacuum rabi splitting with a single quantum dot in a photonic crystal nanocavity. *Nature*, 432:200–203, 2004.
- [5] E. Peter, P. Senellart, D. Martrou, A. Lemaitre, J. Hours, J. M. Gérard, and J. Bloch. Exciton-photon strong-coupling regime for a single quantum dot in a microcavity. *Phys. Rev. Lett.*, 95:067401, 2005.
- [6] C. H. Bennett and D. P. DiVincenzo. Quantum information and computation. *Nature*, 404:247–255, 2000.
- [7] A. Zrenner, E. Beham, S. Stufler, F. Findeis, M. Bichler, and G. Abstreiter. Coherent properties of a two-level system based on a quantum-dot photodiode. *Nature*, 418:612–614, 2002.
- [8] N. Kirstaedter, N. N. Ledentsov, M. Grundmann, D. Bimberg, V. M. Ustinov, S. S. Ruvimov, M. V. Maximov, P. S. Kop'ev, Zh. I. Alferov, U. Richter, P. Werner, U. Gosele, and J. Heydenreich. Low threshold, large  $T_0$  injection laser emission from (InGa)As quantum dots. *Electron. Lett.*, 30:1416–1417, 1994.
- [9] E. Moreau, I. Robert, J. M. Gérard, I. Abram, L. Manin, and V. Thierry-Mieg. Single-mode solid-state single photon source based on isolated quantum dots in pillar microcavities. *Appl. Phys. Lett.*, 79:2865–2867, 2001.
- [10] P. Michler. *Single Quantum Dots: Fundamentals, Applications, and New Concepts*. Topics in Applied Physics. Springer, Berlin, 2003.

- [11] P. Lodahl, A. Floris van Driel, I. S. Nikolaev, A. Irman, K. Overgaag, D. Vanmaekelbergh, and W. L. Vos. Controlling the dynamics of spontaneous emission from quantum dots by photonic crystals. *Nature (London)*, 430:654, 2004.
- [12] Courtesy to R. Kröger, Universität Bremen, 2007.
- [13] S. J. Tans, M. H. Devoret, H. Dai, A. Thess, R.E Smalley, J. Geerligs, and C. Dekker. Individual single-wall carbon nanotubes as quantum wires. *Nature (London)*, 386:474–477, 1997.
- [14] Courtesy to M. Schowalter, Universität Bremen, 2007.
- [15] C. Kruse. *Grüne oberflächenemittierende Halbleiterlaser (VCSEL) auf Basis von II-VI-Verbindungen*. Dissertation, Universität Bremen, 2004.
- [16] L. Tong, R. R. Gattass, J. B. Ashcom, S. He, J. Lou, M. Shen, I. Maxwell, and E. Mazur. Subwavelength-diameter silica wires for low-loss optical wave guiding. *Nature (London)*, 426:816–819, 2003.
- [17] H. Lohmeyer, K. Sebald, C. Kruse, R. Kröger, J. Gutowski, D. Hommel, J. Wiersig, N. Baer, and F. Jahnke. Confined optical modes in monolithic II-VI pillar microcavities. *Appl. Phys. Lett.*, 88:051101, 2006.
- [18] H. Lohmeyer. *Optischer Einschluss, Lasing and Purcell-Effekt in Mikrosäulen auf Basis breitlückiger Halbleiter*. Dissertation, Universität Bremen, 2007.
- [19] K. J. Vahala. Optical microcavities. *Nature (London)*, 424:839–846, 2003.
- [20] S. L. McCall, A. F. J. Levi, R. E. Slusher, S. J. Pearton, and R. A. Logan. Whispering-gallery mode microdisk lasers. *Appl. Phys. Lett.*, 60:289–291, 1992.
- [21] R. E. Slusher, A. F. J. Levi, U. Mohideen, S. L. McCall, S. J. Pearton, and R. A. Logan. Threshold characteristics of semiconductor microdisk lasers. *Appl. Phys. Lett.*, 63:1310–1312, 1993.
- [22] U. Mohideen, R. E. Slusher, F. Jahnke, and S. W. Koch. Semiconductor microlaser linewidths. *Phys. Rev. Lett.*, 73:1785–1788, 1994.
- [23] L. Collot, V. Lefevre-Seguin, M. Brune, J.M. Raimond, and S. Haroche. Very high  $Q$  whispering gallery modes observed on fused silica microspheres. *Europhys. Lett.*, 23:87, 1993.
- [24] V. S Ilchenko, M. L. Gorodetsky, X. S. Yao, and L. Maleki. Microtorus: a high-finesse microcavity with whispering-gallery modes. *Opt. Lett.*, 26(5):256, 2001.
- [25] O. Painter, R. K. Lee, A. Scherer, A. Yariv, J. D. O'Brien, P. D. Dapkus, and I. Kim. Two-dimensional photonic band-gap defect mode laser. *Science*, 284:1819–1821, 1999.

- [26] K. Iga, F. Koyama, and S. Kinoshita. Surface emitting semiconductor lasers. *IEEE J. Quantum Electron.*, 24:1845–1855, 1988.
- [27] J. M. Gérard, D. Barrier, J. Y. Marzin, R. Kuszelewicz, L. Manin, E. Costard, V. Thierry-Mieg, and T. Rivera. Quantum boxes as active probes for photonic microstructures: The pillar microcavity case. *Appl. Phys. Lett.*, 69:449–451, 1996.
- [28] E. M. Purcell. Spontaneous emission probabilities at radio frequencies. *Phys. Rev.*, 69:681, 1946.
- [29] K. H. Drexhage. In E. Wolf, editor, *Progress in Optics*, page 164. North-Holland, Amsterdam, 1974.
- [30] P. Goy, J. M. Raimond, M. Gross, and S. Haroche. Observation of cavity-enhanced single-atom spontaneous emission. *Phys. Rev. Lett.*, 50:1903–1906, 1983.
- [31] R. G. Hulet, E. S. Hilfer, and D. Kleppner. Inhibited spontaneous emission by a Rydberg atom. *Phys. Rev. Lett.*, 55:2137–2140, 1985.
- [32] T. J. Rogers, D. G. Deppe, and B. G. Streetman. Effect of an AlAs/GaAs mirror on the spontaneous emission of an InGaAs-GaAs quantum well. *Appl. Phys. Lett.*, 57:1858–1860, 1990.
- [33] H. Yokoyama, K. Nishi, T. Anan, H. Yamada, S. D. Brorson, and E. P. Ippen. Enhanced spontaneous emission from GaAs quantum wells in monolithic microcavities. *Appl. Phys. Lett.*, 57:2814–2816, 1990.
- [34] J. M. Gérard, B. Sermage, B. Gayral, B. Legrand, E. Costard, and V. Thierry-Mieg. Enhanced spontaneous emission by quantum boxes in a monolithic optical microcavity. *Phys. Rev. Lett.*, 81:1110–1113, 1998.
- [35] L. A. Graham, D. L. Huffaker, and D. G. Deppe. Spontaneous lifetime control in a native-oxide-apertured microcavity. *Appl. Phys. Lett.*, 74:2048–2410, 1999.
- [36] J. M. Gérard and B. Gayral. Strong Purcell effect for InAs quantum boxes in three-dimensional solid-state microcavities. *J. Lightwave Technol.*, 17:2089–2095, 1999.
- [37] B. Lounis and M. Orrit. Single-photon sources. *Rep. Prog. Phys.*, 68:1129–1179, 2005.
- [38] H.-G. Park, S.-H. Kim, S.-H. Kwon, Y.-G. Ju, J.-K. Yang, J.-H. Baek, S.-B. Kim, and Y.-H. Lee. Electrically driven single-cell photonic crystal laser. *Science*, 305:1444–1447, 2004.
- [39] S. M. Ulrich, C. Gies, S. Ates, J. Wiersig, S. Reitzenstein, C. Hofmann, A. Löffler, A. Forchel, F. Jahnke, and P. Michler. Photon statistics of semiconductor microcavity lasers. *Phys. Rev. Lett.*, 98:043906, 2007.

- [40] Y. Yamamoto, S. Machida, and G. Björk. Micro-cavity semiconductor lasers with controlled spontaneous emission. *Optical and Quantum Electronics*, 24:S215–S243, 1992.
- [41] F. De Martini and G. R. Jacobovitz. Anomalous spontaneous-stimulated-decay phase transition and zero-threshold laser action in a microscopic cavity. *Phys. Rev. Lett.*, 60:1711–1714, 1988.
- [42] H. Yokoyama and S. D. Brorson. Rate equation analysis of microcavity lasers. *J. Appl. Phys.*, 66:4801–4805, 1989.
- [43] Y. Yamamoto, S. Machida, and G. Björk. Microcavity semiconductor laser with enhanced spontaneous emission. *Phys. Rev. A*, 44:657–668, 1991.
- [44] P. R. Rice and H. J. Carmichael. Photon statistics of a cavity QED laser: A comment on the laser-phase-transition analogy. *Phys. Rev. A*, 50(5):4318, 1994.
- [45] R. Hanbury Brown and R. Q. Twiss. Correlation between photons in two coherent beams of light. *Nature*, 177:27–29, 1956.
- [46] F. Jahnke, K. Henneberger, W. Schäfer, and S.W. Koch. Transient nonequilibrium and many-body effects in semiconductor microcavity lasers. *J. Opt. Soc. Am. B*, 10:2394–2405, 1993.
- [47] W. W. Chow, S. W. Koch, and M. Sargent. *Semiconductor Laser Physics*. Springer, Berlin, 1994.
- [48] F. Jahnke and S.W. Koch. Many-body theory for semiconductor microcavity lasers. *Phys. Rev. A*, 52:1712–1717, 1995.
- [49] D. S. Chemla and J. Shah. Many-body and correlation effects in semiconductors. *Nature*, 411:549–557, 2001.
- [50] F. Jahnke and S.W. Koch. Theory of carrier heating through injection pumping and lasing in semiconductor microcavity lasers. *Opt. Lett.*, 18:1438, 1993.
- [51] F. Jahnke, S.W. Koch, and K. Henneberger. Dynamics response of short-cavity semiconductor lasers. *Appl. Phys. Lett.*, 62:2313–2315, 1993.
- [52] H. G. Craighead. Nanoelectromechanical systems. *Science*, 290:1532–151535, 2000.
- [53] M. P. Blencowe. Nanoelectromechanical systems. *Contemporary Physics*, 46:249–264, 2005.
- [54] H. Poincaré. *Les Méthodes Nouvelles de la Mécanique Céleste*. Gauthier-Villars, Paris, 1892. Translated by the AIP, History of Modern Physics and Astronomy, Vol. 13, (1993).
- [55] M. V. Berry. Regularity and chaos in classical mechanics, illustrated by three deformations of a circular 'billiard'. *Eur. J. Phys.*, 2:91–102, 1981.

- [56] M. V. Berry. Quantizing a classically ergodic system: Sinai's billiard and the KKR method. *Ann. Phys.*, 131:163–216, 1981.
- [57] M. Robnik. Classical dynamics of a family of billiards with analytic boundaries. *J. Phys. A*, 16:3971–3986, 1983.
- [58] C. W. J. Beenakker and H. van Houten. Quantum transport in semiconductor nanostructures. *Solid State Physics*, 44:1–228, 1991.
- [59] K. Richter. *Semiclassical theory of mesoscopic quantum systems*. Habilitation thesis, Universität Augsburg, 1997.
- [60] C. W. J. Beenakker. Random-matrix theory of quantum transport. *Rev. Mod. Phys.*, 69:731–808, 1997.
- [61] M. C. Gutzwiller. *Chaos in Classical and Quantum Mechanics*, volume 1 of *Interdisciplinary Applied Mathematics*. Springer, Berlin, 1990.
- [62] F. Haake. *Quantum Signatures of Chaos*. Springer, Berlin, 1991.
- [63] L. E. Reichl. *The Transition to Chaos in Conservative Classical Systems: Quantum Manifestations*. Springer, Berlin, 1992.
- [64] H.-J. Stöckmann. *Quantum Chaos*. Cambridge University Press, Cambridge, 2000.
- [65] J. Wiersig. Quantum-classical correspondence in polygonal billiards. *Phys. Rev. E*, 64:026212, 2001.
- [66] J. U. Nöckel and A. D. Stone. Chaos in optical cavities. *Nature (London)*, 385:45–47, 1997.
- [67] C. Gmachl, F. Capasso, E. E. Narimanov, J. U. Nöckel, A. D. Stone, J. Faist, D. L. Sivco, and A. Y. Cho. High-power directional emission from microlasers with chaotic resonators. *Science*, 280:1556–1564, 1998.
- [68] R.K Chang, G. E. Fernandes, and M. Kneissl. The quest for uni-directionality with WGMs in  $\mu$ -lasers: Coupled oscillators and amplifiers. *Transparent Optical Networks*, 1:47–51, 2006.
- [69] M. Kneissl, M. Teepe, N. Miyashita, N. M. Johnson, G. D. Chern, and R. K. Chang. Current-injection spiral-shaped microcavity disk laser diodes with unidirectional emission. *Appl. Phys. Lett.*, 84:2485–2487, 2004.
- [70] M. Lohmeyer. Mode expansion modeling of rectangular integrated optical microresonators. *Opt. Quantum Electron.*, 34:541–557, 2002.
- [71] P. Michler, A. Kiraz, C. Becher, W. V. Schoenfeld, P. M. Petroff, L. Zhang, E. Hu, and A. Imamoğlu. A quantum dot single-photon turnstile device. *Science*, 290:2282–2285, 2000.

- [72] U. Vietze, O. Kraus, F. Laeri, G. Ihlein, G. Schüth, B. Limburg, and M. Abraham. Zeolite-dye microlasers. *Phys. Rev. Lett.*, 81:4628–4631, 1998.
- [73] I. Braun, G. Ihlein, F. Laeri, J. U. Nöckel, G. Schulz-Ekloff, F. Schüth, U. Vietze, Ö. Weiß, and D. Wöhrle. Hexagonal microlasers based on organic dyes in nanoporous crystals. *Appl. Phys. B: Lasers Opt.*, 70:335–343, 2000.
- [74] T. Harayama and T. Fukushima. Stadium and quasi-stadium laser diodes. *J. Select. Top. Quantum Elec.*, 10:1039–1051, 2004.
- [75] M. Kira, F. Jahnke, and S.W. Koch. Microscopic theory of excitonic signatures in semiconductor photoluminescence. *Phys. Rev. Lett.*, 81:3263, 1998.
- [76] J. Fricke. Transport equations including many-particle correlations for an arbitrary quantum system: A general formalism. *Ann. Phys.*, 252:479–498, 1996.
- [77] H. Haug and S. W. Koch. *Quantum Theory of the Optical and Electronic Properties of Semiconductors*. World Scientific, Singapore, 1993.
- [78] H. Grabert and M. H. Devoret. *Single Charge Tunneling-Coulomb Blockade Phenomena in Nanostructures*. Plenum, New York, 1992.
- [79] S. Frank, P. Poncharal, Z. L. Wang, and W. A. de Heer. Carbon nanotube quantum resistors. *Science*, 280:1744–1746, 1998.
- [80] L. Langer, V. Bayot, E. Grivei, J.-P. Issi, J. P. Heremans, C. H. Olk, L. Stockman, C. Van Haesendonck, and Y. Bruynseraeede. Quantum transport in a multiwalled carbon nanotube. *Phys. Rev. Lett.*, 76:479–482, 1996.
- [81] A. Bachtold, C. Strunk, J.-P. Salvetat, J.-M. Bonard, L. Forró, T. Nussbaumer, and C. Schönenberger. Aharonov-Bohm oscillations in carbon nanotubes. *Nature (London)*, 397:673–675, 1999.
- [82] J. Kim, O. Benson, H. Kan, and Y. Yamamoto. A single-photon turnstile device. *Nature*, 397:500–503, 1999.
- [83] P. Michler, A. Imamoğlu, M. D. Mason, P. J. Carson, G. F. Strouse, and S. K. Buratto. Quantum correlation among photons from a single quantum dot at room temperature. *Nature (London)*, 406:968, 2000.
- [84] M. Schwab, H. Kurtze, T. Auer, T. Berstermann, M. Bayer, J. Wiersig, N. Baer, C. Gies, F. Jahnke, J.P. Reithmaier, A. Forchel, M. Benyoucef, and P. Michler. Radiative emission dynamics of quantum dots in a single cavity micropillar. *Phys. Rev. B*, 74:045323, 2006.
- [85] A. Taflove and S. C. Hagness. *Computational Electrodynamics the Finite-Difference Time-Domain Method*. Artech House, London, 2000.
- [86] J. Förstner. *Light propagation and many-particle effects in semiconductor nanostructures*. Dissertation, Technische Universität Berlin, 2005.

- [87] J. U. Nöckel and A. D. Stone. Chaotic light: a theory of asymmetric resonant cavities. In R.K Chang and A.J. Campillo, editors, *Optical Processes in Microcavities*, volume 3 of *Advanced Series in applied Physics*. World Scientific, Singapore, 1995.
- [88] G. Chen and J. Zhou. *Boundary element methods*. Academic Press, San Diego, 1992.
- [89] P. K. Banerjee. *The boundary element methods in engineering*. McGraw-Hill, London, 1994.
- [90] J. Wiersig. Boundary element method for resonances in dielectric microcavities. *J. Opt. A: Pure Appl. Opt.*, 5:53–60, 2003.
- [91] O. J. F. Martin, A. Dereux, and C. Girard. Iterative scheme for computing exactly the total field propagating in dielectric structures of arbitrary shape. *J. Opt. Soc. Am. A*, 11:1073–1080, 1994.
- [92] O. J. F. Martin, C. Girard, and A. Dereux. Generalized field propagator for electromagnetic scattering and light confinement. *Phys. Rev. Lett.*, 74:526–529, 1995.
- [93] A. Hoekstra, J. Rahola, and P. Sloot. Accuracy of internal fields in volume integral equation simulations of light scattering. *Appl. Opt.*, 37:8482–8497, 1998.
- [94] O. J. F. Martin, C. Girard, D. R. Smith, and S. Schultz. Generalized field propagator for arbitrary finite-size photonic band gap structures. *Phys. Rev. Lett.*, 82:315–318, 1999.
- [95] J. U. Nöckel. *Resonances in Nonintegrable Open Systems*. PhD thesis, Yale University, 1997.
- [96] M. Robnik. Quantising a generic family of billiards with analytic boundaries. *J. Phys. A*, 17:1049–1074, 1984.
- [97] V. V. Kozlov and D. V. Treshchev. *Billiards – A Genetic Introduction to the Dynamics of Systems with Impacts*. American Mathematical Society, Providence, RI, 1991.
- [98] A. Bäcker, F. Steiner, and P. Stifter. Spectral statistics in the quantized cardioid billiard. *Phys. Rev. E*, 52:2463, 1995.
- [99] H. Waalkens, J. Wiersig, and H. R. Dullin. The elliptic quantum billiard. *Ann. Phys. (New York)*, 260(1):50–90, 1997.
- [100] C. Dembowski, H.-D. Gräf, A. Heine, R. Hofferbert, H. Rehfeld, and A. Richter. First experimental evidence for chaos-assisted tunneling in a microwave annular billiard. *Phys. Rev. Lett.*, 84:867–870, 2000.
- [101] J. Wiersig. Singular continuous spectra in a pseudointegrable billiard. *Phys. Rev. E*, 62(1):R21–24, 2000.

- [102] J. Nagler, M. Krieger, J. Linke, M. Schönke, and J. Wiersig. Leaking billiards. *Phys. Rev. E*, 75:046204, 2007.
- [103] L. A. Bunimovich. On ergodic properties of certain billiards. *Funct. Anal. Appl.*, 8:254–255, 1974.
- [104] K. F. Huang, Y. F. Chen, H. C. Lai, and Y. P. Lan. Observation of the wave function of a quantum billiard from the transverse patterns of vertical-cavity surface-emitting lasers. *Phys. Rev. Lett.*, 89:224102, 2002.
- [105] T. Gensty, K. Becker, I. Fischer, W. Elsäßer, C. Degen, P. Debernardi, and G. P. Bava. Wave chaos in real-world vertical-cavity surfaces-emitting lasers. *Phys. Rev. Lett.*, 94:233901, 2005.
- [106] S. Lacey and H. Wang. Directional emission from whispering-gallery modes in deformed fused-silica microspheres. *Opt. Lett.*, 26:1943–1945, 2001.
- [107] S. Lacey, H. Wang, D. H. Foster, and J. U. Nöckel. Directional tunneling escape from nearly spherical optical resonators. *Phys. Rev. Lett.*, 91:033902, 2003.
- [108] Lord Rayleigh. *The Theory of Sound*. American edition: Dover, New York, 1945. first published 1877.
- [109] M. Lebental, J. S. Lauret, R. Hierle, and J. Zyss. Highly-directional stadium-shaped polymer microlasers. *Appl. Phys. Lett.*, 88:031108, 2006.
- [110] M. Lebental, J. S. Lauret, J. Zyss, C. Schmit, and E. Bogomolny. Directional emission of stadium-shaped microlasers. *Phys. Rev. A*, 75:033806, 2007.
- [111] T. Tanaka, M. Hentschel, T. Fukushima, and T. Harayama. Classical phase space revealed by coherent light. *Phys. Rev. Lett.*, 98:033902, 2007.
- [112] A. J. Lichtenberg and M. A. Lieberman. *Regular and Chaotic Dynamics*. Springer, Berlin, 1992.
- [113] V. I. Arnol'd. *Mathematical Methods of Classical Mechanics*, volume 60 of *Graduate Texts in Mathematics*. Springer, Berlin, 1978.
- [114] A. N. Kolmogorov. The conservation of conditionally periodic motions with a small variation in the Hamiltonian. *Dokl. Akad. Nauk SSSR*, 98:527–530, 1954.
- [115] V. I. Arnol'd. Small denominators and problems of stability of motion in classical and celestial mechanics. *Russ. Math. Surveys*, 18(6):85–191, 1963.
- [116] J. Moser. On invariant curves of area-preserving mappings of an annulus. *Nachr. Akad. Wiss. Göttingen, Math. Phys. Kl.*, pages 1–20, 1962.
- [117] J. U. Nöckel.  $Q$  spoiling and directionality in deformed ring cavities. *Opt. Lett.*, 19:1693–1695, 1994.

- [118] A. Bäcker. *Classical and quantum chaos in billiards*. PhD thesis, Universität Ulm, 1998.
- [119] S. Fishman, D. R. Grempel, and R. E. Prange. Chaos, quantum recurrences, and Anderson localization. *Phys. Rev. Lett.*, 49:509–512, 1982.
- [120] K. M. Frahm and D. L. Shepelyansky. Quantum localization in rough billiards. *Phys. Rev. Lett.*, 78:1440–1443, 1997.
- [121] O. A. Starykh, P. R. J. Jacquod, E. E. Narimanov, and A. D. Stone. Signature of dynamical localization in the resonance width distribution of wave chaotic cavities. *Phys. Rev. E*, 62:2078, 2000.
- [122] W. Fang, H. Cao, V.A. Podolskiy, and E.E. Narimanov. Dynamical localization in microdisk lasers. *Optics Express*, 13:5641–5652, 2005.
- [123] E. J. Heller. Bound-states eigenfunctions of classically chaotic Hamiltonian systems: Scars of periodic orbits. *Phys. Rev. Lett.*, 53:1515–1518, 1984.
- [124] S. B. Lee, J. H. Lee, J. S. Chang, H. J. Moon, S. W. Kim, and K. An. Observation of scarred modes in asymmetrically deformed microcylinder lasers. *Phys. Rev. Lett.*, 88:033903, 2002.
- [125] N. B. Rex, H. E. Tureci, H. G. L. Schwefel, R. K. Chang, and A. D. Stone. Fresnel filtering in lasing emission from scarred modes of wave-chaotic optical resonators. *Phys. Rev. Lett.*, 88:094102, 2002.
- [126] S.-Y. Lee, S. Rim, J.-W. Ryu, T.-Y. Kwon, M. Choi, and C.-M Kim. Quasicarred resonances in a spiral-shaped microcavity. *Phys. Rev. Lett.*, 93:164102, 2004.
- [127] W. Fang, A. Yamilov, and H. Cao. Analysis of high-quality modes in open chaotic microcavities. *Phys. Rev. A*, 72:023815, 2005.
- [128] T. Fukushima, T. Harayama, and J. Wiersig. Ray-wave correspondence in an unstable quasistadium laser resonator. *Phys. Rev. A*, 73:023816, 2006.
- [129] M. J. Davis and E. J. Heller. Quantum dynamical tunneling in bound states. *J. Chem. Phys.*, 75:246, 1981.
- [130] G. Hackenbroich and J. U. Nöckel. Dynamical tunneling in optical cavities. *Europhys. Lett.*, 39:371, 1997.
- [131] S. Tomsovic and D. Ullmo. Chaos-assisted tunneling. *Phys. Rev. E*, 50(1):145–162, 1994.
- [132] V.A. Podolskiy and E.E. Narimanov. Semiclassical description of chaos-assisted tunneling. *Phys. Rev. Lett.*, 91:263601, 2003.
- [133] V.A. Podolskiy and E.E. Narimanov. Chaos-assisted tunneling in dielectric microcavities. *Opt. Lett.*, 30:474–476, 2005.

- [134] G. D. Chern, H.E. Tureci, A.D. Stone, R. K. Chang, M. Kneissl, and N.M. Johnson. Unidirectional lasing InGaN multiple-quantum-well spiral-shaped micropillars. *Appl. Phys. Lett.*, 83:1710–1712, 2003.
- [135] M. S. Kurdoglyan, S.-Y. Lee, S. Rim, and C.-M Kim. Unidirectional lasing from a microcavity with a rounded isoceles triangle shape. *Opt. Lett.*, 29:2758–2760, 2004.
- [136] J. Wiersig and M. Hentschel. Unidirectional light emission from high- $Q$  modes in optical microcavities. *Phys. Rev. A*, 73:031802(R), 2006.
- [137] J. Wiersig. Hexagonal dielectric resonators and microcrystal lasers. *Phys. Rev. A*, 67:023807, 2003.
- [138] L. Benmohammadi, A. Erodabasi, K. Koch, F. Laeri, N. Owschimikow, U. Vietze, G. Ihlein, F. Schüth, Ö. Weiss, I. Braun, M. Ganschow, G. Schulz-Ekloff, D. Wöhrle, J. Wiersig, and J.U. Nöckel. Microscopic lasers based on the molecular sieve AlPO<sub>4</sub>-5. In *Host-Guest Systems Based on Nanoporous Crystals*, pages 584–617. Wiley-VCH, Weinheim, 2003.
- [139] J. Wiersig. Formation of long-lived, scar-like modes near avoided resonance crossings in optical microcavities. *Phys. Rev. Lett.*, 97:253901, 2006.
- [140] R. Schäfer, U. Kuhl, and H.-J. Stöckmann. Directed emission from a dielectric microwave billiard with quadrupolar shape. *New. J. Phys.*, 8:1–17, 2006.
- [141] J.-W. Ryu, S.-Y. Lee, C.-M. Kim, and Y.-J. Park. Survival probability time distribution in dielectric cavities. *Phys. Rev. E*, 73:036207, 2006.
- [142] S. Shinohara and T. Harayama. Signature of ray chaos in quasi-bound wavefunctions for a stadium-shaped dielectric cavity. *Phys. Rev. E*, 75:036216, 2007.
- [143] H. G. L. Schwefel, N. B. Rex, H. E. Tureci, R. K. Chang, and A. D. Stone. Dramatic shape sensitivity of directional emission patterns from similarly deformed cylindrical polymer lasers. *J. Opt. Soc. Am. B*, 21:923–934, 2004.
- [144] S.-Y. Lee, J.-W. Ryu, T.-Y. Kwon, S. Rim, and C.-M Kim. Scarred resonances and steady probability distribution in a chaotic microcavity. *Phys. Rev. A*, 72:061801(R), 2005.
- [145] S.-B. Lee, J. Yang, S. Moon, J.-H. Lee, K. An, J.-B. Shim, H.-W. Lee, and S. W. Kim. Universal output directionality of single modes in a deformed microcavity. *Phys. Rev. A*, 75:011802(R), 2007.
- [146] J. Wiersig and M. Hentschel. Combining unidirectional light output and ultralow loss in deformed microdisks. *submitted to Phys. Rev. Lett.*, 2007.
- [147] J. D. Jackson. *Klassische Elektrodynamik*. Walter de Gruyter, Berlin, New York, 1983.

- [148] R. H. Landau. *Quantum Mechanics II*. John Wiley & Sons, New York, 2 edition, 1996.
- [149] G. Gamow. Zur Quantentheorie des Atomkernes. *Z. Phys.*, 51:204–212, 1928.
- [150] P. L. Kapur and R. Peierls. The dispersion formula for nuclear reactions. *Proc. Roy. Soc. Lond. A*, 166:277–295, 1938.
- [151] P. W. Barber and S. C. Hill. *Light scattering by particles: computational methods*. World Scientific, Singapore, 1990.
- [152] M. Hentschel and K. Richter. Quantum chaos in optical systems: The annular billiard. *Phys. Rev. E*, 66:056207, 2002.
- [153] P. M. van den Berg and J. T. Fokkema. The Rayleigh hypothesis in the theory of diffraction by a cylindrical obstacle. *IEEE Trans. Antennas Propag.*, 27(5):577–583, 1979.
- [154] M. Kitahara. *Boundary integral equation methods in eigenvalue problems of elastodynamics and thin plates*. Elsevier, Amsterdam, 1985.
- [155] R. D. Ciskowski and C. A. Brebbia, editors. *Boundary element methods in acoustics*. Computational Mechanics Publications and Elsevier Applied Science, Southampton Boston, 1991.
- [156] I. Kosztin and K. Schulten. Boundary integral method for stationary states of two-dimensional quantum systems. *Int. J. mod. Physics C*, 8(2):293–325, 1997.
- [157] A. Bäcker. Numerical aspects of eigenvalue and eigenfunction computations for chaotic quantum systems. In M. Degli Esposti and S. Graffi, editors, *The Mathematical Aspects of Quantum Maps*, volume No. 618 of *Springer Lecture Notes in Physics*, pages 91–144. Springer, Berlin, 2003.
- [158] A. J. Burton and G. F. Miller. The application of integral equation methods to the numerical solution of some exterior boundary-value problems. *Proc. R. Soc. Lond. A*, 323:201–210, 1971.
- [159] P. Gaspard and S. A. Rice. Exact quantization of the scattering from a classical chaotic repellor. *J. Chem. Phys.*, 90(4):2255–2262, 1989.
- [160] P. A. Knipp and T. L. Reinecke. Boundary-element method for the calculation of electronic states in semiconductor nanostructures. *Phys. Rev. B*, 54:1880–1891, 1996.
- [161] I. S. Gradshteyn and I. M. Ryzhik. *Tables of Integrals, Series, and Products*. Academic Press, New York, 1965.
- [162] J. U. Nöckel and A. D. Stone. Resonance line shapes in quasi-one-dimensional scattering. *Phys. Rev. B*, 50:17415–17432, 1994.

- [163] William H. Press, Brian P. Flannery, Saul A. Teukolsky, and William T. Vetterling. *Numerical Recipes in C. The Art of Scientific Computing.* Cambridge University Press, Cambridge, 1988.
- [164] G. R. Hadley. High-accuracy finite-difference equations for dielectric waveguide analysis II: dielectric corners. *J. Lightwave Technol.*, 20:1219–1231, 2002.
- [165] M. Hentschel, H. Schomerus, and R. Schubert. Husimi functions at dielectric interfaces: Inside-outside duality for optical systems and beyond. *Europhys. Lett.*, 62:636–642, 2003.
- [166] C. P. Michael, K. Srinivasan, T. J. Johnson, O. Painter, K. H. Lee, K. Hennessy, H. Kim, and E. Hu. Wavelength- and material-dependent absorption in GaAs and AlGaAs microcavities. *Appl. Phys. Lett.*, 90:051108, 2007.
- [167] H. Rigneault, J. Broudic, B. Gayral, and J. M. Gérard. Far-field radiation from quantum boxes located in pillar microcavities. *Opt. Lett.*, 26:1595–1597, 2001.
- [168] A. F. J. Levi, R. E. Slusher, S. L. McCall, J. L. Glass, S. J. Pearton, and R. A. Logan. Directional light coupling from microdisk lasers. *Appl. Phys. Lett.*, 62:561–563, 1993.
- [169] D. Y. Chu, M. K. Chin, W. G. Bi, C. W. Tu, and S.T. Ho. Double-disk structure for output coupling in microdisk lasers. *Appl. Phys. Lett.*, 65:3167–3169, 1994.
- [170] V. M. Apalkov and M. E. Raikh. Directional emission from a microdisk resonator with a linear defect. *Phys. Rev. B*, 70:195317, 2004.
- [171] J. von Neumann and E. P. Wigner. Über das Verhalten von Eigenwerten bei adiabatischen Prozessen. *Z. Phys.*, 30:467–470, 1929.
- [172] W. D. Heiss. Repulsion of resonance states and exceptional points. *Phys. Rev. E*, 61:929–932, 2000.
- [173] T. Timberlake and L. E. Reichl. Changes in Floquet-state structure at avoided crossings: delocalization and harmonic generation. *Phys. Rev. A*, 59(4):2886–893, 1999.
- [174] H. Schomerus, J. Wiersig, and M. Hentschel. Optomechanical probes of resonances in amplifying microresonators. *Phys. Rev. A*, 70:012703, 2004.
- [175] O. Bohigas, D. Boosé, R. Egydio de Carvalho, and V. Marvulle. Quantum tunneling and chaotic dynamics. *Nucl. Phys. A*, 560:197, 1993.
- [176] S. D. Frischat and E. Doron. Dynamical tunneling in mixed systems. *Phys. Rev. E*, 57:1421–1443, 1998.
- [177] A. Badolato, K. Hennessy, M. Ataüre, J. Dreiser, E. Hu, P. M. Petroff, and A. Imamoğlu. Deterministic coupling of single quantum dots in single nanocavity modes. *Science*, 308:1158–1161, 2005.

- [178] S. A. Backes, J. R. A. Cleaver, A. P. Heberle, J. J. Baumberg, and K. Köler. Threshold reduction in pierced microdisk lasers. *Appl. Phys. Lett.*, 74:176–178, 1999.
- [179] A. I. Rahachou and I. V. Zozoulenko. Effects of boundary roughness on a  $Q$ -factor of whispering-gallery-mode lasing microdisk cavities. *J. Appl. Phys.*, 94:7929, 2003.
- [180] M. Borselli, K. Srinivasan, P. E. Barclay, and P. Painter. Rayleigh scattering, mode coupling, and optical loss in silicon microdisks. *Appl. Phys. Lett.*, 85:3693, 2004.
- [181] B. J. Li and P.-L. Liu. Analysis of far-field patterns of microdisk resonators by the finite-difference time-domain method. *IEEE J. Quantum Elect.*, 33:1489, 1997.
- [182] T. Nobis, E.M. Kaidashev, A. Rahm, M. Lorenz, and M. Grundmann. Whispering gallery modes in nanosized dielectric resonators with hexagonal cross section. *Phys. Rev. Lett.*, 93(10):103903, 2004.
- [183] C. Kim, Y. J. Kim, E. S. Jang, G. C. Yi, and H. H. Kim. Whispering-gallery-modelike-enhanced emission from ZnO nanodisk. *Appl. Phys. Lett.*, 88:093104, 2006.
- [184] C. W. Chen and Y. F. Chen. Whispering gallery modes in highly hexagonal symmetric structures of SBA-1 mesoporous silica. *Appl. Phys. Lett.*, 90:071104, 2007.
- [185] A. Borovoi, I. Grishin, E. Naats, and U. Oppel. Backscattering peak of hexagonal ice columns and plates. *Opt. Lett.*, 25:1388–1390, 2000.
- [186] P. J. Richens and M. V. Berry. Pseudointegrable systems in classical and quantum mechanics. *Physica D*, 2:495–512, 1981.
- [187] A. Hobson. Ergodic properties of a particle moving elastically inside a polygon. *J. Math. Phys.*, 16(11):2210–2214, 1975.
- [188] A.N. Zemlyakov and A.B. Katok. Topological transitivity of billiards in polygons. *Math. Notes*, 18:760–764, 1975.
- [189] R. Artuso, I. Guarneri, and L. Rebuzzini. Spectral properties and anomalous transport in a polygonal billiard. *Chaos*, 10(1):189–194, 2000.
- [190] E. B. Bogomolny, U. Gerland, and C. Schmit. Models of intermediate statistics. *Phys. Rev. E*, 59:R1315–R1318, 1999.
- [191] L. M. Cureton and J. R. Kuttler. Eigenvalues of the Laplacian on regular polygons and polygons resulting from their dissection. *J. Sound Vib.*, 220:83–98, 1999.
- [192] E. E. Narimanov, G. Hackenbroich, P. Jacquod, and A. D. Stone. Semiclassical theory of the emission properties of wave-chaotic resonant cavities. *Phys. Rev. Lett.*, 83(24):4991–4994, 1999.
- [193] A. K. Bhowmik. Polygonal optical cavities. *Appl. Opt.*, 39(18):3071–3075, 2000.
- [194] E. Gutkin. Billiards in polygons: survey of recent results. *J. Stat. Phys.*, 83(1/2):7–26, 1996.

- [195] H. E. Tureci, H. G. L. Schwefel, A. D. Stone, and E. E. Narimanov. A Gaussian-optical approach to stable periodic orbit resonances of partially chaotic dielectric micro-cavities. *Optics Express*, 10(16):752–776, 2002.
- [196] J. W. Ra, H. L. Bertoni, and L. B. Felsen. Reflection and transmission of beams at a dielectric interface. *SIAM J. Appl. Math.*, 24(3):396–413, 1973.
- [197] N. H. Tran, L. Dutriaux, Ph. Balcou, A. Le Floch, and F. Bretenaker. Angular Goos-Hänchen effect in curved dielectric microstructures. *Opt. Lett.*, 20(11):1233–1235, 1995.
- [198] A. W. Poon, F. Courvoisier, and R. K. Chang. Multimode resonances in square-shaped optical microcavities. *Opt. Lett.*, 26(9):632–634, 2001.
- [199] S. Ando, N. Kobayashi, and H. Ando. Hexagonal-facet laser with optical waveguides grown by selective area metalorganic chemical vapor deposition. *Jpn. J. Appl. Phys.*, 34:L4–L6, 1995.
- [200] M. Sasaki, Y. Li, T. Akatu, Y. Fujii, and K. Hane. Anisotropically etched Si mold for solid polymer dye microcavity laser. *Jpn. J. Appl. Phys.*, 39:7145–7149, 2000.
- [201] H. C. Chang, G. Kioseoglou, E. H. Lee, J. Haetty, M. H. Na, Y. Xuan, H. Luo, A. Petrou, and A. N. Cartwright. Lasing modes in equilateral-triangular laser cavities. *Phys. Rev. A*, 62:013816, 2000.
- [202] G. D. Chern, A. W. Poon, and R. K. Chang. Directional laser emission from square, spiral and mismatched semi-circular dye-doped polymer based micropillar cavities. Proceedings QELS, 2002.
- [203] R. Akis, D. K. Ferry, and J. P. Bird. Magnetotransport fluctuations in regular semiconductor ballistic quantum dots. *Phys. Rev. B*, 54(24):17705–17715, 1996.
- [204] R. Akis, D. K. Ferry, and J. P. Bird. Wave function scarring effects in open stadium shaped quantum dots. *Phys. Rev. Lett.*, 79:123–126, 1997.
- [205] I. V. Zozoulenko and K.-F. Berggren. Quantum scattering, resonant states, and conductance fluctuations in an open square electron billiard. *Phys. Rev. B*, 56:6931, 1997.
- [206] D. K. Ferry, R. Akis, and J. P. Bird. Einselection in action: decoherence and pointer states in open quantum dots. *Phys. Rev. Lett.*, 93:026803, 2004.
- [207] R. V. Jensen, M. M. Sanders, M. Saraceno, and B. Sundaram. Inhibition of quantum transport due to scars of unstable periodic orbits. *Phys. Rev. Lett.*, 63:2771–2775, 1989.
- [208] J. S. Hersch, M. R. Haggerty, and E. J. Heller. Diffractive orbits in an open microwave billiard. *Phys. Rev. Lett.*, 83:5342–5345, 1999.

- [209] A. Bäcker, A. Manze, B. Huckestein, and R. Ketzmerick. Isolated resonances in conductance fluctuations and hierarchical states. *Phys. Rev. E*, 66:016211, 2002.
- [210] W. Fang, H. Cao, and G. S. Solomon. Control of lasing in fully chaotic open microcavities by tailoring the shape factor. *Appl. Phys. Lett.*, 90:081108, 2007.
- [211] M. Desouster-Lecomte and V. Jacquest. Avoided overlap between two resonance energies or frequencies: formation of fast and slow decay modes. *J. Phys. B*, 28:3225–3248, 1995.
- [212] E. Persson, I. Rotter, H.-J. Stöckmann, and M. Barth. Observation of resonance trapping in an open microwave cavity. *Phys. Rev. Lett.*, 85:2478–2481, 2000.
- [213] W.-H. Guo, Y.-Z. Huang, Q.-Y. Lu, and L.-J. Yu. Whispering-gallery-like modes in square resonators. *IEEE J. Quantum Elect.*, 39:1106–1110, 2003.
- [214] R. Narevich, R. E. Prange, and O. Zaitsev. Square billiard with magnetic flux. *Phys. Rev. E*, 62(2):2046–2059, 2000.
- [215] Y. F. Chen, K. F. Huang, H. C. Lai, and Y. P. Lan. Rules of selection for spontaneous coherent states in mesoscopic systems: using the microcavity laser as an analog study. *Phys. Rev. E*, 68:026210, 2003.
- [216] R. Hegger, H. Kantz, and T. Schreiber. Practical implementation of nonlinear time series methods: The TISEAN package. *Chaos*, 9:413–435, 1999.
- [217] M. Pelton, J. Vučković, G.S. Solomon, A. Scherer, and T. Yamamoto. Three-dimensionally confined modes in micropost microcavities: quality factors and Purcell factors. *IEEE J. Quantum Elect.*, 38:170–177, 2002.
- [218] J. Vučković, M. Pelton, A. Scherer, and T. Yamamoto. Optimization of three-dimensional micropost microcavities for cavity quantum electrodynamics. *Phys. Rev. A*, 66:023808, 2002.
- [219] Ph. Lalanne, J. P. Hugonin, and J. M. Gérard. Electromagnetic study of the quality factor of pillar microcavities in the small diameter limit. *Appl. Phys. Lett.*, 84:4726–4728, 2004.
- [220] D. Burak and R. Binder. Cold-cavity vectorial eigenmodes of VCSELs. *IEEE J. Quantum Electronics*, 33(7):1205–1215, 1997.
- [221] D. Burak and R. Binder. Electromagnetic characterization of vertical-cavity surface-emitting lasers based on a vectorial eigenmode calculation. *Appl. Phys. Lett.*, 72(8):891–893, 1998.
- [222] D. Burak, S. A. Kemme, R. K. Kostuk, and R. Binder. Spectral identification of transverse lasing modes of multimode index-guided vertical-cavity surface-emitting lasers. *Appl. Phys. Lett.*, 73(24):3501–3503, 1998.

- [223] M. Benyoucef, S.M. Ulrich, P. Michler, J. Wiersig, F. Jahnke, and A. Forchel. Correlated photon pairs from single InGaAs/GaAs quantum dots in pillar microcavities. *J. Appl. Phys.*, 97:023101, 2005.
- [224] M. Benyoucef, S.M. Ulrich, P. Michler, J. Wiersig, F. Jahnke, and A. Forchel. Enhanced correlated photon pair emission from a pillar microcavity. *New J. Phys.*, 6:91, 2004.
- [225] M. Bayer, A. Forchel, T. L. Reinecke, P. A. Knipp, and S. Rudin. Confinement of light in microresonators for controlling light-matter interaction. *phys. stat. sol. (a)*, 191(1):3–32, 2002.
- [226] K. Sebald, P. Michler, T. Passow, D. Hommel, G. Bacher, and A. Forchel. Single-photon emission of CdSe quantum dots at temperatures up to 200 K. *Appl. Phys. Lett.*, 81:2920–2922, 2002.
- [227] M. Klude, T. Passow, H. Heinke, and D. Hommel. Electro-optical characterization of CdSe quantum dot laser diodes. *phys. stat. sol. (b)*, 229:1029–1032, 2002.
- [228] J. M. Gérard. *Top. Appl. Phys.*, 90:269, 2003.
- [229] T. Rivera, J.-P. Debray, J. M. Gérard, B. Legrand, L. Mannin-Ferlazzo, and J. L. Oudar. Optical losses in plasma-etched AlGaAs microresonators using reflection spectroscopy. *Appl. Phys. Lett.*, 74:911, 1999.
- [230] H. Lohmeyer, K. Sebald, J. Gutowski, R. Kröger, C. Kruse, D. Hommel, J. Wiersig, and F. Jahnke. Resonant modes in monolithic nitride pillar microcavities. *Eur. Phys. J B*, 48:291–294, 2005.
- [231] M. Bayer, T. L. Reinecke, F. Weidner, A. Larionov, A. McDonald, and A. Forchel. Inhibition and enhancement of the spontaneous emission of quantum dots in structured microresonators. *Phys. Rev. Lett.*, 86:3168, 2001.
- [232] H. Altug, D. Englund, and J. Vučković. Ultrafast photonic crystal nanocavity lasers. *Nature*, 2:484–488, 2006.
- [233] S. Strauf, K. Hennessy, M. T. Rakher, Y.-S. Choi, A. Badolato, L. C. Andreani, E. L. Hu, P. M. Petroff, and D. Brouwmeester. Self-tuned quantum dot gain in photonic crystal lasers. *Phys. Rev. Lett.*, 96:127404, 2006.
- [234] D. Fattal, K. Inoue, J. Vučković, G. S. Santori, C. Solomon, and Y. Yamamoto. Entanglement formation and violation of Bell’s inequality with a semiconductor single photon source. *Phys. Rev. Lett.*, 92:037903, 2004.
- [235] H.-K. Lo and H. F. Chau. Unconditional security of quantum key distribution over arbitrarily long distances. *Science*, 283:2050–2056, 1999.
- [236] J.-W. Bouwmeester, D. Pan, K. Mattle, M. Eibl, H. Weinfurter, and A. Zeilinger. Experimental quantum teleportation. *Nature*, 390:575–579, 1997.

- [237] D. Fattal, E. Diamanti, K. Inoue, and Y. Yamamoto. Quantum teleportation with a quantum dot single photon source. *Phys. Rev. Lett.*, 92:037904, 2004.
- [238] X. Fan, M. C. Lonergan, Y. Zhang, and H. Wang. Enhanced spontaneous emission from semiconductor nanocrystals embedded in whispering gallery optical microcavities. *Phys. Rev. B*, 64:115310, 2001.
- [239] W. Fang, J. Y. Xu, A. Yamilov, H. Cao, Y. Ma, S. T. Ho, and G. S. Solomon. Large enhancement of spontaneous emission rate of InAs quantum dots in GaAs microdisks. *Opt. Lett.*, 27:948–950, 2002.
- [240] I. L. Krestnikov, N. N. Ledentsov, A. Hoffmann, D. Bimberg, A. V. Sakharnov, W. V. Lundin, A. S. Tsatsul’nikov, A. F. Usikov, Zh. I. Alferov, Yu. G. Musikhin, and D. Gerthsen. Quantum dot origin of luminescence in InGaN-GaN structures. *Phys. Rev. B*, 66:155310, 2002.
- [241] R. A. Oliver, G. A. D. Briggs, M. J. Kappers, C. J. Humphreys, S. Yasin, J. H. Rice, J. D. Smith, and R. A. Taylor. InGaN quantum dots grown by metalorganic vapor phase epitaxy employing a post-growth nitrogen anneal. *Appl. Phys. Lett.*, 83:755, 2003.
- [242] T. Berstermann, T. Auer, H. Kurtze, M. Schwab, M. Bayer, J. Wiersig, C. Gies, F. Jahnke, D. Reuter, and A. Wieck. Systematic study of carrier correlations in the electron-hole recombination dynamics of quantum dots. *arXiv:0706.3673, submitted to PRB*, 2007.
- [243] H. Haug. *Optical Nonlinearities and Instabilities in Semiconductors*. Academic, San Diego, 1988.
- [244] F. Jahnke. *A Many-Body Theory for Laser Emission and Excitonic Effects for Semiconductor Microcavities*. Habilitation thesis, Philipps-Universität Marburg, 1996.
- [245] V. M. Axt and A. Stahl. A dynamics-controlled truncation scheme for the hierarchy of density matrices in semiconductor optics. *Z. Phys. B*, 93:195–204, 1994.
- [246] Nextnano<sup>3</sup> device simulation package. <http://www.wsi.tum.de/nextnano3/>.
- [247] W. Sheng, S.-J. Cheng, and P. Hawrylak. Multiband theory of multi-exciton complexes in self-assembled quantum dots. *Phys. Rev. B*, 71:035316, 2005.
- [248] S. Schulz, S. Schuhmacher, and G. Czycholl. Tight-binding model for semiconductor quantum dots with a wurtzite crystal structure: From one-particle properties to Coulomb correlations and optical spectra. *Phys. Rev. B*, 73:245327, 2006.
- [249] P. Meystre and M. Sargent III. *Elements of Quantum Optics*. Springer, Berlin, 1999.

- [250] M. Kira, F. Jahnke, W. Hoyer, and S. W. Koch. Quantum theory of spontaneous emission and coherent effects in semiconductor microstructures. *Prog. Quant. Electr.*, **23**:189, 1999.
- [251] W. Hoyer. *Quantentheorie zu Exzitonbildung und Photolumineszenz in Halbleitern*. PhD thesis, University of Marburg, Germany, 2002.
- [252] W. Hoyer, M. Kira, and S.W. Koch. Influence of Coulomb and phonon interaction on the exciton formation dynamics in semiconductor heterostructures. *Phys. Rev. B*, **67**:155113, 2003.
- [253] W. Schäfer and M. Wegener. *Semiconductor Optics and Transport Phenomena*. Springer, Heidelberg, 2002.
- [254] M. Linderg, Y. Z. Hu, R. Binder, and S. W. Koch.  $\chi^{(3)}$  formalism in optically excited semiconductors and its applications in four-wave mixing spectroscopy. *Phys. Rev. B*, **50**:18060–18070, 1994.
- [255] F. Jahnke, M. Kira, W. Hoyer, and S.W. Koch. Influence of correlation effects on the excitonic semiconductor photoluminescence. *phys. stat. sol. (b)*, **221**:189, 2000.
- [256] G. Khitrova, H. M. Gibbs, F. Jahnke, M. Kira, and S. W. Koch. Nonlinear optics of normal-mode-coupling semiconductor microcavities. *Rev. Mod. Phys.*, **71**:1591, 1999.
- [257] N. Baer, C. Gies, J. Wiersig, and F. Jahnke. Luminescence of a semiconductor quantum dot system. *Eur. Phys. J. B*, **50**:411–418, 2006.
- [258] G. Hackenbroich, C. Viviescas, and F. Haake. Field quantization for chaotic resonators with overlapping resonances. *Phys. Rev. Lett.*, **89**:083902, 2002.
- [259] R. Bonifacio, P. Schwendimann, and F. Haake. Quantum statistical theory of superradiance. I. *Phys. Rev. A*, **4**:302–313, 1971.
- [260] A. Barenco and M. A. Dupertuis. Quantum many-body states of excitons in a small quantum dot. *Phys. Rev. B*, **52**:2766, 1995.
- [261] P. Hawrylak. Excitonic artificial atoms: Engineering optical properties of quantum dots. *Phys. Rev. B*, **60**:5597–5608, 1999.
- [262] E. Dekel, D. Gershoni, E. Ehrenfreund, J. M. Garcia, and P. M. Petroff. Carrier-carrier correlations in an optically excited single semiconductor quantum dot. *Phys. Rev. B*, **61**:11009, 2000.
- [263] M. Braskén, M. Lindberg, D. Sundholm, and J. Olsen. Spatial carrier-carrier correlations in strain-induced quantum dots. *Phys. Rev. B*, **64**:035312, 2001.
- [264] M. Bayer, G. Ortner, O. Stern, A. Kuther, A. A. Gorbunov, A. Forchel, P. Hawrylak, S. Fafard, K. Hinzer, T. L. Reinecke, S. N. Walck, J. P. Reithmaier, F. Klopf, and F. Schäfer. Fine structure of neutral and charged excitons in self-assembled In(Ga)As/(Al)GaAs quantum dots. *Phys. Rev. B*, **65**:195315, 2002.

- [265] N. Baer, P. Gartner, and F. Jahnke. Coulomb effects in semiconductor quantum dots. *Eur. Phys. J. B*, 42:231–237, 2004.
- [266] N. Baer, S. Schulz, S. Schumacher, P. Gartner, G. Czycholl, and F. Jahnke. Optical properties of self-organized wurtzite InN/GaN quantum dots: A combined atomistic tight-binding and full configuration interaction calculation. *Appl. Phys. Lett.*, 87(23):231114, 2005.
- [267] D. Morris, N. Perret, and S. Fafard. Carrier energy relaxation by means of Auger processes in InAs/GaAs self-assembled quantum dots. *Appl. Phys. Lett.*, 75:3593, 1999.
- [268] T. R. Nielsen, P. Gartner, and F. Jahnke. Many-body theory of carrier capture and relaxation in semiconductor quantum-dot lasers. *Phys. Rev. B*, 69:235314, 2004.
- [269] J. Seebeck, T. R. Nielsen, P. Gartner, and F. Jahnke. Polarons in semiconductor quantum-dots and their role in the quantum kinetics of carrier relaxation. *Phys. Rev. B*, 71:125327, 2005.
- [270] G. Bester, S. Nair, and A. Zunger. Pseudopotential calculation of the excitonic fine structure of million-atom self-assembled  $\text{In}_{1-x}\text{Ga}_x\text{As}/\text{GaAs}$  quantum dots. *Phys. Rev. B*, 67:161306, 2003.
- [271] G. Bester and A. Zunger. Compositional and size-dependent spectroscopic shifts in charged self-assembled  $\text{In}_x\text{Ga}_{1-x}\text{As}/\text{GaAs}$  quantum dots. *Phys. Rev. B*, 68:073309, 2003.
- [272] S. Rodt, A. Schliwa, K. Pötschke, F. Guffarth, and D. Bimberg. Correlation of structural and few-particle properties of self-organized InAs/GaAs quantum dots. *Phys. Rev. B*, 71:155325, 2005.
- [273] S. Nair and Y. Masumoto. Coulomb effects in the optical spectra of highly excited semiconductor quantum dots. *J. Lumin.*, 87-89:438–440, 2000.
- [274] A. Wojs, P. Hawrylak, S. Fafard, and L. Jacak. Electronic structure and magneto-optics of self-assembled quantum dots. *Phys. Rev. B*, 54(8):5604–5608, August 1996.
- [275] M. Kira, F. Jahnke, and S. W. Koch. Quantum theory of secondary emission in optically excited semiconductor quantum wells. *Phys. Rev. Lett.*, 82:3544, 1999.
- [276] J. H. Eberly and K. Wódkiewicz. The time-dependent physical spectrum of light. *J. Opt. Soc. Am.*, 67:1252, 1977.
- [277] A. V. Uskov, A.-P. Jauho, B. Tromborg, J. Mørk, and R. Lang. Dephasing times in quantum dots due to elastic LO phonon-carrier collisions. *Phys. Rev. Lett.*, 85:1516, 2000.
- [278] B. Krummheuer, V. M. Axt, and T. Kuhn. Theory of pure dephasing and the resulting absorption lineshape in semiconductor quantum dots. *Phys. Rev. B*, 65:195313, 2002.

- [279] E. A. Muljarov and R. Zimmermann. Dephasing in quantum dots: Quadratic coupling to acoustic phonons. *Phys. Rev. Lett.*, **85**:1516, 2000.
- [280] P. Borri, W. Langbein, S. Schneider, U. Woggon, R. L. Sellin, D. Ouyang, and D. Bimberg. Ultralong dephasing time in InGaAs quantum dots. *Phys. Rev. Lett.*, **87**:157401, 2001.
- [281] J. Förstner, C. Weber, J. Danckwerts, and A. Knorr. Phonon-assisted damping of Rabi oscillations in semiconductor quantum dots. *Phys. Rev. Lett.*, **91**:127401, 2003.
- [282] K. J. Ahn, J. Förstner, and A. Knorr. Resonance fluorescence of semiconductor quantum dots: Signatures of the electron-phonon interaction. *Phys. Rev. B*, **71**:153309, 2005.
- [283] R. E Slusher and U. Mohideen. Dynamic optical processes in microdisk lasers. In R.K Chang and A.J. Campillo, editors, *Optical Processes in Mircocavities*, volume 3 of *Advanced Series in applied Physics*. World Scientific, Singapore, 1995.
- [284] P. Michler, A. Kiraz, L. Zhang, C. Becher, E. Hu, and A. Imamoğlu. Laser emission from quantum dots in microdisk structures. *Appl. Phys. Lett.*, **77**:184–186, 2000.
- [285] L. Zhang and E. Hu. Lasing from InGaAs quantum dots in an injection microdisk. *Appl. Phys. Lett.*, **82**:319–321, 2002.
- [286] G. S. Solomon, M. Pelton, and T. Yamamoto. Single-mode spontaneous emission from a single quantum dot in a three-dimensional microcavity. *Phys. Rev. Lett.*, **86**:3903–3906, 2001.
- [287] R. Loudon. *The quantum theory of light*. Clarendon Press, Oxford, 2 edition, 1983.
- [288] O. Benson and Y. Yamamoto. Master-equation model of a single-quantum-dot microsphere laser. *Phys. Rev. A*, **59**:4756–4763, 1999.
- [289] C. Wiele, F. Haake, and Y. M. Golubev. Quantum-dot laser with periodic pumping. *Phys. Rev. A*, **60**:4986–4995, 1999.
- [290] I. E. Protsenko and M. Travagnin. Microscopic model of semiconductor laser without inversion. *Phys. Rev. A*, **65**:013801, 2001.
- [291] M. Travagnin. Effects of Pauli blocking on semiconductor laser intensity and phase noise spectra. *Phys. Rev. A*, **64**:013818, 2001.
- [292] C. Gies, J. Wiersig, M. Lorke, and F. Jahnke. Semiconductor model for quantum dot-based microcavity lasers. *Phys. Rev. A*, **75**:013803, 2007.
- [293] M. Lorke, T. R. Nielsen, J. Seebek, P. Gartner, and F. Jahnke. Influence of carrier-carrier and carrier-phonon correlations on optical absorption and gain in quantum-dot systems. *Phys. Rev. B*, **73**:085324, 2006.

- [294] E. Malić, K. J. Ahn, M. J. P. Bormann, P. Hövel, E. Schöll, A. Knorr, M. Kuntz, and D. Bimberg. Theory of relaxation oscillations in semiconductor quantum dot lasers. *Appl. Phys. Lett.*, 89:101107, 2006.
- [295] T. Feldtmann, L. Schneebeli, M. Kira, and S. W. Koch. Quantum theory of light emission from a semiconductor quantum dot. *Phys. Rev. B*, 73:155319, 2006.
- [296] J. Hendrickson, B. C. Richards, J. Sweet, S. Mosor, C. Christenson, D. Lam, G. Khitrova, H. M. Gibbs, T. Yoshie, A. Scherer, O. B. Shchekin, and D. G. Deppe. Quantum dot photonic-crystal-slab nanocavities: Quality factors and lasing. *Phys. Rev. B*, 72:193303, 2005.
- [297] S. Reitzenstein, A. Bazhenov, A. Gorbunov, C. Hofmann, S. Münch, A. Löffler, M. Kamp, J. P. Reithmaier, V. D. Kulakovskii, and A. Forchel. Lasing in high- $Q$  quantum-dot micropillar cavities. *Appl. Phys. Lett.*, 89:051107, 2006.
- [298] S. Ates, S.M. Ulrich, P. Michler, S. Reitzenstein, A. Löffler, and A. Forchel. Coherence properties of high- $\beta$  elliptical semiconductor micropillar lasers. *Appl. Phys. Lett.*, 90:161111, 2007.
- [299] T. Geisel, R. Ketzmerik, and Schedletzky. Classical Hall plateaus in ballistic microjunctions. *Phys. Rev. Lett.*, 69:1680–1683, 1992.
- [300] R. Fleischmann, T. Geisel, and R. Ketzmerik. Magnetoresistance due to chaos and nonlinear resonances in lateral surfaces superlattices. *Phys. Rev. Lett.*, 68:1367–1370, 1992.
- [301] I. Kosztin, D.L. Maslov, and P.M. Goldbart. Chaos in Andreev billiards. *Phys. Rev. Lett.*, 75(9):1735–1738, 1995.
- [302] J. H. Smet, D. Weiss, R. H. Blick, G. Lütjering, K. von Klitzing, R. Fleischmann, R. Ketzmerick, T. Geisel, and G. Weimann. Magnetic focusing of composite fermions through arrays of cavities. *Phys. Rev. Lett.*, 77:2272–2275, 1996.
- [303] M. A. Topinka, B. J. LeRoy, R. M. Westervelt, S. E. J. Shaw, R. Fleischmann, E.J. Heller, K. D. Maranowski, and A. C. Gossard. Coherent branched flow in a two-dimensional electron gas. *Nature (London)*, 410:183, 2001.
- [304] T. M. Fromhold, A. Patane, S. Bujkiewicz, P. B. Wilkinson, D. Fowler, D. Sherwood, S. P. Stapleton, A. A. Krokhin, L. Eaves, M. Henini, N. S. Sankeshwar, and F. W. Sheard. Chaotic electron diffusion through stochastic webs enhances current flow in superlattices. *Nature*, 428:726–7730, 2004.
- [305] G. Stegemann, A. G. Balanov, and E. Schöll. Noise-induced pattern formation in a semiconductor nanostructure. *Phys. Rev. B*, 71:016221, 2005.
- [306] F. Pistolesi and R. Fazio. Charge shuttle as a nanomechanical rectifier. *Phys. Rev. Lett.*, 94:036806, 2005.

- [307] D. K. Arrowsmith and C. M. Place. *An Introduction to Dynamical Systems*. Cambridge University Press, Cambridge, 1990.
- [308] C. Huygens. In M. Nijhoff, editor, *Oeuvres Complètes de Christian Huyghens*, volume 5, page 243. Societe Hollandaise des Sciences, The Hague, 1893. (A letter to his father, dated 26 Feb. 1665).
- [309] E. I. Butikov. Parametric excitation of a linear oscillator. *Eur. J. Phys.*, 25:535–554, 2004.
- [310] J. Wiersig and K.-H. Ahn. Devil’s staircase in magnetoresistance of a periodic array of scatterers. *Phys. Rev. Lett.*, 87:026803, 2001.
- [311] J. Wiersig and K.-H. Ahn. Mode-locking in a periodic array of scatterers. *Physica E*, 12(1-4):256–259, 2002.
- [312] L. Y. Gorelik, A. Isacsson, M. V. Voinova, B. Kasemo, R. I. Shekhter, and M. Jonson. Shuttle mechanism for charge transfer in Coulomb blockade nanostructures. *Phys. Rev. Lett.*, 80:4526, 1998.
- [313] K.-H Ahn, H. C. Park, J. Wiersig, and J. Hong. Current rectification by spontaneous symmetry breaking in coupled nanomechanical shuttles. *Phys. Rev. Lett.*, 97:216804, 2006.
- [314] C. M. Marcus, A. J. Rimberg, R. M. Westervelt, P. F. Hoplins, and A. C. Gossard. Conductance fluctuations and chaotic scattering in ballistic microstructures. *Phys. Rev. Lett.*, 69:506–509, 1992.
- [315] D. Weiss, K. Richter, A. Menschig, R. Bergmann, H. Schweitzer, K. von Klitzing, and G. Weimann. Quantized periodic orbits in large antidot arrays. *Phys. Rev. Lett.*, 70:4118–4121, 1993.
- [316] R. P. Taylor, R. Newbury, A. S. Sachrajda, Y. Feng, P. T. Coleridge, C. Dettmann, N. Zhu, H. Cuo, A. Delage, P. J. Kelly, and Z. Wasilewski. Self-similar magnetoresistance of a semiconductor Sinai billiard. *Phys. Rev. Lett.*, 78:1952–1955, 1997.
- [317] A. Lodder and Yu.V. Nazarov. Density of states and the energy gap in Andreev billiards. *Phys. Rev. B*, 58:5783–5788, 1998.
- [318] M. G. Vavilov, P. W. Brouwer, V. Ambegaokar, and C.W.J. Beenakker. Universal gap fluctuations in the superconductor proximity effect. *Phys. Rev. Lett.*, 86:874–877, 2001.
- [319] A. Ramamoorthy, R. Akis, J. P. Bird, T. Maemoto, D. K. Ferry, and M. Inoue. Signatures of dynamical tunneling in semiclassical quantum dots. *Phys. Rev. E*, 68:026211, 2003.
- [320] J. Feist, A. Bäcker, R. Ketzmerick, S. Rotter, B. Huckestein, and J. Burgdörfer. Nanowires with surface disorder: Giant localization lengths and quantum-to-classical crossover. *Phys. Rev. Lett.*, 97:116804, 2006.

- [321] C. E. Porter. *Statistical Theories of Spectra*. Academic, New York, 1965.
- [322] M.L. Mehta. *Random Matrices and the statistical theory of energy levels*. Academic Press, New York, 1967.
- [323] G. Montambaux. Spectral fluctuations in disordered metals. In E. Giacobino, S. Reynaud, and J. Zinn-Justin, editors, *Quantum Fluctuations*, Proceedings of the Les Houches Summer School, Session LXIII. Elsevier Science, Amsterdam, 1996.
- [324] A.D. Mirlin. Statistics of energy levels and eigenfunctions in disordered systems. *Physics Reports*, 326:259–382, 2000.
- [325] O. Bohigas, M. J. Giannoni, and C. Schmit. Characterization of chaotic quantum spectra and universality of level fluctuation laws. *Phys. Rev. Lett.*, 52:1–4, 1984.
- [326] H. P. Baltes and E. R. Hilf. *Spectra of Finite Systems*. BI Wissenschaftsverlag, Mannheim, 1976.
- [327] J.M.G. Gómez, R. A. Molina, A. Relaño, and J. Retamosa. Misleading signatures of quantum chaos. *Phys. Rev. E*, 66:036209, 2002.
- [328] T. Guhr, A. Müller-Groeling, and H. A. Weidenmüller. Random-matrix theories in quantum physics: common concepts. *Phys. Rep.*, 299:189–425, 1998.
- [329] M. V. Berry and M. Tabor. Level clustering in the regular spectrum. *Proc. R. Soc. Lond. A*, 356:375–394, 1977.
- [330] B.I. Shklovskii, B. Shapiro, B. Sears, P. Labrianides, and H.B. Shore. Statistics of spectra of disordered systems near the metal-insulator transition. *Phys. Rev. B*, 47(17):11487–11490, 1993.
- [331] D. Braun, G. Montambaux, and M. Pascaud. Boundary conditions at the mobility edge. *Phys. Rev. Lett.*, 81:1062–1065, 1998.
- [332] E. B. Bogomolny, U. Gerland, and C. Schmit. Short-range plasma model for intermediate spectral statistics. *Eur. Phys. J. B*, 19(1):121–132, 2001.
- [333] J. Wiersig. Spectral properties of quantized barrier billiards. *Phys. Rev. E*, 65:046217, 2002.
- [334] T. Gorin and J. Wiersig. Low rank perturbations and the spectral statistics of pseudointegrable billiards. *Phys. Rev. E*, 68:065205(R), 2003.
- [335] J. Wiersig and G. G. Carlo. Evanescent wave approach to diffractive phenomena in convex billiards with corners. *Phys. Rev. E*, 67:046221, 2003.
- [336] K.-H Ahn, Y. H. Kim, J. Wiersig, and K. J. Chang. Spectral correlation in incommensurate multi-walled carbon nanotubes. *Phys. Rev. Lett.*, 90(2):026601, 2003.
- [337] K.-H Ahn, Y. H. Kim, J. Wiersig, and K. J. Chang. Spectral properties of incommensurate double-walled carbon nanotubes. *Physica E*, 22(1-3):666–669, 2004.

- [338] K. Ensslin and P. M. Petroff. Magnetotransport through an antidot lattice in GaAs-Al<sub>x</sub>Ga<sub>1-x</sub>As heterostructures. *Phys. Rev. B*, 41:12307–12310, 1990.
- [339] D. Weiss, M. L. Roukes, A. Menschig, P. Grambow, K. von Klitzing, and G. Weimann. Electron pinball and commensurate orbits in a periodic array of scatterers. *Phys. Rev. Lett.*, 66:2790–2793, 1991.
- [340] G. R. Hall. Resonance zones in two-parameter families of circle homeomorphisms. *SIAM J. Math. Anal.*, 15(6):1075–1081, 1984.
- [341] R. Kubo. Statistical-mechanical theory of irreversible processes. I. General theory and simple applications to magnetic and conduction problems. *J. Phys. Soc. Jpn.*, 12:570, 1957.
- [342] E. Ott. *Chaos in Dynamical Systems*. Cambridge University Press, Cambridge, 1993.
- [343] K. von Klitzing, G. Dorda, and M. Pepper. New method for high-accuracy determination of the fine-structure constant based on quantized Hall resistance. *Phys. Rev. Lett.*, 45:494–497, 1980.
- [344] D. C. Tsui, H. L. Stormer, and A. C. Gossard. Two-dimensional magnetotransport in the extreme quantum limit. *Phys. Rev. Lett.*, 48:1559–1562, 1982.
- [345] M. Janssen, O. Viehweger, U. Fastenrath, and J. Hajdu. *Introduction to the Theory of the Integer Quantum Hall Effect*. VCH Verlagsgesellschaft mbH, Weinheim, 1994.
- [346] G. M. Gusev, Z. D. Kvon, A. G. Pogosov, and M. M. Voronin. Nonlinear effects in a two-dimensional electron gas with a periodic lattice of scatterers. *JETP Lett.*, 65:248, 1997.
- [347] A.N. Cleland. *Foundation of Nanomechanics*. Springer, Heidelberg, 2002.
- [348] A. Erbe, C. Weiss, W. Zwerger, and R. H. Blick. Nanomechanical resonator shuttling single electrons at radio frequencies. *Phys. Rev. Lett.*, 87:096106, 2001.
- [349] D. V. Scheible and R. H. Blick. Silicon nanopillars for mechanical single-electron transport. *Appl. Phys. Lett.*, 84:4632, 2004.
- [350] H. Park, J. Park, A. K. L. Lim, E. H. Anderson, A. P. Alivisatos, and P. L. McEuen. Nanomechanical oscillations in a single-C<sub>60</sub> transistor. *Nature (London)*, 407:57, 2000.
- [351] R. G. Mani, J. H. Smet, K. von Klitzing, V. Narayanamurti, W. B. Johnson, and V. Umansky. Zero-resistance states induced by electromagnetic-wave excitation in GaAs/AlGaAs heterostructures. *Nature (London)*, 420:646, 2002.
- [352] V. I. Arnol'd. Remarks on the perturbation-theory for problems of Mathieu type. *Russian Mathematical Surveys*, 38:215–233, 1983.

- [353] N. Nishiguchi. Shot-noise-induced random telegraph noise in shuttle current. *Phys. Rev. Lett.*, 89:066802, 2002.
- [354] R. Saito, G. Dresselhaus, and M.S. Dresselhaus. *Physical Properties of Carbon Nanotubes*. Imperial College Press, London, 1998.
- [355] M. Bockrath, D. H. Cobden, P. L. McEuen, N. G. Chopra, A. Zettl, A. Thess, and R. E. Smalley. Single-electron transport in ropes of carbon nanotubes. *Science*, 275:1922, 1997.
- [356] S.J. Tans, A. R. M. Verschueren, and C. Dekker. Room-temperature transistor based on a single carbon nanotube. *Nature (London)*, 393:49–52, 1998.
- [357] R. Martel, T. Schmidt, H. R. Shea, T. Hertel, and Ph. Avouris. Single- and multi-wall carbon nanotube field-effect transistors. *Appl. Phys. Lett.*, 73:2447–2449, 1998.
- [358] K. Tsukagoshi, B. W. Alphenaar, and H. Ago. Coherent transport of electron spin in a ferromagnetically contacted carbon nanotube. *Nature (London)*, 401:572–574, 1999.
- [359] S. Datta. *Electronic Transport in Mesoscopic Systems*. Cambridge University Press, Cambridge, 1995.
- [360] M. Ge and K. Sattler. Vapor-condensation generation and STM analysis of fullerene tubes. *Science*, 260:515–518, 1993.
- [361] P. G. Collins, M. S. Arnold, and P. Avouris. Engineering carbon nanotubes and nanotube circuits using electrical breakdown. *Science*, 292:706–709, 2001.
- [362] R. Saito, G. Dresselhaus, and M.S. Dresselhaus. Electronic structure of double-layer graphene tubules. *J. Appl. Phys.*, 73:494–500, 1993.
- [363] J.-C. Charlier and J.-P. Michenaud. Energetics of multilayered carbon tubules. *Phys. Rev. Lett.*, 70:1858–1861, 1993.
- [364] S. Roche, F. Triozon, A. Rubio, and D. Mayou. Conduction mechanisms and magnetotransport in multiwalled carbon nanotubes. *Phys. Rev B*, 64:121401, 2001.
- [365] H. Hernández-Saldaña, J. Flores, and T.H. Seligman. Semi-Poisson statistics and beyond. *Phys. Rev. E*, 60(1):449–452, 1999.
- [366] J. T. Chalker, V. E. Kravtsov, and I. V. Lerner. Spectral rigidity and eigenfunction correlations at the Anderson transition. *JETP Lett.*, 64:386–392, 1996.
- [367] J. T. Chalker, I. V. Lerner, and R. A. Smith. Random walks through the ensemble: Linking spectral statistics with wave-function correlations in disordered metals. *Phys. Rev. Lett.*, 77:554–557, 1996.
- [368] Y.-G. Yoon, P. Delaney, and S.G. Louie. Quantum conductance of multiwall carbon nanotubes. *Phys. Rev. B*, 66:073407, 2002.

- [369] Y. Xue and S. Datta. Fermi-level alignment at metal-carbon nanotube interfaces: Application to scanning tunneling spectroscopy. *Phys. Rev. Lett.*, 83:4844–4847, 1999.
- [370] M. Kociak, K. Suenaga, K. Hirahara, Y. Saito, T. Nakahira, and S. Iijima. Linking chiral indices and transport properties of double-walled carbon nanotubes. *Phys. Rev. Lett.*, 89:155501, 2002.
- [371] M.R. Buitelaar, A. Bachtold, T. Nussbaumer, M. Iqbal, and Schönenberger. Multi-wall carbon nanotubes as quantum dots. *Phys. Rev. Lett.*, 88:156801, 2002.
- [372] M.T. Woodside and P.L. McEuen. Scanned probe imaging of single-electron charge states in nanotube quantum dots. *Science*, 296:1098–1101, 2002.
- [373] K.-H. Ahn, K. Richter, and I.-H. Lee. Addition spectra of chaotic quantum dots: Interplay between interactions and geometry. *Phys. Rev. Lett.*, 83:4144–4147, 1999.
- [374] R. Ketzmerick, L. Hufnagel, F. Steinbach, and M. Weiss. New class of eigenstates in generic Hamiltonian systems. *Phys. Rev. Lett.*, 85:1214–1217, 2000.
- [375] A. Bäcker, R. Ketzmerick, and A. Monastra. Flooding of regular islands by chaotic states. *Phys. Rev. Lett.*, 94:054102, 2005.
- [376] A. Bäcker, R. Ketzmerick, and A. Monastra. Universality in the flooding of regular islands by chaotic states. *Phys. Rev. E*, 75:066204, 2007.
- [377] W.T. Lu, S. Sridhar, and M. Zworski. Fractal Weyl laws for chaotic open systems. *Phys. Rev. Lett.*, 91:154101, 2003.
- [378] H. Schomerus and J. Tworzydlo. Quantum-to-classical crossover of quasi-bound states in open quantum systems. *Phys. Rev. Lett.*, 93:154102, 2004.
- [379] T. Harayama, P. Davis, and K. S. Ikeda. Stable oscillations of a spatially chaotic wave function in a microstadium laser. *Phys. Rev. Lett.*, 90:063901, 2003.
- [380] T. Harayama, T. Fukushima, S. Sunada, and K. S. Ikeda. Asymmetric stationary lasing patterns in 2D symmetric microcavities. *Phys. Rev. Lett.*, 91:073903, 2003.
- [381] T. Harayama, S. Sunada, and K. S. Ikeda. Theory of two-dimensional microcavity lasers. *Phys. Rev. A*, 72:013803, 2005.
- [382] S. Sunada, T. Harayama, and K. S. Ikeda. Multi-mode lasing in 2D fully chaotic cavity lasers. *Phys. Rev. E*, 71:046209, 2005.
- [383] S. Shinohara, S. Sunada, T. Harayama, and K. S. Ikeda. Mode expansion description of stadium-cavity laser dynamics. *Phys. Rev. E*, 71:036203, 2005.
- [384] T.-Y. Kwon, S.-Y. Lee, M. S. Kurdoglyan, S. Rim, C.-M. Kim, and Park Y.-J. Lasing modes in a spiral-shaped dielectric microcavity. *Opt. Lett.*, 31:1250–1252, 2006.

- [385] R. H. Dicke. Coherence in spontaneous radiation processes. *Phys. Rev.*, 93:99–110, 1954.
- [386] M. Scheibner, T. Schmidt, L. Worschech, A. Forchel, G. Bacher, T. Passow, and D. Hommel. Superradiance of quantum dots. *Nature Physics*, 3:106–110, 2007.
- [387] V. V. Temnov and U. Woggon. Superradiance and subradiance in an inhomogeneously broadened ensemble of two-level systems coupled to a low- $Q$  cavity. *Phys. Rev. Lett.*, 95:243602, 2005.
- [388] M. Bayer. Private communication, 2007.
- [389] K. An, J. J. Childs, R. R. Dasari, and M. S. Feld. Microlaser: A laser with one atom in an optical resonator. *Phys. Rev. Lett.*, 73:3375–3378, 1994.
- [390] J. McKeever, A. D. Boca, J. R. Buck, and H. J. Kimble. Experimental realization of a one-atom laser in the regime of strong coupling. *Nature*, 425:268–271, 2003.
- [391] M. Born and E. Wolf. *Principles of Optics*. Pergamon Press, Oxford, New York, 1959.
- [392] A. W. Snyder and J. D. Love. *Optical Waveguide Theory*. Chapman and Hall, New York, 1983.

*Bibliography*

---

# **Appendix**

<b>A Hexagonal-shaped cavity</b>	<b>181</b>
<b>B Vectorial transfer matrix approach</b>	<b>185</b>
<b>C Equation of motion for intraband correlations</b>	<b>189</b>
<b>D Analytical results for <math>g^{(2)}(0)</math></b>	<b>191</b>
<b>E Interplay of time constants</b>	<b>193</b>

## *Appendix*

---

# A Hexagonal-shaped cavity

In this appendix, we give some details on the hexagonal-shaped cavity studied in Section 2.4.

## Quantization condition

We assume that an integer number  $m = 1, 2, 3, \dots$  of wavelengths  $\lambda_{\text{inside}} = \lambda/n = 2\pi/n\text{Re}(k)$  fits on the path length of the long-lived ray shown in Fig. 2.26, taking into account the phase shifts at the dielectric boundary. To compute the phase shifts, we consider the textbook treatment of reflection of a plane wave at an infinitely extended dielectric interface; see, e.g., Ref. [391]. This simplified setup is justified if  $\lambda \ll R$ , i.e.,  $\text{Re}(kR) \gg 1$ . We shift the origin of the coordinate system such that  $y = 0$  is the dielectric boundary bounding the lower-index region from below and the higher-index region from above. In the higher-index region there is an incident wave

$$\psi_i = A_i \exp [i\text{Re}(k)n(x \sin \theta_i + y \cos \theta_i)] , \quad (\text{A.1})$$

with amplitude  $A_i$ . We set  $A_i = 1$  without loss of generality. The reflected wave is given by

$$\psi_r = A_r \exp [i\text{Re}(k)n(x \sin \theta_r - y \cos \theta_r)] . \quad (\text{A.2})$$

In the lower-index region there is an emitted wave

$$\psi_e = A_e \exp [i\text{Re}(k)(x \sin \theta_e + y \cos \theta_e)] . \quad (\text{A.3})$$

The boundary conditions

$$\psi_i(x, 0) + \psi_r(x, 0) = \psi_e(x, 0) \quad (\text{A.4})$$

and

$$\frac{\partial \psi_i}{\partial y} \Big|_{(x,0)} + \frac{\partial \psi_r}{\partial y} \Big|_{(x,0)} = \frac{\partial \psi_e}{\partial y} \Big|_{(x,0)} \quad (\text{A.5})$$

lead to  $\theta_i = \theta_r$ , Snell's law  $n \sin \theta_i = \sin \theta_e$ ,  $A_i + A_r = A_e$ , and the Fresnel formula

$$A_r = \frac{1 - i\alpha}{1 + i\alpha} \quad (\text{A.6})$$

with

$$\alpha = \frac{\sqrt{n^2 \sin^2 \theta_i - 1}}{n \cos \theta_i} . \quad (\text{A.7})$$

The quantization (or resonance) condition then reads

$$e^{in\text{Re}(k)l} A_r^6 = 1 , \quad (\text{A.8})$$

with the length of the periodic rays  $l = 3\sqrt{3}R$ . After some algebraic manipulations, we arrive at

$$\text{Re}(kR) = \frac{2\pi}{3\sqrt{3}n}(m + \beta) \quad (\text{A.9})$$

with the total boundary phase shift  $\beta$  given by

$$\tan \frac{\pi}{6}\beta = \alpha . \quad (\text{A.10})$$

## Angular shift

In this paragraph, we discuss the semiclassical deviation of the angle of incidence from  $60^\circ$ . Let us first investigate -- and +-modes. Along the boundary, these modes are periodic with period  $3R$ , i.e.,  $\psi(s + 3R) = \psi(s)$ , where the arclength  $s \in [0, 6R]$  parametrizes the boundary. Hence, the wave function along the boundary can be expanded as the following Fourier series

$$\psi(s) = \sum_{M=-\infty}^{\infty} A_M \exp\left(i \frac{2\pi}{3R} Ms\right) . \quad (\text{A.11})$$

From this, we see that the conjugate momentum to  $s$  or in other words, the momentum component parallel to the boundary is “quantized” according to

$$n\text{Re}(k) \sin \theta = \frac{2\pi}{3R} M , \quad (\text{A.12})$$

with integer  $M$ . Inserting the quantization condition (2.66) leads to

$$\sin \theta = \sqrt{3} \frac{M}{m + \beta} . \quad (\text{A.13})$$

Linearizing this equation around  $\theta \approx \theta_i = 60^\circ = \pi/3$  yield in the semiclassical regime  $m \gg \beta$

$$\Delta\theta = 2\sqrt{3} \left( \frac{M}{m} - \frac{1}{2} \right) - 2\sqrt{3} \frac{M}{m} \frac{\beta}{m} . \quad (\text{A.14})$$

The smallest  $\Delta\theta$  is realized for  $M = m/2$  ( $m$  is an even integer for -- and +-modes, see Table 2.1),

$$\Delta\theta = -\sqrt{3} \frac{\beta}{m} = -\frac{2\pi\beta}{3n\text{Re}(kR)} . \quad (\text{A.15})$$

Analogous arguments concerning -+ and +-modes give the same result as in Eq. (A.15).

---

## Boundary-wave leakage

Here we compute the leakage due to boundary waves. To estimate the loss, we consider the total internal reflection ( $\theta_i > \theta_c$ ) of a plane wave at an infinitely extended dielectric interface. This consideration is justified if  $\text{Re}(kR) \gg 1$  and  $\theta_i$  not too close to the critical angle for total internal reflection  $\theta_c$ . Since  $\theta_e$  is a complex number in Eq. (A.3), the wave in the lower-index region is evanescent, i.e., it decays exponentially with increasing distance from the boundary. Along the boundary the evanescent wave propagates with constant velocity. The corresponding total energy (intensity) flux at a given point at the boundary can be computed by means of

$$\sigma = \int_0^\infty S_x dy , \quad (\text{A.16})$$

where  $S_x$  is the  $x$ -component of the Poynting vector [147]

$$\mathbf{S} = \frac{c}{8\pi} \text{Re}(\mathbf{E} \times \mathbf{H}^*) = -\frac{c}{8\pi k} \text{Re}(i\psi \nabla \psi^*) . \quad (\text{A.17})$$

Integration of Eq. (A.16) using Eqs. (A.17) and (A.3) yields

$$\sigma = \frac{c}{4\pi} \frac{n \sin \theta_i}{k \sqrt{n^2 \sin^2 \theta_i - 1}} \frac{1}{1 + \alpha^2} , \quad (\text{A.18})$$

with  $\alpha$  from Eq. (2.68).

Now we relate the total flux to the intensity inside the resonator. The intensity of the wave function  $\psi_i + \psi_r$  per unit area can be easily calculated to be  $1/4\pi$ . Assuming that the boundary waves fully leave the cavity at corners, the outgoing relative intensity per unit time is given by

$$\Delta I_{\text{bw}} = \frac{c}{A} \frac{n \sin \theta_i}{k \sqrt{n^2 \sin^2 \theta_i - 1}} \frac{\chi}{1 + \alpha^2} , \quad (\text{A.19})$$

where  $\chi$  is the number of corners (where the light is emitted),  $A$  is the area of the resonator covered by the family of long-lived rays. Formula (A.19) is valid for any regular polygon. For the hexagon,  $\chi = 6$  and  $A$  is given by the area of the hexagon minus the region not accessible by the family of long-lived rays as depicted in Fig. A.1. Elementary geometry yields

$$A = \frac{3\sqrt{3}}{2} (R^2 - R_c^2) = \sqrt{3} R^2 . \quad (\text{A.20})$$

The final result for the hexagon is then given in Eq. (2.71).

## Pseudointegrable leakage

In this paragraph, we calculate the pseudointegrable leakage. We put the angular shift  $\Delta\theta$  from Eq. (A.15) into the initial conditions for the ray dynamics. Elementary geometry,

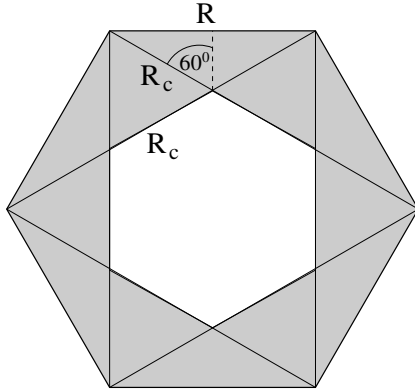


**Figure A.1:** Region (empty hexagon) not accessible by the family of long-lived rays. The region is bounded by a hexagonal “caustic” with side length  $R_c = R/\sqrt{3}$ .

see Fig. 2.26, shows that after one round trip, i.e., 6 bounces, the angular deviation gives rise to the spatial deviation  $\Delta s = |2l\Delta\theta|$ . The time for each round trip is  $\Delta t = nl/c$ .

From Fig. 2.26, it is clear that points on the boundary within the distance  $\Delta s$  from a corner leave the cavity after the next round trip. Hence, the relative outgoing intensity can be computed as

$$\Delta I_p = \frac{1}{R} \frac{\Delta s}{\Delta t} = \frac{4\pi c}{3\text{Re}(k)R^2} \frac{\beta(n)}{n^2}. \quad (\text{A.21})$$

## B Vectorial transfer matrix approach

The vectorial transfer matrix approach (VTMA) is a method to compute the optical modes of pillar microcavities [220–222]. To determine a solution of the vector Maxwell's equations (2.6) and (2.7) for a three-dimensional geometry as shown in Fig. 2.40, the electric and magnetic field is expanded in each pillar layer with respect to the modes of a cylindrical optical waveguide. The expansion coefficients of neighboring layers are related due to the continuity of the transverse components of the electric and magnetic fields at the layer interfaces, as described by Eqs. (2.9) and (2.10). Therefore, a relation between the fields for the topmost and the lowermost pillar layer can be expressed in terms of a transfer matrix. It is worth noting that conventional transfer matrices can only be applied to one-dimensional geometries and, therefore, describe only the mode structure in the longitudinal direction perpendicular to the layers. In contrast, the VTMA also provides the transverse mode structure. The method is exact as long as all waveguide modes are included in the expansions. However, for practical reasons waveguide modes which are unbounded in the transverse direction are ignored. This approximation is justified for pillars with sufficiently large diameter because the radiation in the transverse direction is negligible in this case. On top of this approximation the authors of Ref. [220] propose the so-called common-mode approximation (CMA), where only waveguide modes with the same mode numbers are coupled across interfaces. It turns out that in the regime of large diameters where the transfer matrix approach is valid, the results with and without the CMA are almost identical. In the following, we therefore only consider the method in the CMA.

Let us briefly review the well-known properties of modes in an infinite cylindrical waveguide with refractive index  $n \neq 1$  inside and  $n = 1$  outside the waveguide [392]. Inserting the ansatz (2.11) and (2.12) into the wave equations (2.8) gives Eq. (2.13) with  $\alpha^2 = n^2 \frac{\omega^2}{c^2} - \gamma^2$ . Inside the cavity  $\alpha^2$  is a positive constant which we denote by  $\beta^2$ . Outside  $\alpha^2$  is a negative constant denoted by  $-\delta^2$ . In the case of a circular cross section with radius  $R$ , the wave equation (2.8) together with the continuity conditions (2.9) and (2.10) has a solution provided

$$\left( \frac{n^2 J'_m(\beta R)}{\beta^2 J_m(\beta R)} + \frac{K'_m(\delta R)}{\delta^2 K_m(\delta R)} \right) \left( \frac{J'_m(\beta R)}{\beta^2 J_m(\beta R)} + \frac{K'_m(\delta R)}{\delta^2 K_m(\delta R)} \right) = \frac{m^2 \gamma^2 c^2}{R^2 \omega^2} \left( \frac{1}{\beta^2} + \frac{1}{\delta^2} \right)^2 \quad (\text{B.1})$$

with the  $m$ th order (modified) Bessel function of first kind  $J_m$  ( $K_m$ ) and its derivative  $J'_m$  ( $K'_m$ ). For a given frequency  $\omega$ , this resonance condition gives a set of  $\beta_{\nu m}$  labelled by the two mode numbers  $\nu \in \mathbb{N}$ , describing the field variation in radial direction, and  $m \in \mathbb{Z}$ , describing the field variation in azimuthal direction. Moreover, it is worth to emphasize that a non-vanishing r.h.s. of the resonance condition (B.1) couples TE and TM polarizations. However, it turns out that in the CMA the different polarizations

are effectively decoupled. Explicit formulas for the solutions  $\mathbf{E}(x, y)$  and  $\mathbf{H}(x, y)$  are summarized in Ref. [220].

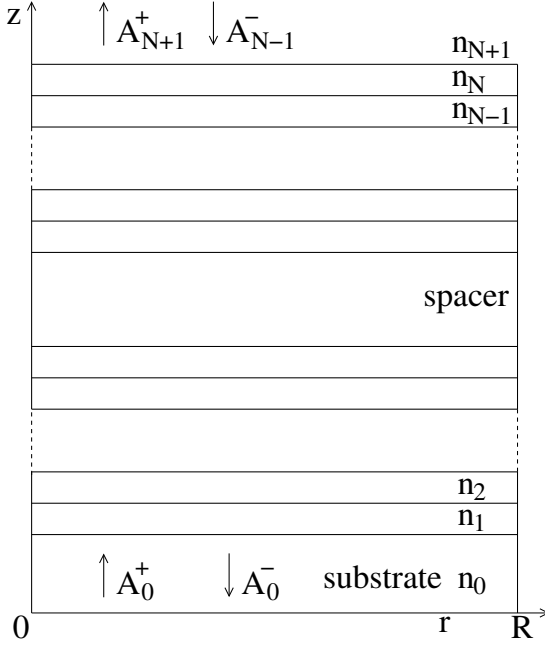


**Figure B.1:** Schematic drawing of the VCSEL-micropillar with radius  $R$  and refractive indices  $n_l$ .  $A_l^\pm$  denote the amplitudes of forward and backward propagating waves.

In the CMA, the fields in each layer are written as a superposition of a *single* pair of a forward and backward propagating waveguide solution

$$\begin{aligned}\mathbf{E}_l(x, y, z) &= [A_l^+ \exp(-i\gamma_l z) - A_l^- \exp(i\gamma_l z)] \mathbf{E}_l(x, y), \\ \mathbf{H}_l(x, y, z) &= [A_l^+ \exp(-i\gamma_l z) + A_l^- \exp(i\gamma_l z)] \mathbf{H}_l(x, y).\end{aligned}$$

The continuity relations (2.9) and (2.10) require that the transversal dependence of the fields is the same in all layers, i.e.,  $\beta_l = \beta$ . The longitudinal propagation constant is then given by

$$\gamma_l = \sqrt{n_l^2 \frac{\omega^2}{c^2} - \beta^2}. \quad (\text{B.2})$$

The amplitudes of the fields are related from one layer to the next as

$$\begin{pmatrix} A_{l+1}^- \\ A_{l+1}^+ \end{pmatrix} = M_l^{\text{TE/TM}} \begin{pmatrix} A_l^- \\ A_l^+ \end{pmatrix}. \quad (\text{B.3})$$

The matrix  $M_l^{\text{TE/TM}}$  is for TE polarization given by

$$M_l^{\text{TE}} = \frac{1}{2} \begin{pmatrix} (1 + 1/\gamma_l^{rel})/e_l^- & (1 - 1/\gamma_l^{rel})/e_l^+ \\ (1 - 1/\gamma_l^{rel})e_l^+ & (1 + 1/\gamma_l^{rel})e_l^- \end{pmatrix}, \quad (\text{B.4})$$

with  $\gamma_l^{rel} = \gamma_l/\gamma_{l+1}$  and  $e_l^\pm = \exp[i(\gamma_{l+1} \pm \gamma_l)z_l]$ . The variable  $z_l$  is the  $z$ -coordinate at the interface between layer  $l$  and  $l+1$ . For TM polarization the matrix takes the form

$$M_l^{\text{TM}} = \frac{1}{2} \begin{pmatrix} (\varepsilon_l^{rel} + \gamma_l^{rel})/e_l^- & (\varepsilon_l^{rel} - \gamma_l^{rel})/e_l^+ \\ (\varepsilon_l^{rel} - \gamma_l^{rel})e_l^+ & (\varepsilon_l^{rel} + \gamma_l^{rel})e_l^- \end{pmatrix}, \quad (\text{B.5})$$

where  $\varepsilon_l^{rel} = n_l^2/n_{l+1}^2$ . Knowing the local transfer matrices  $M_l^{\text{TE/TM}}$  we can relate the amplitudes at the topmost to the amplitudes at the lowermost layer, as schematically shown in Fig. B.1. This leads to

$$\begin{pmatrix} A_{N+1}^- \\ A_{N+1}^+ \end{pmatrix} = M^{\text{TE/TM}} \begin{pmatrix} A_0^- \\ A_0^+ \end{pmatrix} \quad (\text{B.6})$$

with the global transfer matrix

$$M^{\text{TE/TM}} = \prod_{l=0}^N M_l^{\text{TE/TM}}. \quad (\text{B.7})$$

Let us consider an incoming wave from below with normalized amplitude  $A_0^+ = 1$ , a reflected wave with amplitude  $A_0^- = r$  and a transmitted wave with amplitude  $A_{N+1}^+ = t$ . There is no incoming wave from the top,  $A_{N+1}^- = 0$ . For this situation the reflectivity  $R(\omega)$  and transmission  $T(\omega)$  can be computed as

$$R(\omega) = |r|^2 = \left| \frac{M_{12}^{\text{TE/TM}}}{M_{11}^{\text{TE/TM}}} \right|^2, \quad \text{and} \quad T(\omega) = |t|^2 = 1 - R(\omega). \quad (\text{B.8})$$

## Pillars with conical sidewalls

A closer inspection of Fig. 2.40 reveals a small conicity of the micropillar. Since often such a deformation cannot be avoided in the fabrication process it is important to know its impact on the mode properties. We therefore derive an extended version of the VTMA which allows to calculate optical modes in micropillars with small conicity.

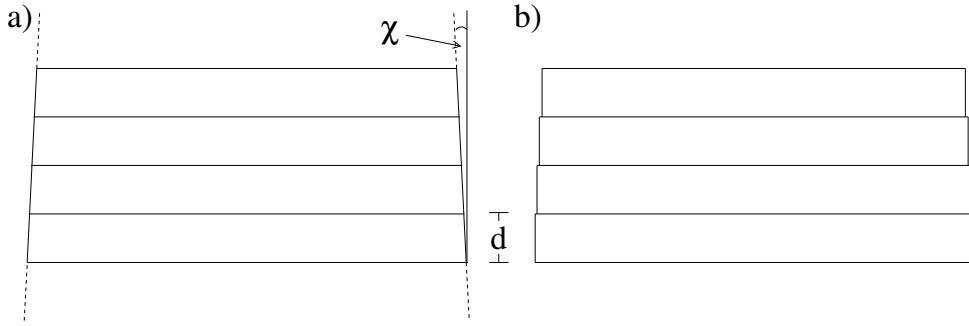


**Figure B.2:** (a) Sketch of a region in a micropillar with conicity. (b) Approximation to the geometry in (a).

Figure B.2(a) illustrates this situation. Typical angles  $\chi$  characterizing the conical shape are around  $5^\circ$  or below. The change of the radius along a layer with thickness  $d$  is  $\Delta R = d \tan \chi$ . With  $d = \lambda/(4n)$  follows  $\Delta R/(\lambda/n) = 0.25 \tan \chi$ . For  $\chi = 5^\circ$  we find that the change of the radius compared to the local wavelength is around two percent. Hence, we can safely approximate each layer by a cylinder with radius  $R_l$  as sketched in Fig. B.2(b). Because of its thickness the spacer layer should be splitted into several cylinders of smaller height.

We start from the VTMA and employ the CMA with  $\beta_l R_l = \beta R$ , where  $\beta$  and  $R$  are the propagation constant and the radius of the spacer layer, respectively. The underlying assumption is that the transversal mode structure changes only adiabatically along the pillar axis. Except for this modification the VTMA can be used in the same way as before.

## C Equation of motion for intraband correlations

The intraband correlations can be obtained in analogy to the derivation of Eq. (3.33). We restrict ourselves here to the equation of motion for the correlations of the conduction-band electrons. A similar equation can be derived for the valence-band carriers by exploiting the symmetry properties of the Hamiltonian (3.8). We find

$$\begin{aligned}
i\hbar \frac{d}{dt} C_{\alpha'\nu\nu'\alpha}^c = & -(\varepsilon_{\alpha'}^c + \varepsilon_\nu^c - \varepsilon_{\nu'}^c - \varepsilon_\alpha^c) C_{\alpha'\nu\nu'\alpha}^c \\
& - (V_{\alpha'\nu\nu'\alpha}^* - V_{\alpha'\nu\alpha\nu'}^*) [(1-f_\nu^c)(1-f_{\alpha'}^c) f_\nu^c f_\alpha^c - f_\nu^c f_{\alpha'}^c (1-f_{\nu'}^c)(1-f_\alpha^c)] \\
& + \sum_{\beta\beta'} \left\{ (f_{\nu'}^c - f_\nu^c) V_{\nu'\beta\beta'\nu} C_{\alpha'\beta\alpha\beta'}^{c+x} - (f_{\alpha'}^c - f_\alpha^c) V_{\alpha\beta\beta'\alpha'} C_{\nu\beta\nu'\beta'}^{c+x} \right. \\
& \quad \left. - (f_{\nu'}^c - f_{\alpha'}^c) V_{\nu'\beta\beta'\alpha'} C_{\nu\beta\alpha\beta'}^{c+x} + (f_\nu^c - f_\alpha^c) V_{\alpha\beta\beta'\nu} C_{\alpha'\beta\nu'\beta'}^{c+x} \right\} \\
& + \sum_{\beta\beta'} \left\{ f_{\beta'}^c V_{\beta'\beta\beta'\alpha'} C_{\beta\nu\nu'\alpha}^c + f_{\beta'}^c V_{\beta'\beta\beta'\nu} C_{\alpha'\beta\nu'\alpha}^c - f_\beta^c V_{\nu'\beta\beta'\beta} C_{\alpha'\nu\beta'\alpha}^c - f_\beta^c V_{\alpha\beta\beta'\beta} C_{\alpha'\nu\nu'\beta'}^c \right\} \\
& + \sum_{\beta\beta'} \left\{ (f_\beta^c + f_\beta^v) V_{\beta'\beta\beta'\alpha'} C_{\beta\nu\nu'\alpha}^c + (f_\beta^c + f_\beta^v) V_{\beta'\beta\beta'\nu} C_{\alpha'\beta'\nu'\alpha}^c \right. \\
& \quad \left. - (f_\beta^c + f_\beta^v) V_{\nu'\beta\beta\beta'} C_{\alpha'\nu\beta'\alpha}^c - (f_\beta^c + f_\beta^v) V_{\alpha\beta\beta\beta'} C_{\alpha'\nu\nu'\beta'}^c \right\} \\
& + \sum_{\beta\beta'} \left\{ (1-f_\alpha^c - f_{\nu'}^c) V_{\nu'\alpha\beta'\beta} C_{\alpha'\nu\beta\beta'}^c - (1-f_{\alpha'}^c - f_\nu^c) V_{\beta\beta'\nu\alpha'} C_{\beta\beta'\nu'\alpha}^c \right. \\
& \quad \left. - (f_{\alpha'}^c - f_\alpha^c) V_{\alpha\beta\alpha'\beta'} C_{\beta\nu\nu'\beta'}^c - (f_{\nu'}^c - f_{\alpha'}^c) V_{\beta\nu'\beta'\alpha'} C_{\beta\nu\beta'\alpha}^c \right. \\
& \quad \left. - (f_{\nu'}^c - f_\nu^c) V_{\beta\nu'\beta'\nu} C_{\alpha'\beta\beta'\alpha}^c - (f_\nu^c - f_\alpha^c) V_{\alpha\beta\nu\beta'} C_{\alpha'\beta\nu'\beta'}^c \right\}. \tag{C.1}
\end{aligned}$$

Here we have used the abbreviation  $C_{\alpha'\nu\nu'\alpha}^{c+x} = C_{\alpha'\nu\nu'\alpha}^c + C_{\alpha'\nu\nu'\alpha}^x$ . The terms can be interpreted in analogy to Eq. (3.33). However, the contribution due to the light-matter interaction vanishes for  $C_{\alpha'\nu\nu'\alpha}^c$  and  $C_{\alpha'\nu\nu'\alpha}^v$ .



## D Analytical results for $g^{(2)}(0)$

In this appendix, we study analytical solutions for the intensity correlation  $g^2(0)$  in the two limiting cases of strong and weak pumping. For this purpose we use the stationary limit of Eqs. (3.49), (3.52), and (3.61)–(3.64). Considering the resonant  $s$ -shell contributions from identical QDs, we replace  $\sum_{\nu'}$  by the number of QDs  $N$ . Inserting in Eq. (3.49) the photon-assisted polarization from Eq. (3.52), ignoring spontaneous emission for the above-threshold solution, and expressing the higher-order correlations with the help of Eqs. (3.63) and (3.64), we obtain from Eqs. (3.48) and (3.61)

$$g^{(2)}(0) - 1 = -\frac{\kappa(\kappa + \Gamma)}{2|g|^2 \langle b^\dagger b \rangle} \left( 1 + \frac{|g|^2 N}{\kappa(\kappa + \Gamma)} (1 - f_s^e - f_s^h) \right). \quad (\text{D.1})$$

In the limit  $\langle b^\dagger b \rangle / N \gg 1$ , the right-hand side vanishes. Hence we obtain  $g^{(2)}(0) = 1$ , i.e., well above threshold the light is coherent.

For the limiting case of weak pumping, we seek again the stationary solution of our coupled system of equations, now under the assumption that in Eq. (3.52) the stimulated emission term and the higher-order correlations  $\delta \langle b^\dagger b c_\nu^\dagger c_\nu \rangle$ ,  $\delta \langle b^\dagger b v_\nu^\dagger v_\nu \rangle$  can be neglected. A convenient way to solve for the intensity correlation function  $\delta \langle b^\dagger b^\dagger b b \rangle$  is to insert Eq. (3.62) into (3.61). The higher-order correlations in Eq. (3.62) are replaced by the static solution of Eqs. (3.63) and (3.64), while in the latter  $\langle b^\dagger v_\nu^\dagger c_\nu \rangle$  is replaced by Eq. (3.49), and  $\delta \langle b^\dagger b^\dagger b v_\nu^\dagger c_\nu \rangle$  is traced back to  $\delta \langle b^\dagger b^\dagger b b \rangle$  with the stationary solution of Eq. (3.61). As explained above, we ignore the quadruplet correlations occurring in Eq. (3.62). Together with Eqs. (3.48) and (3.49) we finally obtain

$$\left( \frac{\kappa(3\kappa + \Gamma)}{|g|^2 N} + (1 - f_s^e - f_s^h) \right) [g^{(2)}(0) - 2] = -\frac{2(f_s^e + f_s^h)}{N} [g^{(2)}(0) - 1] - \frac{2\kappa(3\kappa + 2\Gamma)}{|g|^2 N^2}. \quad (\text{D.2})$$

To evaluate this formula further, we restrict ourselves to the case

$$\frac{\kappa^2}{|g|^2 N} \gg 1, \quad (\text{D.3})$$

or  $2\kappa/\hbar \gg N/\tau_l$ , i.e., the cavity loss rate is much larger than the total rate of spontaneous emission into the laser mode. In this “bad cavity limit” [44], in which typical semiconductor lasers operate, we obtain as an analytical result of our theory

$$g^{(2)}(0) = 2 - \frac{2}{N}. \quad (\text{D.4})$$

This is an important finding because it provides the statistics of thermal light in the limit of many QDs,  $g^{(2)}(0) = 2$ , and in the opposite limit of a single QD it gives the statistics of a single-photon emitter,  $g^{(2)}(0) = 0$ .



## E Interplay of time constants

For the evaluation of our laser theory in Section 3.4, we treat the rate of spontaneous emission into the non-lasing modes  $1/\tau_{\text{nl}}$  as an extrinsic parameter, which is determined by the properties of the laser resonator. Depending on the particular cavity design, other high- $Q$  resonator modes as well as a quasi-continuum of low- $Q$  leaky modes can contribute.

The spontaneous emission into the laser mode can be calculated from the light-matter coupling strength  $|g|^2 = |g_{\xi_l s}|^2$  for this mode,  $\kappa$ , and  $\Gamma$ . Restricting the adiabatic solution of Eq. (3.52) to the spontaneous emission into the laser mode and using Eq. (3.50) to define the corresponding rate  $1/\tau_l$  according to

$$\frac{d}{dt} f_s^{e,h} \Big|_{l,\text{spont}} = -\frac{f_s^e f_s^h}{\tau_l}, \quad (\text{E.1})$$

we find

$$\frac{1}{\tau_l} = \frac{2}{\hbar} \frac{|g|^2}{\kappa + \Gamma}. \quad (\text{E.2})$$

With  $\tau_l$  and  $\tau_{\text{nl}}$  the  $\beta$ -factor follows from Eq. (3.55).

In Section 3.4 we present the figures in the common style where the  $\beta$ -factor is varied, as it is the most important parameter characterizing the cavity efficiency, while the total rate of spontaneous emission  $1/\tau_{\text{sp}} = 1/\tau_l + 1/\tau_{\text{nl}}$  is held constant. To achieve such a situation, for various  $\beta$ -values both  $\tau_{\text{nl}}$  and  $\tau_l$  need to be changed. Note that the latter requires a change of the light-matter coupling strength according to Eq. (E.2), which is possible for a given dipole coupling by a modification of the mode functions, and/or by a change of the lifetime of the cavity mode.

In Section 3.4.6 the presented theory is applied to pillar microcavities with various diameters. In such a situation, the spontaneous emission into non-lasing modes is practically constant due to the unchanging contributions of leaky modes, while the spontaneous emission into the laser mode is modified by the Purcell effect.

The Purcell factor  $F_P$  is defined as the ratio of the rate of spontaneous emission into the cavity mode,  $1/\tau_l$ , to the rate of spontaneous emission into free space,  $1/\tau_{\text{free}}$ . We can express the  $\beta$ -factor in terms of  $F_P$  as

$$\beta = \frac{F_P}{dF_P + \frac{\tau_{\text{free}}}{\tau_{\text{nl}}}} = \frac{\frac{1}{\tau_l}}{\frac{d}{\tau_l} + \frac{1}{\tau_{\text{nl}}}}, \quad (\text{E.3})$$

where additionally a possible degeneracy  $d$  of the fundamental mode has been included, see the article by J.-M. Gérard in Ref. [10].



# Acknowledgements

In the first place, I would like to thank Prof. F. Jahnke in whose research group a significant part of the work was carried out.

I further acknowledge fruitful collaboration on subjects related to this work with Prof. K.-H. Ahn, Prof. J. Hong, Y.-H. Kim, Prof. K. J. Chang, T. Harayama, H. Schomerus, M. Hentschel, N. Baer, C. Gies, P. Gartner, and M. Lorke on the theoretical side and Prof. P. Michler, S. M. Ulrich, S. Ates, M. Benyoucef, Prof. M. Bayer, H. Kurtze, T. Auer, T. Berstermann, F. Laeri, Prof. J. Gutowski, Prof. D. Hommel, Prof. T. Fukushima, H. Lohmeyer, K. Sebald, R. Kröger, and C. Kruse on the experimental side.

Next I would like to thank N. Baer, C. Gies, P. Gartner, H. Lohmeyer, M. Lorke, J. Nagler, F. Anders, S. Ritter, and J. Sebeck for useful comments on the manuscript.

This work was financially supported by the DFG research groups “Quantum Optics in Semiconductor Nanostructures” and “Physics of nitride-based, nanostructured, light-emitting devices”, and grants for CPU time at the Forschungszentrum Jülich (Germany)

Finally, I thank my wife and children for their love, patience, and support.